THE EFFECT OF WATER-SOLUBLE POLYMERS ON THE MICROSTRUCTURE AND PROPERTIES OF FREEZE-CAST ALUMINA CERAMICS

by

Christopher Michael Pekor

BS, University of Pittsburgh, 2003

Submitted to the Graduate Faculty of

Swanson School of Engineering in partial fulfillment

of the requirements for the degree of

Doctor of Philosophy

University of Pittsburgh

2010

UNIVERSITY OF PITTSBURGH

SWANSON SCHOOL OF ENGINEERING

This dissertation was presented

by

Christopher Michael Pekor

It was defended on

March 26, 2010

and approved by

Pradeep P. Fulay, Professor, Mechanical Engineering and Materials Science Department

Jörg M. K. Wiezorek, Associate Professor, Mechanical Engineering and Materials Science Department

John P. Leonard, Assistant Professor, Mechanical Engineering and Materials Science Department

Luis E. Vallejo, Professor, Civil and Environmental Engineering Department

Dissertation Director: Ian Nettleship, Associate Professor, Mechanical Engineering and Materials Science Department

THE EFFECT OF WATER-SOLUBLE POLYMERS ON THE MICROSTRUCTURE AND PROPERTIES OF FREEZE-CAST ALUMINA CERAMICS

Christopher Michael Pekor, Ph.D.

University of Pittsburgh, 2010

Porous ceramics can be divided into three separate classes based on their pore size: microporous ceramics with pores less than 2 nm, mesoporous ceramics with pores in the range of 2-50 nm and macroporous ceramics with pores that are greater than 50 nm. In particular, macroporous ceramics are used in a variety of applications such as refractories, molten metal filtration, diesel particulate filters, heterogeneous catalyst supports and biomedical scaffolds.

Freeze casting is a novel method used to create macroporous ceramics. In this method growing ice crystals act as a template for the pores and are solidified, often directionally, through a ceramic dispersion and removed from the green body through a freeze drying procedure. This method has attracted some attention over the past few years due to its relative simplicity, flexibility and environmental friendliness. On top of this freeze casting is capable of producing materials with high pore volume fractions, which is an advantage over processing by packing and necking of particles, where the pore volume fraction is typically less than 50%. Many of the basic processing variables that affect the freeze cast microstructure, such as the temperature gradient, interfacial velocity and solid loading of the dispersion have been well established in the literature. On the other hand, areas such as the effect of additives on the microstructure and mechanical properties have not been covered in great detail.

In this study the concept of constitutional supercooling from basic solidification theory is used to explain the effects of two water-soluble polymers, polyethylene glycol and polyvinyl alcohol, on the microstructure of freeze cast alumina ceramics. In addition, changes in the observed microstructure will be related to experimentally determined values of permeability and compressive strength.

TABLE OF CONTENTS

LIST OF TABLES

LIST OF FIGURES

PREFACE

The results presented here would not have been possible without assistance from a number of individuals. First and foremost I would like to thank my advisor, Professor Ian Nettleship, for his guidance, support and advice throughout the years. I would also like to thank all of the members of my committee for their insightful discussion regarding my research. I am also grateful to the faculty of the Mechanical Engineering and Materials Science Department for the helpful instruction that I have received from them in and out of the classroom. The technical support provided by Al Stewart is also gratefully acknowledged. Additionally I would like to thank some of the graduate and undergraduate students who have worked with me over the years, particularly; Tony Finoli, Ed Magee and Ben Groth.

Finally I would like to thank my family and friends for all of the support that they have given me over the years. They have been there through all of the bumps in the road and have helped to make this journey easier.

The use of the Materials Micro-Characterization Laboratory in the Mechanical Engineering and Materials Science Department at Pitt is gratefully acknowledged.

This research was supported by the National Science Foundation under grant DMR 0404874.

1.0 INTRODUCTION

In the past the idea of porosity in technical ceramics was viewed as a problem and efforts were made to develop processes that eliminated as much residual porosity as possible, resulting in ceramics at or near theoretical density. On the other hand, traditional porous ceramic materials such as bricks, refractories and cements have been used in structural applications for hundreds of years. The emergence of highly porous technical ceramics is a relatively new field that has gained a great deal of attention over the last decade due to their potential use in a variety of wide ranging applications.

According to the IUPAC [1], ceramics can be divided into three separate classes based on their pore size: microporous ceramics with pores less than 2 nm, mesoporous ceramics with pores in the range of 2-50 nm and macroporous ceramics with pores that are greater than 50 nm. In particular, macroporous ceramics are used in a variety of applications such as refractories, molten metal filtration, diesel particulate filters, heterogeneous catalyst supports and biomedical scaffolds [2-6].

Macroporous ceramics have been successfully made for many years by plastic forming processes such as extrusion, which give high permeability structures with large regular channels. This process is limited by the size constraints of the die, however, and cannot produce structures with pores less than approximately 100 μm in size. Other ways to fabricate macroporous ceramics can be divided into three classes [7], including replication, direct foaming and

templating. Replication involves creating a replica of a suitable structure by coating with a ceramic dispersion, followed by removal of the substructure by thermal decomposition [8]. An example would be the coating of polyurethane foam to create a molten metal filter [9,10]. The foams that are created using this method generally have large pores (>100μm) but low permeabilities compared to extruded structures. Direct foaming uses the introduction of air bubbles into a ceramic dispersion through mechanical agitation or aeration, followed by drying of the liquid and firing. The final method to obtain macroporous ceramics is known as templating, in which a non-ceramic material is introduced which acts as a template for the pore structure in the ceramic material. This has been accomplished in the past by the use of fugitive phases such as wood [11,12], fibers [13] or polymeric spheres [14]. Once processing is complete the template is removed by appropriate means such as thermal decomposition.

Freeze casting is a novel method used to create macroporous ceramics. Of the above mentioned routes to create macroporous ceramics, freeze casting belongs to the templating techniques. In this method growing ice crystals act as the template for the pores and are solidified, often directionally, through a ceramic dispersion and removed from the green body through a freeze drying procedure. This method has attracted some attention over the past few years due to its relative simplicity, flexibility and environmental friendliness. On top of this freeze casting is capable of producing materials with high pore volume fractions, which is an advantage over processing by packing and necking of particles, where the pore volume fraction is typically less than 50%. Many of the basic processing variables that affect the freeze cast microstructure, such as the temperature gradient, interfacial velocity and solid loading of the dispersion have been well established in the literature [15]. Despite the basic processing science being covered there exist a great deal of applied science related to freeze casting that still needs

to be more thoroughly examined. For example the effect of additives on the growth of the ice crystals and the resulting impact on the microstructure has not been systematically studied. On top of this a separation of the effects of particles and additives on the processes that occur during freeze casting must be accomplished to truly understand how to modify the microstructure. Also, there has been limited measurement of the properties of these ceramics. Data exists in the literature concerning compressive strengths [15], but few studies concerning transport properties, such as permeability, have been completed. Permeability is one of the most important properties with regard to macroporous ceramics in all of the desired applications, and as such it is important to not only determine the permeability, but also to understand how changes in microstructure due to altering processing variables affect it.

2.0 BACKGROUND

2.1 SOLIDIFICATION THEORY

Solidification is a basic phase transformation by which a liquid is converted to a solid through the removal of heat. This phenomenon plays an important role in a wide variety of technical fields including materials science, metallurgy, physics, chemistry, geology and most importantly everyday life, as many commercially produced materials involve some type of solidification during their processing. Due to the wide applicability of this topic the amount of literature that has been accumulated over the years is vast. In the field of materials science a proper understanding of the mechanisms that occur during solidification and the factors that control these mechanisms allows one to tailor the properties of materials to suit a variety of needs. The literature on the solidification of metals has seen intense study and the knowledge derived from this can be applied to many non-metallic liquids. Due to this circumstance it is only proper to start with a review of some of the fundamentals of the solidification theory of metals.

2.1.1 The Structure of the Solid-Liquid Interface during Solidification

The first step in any solidification process is the nucleation of solid in the liquid phase. Once a nucleus has been formed it will continue to grow provided that atoms can continually attach to the interface. During the process of growth the solid-liquid interface adopts a specific structure

at the atomic scale that depends on the differences in structure and bonding between the solid and liquid phases. Materials are generally classified as either faceted or non-faceted at the atomic scale based on their differences in atomic attachment kinetics. An illustration of faceted and non-faceted interfaces can be seen below in Figure 1.

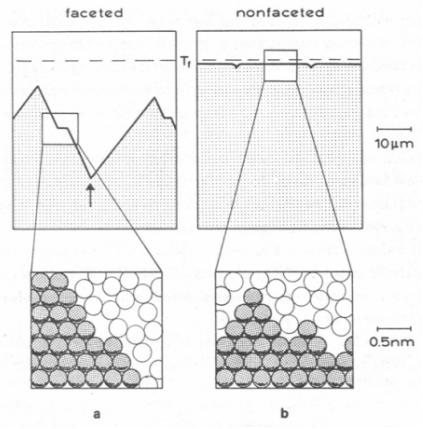

Figure 1. Illustration of a) faceted and b) nonfaceted interfaces at both the microscopic (top) and atomic (bottom) scale [16].

For non-faceted materials, atoms can be added to the growing interface very easily due to the roughness that is present at the atomic scale. Atomic attachment in these materials is largely independent of crystal orientation; that is the atoms can readily attach to the surface and tend not to favor certain crystallographic planes. On the contrary faceted materials are smooth at the atomic scale and atomic attachment is easier on rougher high index planes than on the smoother low index planes, often leading to anisotropy in growth rates along different directions. Faceted materials generally have more complicated crystal structures and directional bonding that give angular surfaces (facets) on the growing crystal. Due to the ease of atomic attachment non-

faceted materials generally grow at a temperature close to the melting point while faceted materials require some local undercooling to promote growth. A criterion exists that helps predict which type of interface a material will solidify with and is shown in equation 1.

$$\alpha = \Delta S_f / R \qquad (1)$$

In this equation α is the dimensionless entropy and ΔS_f is the entropy of fusion, defined as $\Delta S_f = \Delta H_f / T_f$, where H_f is the enthalpy of fusion. The dimensionless entropy is also known as the Jackson alpha factor [17] since this criterion was originally determined by him. In general materials that have an alpha factor less than 2 have a tendency to grow non-faceted while those with an alpha factor greater than 2 tend to grow faceted. Most metals have an alpha factor that is less than 2 and display non-faceted solidification. In general, higher values of the entropy of fusion imply greater differences between the growth rates of low and high index planes.

2.1.2 Morphological Instability of the Solid-Liquid Interface for Pure Substances

In the case of a pure substance perturbations in the solid-liquid interface can develop due to a number of reasons, including the presence of insoluble particles or temperature fluctuations. There are two cases that can occur once this perturbation has been established. The first case is that the perturbation will amplify and the interface will become unstable, while in the second case the perturbation itself will become unstable and disappear, leading to a planar interface. During the solidification of a pure substance the stability depends entirely on the direction of heat flow. In the case of columnar (directional) solidification the heat flow is opposite of the solidification direction. If a perturbation forms the temperature gradient in the liquid will increase while the gradient in the solid tends to decrease. This leads to a situation where more heat flows into the tip of the perturbation than the solid, causing the tip to melt back. On the

other hand in equiaxed casting, the crystals grow out into an undercooled melt. In this case a negative temperature gradient exists into the liquid and the tip of the perturbation rejects more heat. This causes the local growth rate to increase, the perturbation to amplify and the interface becomes unstable. From these two situations it is concluded that if the temperature gradient is positive then the interface will tend to be stable while if the temperature gradient is negative instability will be favored.

$$G = dT_q/dz < 0 \quad \text{instability} \qquad (2)$$

$$G = dT_q/dz > 0 \quad \text{stability} \qquad (3)$$

In equations 2 and 3 G is the temperature gradient and z is the directional coordinate relating to the distance from the solid-liquid interface. In the case of pure substances the conditions that dictate stability and instability are determined completely by temperature gradients. However, this is an ideal case as often some type of impurity or solute is present during solidification. Even more common is the case of the solidification of alloys where a certain amount of one metal is dissolved in the other. The stability of these interfaces will now be examined.

2.1.3 Interface Stability during the Solidification of Binary Alloys

When a crystal is formed in the melt of an alloy a local change in the composition is created. This arises because the chemical potentials of the liquid and solid phases for the two components of the alloy, say A and B, must be at equilibrium according to:

$$\mu_l^A = \mu s^A \qquad (4)$$

$$\mu_l^B = \mu_s^B \qquad (5)$$

In this case the subscripts *l* and *s* denote liquid and solid, respectively. The composition difference at the interface can be described by the distribution coefficient which is defined as:

$$k = C_o / C_l \qquad (6)$$

In this case C_o and C_l represent the bulk and liquid compositions, respectively. These compositions are illustrated in Figure 2, which is an expanded part of a binary eutectic phase diagram.

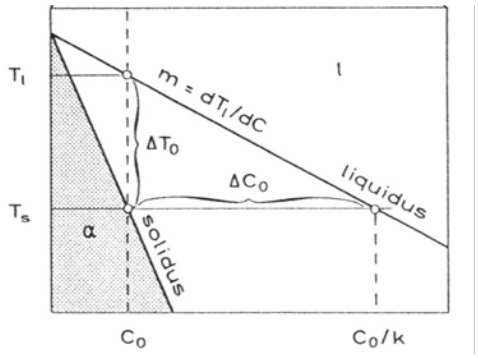

Figure 2. An expanded portion of a simple binary eutectic phase diagram where the solidus and liquidus lines have been assumed straight to simplify mathematical analysis [16].

It should be noted that the solidus and liquidus lines in Figure 2 are assumed to be straight, which is in violation of the conditions for thermodynamic equilibrium. By assuming this, the values of the distribution coefficient (k) and the liquidus slope (m) become constants and simplify the mathematical analysis. Two other quantities that are useful in the study of stability in binary systems are the temperature difference between the liquidus and solidus (ΔT_o) and the solute concentration difference between the liquid and solid solute contents at the solidus temperature (ΔC_o). These quantities are illustrated in Figure 2 and are defined as:

$$\Delta T_o = -m\Delta C_o = T_l - T_s \qquad (7)$$

$$\Delta C_o = C_o(1-k) / k \qquad (8)$$

During alloy solidification solute is rejected and piles up in front of the growing interface since the solubility of the solute is lower in the newly formed solid than in the liquid. The solute forms a boundary layer in front of the interface which is depicted in Figure 3 for a planar solid-liquid interface.

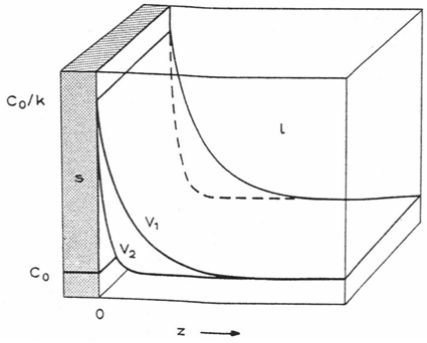

Figure 3. Illustration of a steady state boundary layer that form as a result of solute rejection in front of the planar solid-liquid interface. The boundary becomes steeper with increasing growth rate ($V_2>V_1$) due to a higher rate of solute rejection [16].

This boundary layer is created during a transient state before steady-state solidification begins. The solute concentration in the boundary layer decreases exponentially from a value of C_o/k to Co according to equation 9 [18].

$$C_l = C_o + \Delta C_o \exp(-Vz / D) \qquad (9)$$

In this equation V is the growth rate, or interfacial velocity and D is the diffusion coefficient of the solute in the liquid. The thickness of this boundary layer (δ_c) is mathematically infinite but can be estimated as an "equivalent boundary layer" which is defined as:

$$\delta_c = 2D / V \qquad (10)$$

The thickness of this boundary layer is inversely proportional to the growth rate; hence the curve becomes steeper with increasing V, as seen in Figure 3. If a flux balance is performed at the interface the interfacial concentration gradient in the liquid (G_c) can be determined as [16]:

$$G_c = -(V/D)\Delta C_o \qquad (11)$$

It has now been established that the concentration ahead of the solid-liquid interface changes substantially during solidification. These changes in concentration in turn affect the local equilibrium solidification temperature in the liquid which is given by:

$$T_l(C_o) - T_l = m(C_o - C_l) \qquad (12)$$

where $T_l(C_o)$ is the liquidus temperature at the initial composition (C_o). The concentration boundary layer that was depicted in Figure 3 can be converted into a liquidus-temperature boundary layer through the use of the phase diagram for the system. This is illustrated in Figure 4.

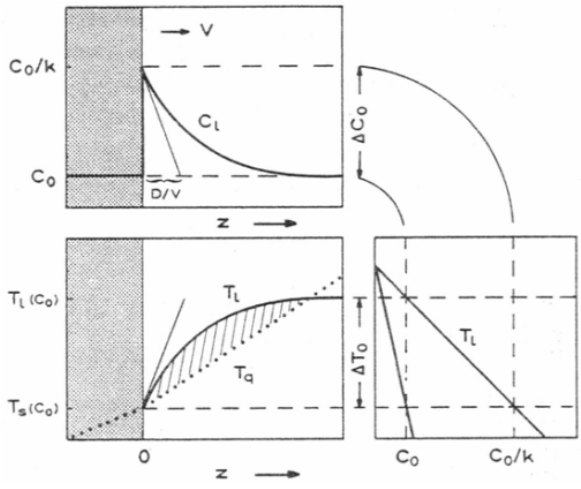

Figure 4. Illustration of the origin of constitutional supercooling. When the temperature gradient imposed by the external heat flow (T_q) is less than the gradient imposed by the liquidus (T_l) the liquid is undercooled. This is represented by the cross-hatched region in the lower left figure [16].

As the liquid concentration (C_l) in the steady-state boundary layer decreases as the distance (z) from the solidification front is increased the local equilibrium liquidus temperature (T_l) increases as given by the phase diagram. This is depicted by the heavy curve in Figure 4. The dashed line T_q represents the temperature gradient in the liquid imposed by the external gradient from heat flow, as defined in equations 2 and 3. For atomic addition to continue at the solid-liquid interface ($z = 0$) T_q must be less than or equal to T_s. Due to this the liquid in front of the interface may find itself at T_q, which is below the equilibrium liquidus temperature, and is said to be 'undercooled'. The cross-hatched region in Figure 4 depicts an area where the gradient of T_q is less than the gradient of T_l and is known as the zone of *constitutional supercooling*. This condition was first qualitatively discussed by Rutter and Chalmers [19] and later elaborated on by Tiller et al. [18]. Any liquid that is in this zone is metastable and a driving force for perturbations to form exists. If such a perturbation does form the local concentration gradient and the local liquidus temperature gradient will increase, thus preserving the constitutionally supercooled zone. The condition for a zone of constitutional supercooling to exist is that the temperature gradient (G) at the solid-liquid interface must be less than the gradient of the liquidus temperature change. The liquidus temperature change gradient is obtained by multiplying the concentration gradient G_c by the liquidus slope (m) thus giving the condition for undercooling as:

$$G < mG_c \qquad (13)$$

The interface concentration gradient in the liquid (G_c) has already been defined in equation 11 and can be substituted into equation 13 to yield:

$$G < -\frac{mV\Delta C_o}{D} \qquad (14)$$

Furthermore equation 7 can be used to simplify the expression to its usual form of:

$$\frac{G}{V} = \frac{\Delta T_0}{D} \qquad (15)$$

Therefore if the quantity on the left hand side of equation 15 is less than quantity on the right instability of the interface will result. Even for very low solute concentrations high temperature gradients must be imposed to suppress instability. The criterion established above allows one to predict the onset of instability but gives no indications of either the form or scale of the perturbations that will develop, which can be obtained using perturbation analysis.

The constitutional supercooling theory has a major drawback, which is that it ignores the effect of surface tension at the interface, which should have an effect on the overall stability. Perturbation analysis, also known as linear stability analysis involves mathematically perturbing an interface and examining whether these disturbances grow or disappear. Assume that the perturbed interface can be described by a simple sine function:

$$z = \varepsilon \sin(\omega y) \qquad (16)$$

In this equation ε is the amplitude of the perturbation and $\omega = 2\pi/\lambda$ is the wave number. Such an interface is depicted in Figure 5.

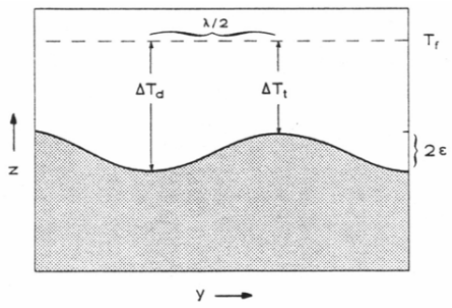

Figure 5. Illustration of a perturbed solid-liquid interface showing the onset of a morphological instability that can be approximated as a sinusoidal curve [16].

The temperature of such an interface (T^*) can be calculated by considering temperature differences due to local interface composition and local interface curvature. These quantities are accounted for by the last two terms in equation 17, respectively.

$$T^* = T_f + mC_l^* - \Gamma K^* \qquad (17)$$

In this equation T_f is the melting point, $\Gamma = \sigma/\Delta s_f$ is the Gibbs-Thomson coefficient and $K^* = 1/r_1 + 1/r_2$ is the interface curvature. Based on equation 17 the temperature difference between the tips (T_t) and the depressions (T_d) in Figure 5 is given by:

$$T_t - T_d = m(C_t - C_d) - \Gamma(K_t - K_d) \qquad (18)$$

The curvatures K_t and K_d can be obtained by taking the second derivative of equation 16 and are given by:

$$K_t = -K_d = \frac{4\pi^2 \varepsilon}{\lambda^2} \qquad (19)$$

It is assumed that the temperature and concentration fields near the interface are unaffected by the presence of a small perturbation. Due to this the differences in temperature and concentration between the tips and depressions is obtainable using the gradients that exist at the interface. This gives:

$$T_t - T_d = 2\varepsilon G \qquad (20)$$

$$C_t - C_d = 2\varepsilon G_c \qquad (21)$$

Now equations 19-21 can be substituted back into equation 18 to give:

$$\lambda = 2\pi(\Gamma/\varphi)^{1/2} = \lambda_i \qquad (22)$$

where $\varphi = mG_c - G$ is the degree of constitutional supercooling. For $\varphi > 0$ a positive driving force for perturbation growth exists and $\varphi = 0$ is the limiting condition for constitutional supercooling. Equation 22 defines a critical perturbation wavelength (λ_i) that is stationary and will experience neither tip nor depression growth. The term Γ/φ is the ratio of the capillarity force to the driving force for instability. As φ goes to zero the critical wavelength becomes infinite, which makes sense since the planar interface should still be present at the limit of instability. If the system is far from the limit of instability a situation arises where $G << mG_c = (\Delta T_o V)/D$. In this situation the wavelength becomes:

$$\lambda_i = 2\pi\left(\frac{D\Gamma}{V\Delta T_o}\right)^{1/2} \qquad (23)$$

Equation 23 shows that the wavelength associated with the unstable morphology depends on the diffusion length (D/V) and the capillarity length ($\Gamma/\Delta T_o$). Thus, by decreasing V or ΔT_o the minimum unstable wavelength is increased.

A more complicated analysis was performed by Mullins and Sekerka [20] that provides a relationship between ε and λ that is time dependent. The mathematics of this analysis is lengthy and will not be presented here. Instead a simplified result from this analysis is given by:

$$\frac{\dot{\varepsilon}}{\varepsilon} = \left(\frac{V}{mG_c}\right)\left(b - \frac{V}{D}\right)\left(-\omega^2\Gamma - G + mG_c\right) \qquad (24)$$

where $\dot{\varepsilon}$ = dε/dt describes the rate of development of the amplitude of the small perturbation and b is a constant. A representative plot of equation 24 can be seen in Figure 6.

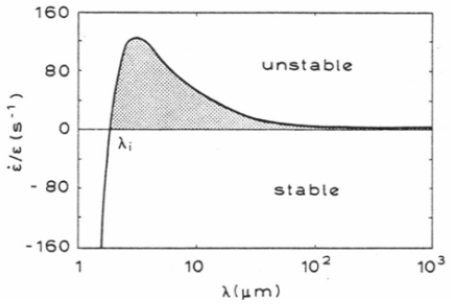

Figure 6. Plot of the rate of development of a perturbation at a constitutionally supercooled interface. The plot illustrates the critical perturbation wavelength and regions of stability and instability for an Al-2wt%Cu alloy [16].

As can be seen in Figure 6 for the case of wavelengths below λ_i the perturbation disappears due to high curvature and the interface is stable. The converse is true for wavelengths above λ_i as the sinusoidal perturbation becomes amplified and the interface is unstable. At the value of λ_i the system is at the limit of stability under conditions of constitutional supercooling. At this point the second term in equation 24 vanishes as λ is infinite here and the third term goes to zero when $\omega^2\Gamma = mG_c - G = \varphi$, as φ is equal to zero at the limit for constitutional supercooling. The end result of the second and third terms dropping out is that we end up with equation 22, proving the validity of either approach.

Now that the conditions leading up to interfacial instability have been discussed it is important to understand how these propagate through the melt and form the final solidified structure.

2.1.4 Cells and Dendrites – Development of Solidification Microstructures

Once a system has passed the limit of stability due to constitutional supercooling effects, the perturbations will grow rapidly into the liquid either as cells or dendrites, depending on the cooling conditions and hence heat flow during solidification.

In directional or columnar solidification the heat flow is opposite to the growth direction, as mentioned in the section 2.1.2. This situation is referred to as constrained growth, since the growing dendrites are constrained to grow at a given velocity dictated by the rate of heat removal. In this case the growing dendrites are parallel to one another and exhibit a characteristic spacing known as the primary spacing (λ_1). On the other hand, in equiaxed solidification the heat flows directly from the crystal into the melt and the dendrites can grow freely and as fast as the supercooling allows. In this case the dendrites will grow radially until they impinge upon another dendrite, forming a grain boundary, with each grain made up of a single dendrite. The primary spacing in this case is usually taken as the grain diameter. The spacing of the secondary branches off of the primary dendrite can be defined in both directional and equiaxed solidification.

Dendrite growth begins with the breakdown of an initially planar interface due to solute rejection and constitutional supercooling, as discussed earlier. As the tip begins to grow into the supercooled liquid it begins to reject solute laterally. The depressions accumulate the excess solute and advance much slower than the tips. Eventually the interface breaks down into a series of cells, which are significantly amplified perturbations. A depiction of a cellular interface can be seen in Figure 7.

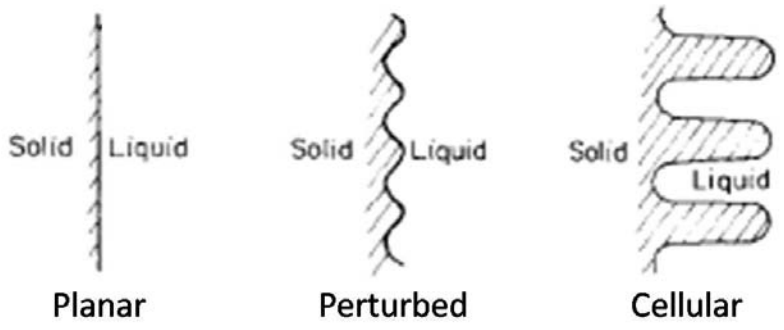

Figure 7. Illustration of the breakdown of a planar interface into a cellular interface through the growth of perturbations. [21]

It should be noted that the cell spacing that is exhibited is significantly larger than the initial wavelength of the perturbation. Cells are only found during the directional solidification of alloys and grow under conditions that are close to the limit of stability of the planar interface. The cellular morphology typically breaks down into a dendritic morphology due to solute rejection into the intercellular liquid that causes destabilization of the interface and the formation of secondary dendrite arms. Since the dendritic growth morphology is often encountered in solidification the focus of the rest of this section will deal with dendrite growth.

Dendrites are crystals that unlike cells grow far from the limit of stability and tend to adopt orientations that are close to the direction of heat removal but still along a preferred crystallographic orientation. In the case of equiaxed solidification the dendrites grow along all of the crystallographically preferred growth directions provided that the heat removal is uniform in all directions, as in an undercooled melt. Dendrites can form branches of various orders, that is, depending on the growing conditions further branching beyond secondary arms can occur. A growing dendrite is depicted below in Figure 8.

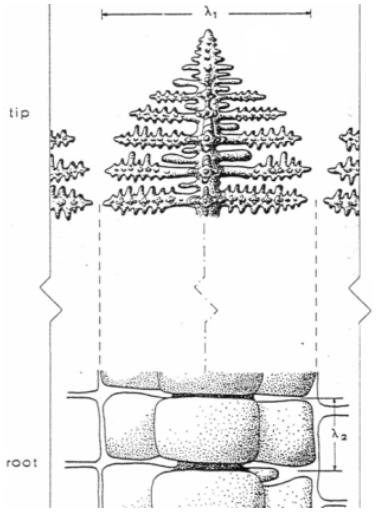

Figure 8. Illustration of a growing dendrite with both the primary (λ_1) and secondary (λ_2) spacing depicted. The two parts of the figure represent the root and tip of the dendrite and are drawn at the same scale, illustrating the coarsening that takes place during the growth of a dendrite [16].

Dendrites are commonly characterized by their primary (λ_1) and secondary (λ_2) arm spacing. The primary spacing is established early in the solidification and under steady state conditions will remain constant. The spacing of secondary dendrite arms can increase enormously due to the fact that once a growing arm impinges upon the diffusion field of another arm it will stop growing and begin to coarsen. In other words the secondary arms experience a long time in contact with the liquid. On top of this the ripening process can cause small tertiary and higher order arms to melt back, thus increasing the secondary spacing.

Many factors such as the growth rate and dendrite spacing are heavily dependent upon the processes that occur at the tip of the dendrite. As the dendrite grows the tip is able to reject both heat and solute. In the case of directional growth, provided that the temperature gradient is greater than zero, the heat is transported through the solid and the dendrite tip only rejects solute. This greatly simplifies the analysis of dendrite growth and will now be considered in more detail. The solute rejection at the dendrite tip is similar to that at a planar solid-liquid interface, as a

diffusion boundary layer is introduced as well as a situation that promotes constitutional supercooling. The diffusion boundary layer thickness around the tip is proportional to the tip radius with sharper tips being able to reject solute more efficiently and hence grow more rapidly. The limit to the sharpness of the dendrite tip is the critical radius of nucleation, at which point the growth rate is zero. Often when analyzing dendrite growth the tip is assumed to be spherical to simplify the mathematics involved, even though the shape is more closely approximated by a paraboloid of revolution. An expression for the approximation of the tip radius of a dendrite growing close to the limit of marginal stability was developed by Kurz and Fisher [22] and is as follows:

$$R^2V = \frac{4\pi^2 D\Gamma}{\Delta T_o k} \qquad (25)$$

In this equation k is the distribution coefficient and R is the dendrite tip radius, which influences other morphological parameters of the growing dendrite such as the primary and secondary spacing.

The primary spacing of dendrites after steady state directional growth is one of the most important parameters to understand as it has a direct link to the mechanical properties of the solid. This quantity can be difficult to measure directly so efforts came about by numerous authors [22-25] to develop relationships to calculate this quantity. For the case of directional growth the dendrite cross section can be approximated as an ellipse, of which the smaller radius of curvature is given by:

$$R = b^2/a \qquad (26)$$

The quantities b and a are defined as the lengths of the minor and major half-axes, respectively and are illustrated in Figure 9.

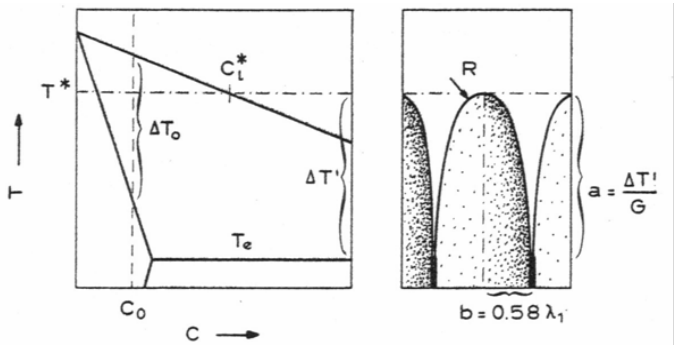

Figure 9. Illustration of the relevant geometry of a growing dendrite tip and the associated quantities on the phase diagram necessary to derive a relation for primary dendrite spacing [16].

The minor half-axis b is proportional to the primary spacing with the constant of proportionality depending on the geometrical model used. If a hexagonal arrangement of dendrites is assumed the last liquid to solidify would be at the center of gravity of an equilateral triangle that is formed by three packed dendrites. From simple geometry this leads to $b = 0.58\lambda_1$. The value of a is defined as the difference between the temperatures at the tip and the root of the dendrite divided by the temperature gradient.

$$a = \frac{\Delta T'}{G} = \frac{T^* - T_s^{'}}{G} \qquad (27)$$

In equation 27 T^* and $T_s^{'}$ are the tip and root temperatures, respectively, with $T_s^{'}$ being equal to the eutectic temperature (T_e) for systems that contain a eutectic. By purely geometric arguments it is assumed that the primary spacing is determined by the tip radius and the length of the zone that contains the interdendritic liquid. By solving equation 26 for primary spacing one gets $\lambda_1 \propto (Ra)^{1/2}$. By substituting equation 27 into this expression one gets:

$$\lambda_1 = \left(\frac{3\Delta T' R}{G} \right)^{1/2} \qquad (28)$$

A large change in tip temperature caused by varying the velocity of the interface will affect the quantity $\Delta T'$ and hence the primary spacing. At moderate growth rates the commonly used equation for primary spacing can be arrived at by substituting equation 25 into equation 28 while assuming that $\Delta T'$ is approximately ΔT_o. The result is:

$$\lambda_1 = \frac{4.3(\Delta T_o D\Gamma)^{0.25}}{k^{0.25} V^{0.25} G^{0.5}} \qquad (29)$$

From this equation it can be seen that a number of factors control the primary spacing, including the growth rate (V), temperature gradient (G) and supercooling (ΔT_o). It should be noted that the effect of supercooling on this spacing is rather small and that the temperature gradient has a more pronounced effect on the spacing than a variation in the growth rate. The derivation of this equation uses a simplified model and thus only gives an estimate for the primary spacing, but still shows that G and V have different functional dependences, which is a conclusion arrived at by more complicated models [23,24].

As mentioned previously the secondary dendrite arms undergo a significant ripening process during which highly branched arms become coarser and more widely spaced. In fact the secondary and higher order arms tend to be eliminated if their length is less than $\lambda_1/2$. The ripening process is similar to that which occurs in the Ostwald ripening of precipitates. The overall driving force for this ripening is the difference in chemical potential of crystals with different curvatures. Since this process is similar to Ostwald ripening it turns out that λ_2 is

proportional to the cube root of the local solidification time (t_f). There have been studies [26,27] that have arrived at the general relation:

$$\lambda_2 = 5.5(Mt_f)^{1/3} \qquad (30)$$

In this equation the quantity M is a constant that is given by:

$$M = \frac{\Gamma D \ln\left(\frac{C_l^m}{C_o}\right)}{m(1-k)(C_o - C_l^m)} \qquad (31)$$

The constant C_l^m is often taken as the eutectic composition (C_e) for systems displaying a eutectic. The value of M depends on a wide variety of parameters and can vary over an order of magnitude. However the cube root dependency of solidification time makes these differences relatively small. The local solidification time for directional solidification processes is:

$$t_f = \frac{\Delta T'}{\dot{T}} \qquad (32)$$

The quantity $\dot{T}$ is the cooling rate and is given by $\dot{T} = GV$. Overall though, it can be seen that as the local solidification time increases that the secondary dendrite arm spacing will increase.

Figure 10 illustrates the effect of independently varying G and V on the observed solidification morphology for a typical alloy. It was concluded from equation 29 that G and V are the main variables that affect the solidification morphology.

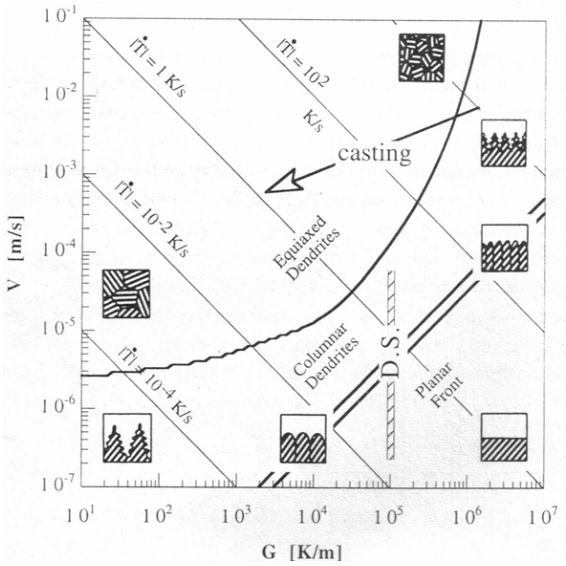

Figure 10. Summary of solidification morphologies attainable by independently changing the thermal gradient (G) and the interfacial velocity (V). In the figure D.S. stands for directional solidification and represents the typical combinations of G and V used to obtain oriented dendritic microstructures [16].

It can be seen from observing this figure that by independently varying G and V that a wide range of growth morphologies can be obtained even for a single alloy. This control allows one to fine tune the properties of a material starting with the solidification process.

2.2 PARTICLE-SOLIDIFICATION FRONT INTERACTIONS

Now that the basic theory of alloy solidification has been established, as well as a general understanding of the various growth morphologies that are attainable, the effects of foreign particles on solidification behavior will be discussed.

2.2.1 Experimental Observations and Single Particle Models

The interaction of foreign particles with a moving solid-liquid interface is a topic that has attracted a great deal of attention over the years due to its wide applicability in a variety of fields, such as metallurgy, materials science and cryobiology. Often it is desired to remove these particles from the primary phase (as when removing pollutants) but other times, as in the case of particulate reinforced composites a homogeneous dispersion of the particles is desired. From a biological standpoint it is important to understand how the cells will interact with growing ice crystals during cryogenic freezing. Many theoretical and experimental studies have been performed in this field to try and gain a better understanding of how foreign particles interact with advancing solid-liquid interfaces but the field is still an active area of research.

When a particle interacts with a moving solid-liquid interface there exist two possible scenarios: the particle can be engulfed by the interface or rejected and continually pushed ahead. One of the earliest studies dealing with the interaction between particles and a solid-liquid interface was performed by Uhlmann et al. [28]. Their experiments examined a large variety of both metallic and non-metallic particles that ranged in size from one to several hundred microns and were solidified in a variety of organic liquids as well as water. Their findings showed that at small growth velocities particles are generally rejected and that the moving planar interface can push large amounts of particles over long length scales (on the order of centimeters). As the interface velocity is increased a speed is reached where the particle is no longer pushed by the interface and instead becomes trapped in the solid phase. This is known as the critical velocity, and its value is affected most significantly by the size of the particles encountered by the interface, although other factors such as the viscosity of the liquid have an effect as well. The authors also noted that for aqueous systems if the moving interface broke down into cells and

dendrites that the particles are pushed in between the growing ice crystals yielding a lamellar structure of ice and particles.

A particle that is pushed in front of a growing solid-liquid interface will be acted upon by two counteracting forces, an attractive force due to viscous drag from fluid flowing around the particle, and a repulsive force due to differences in interfacial free energy. While the particle is being pushed it does not directly touch the interface; rather a thin film of liquid exists that allows continual transport of molecules to the growing crystal surface. This film varies in width and decreases as the velocity of the interface increases, resulting in an increase in both the attractive and repulsive forces. Once the critical velocity is reached the film thickness is no longer sufficient to allow continued growth of the crystal and the particle becomes engulfed by the interface.

Figure 11 shows a sketch of a single spherical particle being pushed by a solidification front at a distance d << r.

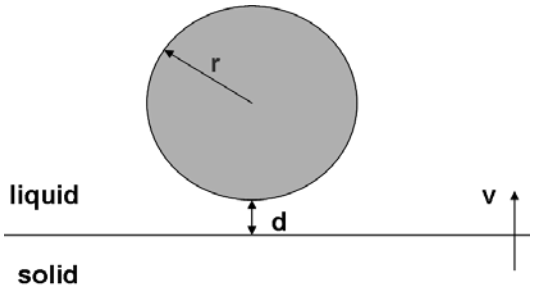

Figure 11. Schematic of a particle of radius r being pushed by a solid-liquid interface moving at velocity v for the situation where d << r.

The attractive drag force experienced by a particle moving very close to a flat solidification front can be expressed as [29]:

$$F_n = 6\pi \eta v r^2 / d \qquad (33)$$

In this equation η is the viscosity of the liquid. The repulsive force arrives primarily from the thermodynamic argument that the particle will only be rejected if an overall increase in free energy occurs when the particle is engulfed by the solid phase [29]. This criterion can be seen in equation 34.

$$\Delta\sigma = \sigma_{sp} - (\sigma_{sl} + \sigma_{lp}) > 0 \qquad (34)$$

In this equation σ_{sp}, σ_{sl}, and σ_{lp} are the interfacial free energies for the solid-particle, solid-liquid and liquid-particle interfaces, respectively. If equation 34 is not satisfied then the system is at its lowest energy state when the particle is engulfed. The repulsive force for a spherical particle in direct contact with a planar solidification front is:

$$F_\sigma = 2\pi r \Delta\sigma_o \qquad (35)$$

As mentioned previously a film of liquid exists between the particle and the interface so this equation must be modified to account for this. Uhlmann et al. [28] accounted for the surface energy of the thin liquid layer as a function of its thickness which changes equation 35 to

$$F_\sigma = 2\pi r \Delta\sigma_o \left(\frac{a_o}{d} \right)^n \qquad (36)$$

In this equation a_o is the average intermolecular distance in the film and n is a positive integer that varies from 1 to 5 depending on the model used [28]. The critical velocity can then be determined by equating the forces in equations 33 and 36 and solving for v, yielding the result seen in equation 37.

$$v_c = \frac{\Delta\sigma_o d}{3\eta r}\left(\frac{a_o}{d}\right)^n \qquad (37)$$

From this equation it can be seen that the critical velocity (v_c) is inversely proportional to the particle radius and liquid viscosity. The main complications with equation 37 are in determining correct values for d and n and also the fact that experimental values of $\Delta\sigma_o$ can vary. Also equation 37 holds only for a planar interface whereas many interfaces may be perturbed or even broken down into cells or dendrites. There is a wealth of studies that deal with more complicated models [30-35]. An expression for a spherical particle ahead of an arbitrary interface was developed [33] and can be generalized to

$$v_c = k'\frac{1}{\eta r^m} \qquad (38)$$

In this case the constant k' is a proportionality factor that depends on the interface geometry and $\Delta\sigma_o$ and m is an exponent that varies between 1 and 1.5. In spite of the difficulties of applying equations 37 and 38 to practical situations, they aid in understanding the basic factors that control particle entrapment and rejection.

Another important factor to consider is that the particles themselves can interact with and cause changes to the advancing solid liquid interface. It has been known for some time that the presence of a particle near a solidification interface can induce interfacial deformations. There have been both experimental [36,37] and theoretical [38,39] studies that have examined this topic. For a long time it was assumed that since the particles were small that they would have a minimal effect on the morphological stability of the interface. It was thought that the particle could provide a perturbation that would either decay or evolve if the interface was unstable due to other thermodynamic considerations. Experiments by Sekhar and Trivedi [37] using a variety

of different particles in 99.5% succinonitrile showed that cellular and dendritic structures could be obtained. The particles were incorporated into the dendrites by either being engulfed when solidifying above the critical velocity or trapped in between secondary dendrite arms close to the tip of the growing dendrite. It was also found that particles can destabilize the dendrite tip and lead to tip splitting of the primary dendrite. A more recent study by Shanti and Halloran [40] examined the trapping of alumina particles by camphene dendrites. They found that the particles were again trapped in between secondary dendrite arms and were continually pushed as solidification continued. When a critical packing fraction of the particles was reached "breakthrough" of the solid-liquid interface into the interparticle spaces occurred.

Some studies, including some that used linear stability analysis, [38,39] have concluded that the mechanism as to why particles can cause interfacial perturbations is the particles altering the thermal gradient ahead of the solidification front.

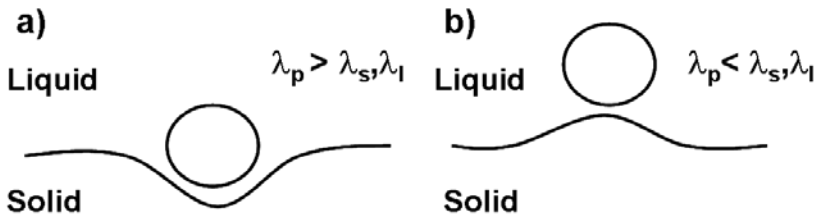

Figure 12. The effect of differing particle and solid/liquid thermal conductivities on interfacial perturbations for a) a particle with higher thermal conductivity than the solid and melt and b) a particle with lower thermal conductivity than the solid and melt.

If a particle with higher thermal conductivity than the liquid is in front of a solid-liquid interface, as depicted in Figure 12a, the heat flow will be preferentially through the particle, resulting in local destabilization of the interface and the development of a concave depression

behind the particle. On the other hand, when the particle has a lower thermal conductivity it acts as a thermal shield for the area directly behind it, thus promoting faster growth there and causing the development of a convex perturbation. For both situations, provided that the particles are still pushed, that is a small film of liquid remains between them and the interface, the perturbations will become amplified. It should be noted that these explanations pertain to a single particle in front of a planar solid-liquid interface, where as in actual situations the interface may already be broken down into cellular or dendritic structures. Nonetheless, even though a particle seems small compared to the size of the overall system, it can have significant effects on the final morphology of the interface.

2.2.2 The Solidification of Colloids

The above studies have generally been concerned with single, large particles ahead of a planar interface. While these studies are useful as they provide a basic understanding of whether particles will be engulfed or rejected by a moving interface, the concepts they are highly simplified and do not reflect the conditions that are commonly found in colloidal systems, where there are numerous submicron size particles present in front of the interface. Therefore the conclusions from these studies are difficult to extrapolate to the colloidal scale. More recently, theoretical and experimental studies on the solidification of colloids made up of clays [41-43] and alumina particles [44-46] have been performed. Peppin et al. [41-43] have shown mathematically that the stability of a planar interface is sensitive to the size and concentration of particles ahead of it. Their models accounted for the concentration dependence of a number of important quantities, such as the diffusivity and freezing temperature of the colloid, which were found to both behave in a non-linear fashion as the solid content was increased. In these

colloidal systems Brownian diffusion is strong for small (< 0.1 μm) particles and low interfacial velocities (0.1-1 μm/sec), hence the particles have sufficient time diffuse away from the interface. On the other hand for higher solidification rates a diffuse boundary layer (similar to Figure 3) can form in front of the interface, which can lead to constitutional supercooling and subsequent instability of the interface, as is seen in binary alloys. For larger particles Brownian diffusion is negligible and in the absence of extremely low solidification rates the particles form a close packed porous medium in front of the interface. This porous interface can become supercooled and unstable leading to breakdown, depending on the interfacial velocity. If the porous medium remains stable while it is supercooled it can lead to secondary ice nucleation at the surface of the layer. Linear stability analysis of these models found that increasing the concentration of particles will tend to destabilize the interface while increasing the particle radius stabilizes the interface. This stabilization is limited, as increasing the particle size greatly decreases the diffusivity and can also cause viscous forces to increase such that the particles are engulfed by the interface. Additionally these studies found that the particle size also greatly affects the temperature at which the ice is able to invade the pores between particles. This is due to curvature and it was found that the ice entry, or 'breakthrough' temperature was -0.1°C for a 1 μm pore and -100°C for a 1 nm pore. Therefore even when the interface is stable if the particles reach a critical packing fraction, which was defined by Shanti [40], and the interface reaches the ice entry temperature the particles will be engulfed. These models were tested experimentally for 0.5 μm colloidal bentonite particles at a solid loading of 2 vol% and it was found that the interface remained stable for a 0.1 μm/sec freezing velocity but became unstable as the velocity was increased to 0.8 μm/sec. In general, the studies by Peppin show mathematically that the presence of particles in front of a solid-liquid interface can lead to morphological instability,

even in the absence of any type of solute. Deville et al. [44,45] performed *in situ* x-ray radiography and tomography of alumina colloids with 0.4-3.4 μm Al_2O_3 particles and found that the particles are redistributed by a direct interaction with the solid-liquid interface following breakdown but that a concentrated particle layer as seen by Peppin can exist and depends heavily on the particle size in the colloid.

Colloidal processing requires that the particles be well dispersed in the liquid. This is often accomplished through the use of dispersants or by modifying the pH of the liquid (see Section 2.4). Both of these cases introduce solute into the system that can be rejected in front of the interface and potentially lead to constitutional supercooling. It should be noted that interfaces can also be destabilized by supercooling effects due to solute rejection, as discussed previously, and that particles can also interfere with solute redistribution. Peppin et al. acknowledged in their experimental verification [43] of their theories that sodium ions were present which may have acted to destabilize their interface. Therefore in systems where both solute and particles are present there are two active mechanisms that can act to destabilize the interface. At this point it is uncertain as to which of these two mechanisms dominate during solidification.

2.3 ICE

The freezing of water is one of the most common and widely studied solidification processes and a great deal of literature exists on the topic due to its importance in a wide variety of fields including geology, atmospheric science, materials science, physics and cryobiology.

2.3.1 Types of Ice

Water possesses a great number of polymorphs of its solid phase, generally referred to as ice. In fact, water forms more solid phases than any other known substance on earth. The ice phase diagram can be seen in Figure 13.

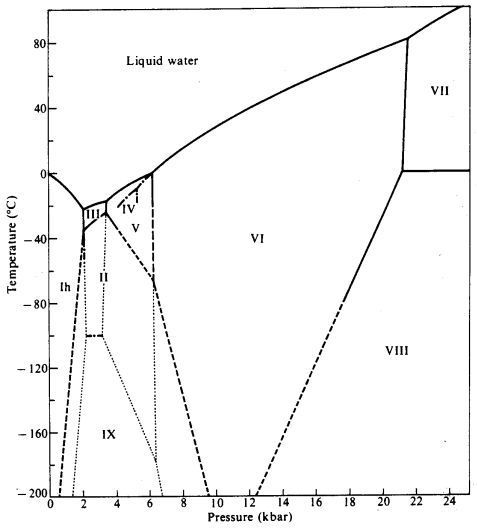

Figure 13. The phase diagram for ice, excluding the gaseous phase. [47]

There are 13 different types of ice as well as amorphous states. Most of these are high pressure polymorphs that are generally made under laboratory conditions. The high pressure polymorphs account for ice phases II through XII. These phases belong to a wide variety of crystal systems and most are able to exist only over a specific range of temperatures and pressures. The other phases of ice are low pressure forms that are able to be obtained at atmospheric pressure. These phases are hexagonal (Ih), cubic (Ic) and certain forms of

amorphous ice. Hexagonal ice is the most common form and is obtained by freezing water at atmospheric pressure or by deposition of vapor at temperatures above approximately -120°C. When water freezes to form hexagonal ice it undergoes a volume expansion of approximately 9 percent, resulting in a solid phase that is less dense than the liquid phase. Cubic ice is a metastable variant of hexagonal ice in which the oxygen atoms are arranged in a diamond cubic structure as opposed to residing on a hexagonal lattice. Cubic ice is generally obtained by deposition of water vapor at temperatures between -143 to -123°C (130-150 K). Amorphous ice is formed when water vapor is deposited at temperatures lower than -143°C (130 K). There are two distinct forms of amorphous ice: a low density form that is obtained at atmospheric pressure and a higher density form that is obtained at elevated pressure. At atmospheric pressure, using simple freezing baths in the lab, hexagonal ice would be expected.

2.3.2 Crystallography of Hexagonal Ice

The basic structure of hexagonal ice as proposed by Pauling is illustrated in Figure 14. In this figure the oxygen atoms are depicted by the open circles and are arranged on a hexagonal lattice in the form of the wurtzite (hexagonal form of ZnS) structure. The oxygen atoms are tetrahedrally coordinated which gives rise to the hexagonal symmetry. Hydrogen atoms are notated by dark circles and are covalently bonded to oxygen atoms to form H_2O molecules. The water molecules are linked together by hydrogen bonds. It should be noted that Pauling's model shows no long range order in the orientation of the water molecules or the hydrogen bonds, but they still reside on the hexagonal lattice. The lack of long range order makes it difficult to see

the hexagonal symmetry but when a section of the structure is projected onto the $(10\bar{1}0)$ plane (Figure 14b) the hexagonal symmetry is clear.

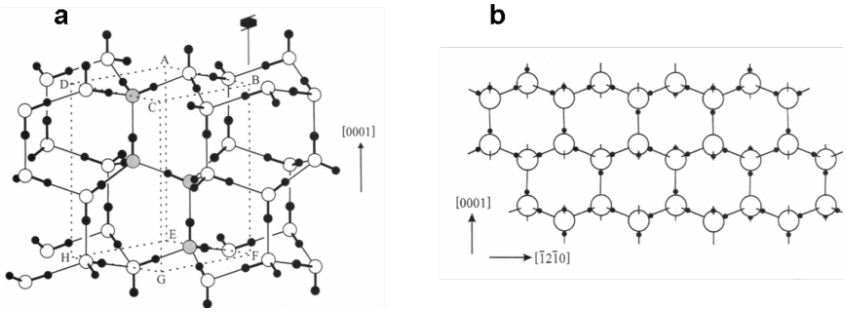

Figure 14. a) The crystal structure of hexagonal ice (Ih) showing the disordered arrangement of the water molecules on a hexagonal lattice. b) Ih structure along the $(10\bar{1}0)$ plane showing the hexagonal symmetry [48].

The unit cell of hexagonal ice is relatively open and exhibits a packing factor of less than 0.34, thus explaining why it has a lower density (ρ = 0.918 g/cm^3) than liquid water (ρ = 1 g/cm^3). The lattice parameters for ice near its melting point are a = 0.4523 nm and c = 0.7367nm. The c/a ratio of 1.628 is very close to the ideal ratio of 1.633 and does not change with temperature. The molecules present in hexagonal ice are all concentrated close to a series of parallel planes known as the basal planes. Figure 15 depicts a simplified understanding of hexagonal ice crystallography.

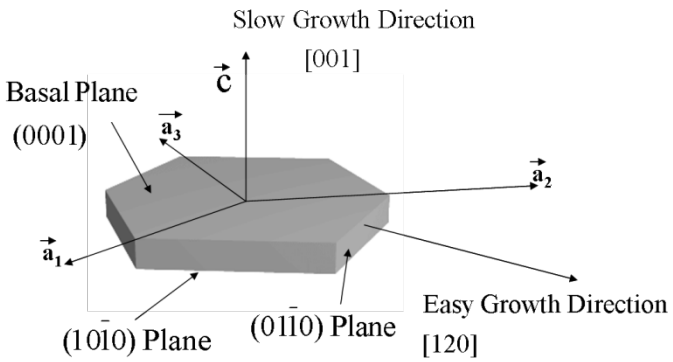

Figure 15. Illustration of hexagonal ice with some of the common planes and directions indicated.

The two prominent types of planes in hexagonal ice are the basal planes (0001) and the family of prismatic planes, notated as {1010} using the four index Miller-Bravais system. These planes play a large role in the observed morphology exhibited by hexagonal ice after freezing.

2.3.3 Crystallization of Hexagonal Ice

One of the most unique properties of water is that it experiences its greatest density at 4°C and undergoes significant (~9%) volume expansion during freezing, resulting in a solid that is less dense than the liquid phase.

As discussed above the crystal structure of ice is relatively complicated and displays directional bonding. Due to these considerations it would be expected that hexagonal ice would display faceted growth. For water the Jackson alpha factor, defined in equation 1, has a value of 2.63 [17,49]. It was previously stated that materials with an alpha factor greater than 2 tend to display faceted growth. This is indeed the case for water. Since the c/a ratio of ice is not ideal there is slightly more binding energy associated with bonds in the basal plane than for those that occur normal to the basal plane. By nature the basal plane is much smoother than the prismatic

planes and atomic attachment is much more easily facilitated on the latter. Based on this fact it is expected that ice should grow more easily in directions that are parallel to the basal plane (easy growth directions in Figure 15) than in directions that are normal to the basal plane (along [001]). This anisotropy in growth kinetics has been verified by both experimental work [50,51] and modeling [52]. It has also been reported that the thermal conductivity is higher parallel to the basal plane than in other directions [53]. Overall the ice front velocity parallel to the c-axis is 10^2 to 10^3 times lower than perpendicular to this axis [54]. In natural situations, such as the freezing of ice on a lake it is often found that the first ice that forms has c-axes that are vertical, allowing rapid growth of the ice over the surface of the lake along the easy growth directions [48]. As the ice grows down into the lake there have been studies that have found the majority of the c-axes in the horizontal plane [55], that is, perpendicular to the direction of heat flow, while some other studies have found that the c-axes are vertical. The majority of laboratory studies [50,56,57] have found that the tendency is for the c-axes to be oriented perpendicular to the direction of heat flow. In fact, Ketcham and Hobbs [50] performed a controlled experiment that examined over 2000 pairs of adjacent ice grains that made various angles with each other and found that the grain that was eliminated was the one with the smaller angle between the c-axis and the growth direction. This fact is supplemented by the fact that observations in sea ice have found that the ice plates that are formed are perpendicular to the [0001] direction [48]. In terms of modeling, Nada and Furukawa [52] performed molecular dynamics simulations of ice-water interfaces for an (0001) plane and a prismatic $(10\bar{1}0)$ plane and found that the growth kinetics were extremely different for the two cases. The basal plane propagated in a slow layer by layer process while the prismatic plane propagated by a faster collected molecule process. It can be concluded that anisotropy in growth kinetics for ice definitely exists and that the preferred

orientation of growth is generally one where the c-axis is perpendicular to the direction of heat flow.

An important fact about hexagonal ice is that it has very little tolerance for solute or any kind of foreign material. Therefore during the solidification of ice these solutes will be rejected in front of the growing interface. This is common in sea ice as the salts and biological organisms that are present are rejected and collected in brine channels [48,58,59] as seen in Figure 16.

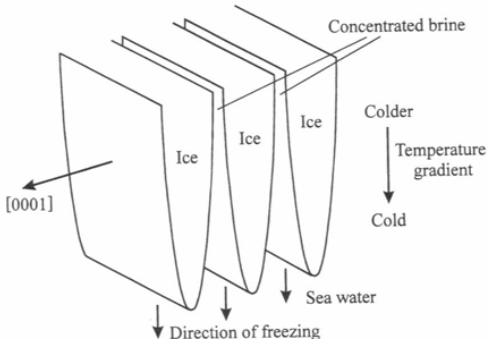

Figure 16. Illustration of the growth of sea ice showing parallel plates of pure ice with brine layers in between them. Note the direction of the c-axis with regard to the temperature gradient [48].

The freezing of salt solutions has also been investigated in the laboratory [21,60-64]. Körber and Scheiwe [60] performed an experiment where the freezing of a salt solution was observed using a light microscope. In the study visual confirmation of solute rejection leading to the breakdown of a planar interface into dendrites was observed during the freezing at steady state. The solute concentration in between dendrites was also measured and the authors concluded that the solidification of the salt solution was in agreement with basic solidification theory principles for metals. This study is of particular importance because it shows the applicability of the ideas and equations of solidification theory to an aqueous system. In other

words the solidification of an aqueous solution containing solute leads to solute rejection that in turn destabilizes the interface due to the constitutional supercooling arguments that were outlined in an earlier section.

The interaction of foreign particles for aqueous systems has also been studied with a vast majority of the studies being related to determining the critical velocity [28-30,32,34] for various metallic and non-metallic particles during the freezing of water. Perhaps one of the most important studies relating to the interaction of foreign particles with ice is one of the earliest studies on the matter by Uhlmann et al. [28]. In this study a variety of particles suspended in water were observed during solidification. It was noted that the particles were either pushed long distances or engulfed by the growing planar interface depending on whether the solidification took place below or above the critical velocity for the system. However it was also noted that when the particles were rejected by the interface that they were deposited in between the growing cells after the interface broke down. Cissé and Bolling [34] also examined the interaction of foreign particles with a planar ice front and found that the particles could be trapped in between dendrite arms provided they were rejected from the growing interface. Another study by the same authors [33] suggested at least qualitatively that foreign particles can deform the growing ice interface. This effect of particles on the growing ice morphology was investigated by Peppin [41-43] and it was found that clay particles could cause morphological instability on ice interfaces. Further analysis by Deville [44-46] using x-ray tomography and radiography showed that once an interface is broken down that particle accumulation between ice crystals results from a direct interaction between the growing crystals and the particles.

Growing ice can exhibit a variety of morphologies depending on the solidification conditions that it is subjected to. An early study by Harrison and Tiller [56] on the ice interface

morphology that is adopted during freezing revealed that the initially smooth planar interface gave way to “knife-edge like” rows of elongated cells that resulted from a destabilization of the interface due to constitutional supercooling effects. Eventually due to further destabilization of the cells a full transformation to the commonly observed dendritic morphology was observed. These experimental observations alone reveal that ice can grow with a cellular or dendritic morphology provided there is a driving force for destabilization of the surface.

While the typical growth of hexagonal ice involves rapid propagation along the prismatic planes and slow growth perpendicular to the basal plane, there exist ways to drastically alter the solidification behavior of ice. This is usually accomplished by some additive that binds to a specific crystal face and greatly inhibits the growth there. One of the first additives discovered was antifreeze glycoproteins from polar fishes that help lower the freezing point of fish blood [65,66]. Similar behavior was also noted for lectins found in rattlesnake venom [67]. Both of these proteins are reported to bind to some or all non-basal planes and inhibit the growth there. The end result is the production of spicular, faceted ice crystals in the case of lectins and the termination of any ice growth after limited basal plane growth for the case of fish antifreeze glycoproteins. These antifreeze proteins have potential applications such as preventing intracellular ice formation during the cold storage of tissues. Since the antifreeze proteins are extremely expensive, as well as not stable at room temperature, research was conducted to find out if there were any cheaper substances that could effectively replicate what they do. It was subsequently determined that polyvinyl alcohol adsorbs to the prismatic faces in hexagonal ice and causes changes in the growth habit [68]. The proposed mechanism is that the PVA adsorbs to the prismatic face and that for further growth to occur curvature of the ice interface at places

not blocked by the PVA would be required. The curvature then reduces the local melting point of the ice and hence reduces or stops ice growth on those faces.

Overall the growth of hexagonal ice appears to obey traditional solidification theory and therefore by proper control of solidification parameters such as the thermal gradient or interfacial velocity a range of different morphologies can be expected. Also solidification modifiers can be added to introduce growth morphologies that could not be obtained under any combination of normal solidification techniques.

2.4 PROCESSING OF MACROPOROUS CERAMICS

There exist three main processing routes to obtain macroporous ceramics. The first is replication, in which a ceramic replica of a structure is made. This generally entails coating a suitable structure, often polymeric, with a liquid dispersion of ceramic particles, followed by removal of the substructure by thermal decomposition. An example of this process is the creation of ceramic foams from a polyurethane sponge, which can be used for molten metal filtration [3,9,10] or scaffolds for bioreactors [69]. The second method is direct foaming [7,70-72], in which bubbles are introduced into a ceramic dispersion by a means such as mixing or aeration, followed by controlled drying of the liquid. The final route to obtain macroporous ceramics is known as templating. In this method a non-ceramic material is introduced which acts as a template for the pore structure in the ceramic material. Following the processing the template is removed by appropriate means such as thermal decomposition or freeze drying. Examples of templating include using fugitive phases [11-13] such as wood or fibers which are added to a mold prior to casting a dispersion of ceramic particles around the template.

Ceramics are most commonly available as powders which can range in particle size from a few nanometers to a few microns. To formulate ceramic bodies by any of the three methods listed above it is necessary to create a stable dispersion of the particles in an appropriate carrier fluid, which is most often water. A stable dispersion of ceramic particles in water is commonly referred to as a *slip*. When ceramic powders are added to water they spontaneously agglomerate and settle to the bottom of the liquid due to gravitational forces. This is due to weak attractive interparticle forces which cause the powders to flocculate and become extremely difficult to disperse.

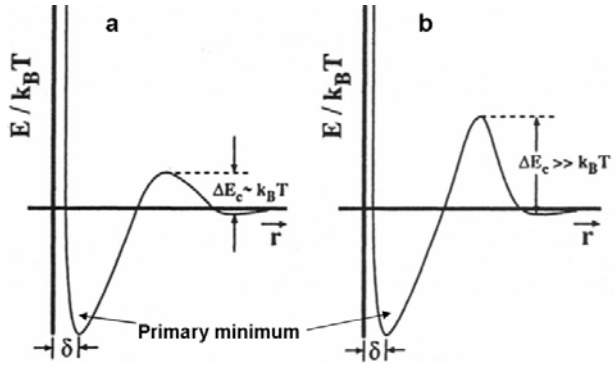

Figure 17. Plots of the interaction energy as a function of interparticle spacing for a) an unstable dispersion and b) a stable dispersion. Modified from Hiemenz [73].

Figure 17 shows a plot of the interaction energy of two particles as a function of interparticle spacing. Naturally these particles will remain separated by a distance δ, which is thermodynamically favored as it is the minimum energy state known as the primary minimum. This minimum energy state corresponds to a state of flocculation and leads to an unstable dispersion. The activation barrier (ΔE_c) that prevents the particles from residing at the primary

minimum is often on the order of the kinetic energy of the particles (k_BT), so additional measures must be taken to increase this barrier such the particles are not at the equilibrium separation. Achieving this will result in a deflocculated or well dispersed slip. This can be accomplished by introducing like charges or attaching long chain molecules to the particle surfaces resulting in repulsion or steric hindrance, respectively. A common way to introduce charge to the particles is by altering the pH of the water through the addition of an acid or a base leading to protonation or deprotonation of the surface, respectively. The pH range over which different ceramics will become dispersed varies. For every ceramic there exists a state where there is no *net* charge on the surface of the particles, known as the isoelectric point, where the viscosity of the slip increases dramatically. To achieve a well dispersed system care must be taken that the pH of the system is not in this range. Steric hindrance can be introduced by the addition of surfactants, which are commonly long chain amphiphilic polymers whose hydrophobic head attaches to the surface of the particles while the hydrophilic portion rests in the water. The physical interaction of the hydrophilic portions increases the separation distance between the particles, as can be seen in Figure 18a.

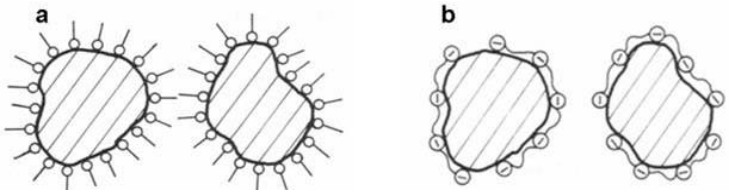

Figure 18. Illustration of a) surfactant and b) an anionic polyelectrolyte on particles. Modified from Reed [74].

A combination of these two methods can be accomplished by using polyelectrolytes, which are long chain surfactant molecules with water soluble side groups. Once again the hydrophobic heads will attach to the particle surface and provide steric hindrance, while the side groups will dissociate in water and introduce a charge, as seen in Figure 18b. The amount of polyelectrolyte that is necessary directly correlates with the surface area of the powder particles, as they should be completely covered with the polymer chains. An excess of polyelectrolyte can lead to a buildup of excess charge which leads to coagulation, or the formation of loose networks of particles. All of the above mentioned methods increase the energy barrier as in Figure 17b and prevent the particles from residing in the primary minimum, thus leading to a stable dispersion.

2.5 FREEZE-CASTING OF CERAMIC MATERIALS

Freeze casting is a processing technique used to create macroporous ceramics with controlled porosity. Briefly, this method entails directional freezing of a liquid suspension of ceramic particles followed by sublimation of the solid phase to yield a porous green body that can eventually be sintered to densify the ceramic struts. Of the three methods previously mentioned, freeze casting falls under templating. In freeze casting the crystals of the solidified liquid phase provide the template for the pores and are later removed. Freeze casting has attracted significant attention over the past years due to its relative simplicity and flexibility.

2.5.1 Mechanism of Freeze Casting

The general idea behind freeze casting is to create a liquid (not necessarily aqueous) dispersion of ceramic particles (commonly 10-40 vol%), which is then poured into a mold and unidirectionally solidified, followed by sublimation to remove the frozen solid. A schematic of the freezing process can be seen in Figure 19.

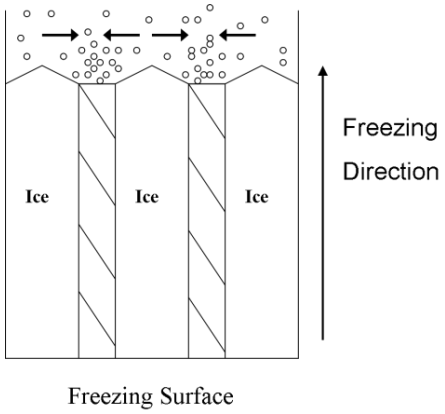

Figure 19. Illustration of the active mechanisms during freeze casting.

During the freezing process the particles must be rejected from the growing crystals. For the case of an aqueous dispersion, ice crystals have very low tolerance for any foreign material. Thus, provided that the solidification takes place below the critical velocity the particles will be rejected from the solid-liquid interface. For freeze casting it is crucial that the solid-liquid interface does not remain planar, as in this case the particles will be continually pushed and wind up on one side of the sample. The rejected particles then accumulate between the growing crystals and form what will become the pore walls. Deville [44-46] used x-ray radiography to

show that the particles are redistributed by a direct interaction with the ice crystals. Following freezing a freeze-drying process must take place that causes the solid to sublimate. This is done to avoid drying stresses that can lead to warping and cracking of the body. For aqueous colloids this is accomplished by placing the frozen sample in a vacuum chamber and lowering the pressure below the triple point of water, followed by gradual heating to cause sublimation. This is depicted in Figure 20.

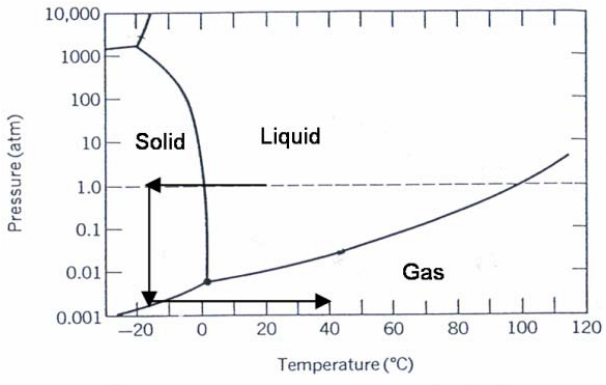

Figure 20. Pressure-temperature diagram for water with a superimposed freeze drying path.

2.5.2 A Summary of Freeze Casting Literature

Some of the earliest work related to freeze casting dealt with the creation of silica fibers [75,76]. This method utilized the irreversible gelling of silica sols during freezing to produce oriented fibers. Many years later research on the freezing and subsequent gelation of silica sols re-emerged and the general process was termed freeze gelation. Most of the freeze gelation work

dealt with silica sols containing various filler particles such as zirconia [77] or alumina [78]. Freeze casting differs from freeze gelation since the liquids that are used in freeze casting must be sublimed after freezing, whereas the gelled sol does not require this.

Freeze casting has been performed with a variety of materials including alumina [40,54,79-95], silicon nitride [96], hydroxyapatite [97-106], yttria stabilized zirconia [107-109], silica [110-112], silica-alumina [113], titanium dioxide [114,115], NiO-YSZ [116], Ni-YSZ [117], PZT-PZN [118], mullite [119], silicon carbide [120,121], Bioglass® [122,123], zirconia [124-126], alumina-zirconia [127], glass [128] and even collagen [129,130]. Porous titanium bodies have also been made by freeze casting titanium particles [131] or TiH_2 [132]. The method has also been extended to create polymeric structures by freezing solutions of polyvinyl alcohol [133]. The fact that this method has been accomplished using so many different materials suggests that the method is not material dependent but rather relies on a physical interaction between the growing crystals and the particles.

One of the most beneficial aspects of freeze casting, other than the relative simplicity, is that the resulting structure can be altered by varying different parameters during freezing. Since the ice crystals (in the case of an aqueous dispersion) provide the template for the resulting pore structure, any variable that alters how they grow in turn changes the final pore morphology. Early work by Fukasawa et al. [80] on freeze casting of aqueous alumina colloids demonstrated that as the solid loading of the slip was increased from 28 to 45 vol% that the porosity of the sintered bodies decreased from roughly 60 to 40%. This showed that the porosity is directly related to the amount of water contained in the slip and can hence be tuned to a specific value by changing the solid loading. A variety of other studies utilizing aqueous slips [54,81,84,96,97,99,114,116,127,134] and camphene based slips [40,86,103,118] that

incorporated various types of ceramics showed similar findings. The general trend of decreasing porosity with increasing solid loading for numerous studies was compiled by Deville [15] can be seen below in Figure 21.

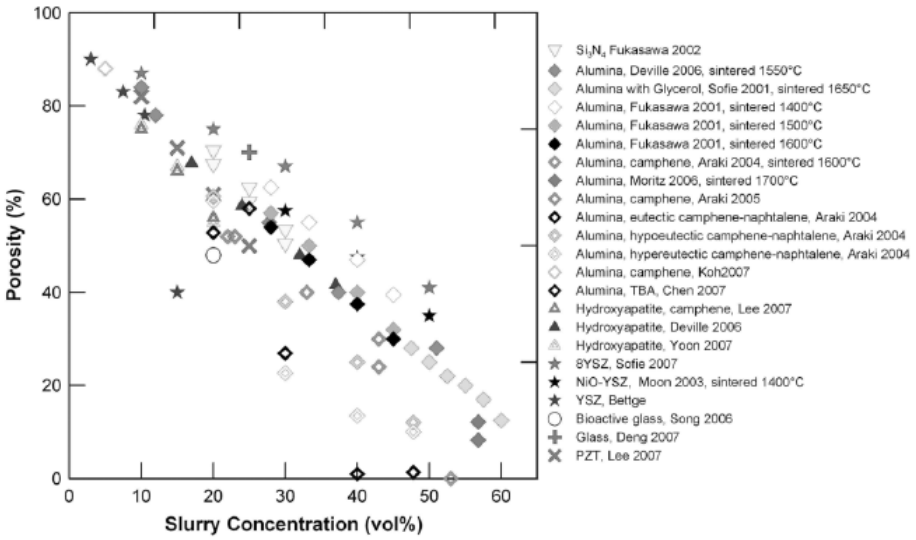

Figure 21. Plot of the variation in percentage porosity with solid loading for sintered freeze cast bodies made using a variety of different ceramics [15].

As can be seen in the above plot the range of solid loadings that have been used in freeze casting varies greatly, but common solid loadings are usually 10-40 vol%. It should be noted however that solid loadings as low as 2 vol% of clay particles have been used by Beppu et al. [134] to form large size bodies with ultra-high levels of porosity (> 95%). Other attempts to use very low solid loadings (5 vol%) for alumina based systems [86] resulted in bodies that were extremely fragile.

Another variable that was examined in the early study by Fukasawa et al. was the effect of the cooling bath temperature on the pore size. The study used ethanol based cooling baths to

provide chill plate temperatures of -20°C, -50°C and -80°C and found that the resulting pore size at -80°C was about half of that of the sample frozen at -20°C for a sample containing 28 vol% solids. By using colder temperatures the gradient across the sample becomes larger and hence the ice crystals that grow become smaller according to equation 29. Other studies using aqueous slips [54,82,84,89,91,97,111] and camphene based slips [103,106,120,121] also supported the general trend of decreasing pore size for increased thermal gradient or solidification velocity.

Another finding was that as the sintering temperature of the green bodies was increased, the pore size consequently decreased. This was first reported by Beppu et al. [134] for freeze casting of aqueous silicate slips and was also reported by a variety of other groups [80,81,96,117]. The explanation of this is quite simple as higher sintering temperatures generally promote increased densification that is accomplished through the removal of fine porosity.

Most of the early studies on freeze casting used aqueous slips, since water is the most common liquid utilized in ceramic processing. The drawback to using water for freeze casting is the fact that it expands approximately 9% during solidification and requires a time consuming low pressure freeze drying process. The use of camphene-based slips was first reported by Araki and Halloran [93] and has since been used by numerous other authors [40,83,85,86,94,98,102,103,106,107,117,118,120-126]. This organic liquid was chosen as the solidification medium because it does not expand, but rather shrinks approximately 3.1% during freezing. Another advantage is that camphene solidifies at much warmer temperatures (44-48°C), eliminating the use of extremely cold baths, and sublimates readily at room temperature and atmospheric pressure, thus eliminating the time consuming freeze drying step. Camphene always solidifies dendritically and thus offers an alternative pore morphology to the usual

lamellar structures that are obtained using aqueous systems. Other than the fact that camphene always solidifies dendritically, the same general trends of increasing solid loading and cooler freezing conditions lowering the porosity and pore size that were noted for aqueous dispersions were also observed for camphene based systems, as mentioned previously. The ability to use different solidification liquids and obtain similar trends is another reason why the freeze casting process exhibits great flexibility.

The nature of freeze-casting introduces a situation where heat is extracted through an increasing amount of solidified material. As this occurs both the thermal gradient across the sample and the interfacial velocity are slowly decreasing. According to solidification theory this results in a situation where the growing ice crystals are able to coarsen appreciably by selective overgrowth of more favorably oriented crystals. This was first reported by Koch et al. [82], who examined both the temperature gradient and pore size at various positions throughout the height of the sample for aqueous alumina colloids that contained silica. A few other studies have also reported this effect for different systems [40,88-90] including the application of freeze casting to traditional tape casting [109,114]. Some studies have even intentionally utilized the coarsening and overgrowth that takes place to create very large (> 100 μm) pores [94,106] or functionally gradient materials [132].

Often it is desired to achieve materials with homogeneous pore structures. To accomplish this ice crystal coarsening must be minimized. To avoid the situation where the ice crystals are able to coarsen, a constant thermal gradient should be present across the sample which eventually yields steady state solidification. Experimental setups that allow control over both the thermal gradient and the interfacial velocity have been developed over the years to solidify superalloys [135]. Of these methods the Power-Down method has been applied to

cryobiology by a few authors [129,136]. The basic principle of the Power-Down technique is to solidify a sample placed between two adjacent blocks that are temperature controlled, setting up an initial thermal gradient. Following this the blocks are both lowered in temperature at the same cooling rate and the directional solidification occurs. By altering the initial gradient that is established between the blocks the interfacial velocity established during freezing is also changed. This method has recently been adapted for freeze casting of PVA and nanoparticles [133] and ceramics such as alumina [44-46,54,84,91] and hydroxyapatite [97] and has been further modified create large sample that exhibited no coarsening [137].

Some of the more thorough reports on the control of freeze cast ceramics have been reported by Deville et al. A report by this group on the freeze casting of alumina [54] using a Power-Down technique presented a mechanism by which the microstructure evolves during freezing. Alumina slips with solid contents ranging from 30 to greater than 80 vol% with 2 wt% PVA binder relative to the solids were frozen using a wide range of freezing conditions that were achieved by varying gradients and cooling rates. The structures that were obtained were generally lamellar, with the exception of the 80 vol% sample that showed little connected porosity. This study utilized more controlled solidification conditions to verify a number of observations made in early studies, such as increasing interfacial velocities yielding finer microstructures and increasing solid contents giving decreased porosity. It was found that once steady state was reached the lamellar porous architecture showed regular patterns in directions both parallel and perpendicular to the solidification direction, with continuous porosity running from the top to the bottom of the sample.

The evolution of the microstructure with distance from the freezing surface can be seen below in Figure 22. An interesting observation was that the first few microns of the structure

result in a dense layer during which the planar ice front is engulfing the particles due to propagation at an extremely high interfacial velocity. In a subsequent study [44] this velocity was determined using x-ray radiography as 750 μm/sec, which is well above the calculated critical velocity of 100 μm/sec for 0.4 μm Al_2O_3 particles [54]. Eventually the interface becomes unstable and breaks down into a series of cells, while the particles accumulate in between the growing ice crystals, in agreement with the schematic shown in Figure 19.

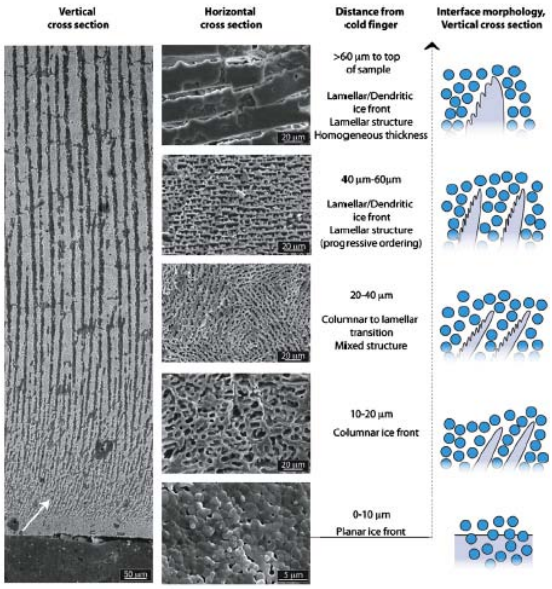

Figure 22. Evolution of microstructural morphology during freeze casting as reported by Deville for freeze casting of aqueous alumina colloids [54].

The nature of the destabilization could be a result of particles or rejected solute (the dispersant and PVA binder) causing a zone of constitutional supercooling to exist in front of the interface. Evidence of supercooling is supported by the fact that the cells eventually start to become destabilized and show branching. Eventually steady state is reached and a homogeneous

lamellar structure is obtained. An important conclusion of this study is that the microstructure is affected not only by the freezing rate but also the interactions of particles and solute, hence the slurry concentration and amount of binder present in the sample. The destabilization of the interface could have been due to the particles, the solute or a combination of both.

It was previously mentioned that Peppin et al. [41-43] showed that colloidal particles can destabilize an interface even with no solute present. In an effort to see the effect of particles on the interface, the solidification behavior of aqueous alumina colloids during freeze casting was examined by Deville et al. using x-ray radiography and tomography [44-46]. The study examined 0.2 – 3.4 μm particles at solidification velocities ranging from 20-40 μm/sec. These velocities are significantly above the low velocities (~1μm/sec) that were used by Peppin et al. for their experiments on interfacial stability. It was determined that under conditions of freeze casting that the particles are concentrated in between the crystals by a direct interaction with the moving solidification interface. The main parameters that affected the particle redistribution included the interface velocity and the particle size. For 0.2 μm particles a very small concentrated particle layer appeared in front of the moving interface, with the tips of the ice crystals protruding through this layer. For 3.4 μm particles a thick concentrated particle layer built up with increasing time. This cannot be explained by particle diffusion, as Brownian diffusion is very low for such large particles, especially at the velocities encountered in the study. This effect was likely related to the difficulty of packing larger particles in between ice crystals with spacings on the order of a few particle diameters. The efficiency with which particles pack between the ice crystals will also determine the minimum feature size [15] and roughness of the pore walls that is able to be created using freeze casting. In general for freeze cast materials the particles are rearranged by a direct interaction with the ice crystals and not by

diffusion. Also, as an ammonium polymethacrylate dispersant was used in the study it was unable to be determined if the interface instability was due to solute or particle effects. In another study Deville et al. [46] determined a stability diagram for the solidification of alumina colloids. The stability of the interface was dependent upon the particle size and interfacial velocity and resulted in four separate regimes, as can be seen below in Figure 23. For very low interfacial velocities all of the particles are rejected and the interface remains stable. Eventually a velocity is reached where the interface becomes unstable. In this region Deville postulates that partial diffusion of the particles away from the interface leads to a supercooled particle zone in front of the interface that allows both dendrites (local instabilities) and larger global instabilities, defined as growth of ice in concentrated particle zone, to grow.

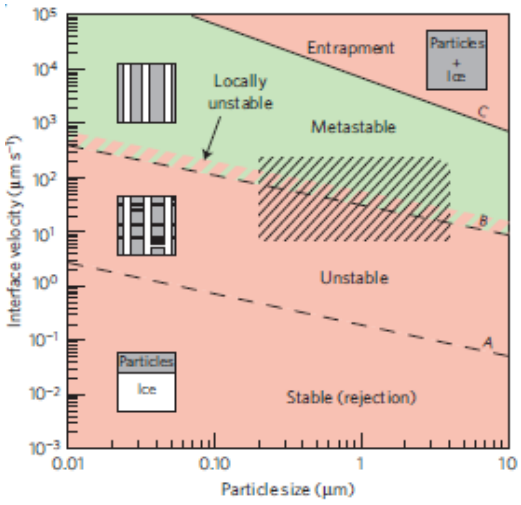

Figure 23. Stability diagrams for the solidification of aqueous alumina suspensions. The shaded region represents typical conditions used for freeze casting [46].

The metastable region is one where only local instabilities such as dendrite arms are created and the end result is a homogeneous microstructure. The results of this study are important as they outline a suitable processing range for uniform freeze cast ceramic materials. From the studies of Peppin and Deville it can be seen that particles do appear to have an effect on the solidification interface.

While the results of the studies on particles on interface stability [41-46] do present interesting results it is important to remember that during freeze casting the presence of a water soluble polymer is often added to give the green body strength before sintering. Such polymers can be expected to act as a solute that can be rejected in front of the interface and lead to interfacial instability. To date some studies have dealt with varying the concentration of these polymers [85,103,105,108,115] but have done little more than report changes in porosity in the samples and morphological changes to the microstructures. Zuo et al. [108] examined the effect of varying PVA concentration (0-6 wt%) for 75 vol% YSZ slips and found that as the PVA was increased the structure became finer and morphologically different. The change in morphology was attributed to the PVA altering solidification by some means, but no further explanation was given. Ren et al. [115] performed a similar study with ZrO_2 and gave similar explanations for the changes in pore morphology. Zhang et al. [105] examined the effect of 0-6 wt% gelatin addition on the microstructure of freeze cast hydroxyapatite and found that the pore structure could be changed considerably from a lamellar structure to a more reticulated structure. A somewhat more systematic study was performed by Koh et al. [85], who examined the effect of increasing amounts of polystyrene to a 5 vol% alumina-camphene slip. The original goal of the study was to see if the polystyrene remedied the problem in a previous study [86] where the samples were extremely delicate. The strength was indeed increased but the structure became

finer with increasing amounts of polystyrene. The authors determined that the polystyrene most likely changed the degree of supercooling and promoted side-branching of camphene dendrites, thus promoting finer structures. While the results of these studies show the effect of these additives on microstructure a more careful correlation of the effect of these solutes on measured microstructural quantities such as pore size and wall thickness could be useful.

Other additives have been examined as they were expected to affect the growth of ice crystals during solidification, thus giving different pore morphologies. The addition of glycerol to aqueous colloids has been performed for some time in the cryopreservation field due to the fact that it gives finer ice crystals as a result of increased viscosity. The effect of glycerol additions was first demonstrated by Sofie [79] and more recently by other authors [91,100,101] and gave very fine dendritic pore structures in the materials. Cellular pores were able to be obtained by Fu et al. [100,101] upon the addition of 60 wt% dioxane to aqueous hydroxyapatite slips. Munch et al. [91] examined the effect of a variety of additives, including sucrose, trehalose, sodium chloride, citric acid, and ethanol on the observed morphology of freeze cast alumina ceramics. It was found that the different additives could not only modify the pore morphology, but also the roughness of the lamellae and the frequency and thickness of ceramic bridges [54] that often connect lamellae and increase the strength of the structure. It was noted that sucrose and trehalose additions caused the growth of dendrites on the surface of the lamellae and that these features could be refined by increasing the concentration of the additive, much like would be expected from alloy solidification theory.

It can be seen that a variety of additives have been examined for freeze cast materials, yielding different unique pore morphologies. Despite this the majority of the studies that exist

which deal with the effect of increasing solute are qualitative in nature and therefore a great deal of work in this area still remains in terms of relating microstructure to the solute content.

In the literature few properties of freeze-cast ceramics have been measured since the bulk of the early work was dedicated to understanding how to control the structure through varying processing conditions. The most commonly reported property measurement is the compressive strength [84,88,94,95,97,98,100-103,106,108,119,124-128] since this is one of the most important properties to quantify for macroporous ceramics. This is especially true for hydroxyapatite freeze cast ceramics, where one potential application is as scaffolds in bone replacement. In order for these to be a viable option the compressive strength needs to be similar to that of human compact bone, which is on the order of 180 MPa [97]. Due to this many of the studies that have reported compressive strength values have been for hydroxyapatite [84,97,98,100-103,106] although there have also been reports for Al_2O_3 [91,94], YSZ [108], SiC [121], ZrO_2 [124-126], Al_2O_3-ZrO_2 [127] and glass [128] as well. It has been found that the compressive strength generally decreases with increasing porosity, as would be expected with less solid present and presumably thinner walls. The general trends for selected studies can be seen below in Figure 24.

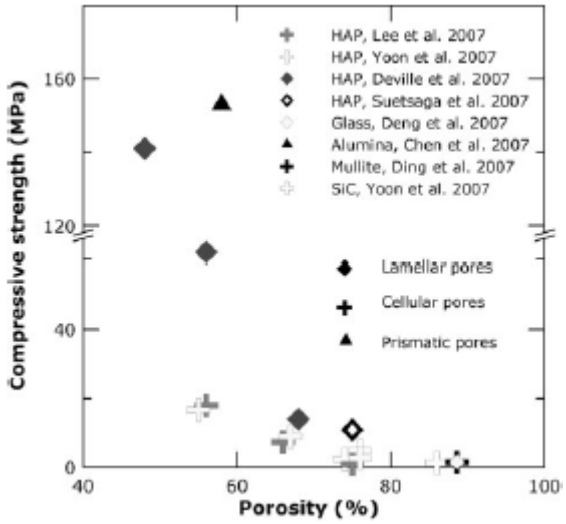

Figure 24. Plot of compressive strength of freeze cast ceramics against total sample porosity for a variety of studies as compiled by Deville [15].

With regard to hydroxyapatite (HA), Deville [84] noted significant improvements for the compressive strength of lamellar freeze cast aqueous HA slips over values that were found in the literature for porous HA processed by other methods. They noted that for high porosity content (>60 vol%) that the observed compressive strength is comparable to that which exists in the literature (16 MPa). However, when the porosity is decreased to 56 and 47 vol% the compressive strength increases to 65 and 145 MPa respectively, which are indeed significant increases. These values are also significantly higher than values obtained for freeze casting of HA with camphene based slips [98,100-103,106] which yielded values of 0.94 – 17 MPa. One reason why these structures may have such vast differences in compressive strength when compared at similar amounts of porosity is due to a difference in morphology. Camphene always solidifies dendritically, giving more of a cellular like structure while the aqueous systems yield a lamellar morphology which could possibly exhibit higher strength, at least parallel to the freezing direction due to the aligned, thicker and more continuous pore walls. Compressive

strength values for camphene based freeze cast ceramics have ranged from 0.94 – 95 MPa, but are commonly lower than lamellar structures with similar porosity. For comparison the compressive strength values of lamellar freeze cast ceramics have ranged from 15 – 145 MPa. Additionally, the strength of lamellar freeze cast materials tends to be significantly higher parallel to the growth direction compared to what has been observed perpendicular to the growth direction [91,100,101,106].

The permeability of freeze cast ceramic materials is a very important property, especially with target applications in exhaust filtration, catalyst carriers and even tissue engineering scaffolds. Despite the importance of this property only an isolated study on the permeability of raidally oriented freeze cast SiC ceramics [138] exists in the literature. The authors determined that the permeability of the samples was affected by the total porosity in the samples as well as the observed pore morphology. If freeze cast ceramics are ever to be used in any application that requires fluid flow it will be necessary to carefully correlate the effects of processing conditions and microstructure on the measured permeability.

Overall for freeze casting a basic understanding of the effect of changing variables such as freezing bath temperature, interfacial velocity and slurry concentration is known and an understanding of how to obtain different crystal morphologies by using different liquids and certain additives is known. Additionally, data concerning properties other than compressive strength of freeze cast ceramics is limited. While much clarification of the effects of particles on interfacial stability has been achieved recently, any conclusions regarding the effect of solute during solidification have been very qualitative in nature, for the most part. Also it is still uncertain as to whether the effects of particles or solute dominate during the solidification. On top of this a more thorough understanding of how different variables affect measured properties

such as compressive strength and permeability needs to be accomplished to see if freeze cast ceramics are indeed suitable for the applications that they are suggested for.

3.0 HYPOTHESIS

The effect of water-soluble polymers on the morphology and scale of directionally frozen porous ceramics can be explained by their effects on constitutional supercooling and the consequent effect on instabilities in the solid-liquid interface during solidification. Any change in the amount of supercooling will cause differences to exist in the microstructure that will significantly affect the measured properties of the materials.

4.0 EXPERIMENTAL PROCEDURES

4.1 SAMPLES PREPARED WITH POLYETHYLENE GLYCOL BINDER

The following sections cover the experimental procedures related to the preparation and analysis of freeze cast alumina samples that were prepared with polyethylene glycol as the water-soluble binder. The freezing, freeze drying, sectioning, polishing and microscopy of these samples will be presented in detail.

4.1.1 Samples with Varying Solid Loading and Freezing Conditions

These samples contained varying amounts of solid and were frozen with two different freezing baths. Details about the slip preparation, freeze casting and post-processing analysis can be found in the following sections.

4.1.1.1 Freeze Casting

Oriented porous ceramics were created using an alumina powder (A16SG, Almatis, Germany) with an average particle size of 0.4 μm. Slips were created by adding 50 grams of the powder to deionized water that contained 1.7 ml of an ammonium polymethacrylate dispersant (Darvan C, R.T. Vanderbilt Co., Norwalk, CT) and 4 wt% relative to solids of polyethylene glycol binder (Carbowax Sentry 900 NF, Union Carbide, Danbury, CT). The amount of

deionized water was adjusted so that solid loadings ranging from 20 to 40 vol% could be achieved. Following this the slip was milled without media for 24 hours to achieve a good dispersion of the particles before casting. Directional solidification molds were made by cutting sections of rubber tubing such that samples 20 mm in diameter and 10 mm tall were created. The tubing was then placed onto a small piece of aluminum foil and sealed at the bottom using petroleum jelly. This mold was then placed directly onto a large aluminum chill block that was immersed in a cooling bath. The temperature of the chill surface was able to be varied by using different coolants. The three freezing baths that were used included liquid nitrogen, an ethanol-dry ice mixture and a salt water-ice mixture. These baths gave temperatures of -196°C, -75°C and -10°C at the chill surface of the directional solidification mold. The time required to freeze typical samples was approximately 5 minutes using a liquid nitrogen bath, 15 minutes using an ethanol-dry ice bath and 25 minutes using a salt water-ice bath.

A second set of samples was prepared using varying amounts of PEG binder and 25 vol% Al_2O_3. The slips were prepared using the same alumina powder and used the same dispersant. The polyethylene glycol (MW = 900, Carbowax Sentry 900 NF, Union Carbide, Danbury, CT) was added to give 1.1, 2.3, 4.5 or 6.6 vol% binder relative to the water, which corresponded to 1, 2, 4 and 6 wt% relative to the amount of alumina powder. These slips were then milled for 24 hours without media and frozen at -75°C and -196°C using identical molds.

When solidification was complete the samples were placed onto a large aluminum block that was placed into a liquid nitrogen bath to ensure that the samples were as close to -196°C as possible. This block was then transferred into a freeze dryer, which the samples were kept in for 24 hours to ensure complete sublimation of the ice. Following freeze drying the dimensions of

the green bodies were recorded and the samples were placed in an alumina crucible and sintered in air for 1 hour at 1400°C using a heating rate of 5°C/min and a cooling rate of 10°C/min.

4.1.1.2 Density Measurement

Next, dimensions of the sintered samples were measured so that sintering shrinkage values could be determined. The densities of the samples were then calculated using the Archimedes method (ASTM C373). This method involves obtaining the dry weight (w_{dry}) of the sample and then placing the samples under vacuum before submerging them in water. After soaking overnight the weight of the sample suspended in water (w_{susp}) was determined, followed by measurement of the wet weight (w_{wet}) of the sample after removing excess water from the sample surface. The bulk density and apparent density of the bodies can then be calculated using equations 39 and 40, respectively.

$$\rho_{bulk} = \frac{w_{dry}}{w_{wet} - w_{susp}} \qquad (39)$$

$$\rho_{apparent} = \frac{w_{dry}}{w_{dry} - w_{susp}} \qquad (40)$$

4.1.1.3 Preparation of Microstructural Sections and Imaging

Following this the samples were sectioned both parallel and perpendicular to the freezing direction using a diamond blade saw and dried in air in an oven at 80°C. For each individual sample a mixture of 13.23 grams of epoxy resin (Epo-Thin, Buehler Co.) and 4.77 grams of hardener (Epo-Thin, Buehler Co.) was prepared. Following this the samples were vacuum mounted in individual sample cups and allowed to cure for 24 hours over desiccant.

Grinding and polishing of the samples was accomplished using a polishing machine (Ecomet 4, Buehler Co.) with an automated head attachment (Automet 2, Buehler). During grinding and polishing both the wheel and sample holder were rotated in a counter-clockwise direction. First the sections were ground flat for 10 minutes using a 45 μm diamond wheel rotating at 60 rpm with water as the lubricant and the samples being pressed against the wheel with 18 pounds of force. Following this the samples were pre-polished for 1 hour using a 30 μm diamond wheel rotating at 60 rpm with water as the lubricant and the samples being pressed against the wheel with 18 pounds of force. Pre-polishing of the samples was continued for 2 more hours by using 15 μm diamond paste (Metadi II, Buehler Co.) on a nylon cloth wheel with diamond compound extender (LECO Corporation) used as the lubricant. This wheel was rotated at 70 rpm and the samples were applied with a load of 17 pounds of force. The samples were first polished for 1 hour using 6 μm diamond paste (Metadi II, Buehler Co.) on a nylon wheel with diamond compound extender (LECO Corporation) as the lubricant. The wheel was rotated at 50 rpm and the samples were applied with a load of 16 pounds. The samples were then given a final polish for 1 hour using 1 μm diamond paste (Metadi II, Buehler) on a nylon wheel. This wheel was rotated at 50 rpm and the samples were applied with a load of 16 pounds. The samples were cleaned using an ultrasonic bath (Branson 5200) for 5 minutes whenever changing to a different size diamond paste to avoid cross-contamination of the polishing wheels.

The polished samples were then examined with an SEM (XL-30 FEG, Philips). The samples were first coated with a thin (2-5 nm) coating of palladium using a low voltage DC magnetron sputter coater (Model 108 auto, Cressington Scientific Instruments, Ltd., Watford, UK). Coating times to achieve this thickness generally ranged between 40 – 60 seconds. Aluminum tape was used to connect the sample to the metallic holder and drain accumulating

charge from the surface. The epoxy mounted specimens were examined primarily using back-scattered electron imaging at voltages ranging from 10 – 20 kV and 25 – 5000 times magnification. For fracture surface analysis the samples were once again sputter coated with a thin (3-5 nm) coating of palladium. Following this the samples were affixed to a holder using a small piece of carbon tape and thin layer of conductive carbon paste was applied to the sides of the sample to create a drain for accumulating charge. Fracture surface samples were generally analyzed using secondary electron imaging at 10 kV, although in some cases back-scattered electron imaging at 10 kV was employed. Micrographs were captured at magnifications ranging from 25 to 10,000 X.

4.1.1.4 Microstructural Measurements

Microstructural measurements were then performed on micrographs taken from samples parallel to the freezing direction. Each sample had a series of 10 randomly placed micrographs captured at a particular magnification. The magnification chosen for each sample varied from 100 to 500 X depending on the scale of the structure, with the main criteria being that a minimum of 20 pore / solid intercepts be on a single test line. For each image a series of 5 test lines were drawn perpendicular to the oriented pores and the number of intercepts between pore and solid phases were determined with the goal of obtaining the pore and solid intercept lengths. An example of the measurement technique can be seen below in Figure 25.

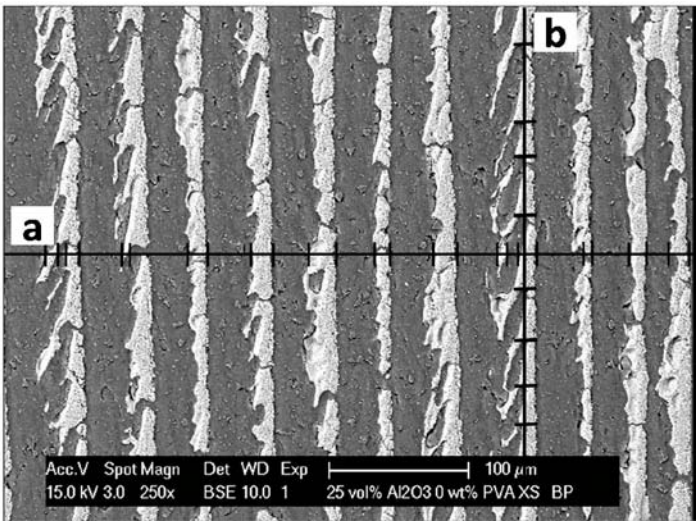

Figure 25. Example of the application of test lines to a representative image from a section parallel to the freezing direction. Line (a) was used to measure pore size and wall thickness values while line (b) was used to estimate the secondary dendrite arm spacing.

The pore intercept length λ_p is defined, using line (a) in Figure 25, as the average distance in the pore phase and can be calculated by using equation 41:

$$\overline{\lambda}_p = \frac{4 L_L^p}{S_v^{sv}} \qquad (41)$$

In this equation L_L^P is the fractional line length in the pore phase and S_v^{sv} is the surface area density of pore boundaries given by equation 42.

$$S_v^{sv} = 2 P_L^{sv} \qquad (42)$$

The quantity P_L^{sv} in equation 42 is defined as the number of intercepts between the solid and pore phases per unit length of test line. The thickness of the pore walls L_s was also calculated using intercept measurements through equation 43:

$$\overline{L}_s = \frac{4L_L^s}{S_v^{sv}} \qquad (43)$$

where L_L^s is the fractional line length in the solid phase and is defined as $L_L^s = 1 - L_L^P$.

The microstructural measurements were performed on a series of 10 micrographs taken at the same magnification for each sample. The magnification for each sample was carefully chosen so as to ensure that at least 1200 intercepts were used for the measurement of each sample. Once values for the average intercept length in both the pore and solid phases were obtained, a 95% confidence interval was calculated to determine the variation between the images for each sample.

To quantify the extent of ice crystal coarsening that occurred in the samples image analysis was performed on sections parallel to the solidification direction that were taken from the top, middle and bottom of representative samples. The bottom was within 1 mm of the chill surface, the middle was within a millimeter of the centerline of the sample and the top was within 1 mm from the very top of the sample. At each of the selected heights a series of 5 random images were taken on the SEM and the image analysis techniques mentioned previously were employed along with equations 41, 42 and 43 to determine both the pore size and wall thickness values.

Finally the secondary dendrite spacing in the samples was estimated by applying test lines such as line (b) in Figure 25 to the images along the pore walls that had secondary dendrite features within the measurement plane. Not all of the pore walls satisfied this condition. At least 150 tip spacings were used from six images for each measurement.

4.1.2 Samples Freeze-Cast with PEG for Permeability Tests

In order to determine the effect of PEG content on the air permeability of freeze-cast ceramics samples were created using a smaller two-part polymeric mold that gave cylindrical samples 11 mm in diameter and 10 mm in height such that they were able to fit in the permeability measurement apparatus after sintering. The slips were made using the same alumina powder, dispersant and polyethylene binder as outlined in the previous section. The solid loading of the slips was fixed at 25 vol% Al_2O_3 and PEG was added to give contents of 2, 5, 10, 15 and 20 wt% relative to the amount of water in the slips. The two-part mold had a thin piece of aluminum foil affixed to the bottom using petroleum jelly to create a seal and prevent any slip from leaking out of the mold before the sample was frozen. Once the slip was poured into the mold it was placed onto a large aluminum chill block which was immersed in an ethanol-dry ice freezing bath and provided a freezing temperature of -73°C. The time required for each sample to freeze was recorded, with the average time required being 10 minutes. Once the sample was frozen the entire mold was quenched into liquid nitrogen (-196°C) to facilitate sample removal. The two-part mold was allowed to return to room temperature (23°C) before the next sample was cast. A group of six samples were cast for each PEG content. The frozen samples were freeze dried at reduced pressure for 24 hours to yield green porous ceramic bodies. The samples were then sintered in air at 1400°C for 1 hour using a heating rate of 5°C/min and a cooling rate of 10°C/min. For PEG contents greater than 5 wt% a pre-sintering treatment of heating at 1°C/min to 900°C was used to slowly burn out the PEG binder while preserving the integrity of the samples. Following sintering one of the samples from each group was sectioned both parallel and perpendicular to the freezing direction so that samples could be mounted and polished for SEM analysis. The mounting, polishing, SEM and measurement techniques that were used on

these samples were identical to those used for the samples described in detail in Section 4.1.1. The remaining 5 samples from each group had the top and bottom portions of the sample cut off using a diamond saw, resulting in a specimen with a height of 5mm and a diameter of 11mm, which was suitable for both permeability and compression testing. The experimental details concerning the permeability and compression testing of these samples will be covered in a separate section.

4.1.3 Coupled Zone Samples

Solidification of samples with compositions in the coupled growth zone of the PEG-H_20 binary eutectic system were made by adding the same alumina powder as used in previous studies to deionized water such that the solid loading was 25 vol%. The same polyelectrolyte dispersant was used to achieve proper dispersion of the alumina particles in the water. Polyethylene glycol (MW = 900g/mol) was added in the amount of 40, 45 and 47.5 wt% relative to the amount of water in the slips. Once each slip was prepared it was milled without media in a polyethylene jar for 24 hours. The samples were frozen using an ethanol-dry ice bath (-73°C) and the same 2-part polymeric mold that was used for the permeability samples in Section 4.1.2. This produced specimens 13 mm in diameter and 10 mm in height.

A second molecular weight of PEG (1450 g/mol) was used to make a slip containing 25 vol% alumina and 40 wt% PEG relative to the water content. This slip, as well as the 900 g/mol slips containing 40 and 45 wt% PEG were solidified at -73°C using rubber tubing molds identical to those used to create the samples from section 4.1.1. The height of the samples was varied from 5 to 10 mm while the diameter was held constant at 10 mm.

After each sample was frozen it was removed from its respective mold and placed on a chill block maintained at -73°C. Once all of the samples were prepared they were transferred to a block at -196°C for 10 minutes. This block was then transferred to the chamber of the freeze dryer and the samples were subject to drying at reduced pressure for 24 hours. Any samples that remained intact after the freeze drying procedure were pre-fired at 900°C for 30 minutes using a heating ramp of 0.5°C/min and a cooling ramp of 10°C/min. The samples were then fired at 1400°C for 1 hour using a heating ramp of 5°C/min and a cooling ramp of 10°C/min.

4.1.4 Pseudo-Bridgman Solidification with Varying Molecular Weight PEG

An alternate method of solidification that was employed was a pseudo-Bridgman technique that provided a constant solidification front velocity. This method involved the use of a tensile testing machine (Applied Test Systems Inc. 900) that had a mechanically controlled adjustable crosshead speed. The bottom tensile grip on the machine was replaced with a compression platen, upon which the freezing bath was placed. The slip was placed in a glass vial and suspended from the upper tensile grip, which remained stationary during solidification. A picture of the experimental apparatus can be seen below in Figure 26.

Figure 26. Photograph of the pseudo-Bridgman solidification apparatus with inset detail of the sample being immersed into the freezing bath.

To initiate solidification the bottom platen was raised at a constant crosshead speed until the glass vial was completely immersed in the freezing bath. The crosshead speed must be carefully chosen such that the solid-liquid interface in the sample is always just ahead of the freezing bath liquid at all times. Experiments were performed on slips containing 25 vol% Al_2O_3 and 5 wt% PEG (relative to the water content of the slip) to determine the optimum solidification velocity using this apparatus. The crosshead speed during these experiments was varied between 20 and 90 μm/s. The resulting samples were freeze dried under vacuum for 24 hours and then sintered, mounted, polished and examined on the SEM using the methods outlined in section 4.1.1. The degree of ice crystal coarsening was determined by measuring the pore size at the top and the bottom of the sample using at least 60 individually measured intercepts at each location. It was determined that a velocity of 55 μm/s was the optimal for solidification of these samples and this value was used for all further experiments using this solidification method. See Appendix B for further details.

To examine the effect of the molecular weight of the binder on the observed microstructure slips were created using varying molecular weights of PEG. The molecular weights of PEG used were 400, 900, 1350 and 3350 g/mol (Carbowax Sentry 400 NF, Carbowax Sentry 900 NF, Carbowax Sentry 1350 Flake and Carbowax Sentry 3350 Flake, Union Carbide, Danbury, CT). Additionally a slip containing ethylene glycol (99%, Alfa Aesar, Ward Hill, MA), which is the monomer of polyethylene glycol was prepared so that a very low molecular weight (62 g/mol) could be included in the comparison. All of the slips were made using the same alumina powder and dispersant as for all the slips containing PEG that were previously discussed. The solid loading of alumina was fixed at 25 vol% and the amount of PEG added was 5 wt% relative to the amount of water in the slip. After initially mixing the powder into the water, each of the slips were subjected to 5 minutes of mixing at a high shear rate to ensure proper dispersion of the particles in the higher molecular weight PEG solutions. Following this the slips were milled for 24 hours without media. An appropriate amount of each slip was then poured into glass vials with an inner diameter of 12.4 mm and a wall thickness of 0.05 mm such that samples with a height of 12.5 mm were obtained. Each sample was then solidified with the pseudo-Bridgman apparatus described previously using an immersion velocity of 55 μm/sec into an ethanol-dry ice freezing bath. The time required for complete freezing and the total displacement of the crosshead were recorded such that the average velocity of the freezing interface could be calculated. Once a sample was completely frozen it was quenched into liquid nitrogen and carefully removed from the glass vial using a small hammer. The samples were then freeze dried under vacuum for 24 hours to ensure complete sublimation of the ice from the sample. After being removed from the freeze dryer the green bodies were placed into a crucible for sintering. The samples were then sintered in air at 1400°C for 1 hour using a heating rate of

5°C/min and a cooling rate of 10°C/min. Following this the samples were sectioned both parallel and perpendicular to the ice growth direction and prepared for SEM analysis using a procedure identical to that which was used for previous samples. The measurement techniques described previously were also used on SEM images from sections parallel to the freezing direction to determine the average pore size for the samples.

4.2 SAMPLES WITH VARYING POLYVINYL ALCOHOL CONTENT

A set of samples that was similar in nature to those that were created in section 4.1.2 for permeability testing were made with PVA as the additive. The samples were made to characterize changes in the microstructure and properties of the samples with varying PVA content.

4.2.1 Samples Freeze-Cast with PVA for Permeability Tests

The effect of polyvinyl alcohol (PVA) on the microstructure was examined by preparing slips using an alumina powder (A16SG, Almatis, Germany) with an average particle size of 0.4 μm. The slip was created by adding 50 grams of this powder to deionized water containing a varying amount of PVA (9,000-10,000MW, 80% hydrolyzed, Sigma Aldrich) and 1.7 ml of an ammonium polymethacrylate dispersant (Darvan C, R.T. Vanderbilt Co., Norwalk, CT), with the solid loading of alumina being 25 vol%. The amounts of PVA contained in the water were either 0, 5, 10, 15 or 20 wt% relative to solids. A mold identical to the samples created using PEG binder was constructed out of rubber tubing and aluminum foil, giving samples roughly 20 mm

in diameter and 15 mm in height. A second set of samples was also cast using a smaller mold that was 13 mm in diameter and 10 mm in height such that the samples were able to fit in the permeability measurement apparatus. All of the samples in this study were frozen using an ethanol / dry ice bath that provided a chill surface temperature of -75°C. The freezing time for the samples was generally around 10 minutes. Following freezing the samples were placed onto a large aluminum block and immersed in a liquid nitrogen bath (-196°C) to ensure that they would remain frozen during the freeze drying procedure. The samples were then placed into a freeze dryer for 24 hours to ensure that all of the ice was removed from the pores. Following removal from the freeze dryer the green bodies were placed into a crucible for sintering. The samples were then sintered at 1400°C for 1 hour using a heating rate of 5°C/min and a cooling rate of 10°C/min. For samples that contained greater than 5 wt% PVA a pre-sintering schedule of heating at 1°C/min to 900°C and holding for 30 minutes was used to burn out the excess PVA without disturbing the pore structure. Following sintering the densities were measured using the Archimedes method, as outlined for the PEG samples. Finally the samples were sectioned and polished such that they were ready for SEM analysis using the same protocol as was outlined for the previous samples. During SEM examination voltages and magnifications similar to those used to image the samples prepared with PEG binder were used. For each sample 10 random images from sections parallel and perpendicular to the freezing direction were obtained and microstructural measurements were performed to determine the pore and solid intercept lengths. For the images taken parallel to the freezing direction the same image analysis techniques outlined previously were used along with equations 41, 42 and 43 to evaluate both the pore size and wall thickness in the samples. Approximately 1400 intercepts were used for each measurement.

To quantify the pore size and wall thickness on sections perpendicular to the freezing direction a slightly modified procedure had to be used since the microstructure contained oriented lamellar colonies. Due to this the pore size measurement may be influenced by the scale of the micrographs relative to the colony size unless there are enough colonies in the image to give a representation of the average structure. If only one or two colonies were present in the micrograph, measurements on parallel lines will be sensitive to the line orientation. To avoid this issue test lines were applied to the micrographs using a random number generator to locate a point on a grid placed over the image and an orientation angle in the plane of the image. An example of this measurement technique can be seen below in Figure 27.

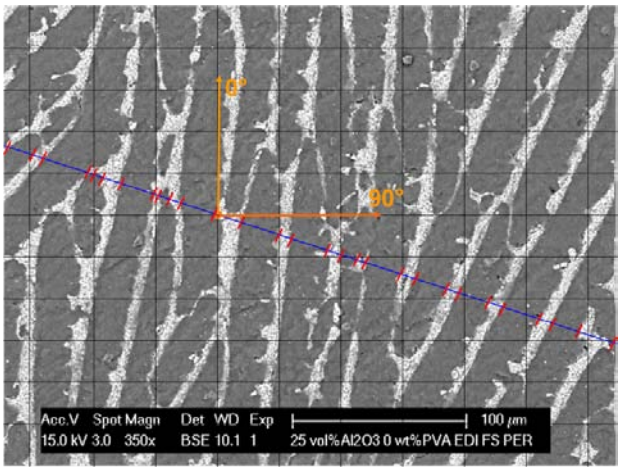

Figure 27. Example of the application of test lines to a representative image from a section perpendicular to the freezing direction.

The intercepts were then measured along the length of the line contained in the area of the image. Five test lines were applied to each of 10 images taken at randomly selected locations

on the section. The pore size and the pore wall thickness were then calculated from the measured intercepts using equations 41, 42 and 43.

Since gradients in pore size can exist for freeze cast materials due to the deceleration of the solidification front during casting, test lines were applied to sections cut parallel to the casting direction at the top and bottom of the samples used for permeability measurements. The pore size was evaluated at each location using at least 60 individually measured intercepts.

4.2.2 PVA Gelation Tests

To assess the feasibility of removing the freeze drying step from the processing protocol outlined so far in the previous experimental procedures a slip containing a high amount of PVA was investigated. The slip was prepared using the same alumina powder and dispersant that was used for all of the previously discussed samples. The solid loading of the slip was 23 vol% Al_2O_3 and the PVA content was set at 20 wt% relative to the solid loading. The same PVA binder that was used in section 4.2.1 was used in this study and was slowly added to the water until it was all dissolved. Following this the viscous PVA solution was transferred to a high shear mixer so that the alumina powder could be added gradually over a period of 15 minutes. Once all of the alumina powder was added the resulting slip was subjected to 10 minutes of high shear mixing to ensure good dispersion of the particles in the viscous PVA solution. This slip was then transferred to a polyethylene bottle and milled without media for 24 hours. When the slip was removed from the mill it was poured into 8 separate glass vials with an inner diameter of 19 mm to give samples with a height of 8 mm. Following this a thin layer of canola oil was layered on top of the slip in the vial to prevent any water evaporation during the dwell period between freezing tests. All of the vials had their lids securely placed on top and were allowed to dwell at

room temperature, with the exception of two vials that were placed in an oven at 60°C. One of the room temperature samples was then immediately frozen by placing the vial on a large aluminum chill block that was immersed in a liquid nitrogen bath (-196°C). After freezing the sample was carefully removed from the glass vial using a small hammer and was placed on a piece of filter paper that rested on an ordinary sponge, which served to absorb the water as it was removed from the sample. The sample was then observed while returning to room temperature and digital photographs were captured using a Canon PowerShot A720 IS 8 Megapixel digital camera at 10 minute time intervals until the sample began to melt, at which point the time interval was decreased to 5 minutes. The remaining room temperature samples were frozen and subsequently allowed to melt at dwell times of 2, 4, 23 and 98 hours while the samples that were held at 60°C were tested at 24 and 98 hours from the time that they were placed into their respective vials.

A final set of samples were tested using a slip that was made of the same alumina powder and dispersant as used for the previous samples with the only alteration being that the PVA in the slip was replaced with agar, a natural seaweed derivative that gels easily upon cooling. The slip contained 25 vol% Al_2O_3 and 6.3 wt% agar relative to the solid loading. The agar was added to the deionized water at room temperature and the alumina powder was then slowly added to create the final slip. This slip was milled for 24 hours without media in a polyethylene bottle and was then poured out into two of the glass vials described above. Both of the vials were put into an oven at 80°C for 30 minutes to allow the agar to dissolve into the water. Following this thermal treatment the vials were removed from the oven and the slips were allowed to return to room temperature (23°C). The samples were then frozen, removed from the glass vials and the behavior as the samples returned to room temperature was observed and recorded in the same

manner as the samples that contained PVA. Any samples that retained their shape were then fired in air at 1400°C for 1 hour using a heating ramp of 5°C/min and a cooling ramp of 10°C/min. The samples were then sectioned both parallel and perpendicular to the ice crystal growth direction and prepared for SEM analysis in the same fashion as the samples described in section 4.1.1.

4.3 PERMEABILITY MEASUREMENT OF FREEZE-CAST SAMPLES

The permeabilities of specimens containing 25 vol% Al_2O_3 and 0-20 wt% of either PVA or PEG were determined by measuring the pressure drop and resulting flow rates of dry air through the sample. The experimental setup involved a tank of dry air that was attached to a digital pressure gauge (DPG-1200, Omega Engineering), allowing the pressure drop across the sample to be determined. The sample was fitted into a custom designed plastic mold, and the resulting flow rate of the air through the sample was determined using a digital flowmeter (Optiflow 650, Agilent Technologies). A diagram of the experimental apparatus can be seen below in Figure 28.

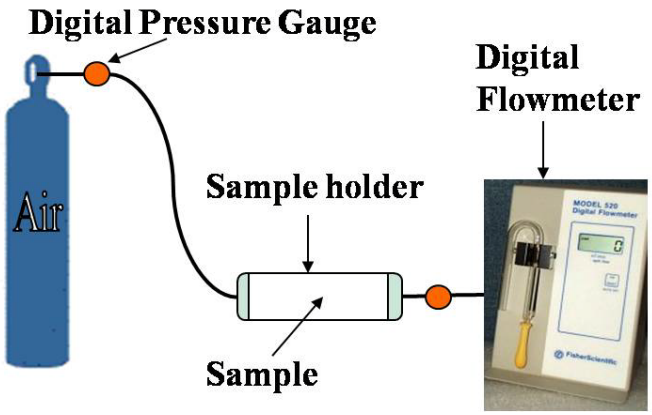

Figure 28. A schematic of the permeability measurement apparatus that was used in these studies. The sample was sealed in between O-rings in the sample chamber in order to force air through the sample.

Four samples for each of the different PVA contents were tested over a pressure range of 2 – 10 psi. Darcy's law was used to calculate the resulting permeability and is defined as seen in equation 44.

$$\frac{\Delta P}{L} = \frac{\mu}{k_1} v_s \qquad (44)$$

In this equation ΔP is the pressure drop, L is the length of the sample, μ is the viscosity of the fluid, k_1 is the Darcian permeability and v_s is the superficial fluid velocity, defined as $v_s = Q/A$, where Q is the volumetric flow rate and A is the area of the sample exposed to fluid flow. For each of these samples a 95% confidence interval was calculated to determine the variance in permeability.

To account for possible non-Darcian (inertial) flow in the samples the Forchheimer correction, defined in equation 45, was also used.

$$\frac{\Delta P}{L} = \frac{\mu}{k_1} v_s + \frac{\rho}{k_2} v_s^2 \qquad (45)$$

In this equation k_2 is the non-Darcian permeability and ρ is the density of the fluid. To determine the Darcian and non-Darcian permeabilities a plot of the pressure drop against the superficial velocity was fitted with a second order polynomial with constants equal to μ/k_1 and ρ/k_2. Once the values of k_1 and k_2 were determined, the percentage of Darcian (viscous) flow was determined by first calculating the Forchheimer number (F_o), which is defined in equation 46 [139].

$$F_o = \frac{\rho v_s}{\mu}\left(\frac{k_1}{k_2}\right) \qquad (46)$$

Once this quantity was calculated the percentage of Darcian flow was obtained by using equation 47 [139].

$$\frac{\Delta P_{Darcian}}{\Delta P_{Total}} = \frac{1}{1+F_o} \qquad (47)$$

The results obtained using equation 47 were used to assess whether or not Darcy's Law was applicable to the testing of these materials over the pressure ranges specified previously.

4.4 COMPRESSIVE STRENGTH MEASUREMENT

The compressive strengths of porous freeze cast ceramics (20-40 vol% Al_2O_3 with 0-20 wt% PEG or PVA) frozen using EDI and LN_2 baths were measured using a compression testing apparatus (Instron Model 4204, Frame Model 55R4204) equipped with a 50kN static load cell. The compression testing rig was controlled by computer software (Instron Bluehill, Version 2.0) that interfaced with the load cell through a transducer, thus allowing a continuous stream of data to be recorded such that a loading curve could be obtained.

Prior to testing, all of the porous ceramic samples had the top and bottom 5 mm of the sample machined off using a diamond cutting saw to give cylindrical specimens of approximately 5 mm in height and 10 mm in diameter. This was done to ensure that the sample being tested was representative of the section upon which pore size measurements were performed. The samples were then carefully ground with SiC paper to ensure that their top and bottom surfaces were parallel to ensure homogeneous loading of the sample during testing.

Before the tests could be initiated the load cell was calibrated with a 50 kN load by using the manual calibration feature in the Bluehill software. Following this the diameter of each sample was measured and input into the computer when prompted by the control program, with a minimum of 3 samples being tested for each combination of solid loading and freezing temperature. Once the dimensions were input the sample was placed onto the lower compression platen and the upper platen was lowered until it almost touched the sample. At this point the load was balanced (zeroed) and a fine position adjustment was used to bring the platen into contact with the sample at some nominal load. Finally the gauge length was reset to zero and the test was initiated. During the test the load was applied axially and the top compression platen traveled downwards at a rate of 1 mm/min while the bottom platen remained stationary. Due to strain rate sensitivity of the samples a low strain rate was used to ensure that the measured compressive strength was representative of the material and not skewed to larger values at high strain rates. The test was allowed to run until the maximum displacement (set by the user prior to the test) was reached. In certain cases the compressive load on the sample began to increase again after failure due to the sample fragments becoming tightly packed. In this case the test was manually aborted. After testing, the maximum compressive load and cross-sectional area of the sample was used to calculate a maximum compressive stress. This procedure was repeated until

all of the samples in a specific group were tested. At the conclusion of the testing of the final sample in the group the computer program generated a file containing the loading curves (compressive stress plotted against compressive strain) for each sample as well as an average compressive strength and 95% confidence interval for the strength values.

5.0 RESULTS AND DISCUSSION

5.1 SAMPLES FREEZE-CAST WITH POLYETHYLENE GLYCOL (PEG)

5.1.1 Effect of Bath Temperature and Solid Loading on Pore Size and Wall Thickness

The first group of samples that were examined contained solid loadings varying from 20 to 40 vol% alumina with 4 wt% polyethylene glycol relative to solids. These samples were frozen using three different chill baths, namely liquid nitrogen (LN_2) -196°C, an ethanol-dry ice (EDI) mixture (-75°C) and a salt water-ice mixture (-15°C). The aim of this experiment was to examine the effects of both solid loading and freezing bath temperature on the resultant pore size and pore wall thickness of the directionally cast samples. The results for the bulk and apparent densities obtained for these samples using the Archimedes method can be seen below in Figure 29 and Figure 30, respectively.

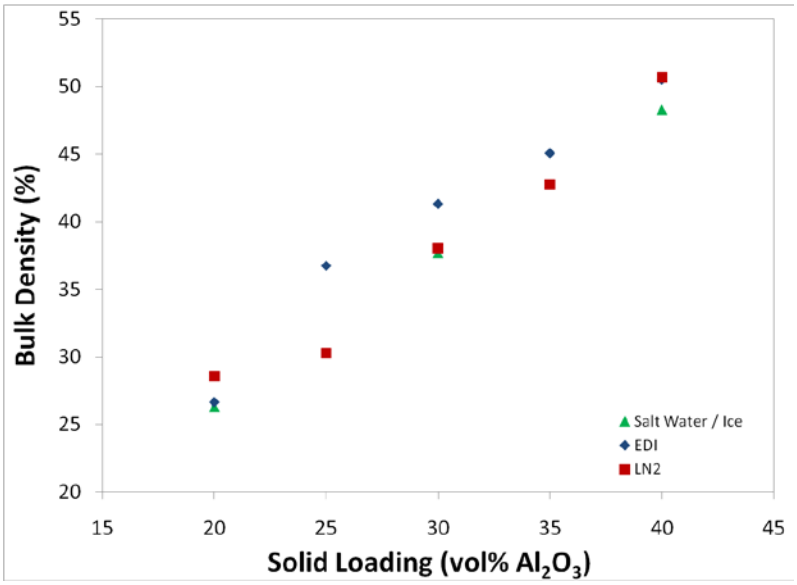

Figure 29. Plot of the bulk densities obtained for the directionally cast samples containing 20-40 vol% solids frozen using LN_2 (-196°C), Ethanol-Dry Ice (-75°C) and a Salt Water-Ice bath (-15°C).

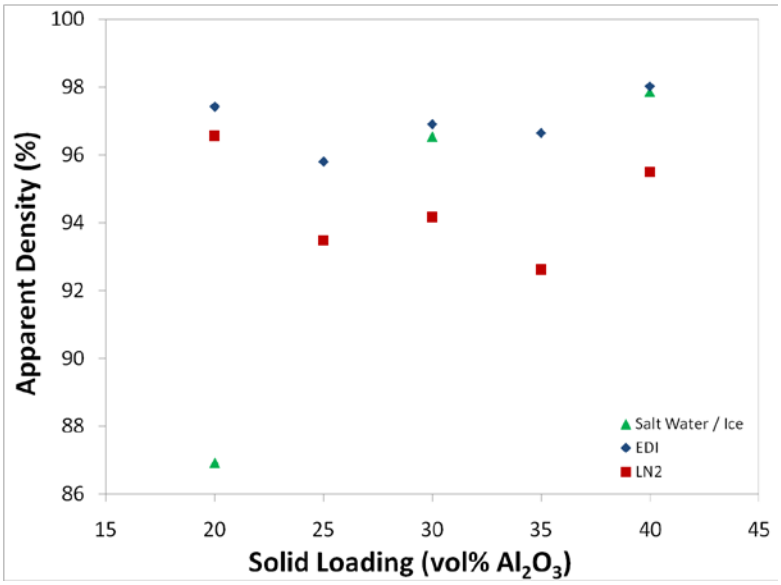

Figure 30. Plot of the apparent densities obtained for the directionally cast samples containing 20-40 vol% solids frozen using LN_2 (-196°C), Ethanol-Dry Ice (-75°C) and a Salt Water-Ice bath (-15°C).

It can be seen that the values of the bulk densities for the samples were linearly related to the solid loading independent of the freezing condition. This is expected as the bulk density of a sample is a function of the solid volume fraction in the initial slip. The results for apparent density from Figure 30 show that most of the samples have relative apparent densities in the range of 92-98%, suggesting that most of the porosity in the samples is open. It can be seen that the samples frozen with liquid nitrogen contained more closed porosity than samples that were frozen using an EDI bath. The 20 vol% Al_2O_3 sample that was frozen in the salt water bath displayed the most closed porosity with a relative apparent density of 87%. The total porosity for these samples was calculated based on the bulk density values that were obtained using the Archimedes method. The total porosity in the samples is a function of the amount of water that is present in the initial slip; hence higher solid loadings should give lower total porosity in the samples. The calculated total porosity values can be seen below in Figure 31 for samples that were frozen using EDI and LN_2 baths.

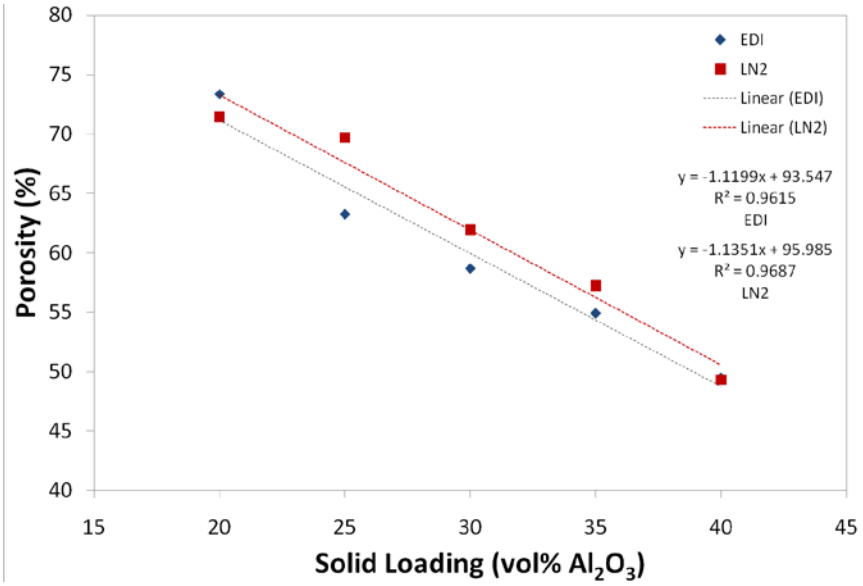

Figure 31. The effect of solid loading on the measured total porosity for samples containing 20-40 vol% solids frozen using LN_2 (-196°C), Ethanol-Dry Ice (-75°C).

As was expected based upon the bulk density measurements the total porosity for samples frozen with EDI or LN_2 was linearly dependent upon the initial solid loading of the slip. For samples cast with an EDI bath the sample porosity (P) can be varied according to the relation $P = 93.5 - \Phi$, where Φ is the solid loading of the slip. The corresponding function for the liquid nitrogen samples was $P = 95.9 - \Phi$. Therefore the total porosity for these freeze cast samples can be tuned easily by adjusting the initial solid loading of the slip. These results are consistent with what has been seen for freeze cast ceramics by other authors in the literature [15,80,81].

The bath temperature that the samples were cast with was expected to have a major effect on the scale of the final microstructure that was obtained. As the temperature gradient across the sample was increased the overall scale of the microstructure was expected to decrease. Figure 32 shows representative micrographs of samples cast using liquid nitrogen (LN_2) (-196°C), an

ethanol-dry ice (EDI) bath (-75°C) and a salt water-ice bath (-15°C). All of the micrographs show sections taken parallel to the freezing direction during casting of the samples.

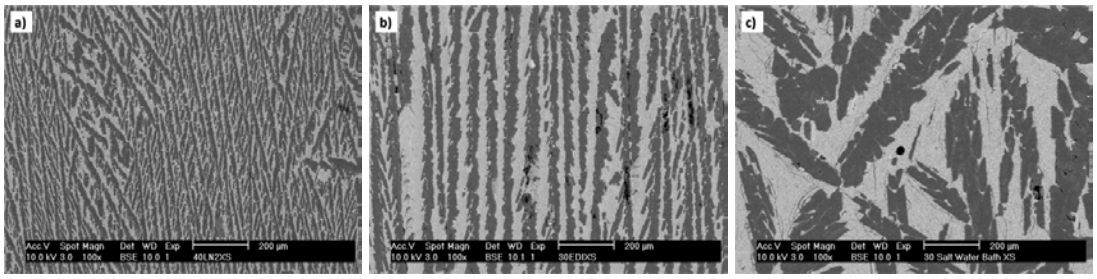

Figure 32. Micrographs of samples containing 30 vol% solids frozen in a) liquid nitrogen, b) ethanol-dry ice and c) salt water-ice baths. The magnification for all three micrographs is 100x.

As can be seen from the above micrographs the overall scale of the microstructure is finest for the samples frozen using LN_2 and gets progressively larger for the EDI and salt water-ice baths. It should be noted that in the case of the sample frozen using the salt water-ice bath the directional nature of the pores in the sample has been lost. This was most likely due to the fact that the gradient across the sample was sufficiently low enough to cause directional solidification to break down and nucleation of ice crystals throughout the liquid.

It was seen above that the chill temperature had a profound effect on the overall scale of the microstructure that was obtained. Therefore the pore size obtained for samples frozen using different baths should also follow this trend. Additionally, the solid loading of the initial colloid should also have an effect on the final pore size that is obtained using freeze casting since the particles present could act to help destabilize the solid-liquid interface. The results of the pore intercept measurements for samples cast using two different bath temperatures and a variety of

solid loadings can be seen below in Figure 33. Samples cast using the salt water-ice bath were not included in this plot since their lack of directional pores prohibited application of pore size measurement methods that were used for the other samples.

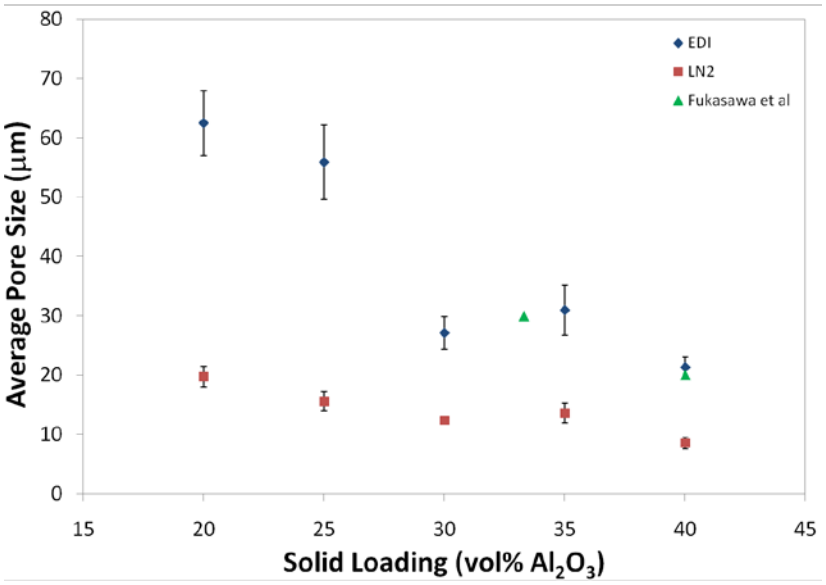

Figure 33. Plot of the average pore intercept length (pore size) against solid loading for samples containing 20-40 vol% alumina with 4 wt% PEG relative to solids frozen using LN_2 (-196°C) and EDI (-75°C).

The results show a difference in behavior for the samples frozen with LN_2 and EDI. While both sets of samples showed a general decrease in pore size with increasing solid loading the trend was far more pronounced for samples frozen with EDI compared to LN_2. This is consistent with a dominant effect of the solidification rate on the number of interfacial instabilities at the beginning of solidification. Freezing with LN_2 leads to a situation where an increased number of instabilities are present on the solidification front, and these instabilities have much less time to coarsen since the temperature gradient is much larger. This leads to

smaller ice crystals and a smaller measured pore size regardless of the solid loading. The two pore size values represented by triangular markings in Figure 33 were from those of a study by another author who used similar freezing temperatures and solid loadings but used mercury porosimetry to quantify the pore size. The results for the samples containing 35 and 40 vol% solids agreed quite well with these previous findings even though they were measured using different techniques. It was therefore found that the solid loading does have an effect on the pore size but as expected the temperature gradient had a far more significant effect [81].

As the amount of particles present in the slip was increased it was expected that the thickness of the pore walls would increase accordingly. The bath temperature that was used was also expected to play a role in determining the size of the pore wall thickness since this plays a large role in determining the amount of instabilities that are present on the solid-liquid interface. The results of pore wall thickness for samples cast using LN_2 and EDI baths with solid loadings ranging from 20 to 40 vol% can be seen below in Figure 34.

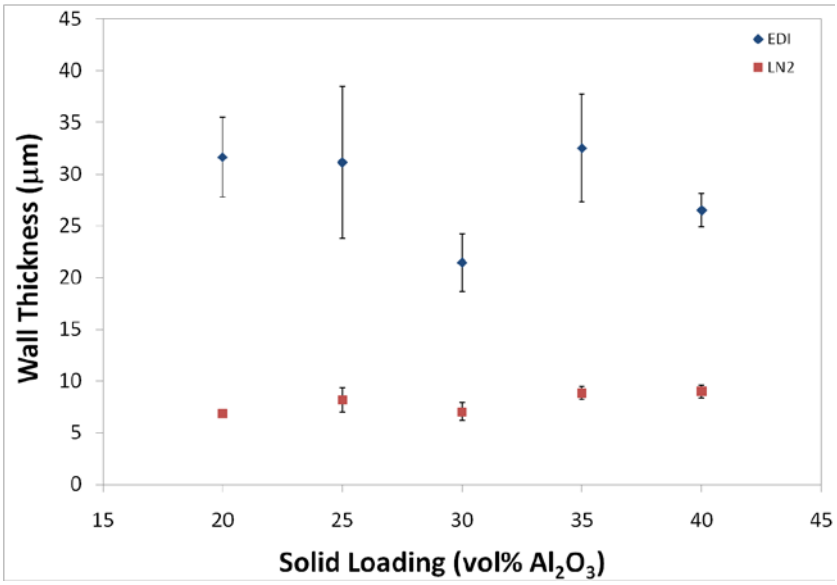

Figure 34. Plot of pore wall thickness against solid loading for 20-40 vol% alumina samples frozen in EDI (-75°C) and LN_2 (-196°C) baths.

As can be seen in this figure the samples cast using liquid nitrogen had wall thickness values much lower than those samples that were cast using EDI. This was once again likely due to the effect of the thermal gradient on the initial number of instabilities on the solidification front. For the samples frozen with liquid nitrogen there appeared to be no measurable effect of solid loading on the wall thickness, much like there was no measurable change in pore size under these conditions. For the samples cast using EDI there appears to be a small increase in wall thickness as the solid loading of the samples is increased, although this increase is not very significant. The increase is most likely due to the higher solid loading causing the walls to be thicker.

5.1.2 Effect of Freezing Bath Temperature and Solid Loading on Compressive Strength

It was seen in the previous section that the bath temperature and solid loading had a considerable effect on the morphology of the microstructure as well as the measured pore size and total porosity. Mechanical properties of macroporous ceramics, such as the compressive strength, are affected by changes in the microstructure and were examined by applying a uniaxial compressive load in a direction parallel to the pore channels of the specimens. The compressive strength of samples containing 20 – 40 vol% Al_2O_3 and 4 wt% PEG were measured on uniform cylindrical specimens with a diameter of 10 mm and a height of 5 mm. Further details concerning the testing can be found in the experimental procedures section.

The loading curves that were obtained for these samples could be divided into two types. The first type had an elastic region followed by a peak at the maximum compressive stress and then a gradual, step-like decrease in the compressive strength with increasing compressive strain. An example of this type of loading curve can be seen below in Figure 35 for a sample containing 25 vol% solids that was frozen using a liquid nitrogen bath.

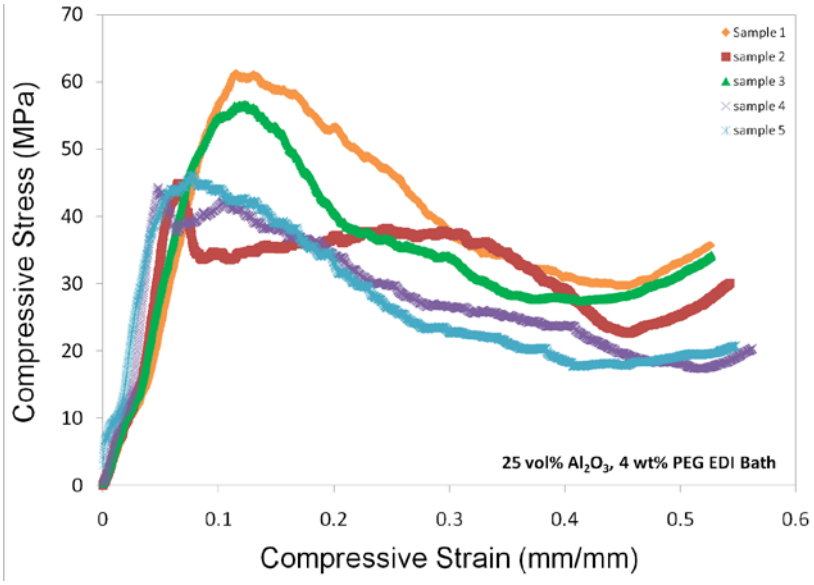

Figure 35. Loading curves generated from uniaxial compression testing of 5 identical cylindrical samples of freeze cast ceramics containing 25 vol% Al_2O_3 and 4 wt% PEG at a strain rate of 1 mm/min.

The gradual step-like decay of the curve after the maximum compressive strength can likely be attributed to the sample failing progressively rather than catastrophically, like a typical linear elastic ceramic. Additionally the compressive strains for these samples were commonly around 10%. This behavior was due to the sample behaving like a composite material, that is the weakest lamellae (pore walls) fail and the load is transferred to the remainder of the sample. This causes the compressive stress to either remain constant or briefly rise until fracture of another group of lamellae occur. This process occurs repeatedly until enough damage has accumulated to cause the sample to fail. Once failure is reached the sample begins to compact, which causes a rise in the measured compressive stress at higher compressive strain values. Another way to think of this failure regime is the progressive buckling of a series of columns. Curves such as this were obtained for samples that contained 20 – 30 vol% Al_2O_3 regardless of the freezing bath temperature and are similar to what has been seen by other authors that used

comparable solid loading and polymer contents [100,101,108]. Another type of loading curve that was obtained during testing of these samples displayed an elastic region followed by a very sharp, well defined maximum compressive stress. Once the maximum compressive stress was reached the curve experienced a quick drop followed by a final more gradual decay that was seen for the other samples. This type of loading curve was only seen for samples that contained 35 or 40 vol% Al_2O_3 and can be seen below in Figure 36 for a sample containing 35 vol% solids that was frozen using an EDI bath.

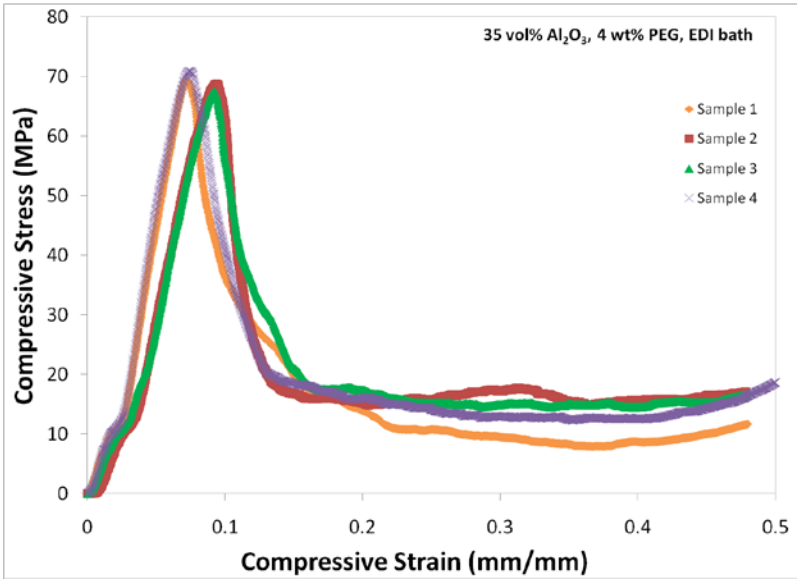

Figure 36. Loading curves generated from uniaxial compression testing of freeze cast ceramics containing 35 vol% Al_2O_3 and 4 wt% PEG at a strain rate of 1 mm/min.

The 35 vol% Al_2O_3 ceramics cast in an EDI bath gave the sharpest dropoff after the maximum compressive load. The severity with which the curve dropped off varied somewhat for other samples that gave loading curves similar to what was seen above, with some specimens

showing a quick short drop followed by a more gradual step-like region. The rapid drop was likely due to a larger fraction of lamellae failing at the same applied load and could indicate that the lamellae are more laterally connected, thus behaving somewhat less like individual columns. Regardless of the type of loading curve that was observed the samples did not fail catastrophically and reached a maximum compressive stress at compressive strain values that were commonly around 10%, which is rather good for highly porous ceramic materials.

The compressive strength values obtained for samples containing 20 – 40 vol% Al_2O_3 and 4 wt% PEG relative to the solid loading are presented below in Figure 37.

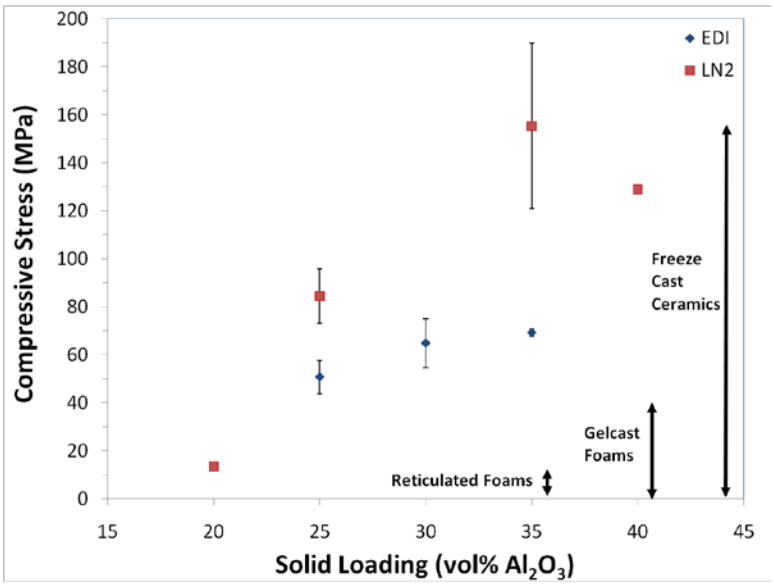

Figure 37. Uniaxial compressive strength values for samples containing 20 – 40 vol% Al_2O_3 and 4 wt% PEG frozen using either an EDI or LN_2 bath. The load was applied to the samples at a strain rate of 1 mm/min. Ranges of compressive strength values for different macroporous ceramics have been added as a reference point.

In general the compressive strength of samples cast with either freezing bath increased as the solid loading was raised, with the samples prepared using an EDI bath showing a less

significant increase. Additionally it was noted that the variation in compressive strength between samples was small, with the exception of the 35 vol% Al_2O_3 sample that was cast using an LN_2 bath. The large variation for this sample was due to the fact that one of the samples that were tested reached a maximum compressive stress at a very low strain before cracking down the centerline.

The compressive strength of freeze cast ceramics is sensitive to the amount of porosity contained in the sample. Generally it has been observed that the compressive strength increases as the amount of porosity in the sample is decreased [15]. This is likely due to the fact that higher solid loadings give increased load bearing area. The increases in compressive strength with solid loading that were noted above for samples cast with both EDI and LN_2 are consistent with what has been seen in the literature. Often when the solid volume fraction of a porous ceramic material is increased the associated rise in strength can be attributed to an increase in the minimum solid load bearing area. The minimum solid area model [140-142] is based on regular stacking of simple pore geometries and obeys the following relation:

$$\frac{\sigma}{\sigma_o} = e^{-bP} \qquad (48)$$

In this equation P is the porosity, b is a constant that depends on the pore geometry and σ and σ_o are the strengths of the porous and dense bodies, respectively. A common value of b for cylindrical pores, which represent the closest approximation to the pores in this study, is 1.4. Equation 48 shows that the strength of the material is exponentially dependent upon the porosity. The data in Figure 37 as a whole are not well represented by the minimum solid area model and a poor fit resulted. Interestingly when the data for the samples frozen using EDI and LN_2 baths were fit separately it was determined that the EDI samples reflected the changes predicted by the

minimum solid area model to a much larger degree than the LN_2 samples, however the fit was still not great ($R^2 = 0.819$). The samples created with the LN_2 bath give incremental increases in strength that are significantly larger than what is predicted by the minimum solid area model. It is not surprising that this model does not fit the experimental data well since the assumption that the pores in the sample are uniform and cylindrical does not accurately reflect their true morphology.

Other models that are used to predict the strength of porous ceramics are Gibson-Ashby models [140,143]. In a manner similar to the minimum solid area model, these models idealize the structure as a series of stacked cells with simple pore geometries. The mechanical behavior of the material then scales with the properties of the cell wall material and the cell geometry. These models are often used for cellular materials such as direct and reticulated foams. Gibson-Ashby type models are typically represented by an equation of the form:

$$\frac{\sigma}{\sigma_o} = k(\rho/\rho_o)^n \qquad (49)$$

In this equation ρ/ρ_o is the relative density of the material, k and n are constants that depend on the geometry of the cell and σ and σ_o are the strengths of the porous and dense ceramic, respectively. Predicted values of n for ceramic foams range from 2 for closed cell foams to 1.5 for open cell foams [144] although deviations from these values have been reported [145,146]. The relative compressive strength values plotted against the relative density for freeze cast samples with 20 – 40 vol% Al_2O_3 can be seen below in Figure 38.

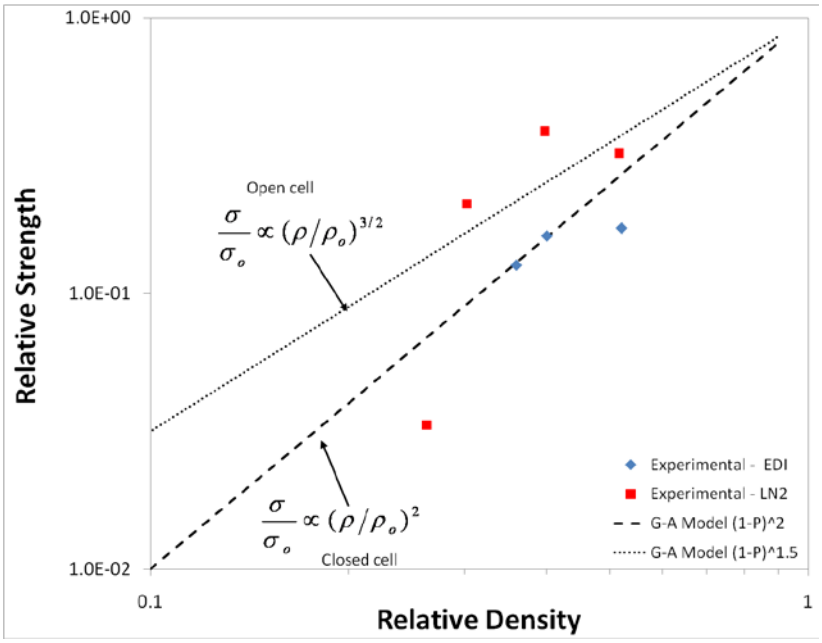

Figure 38. The relative strength of freeze cast ceramics with 20 – 40 vol% Al_2O_3 as a function of relative density. The dashed and dotted lines represent trends that would be expected from Gibson-Ashby models for open cell (dotted line) and closed cell (dashed line) foams.

In this figure the expected dependencies from the Gibson-Ashby model for open cell and closed cell foams have been added as these structures have similar relative density values to the freeze cast ceramics that were studied. It can be seen that the experimental data spans a wide range from values lower than what would be expected for closed cell foams to larger values than would be expected for open cell foams. The data for freeze cast ceramics frozen with an EDI bath is somewhat consistent with the predicted results for closed cell foams. In general it was noted that the Gibson-Ashby model does not appear to reliably predict the strength of freeze cast ceramics.

It was mentioned previously that the trends observed for foams in the literature differ somewhat to substantially from what is predicted by Gibson-Ashby models. The variations in these materials are often attributed to the effects of cell struts; that is to say that the strength of

foams is directly related to the strength and integrity of the solid struts. In particular it was noted by Dam et al. [146] and Brezny et al. [147] that the compressive strength of open cell foams increased as the cell size was decreased. While these results are not directly comparable to the freeze cast materials from this study it was interesting to note this change since samples frozen with LN_2 showed a similar trend when compared to those cast with EDI.

It is apparent that Gibson-Ashby and minimum solid area models do not well represent the strength values that were obtained in this study for freeze cast ceramics. As mentioned previously the general increase in strength could be attributed, at least in part, to decreasing amounts of porosity in the samples. This still does not account for the differences that were noted between the EDI and LN_2 samples, as the LN_2 samples gave significantly higher strengths when compared to EDI samples at the same solid loading. In Figure 33 a clear decrease in pore size was seen for samples made using an EDI bath. In the literature for freeze cast ceramics some authors attribute a strength increase to a decrease in pore size [106,108]. This argument might not be appropriate for lamellar freeze cast ceramics as they are porous structures rather than homogeneous porous materials, where the pores are regularly distributed in a dense body. As was seen with foam materials, the strength of lamellar freeze cast materials should depend on the size and integrity of the pore walls. A study by Munch et al. on Al_2O_3 freeze cast ceramics [91] found that a decrease in pore wall thickness for samples with similar amounts of porosity resulted in compressive strength values that were almost an order of magnitude higher. It was noted in Figure 34 that the pore wall thickness values for the LN_2 samples were much lower the corresponding EDI samples, therefore the thinner walls could have helped to increase the strength, provided that the walls were dense and defect free. Figure 39 compares sections taken

from a direction perpendicular to the freezing direction for samples with 35 vol% Al_2O_3 and 4 wt% PEG that were frozen using EDI (-75°C) and LN_2 (-196°C) baths.

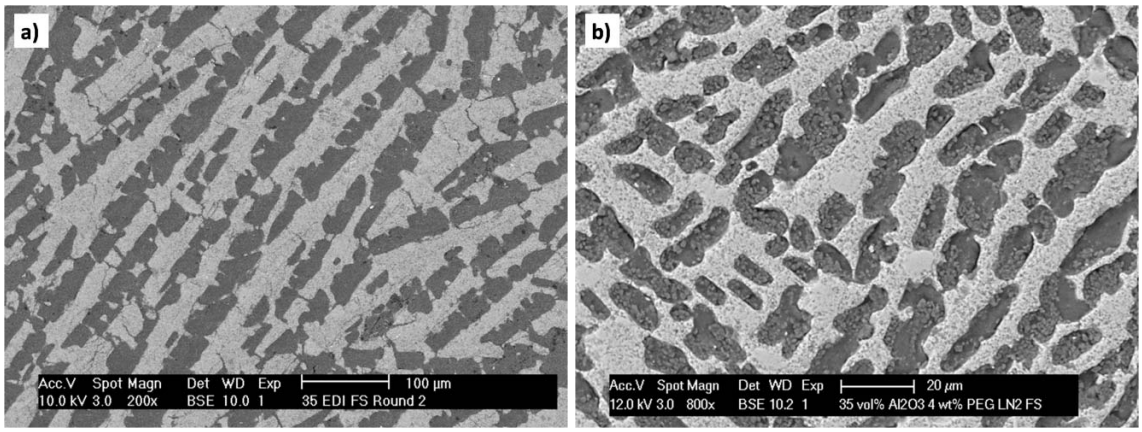

Figure 39. A comparison of sections perpendicular to the freezing direction for samples containing 35 vol% Al_2O_3 and 4 wt% PEG that were frozen in a) an EDI bath (-75°C) and b) an LN_2 bath (-196°C). Magnifications of the micrographs are a) 200x and b) 800x.

It can clearly be seen that the sample frozen with an EDI bath had walls that were cracked, whereas the sample frozen with LN_2 displayed dense and defect free pore walls. The cracks that are present in the EDI sample will clearly limit the compressive strength and help to explain why such a difference exists between these samples. In general the integrity of the pore walls became greater with increased solid loading, a fact that is supported by higher corresponding strength values. A possible reason for the better pore wall integrity that is observed is that as the solid loading is increased less water is required to make the slip. Therefore upon freezing there is less water present to expand and cause cracking in the walls.

Another factor that could help account for the differences in strength for samples cast with EDI and LN_2 baths is the degree of branching present in the structure. As can be seen in

Figure 32 samples that were cast with an LN_2 bath were more highly broken down when compared to samples cast with EDI at similar loadings. Dendritic branching can create connections between adjacent lamellae due to particles that accumulate between the dendrite arms. These 'bridges' have been commented on before by Deville et al. [54,91] and could possibly help increase the strength of freeze cast ceramics by stabilizing the pore walls. Micrographs illustrating these bridges can be seen in Figure 40 for freeze cast samples with 20 and 30 wt% Al_2O_3 and 4 wt% PEG.

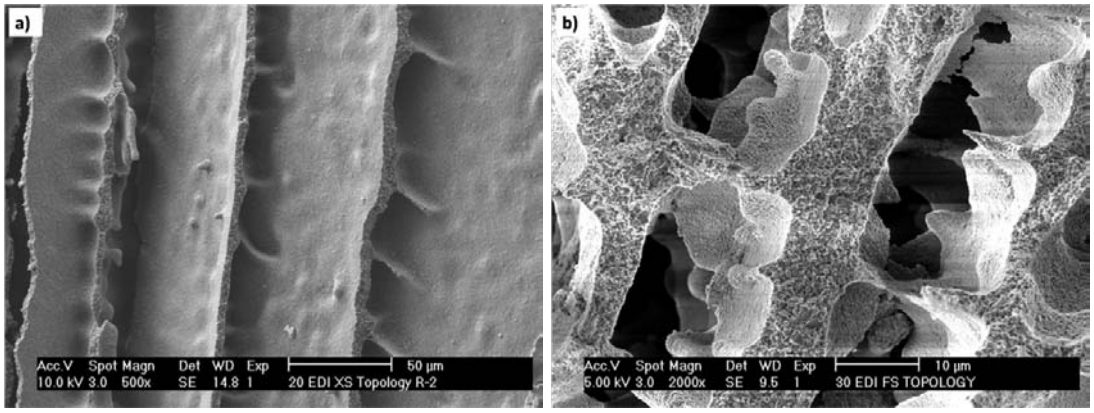

Figure 40. SEM micrographs of fracture surfaces of samples containing a) 20 vol% Al_2O_3 and 4 wt% PEG and b) 30 vol% Al_2O_3 and 4 wt% PEG that illustrate the connectivity that can exist between ceramic lamellae in freeze cast ceramics.

Therefore the more broken down structures that result from freezing with LN_2 should have an increased number of these bridges, hence becoming more laterally connected, giving rise to higher strengths. This could also help explain the increase in strength for the EDI samples as the degree of branching was increased when the solid loading was increased, likely due to effects from increased PEG concentration due to the smaller amounts of water used to prepare the slips.

Figure 37 also shows ranges of compressive strength values that can be found in the literature for a variety of macroporous ceramics. The values that were obtained for the freeze cast samples in this study were for the most part higher than what has been found for both reticulated ceramics and gelcast foams [7,148-151]. Both of these types of materials tend to have total porosity values that are somewhat higher (commonly >70%) than those in this group of samples (49% - 71%) which is largely responsible for why freeze cast materials exhibit greater strength values. Additionally these materials often have defects, such as large cracks in their struts that limit the strength. In contrast, the denser walls (Figure 40b) and ceramic 'bridges' between adjacent lamellae could possibly help increase the strength of freeze cast ceramics by stabilizing the pore walls. The range of strength values for these materials also falls well within the range that has been found in the literature [15] for other lamellar freeze cast ceramics. A more complete discussion of the comparison of these results with what has been found in the literature can be found in section 5.3.3.

5.1.3 Determination of the Extent of Coarsening in Freeze-Cast Samples

The conditions of freeze casting present a situation where the solid-liquid interface and temperature gradient across the sample decrease as heat is removed through increasing amounts of solidified material. Therefore it was expected that the growing ice crystals would coarsen with increasing distance from the chill surface as the heat transfer further constrains the solidification rate and the interface slows down. To verify that this was indeed the case a series of samples was frozen using 25 vol% Al_2O_3 and 1 wt% PEG relative to solids. These samples were frozen using both EDI and LN_2 baths to examine the effect of the overall temperature gradient on the degree of coarsening experienced by the ice crystals. Measurements were taken

from three separate locations on these samples. The results of this experiment can be seen below in table 1.

Table 1. The trend in pore size and wall thickness with measurement location for samples with 25 vol% Al_2O_3 and 1 wt% PEG relative to solids.

	Ethanol/Dry Ice		Liquid Nitrogen	
	Pore Size /μm	Wall Thickness/μm	Pore Size/μm	Wall Thickness/μm
Top	50.8±3.5	23.3±5.5	34.3±5.7	10.7±0.8
Middle	26.2±0.8	11.9±1.0	22.9±2.4	7.6±0.7
Bottom	17.0±1.8	6.7±1.2	16.0±0.9	5.2±0.3

For these samples the 'bottom' is within 1 mm of the bottom of the sample, the 'middle' is within 1 mm of the center of the sample and the 'top' is within 1 mm of the top of the sample, representing the last material to freeze. With regard to the pore size two important points are noted. The first is that the degree of coarsening becomes more pronounced close to the top of the samples whether casting with EDI or LN_2, suggesting that the more favorably oriented ice crystals are able to overtake those that are less favorably oriented. It is also important to note that the pore size is finer for samples solidified with LN_2 at comparable points in the sample, which agrees with what is expected based on solidification theory. It was also noted that the EDI samples were able to coarsen to a larger degree than those that were solidified using LN_2, most likely due to the lower temperature gradient and interfacial velocities that were encountered. The wall thickness values also increased with distance from the chill surface for both samples frozen with EDI and LN_2. Once again the amount of change was greatest for the samples frozen with EDI. The increase in wall thickness makes sense since overgrowth of favorably oriented ice crystals will yield fewer crystals with thicker walls in between them.

5.1.4 Effect of PEG on Microstructure

The experiments discussed in section 5.1.1 examined the effect of solid loading on both pore size and pore wall thickness. In this case by varying the solid loading the amount of polyethylene glycol was also varied. In order to determine the effect of solute on the microstructure the solid loading of the slips was held constant while the PEG concentration was varied. The slips that were solidified contained 25 vol% Al_2O_3 and 0-25 wt% (relative to H_2O content) of 900 g/mol polyethylene glycol. All of the samples were frozen using a 2 part polymeric mold and an ethanol-dry ice (EDI) freezing bath that gave a chill block temperature of -73°C.

When no polyethylene glycol was present it was found that the pores in the sample were rather continuous for the most part as they extended from one side of the micrograph to the other. Also it was found that the pore walls for this sample were regularly cracked, which was likely due to the expansion that takes place when ice solidifies coupled with the lack of a polymeric binder to help the pore walls accommodate such an expansion. It should also be noted that the pore walls in Figure 41a have some very small secondary dendrite features associated with them that give the walls a slightly rough look. Even though there was no PEG present during solidification, the polyelectrolyte that was used to disperse the particles is water soluble and hence is a solute that can be rejected in front of the solidification interface during freezing, leading to interfacial instability and consequent breakdown. The amount of dispersant that is used is very small, accounting for less than 2% by weight of the total slip. Therefore it is reasonable to expect that any secondary dendrites would not be very pronounced.

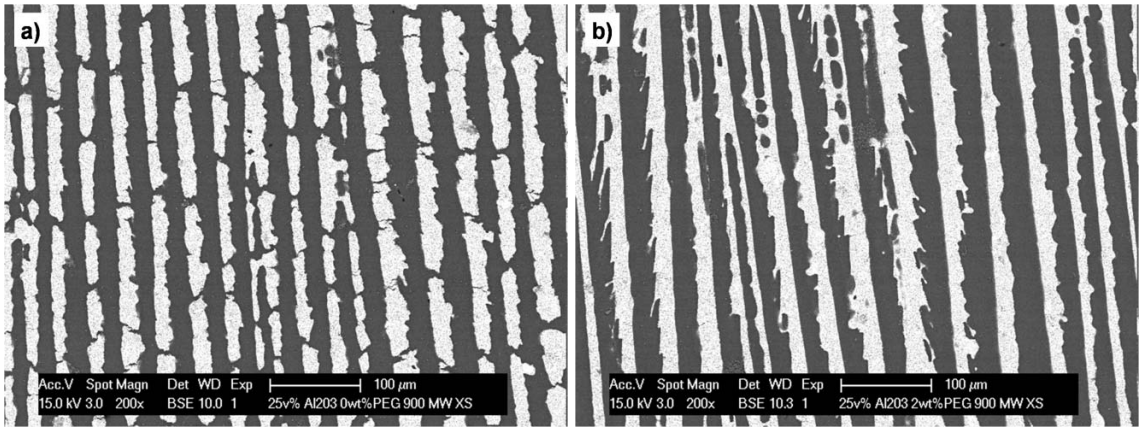

Figure 41. Micrographs taken from a section parallel to the freezing direction of samples containing 25 vol% Al_2O_3 and a) 0 wt% PEG (900 g/mol), b) 2 wt% PEG (900 g/mol) Magnifications of the micrographs are both 200x.

Upon addition of 2 wt% PEG the structure parallel to the freezing direction is somewhat more refined, with smaller pores, and the secondary dendrite arms are beginning to become more prevalent, especially when compared to those found for the sample containing no PEG. The presence of these arms can be seen in Figure 41b where some of the arms are in the plane of the section parallel to the freezing direction. Additionally, the smaller features in some of the pore walls are due to secondary dendrite arms that are not in the plane of the micrograph. The presence of a water soluble polymer, such as PEG, can lead to constitutional supercooling as it is rejected from the moving solid-liquid interface. As the PEG piles up in the liquid in front of the solidification front the local equilibrium solidification temperature can be depressed, stabilizing the growth of dendrite tips into the melt and leading to refinement of the structure. Based on steady state solidification theory (Equation 29) it was expected that the temperature gradient across the solidification interface and the interfacial velocity would have the largest effect on both the pore size and wall thickness values while constitutional supercooling plays a smaller role. These experiments were not at steady state due to the decreasing thermal gradient and

interfacial velocity encountered as heat was extracted through an increasing amount of solid material. If the effect of the PEG was strictly limited to supercooling (ΔT) then one would expect a decrease in pore size upon addition of the smallest amount of PEG. The pore size would then gradually diminish due to decreasing ΔT as the PEG content is increased. As mentioned previously, however, these effects are expected to be much smaller than the effect of the thermal gradient. Based on these arguments the observed refinement in the microstructure for the 2 wt% PEG sample compared to the case with no polymer agrees with what is expected from solidification theory.

When the PEG content was increased to 5 wt% there did not appear to be many changes compared to the sample that was processed with 2 wt% PEG, except that the some of the secondary dendrite arms appeared to be more prominent. This was the case for only a few arms so this could be a manifestation of arms that are from a crystal that is tilted at a different orientation than others that are in the same image.

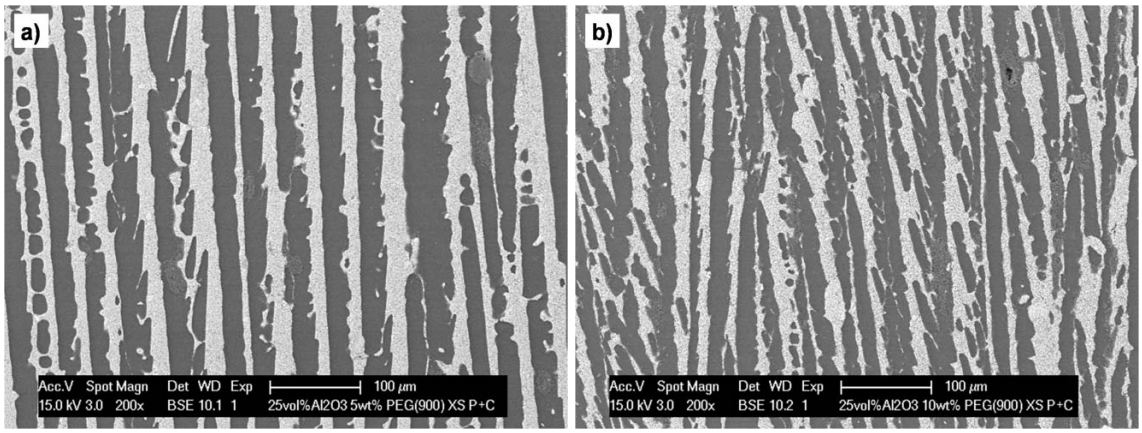

Figure 42. Micrographs taken from a section parallel to the freezing direction of samples containing 25 vol% Al_2O_3 and a) 5 wt% PEG (900 g/mol), b) 10 wt% PEG (900 g/mol) Magnifications of the micrographs are both 200x.

The sample containing 10 wt% PEG began to display a somewhat different morphology than what was found for the samples containing smaller amounts of PEG. In this case the structure is becoming much more broken down and the secondary dendrite arms are becoming somewhat finer. It also appeared that the primary dendrites were smaller than what was observed for previous compositions. The gradual refinement of the structure continued when the polymer content was increased to 15 wt% PEG as both the primary and secondary dendrites appeared to decrease in size.

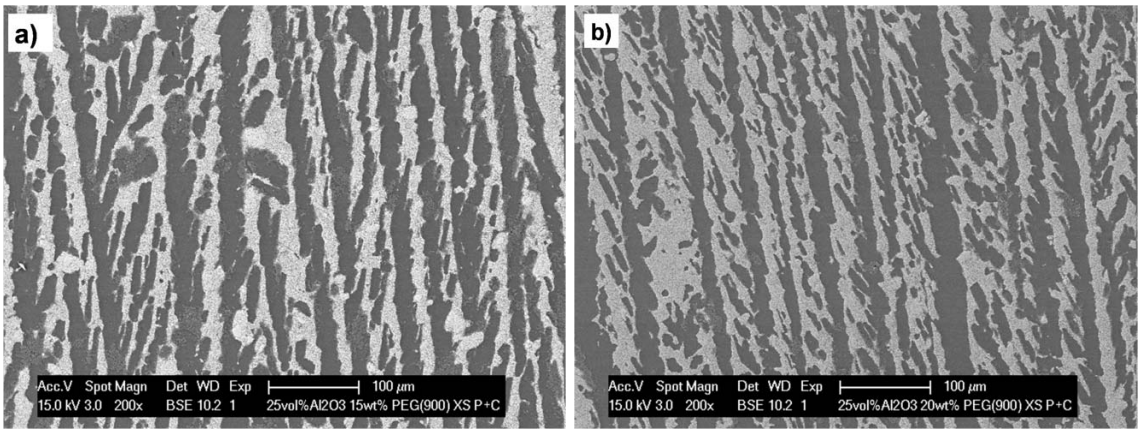

Figure 43. Micrographs taken from a section parallel to the freezing direction of samples containing 25 vol% Al_2O_3 and a) 15 wt% PEG (900 g/mol), b) 20 wt% PEG (900 g/mol) Magnifications of the micrographs are both 200x.

Interestingly, some of the secondary dendrites in the 15 wt% PEG sample (Figure 43a) appear to be somewhat coarser and more prominent than those found in the 10 wt% PEG sample. The microstructure of the 20 wt% PEG sample can be seen in Figure 43b and displays the finest primary and secondary dendrites of any of the samples that were examined in this series. The

microstructure is made up of rather fine primary dendrites with numerous thin secondary dendrite arms extending out from them and terminating at the wall of particles accumulated in between it and the next primary ice crystal. When the polymer content was increased to 25 wt% PEG the microstructure displayed some very drastic changes, as can be seen in Figure 44.

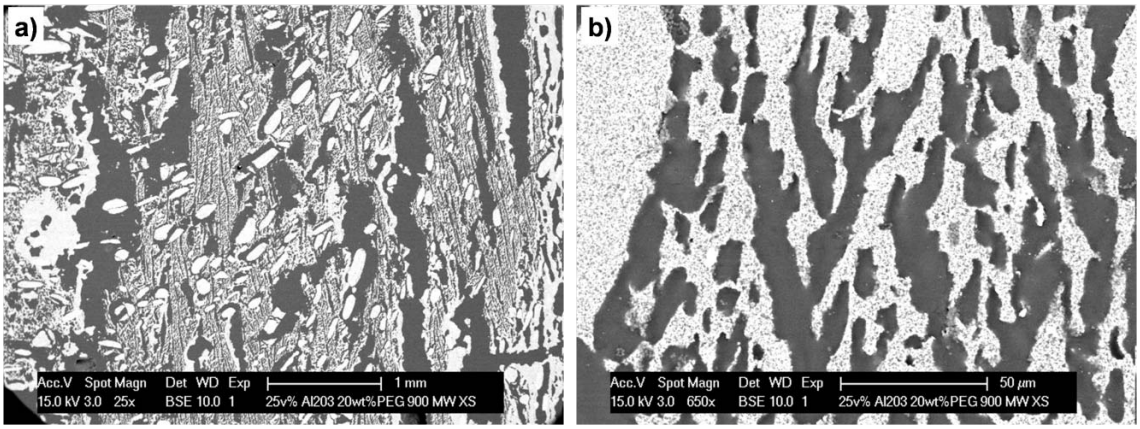

Figure 44. Micrographs taken from a section parallel to the freezing direction of a sample containing 25 vol% Al_2O_3 and 25 wt% PEG (900 g/mol). Magnifications of the micrographs are a) 25X and b) 650X.

The low magnification micrograph in Figure 44a shows that large portions of the sample were made up of voids and dense regions despite some of the sample still displaying directionality. A higher magnification micrograph of one of the directional regions, seen in Figure 44b shows that these areas were fine and dendritic in nature, as would be expected due to the increased amount of PEG in the slip. The sample also displayed a large amount of agglomerates, which were clearly evident in the low magnification micrograph. These agglomerates were most likely a result of poor particle dispersion as a result of the increased viscosity of the slip. The large voids and dense regions were likely due to segregation of large

amounts of PEG during freeze drying, as the samples partially melted before the ice was completely sublimated. Due to the multiple deficiencies found while observing the 25 wt% PEG sample on the microscope it was not analyzed any further.

Additionally, polymer contents ranging from 30 to 47.5 wt% PEG were also tested in an effort to create extremely fine structures. This was motivated by the fact that PEG forms a binary eutectic with water [152], so it was reasoned that using compositions close to the eutectic would give very fine porosity as a result of coupled growth. The results of these tests were non-conclusive as many difficulties were experienced with sample preparation and freeze drying. The effects that were noted for the sample with 25 wt% PEG were greatly magnified when the polymer content was increased, resulting in samples that partially melted and ruptured during freeze drying. The cause of the failure of the samples was linked to inhomogenous gas evolution during freeze drying due to a lack of temperature control that allowed the PEG to flow as the temperature increased. The details of these trials and further discussion can be found in Appendix A. Based on the difficulties that were experienced with higher polymer contents it appears that in the polyethylene glycol-water binary system that using concentrations above 20 wt% PEG will result in degradation of the expected directional structure.

Micrographs from sections taken perpendicular to the direction of solidification were also analyzed for these samples and can be seen below in Figure 45 through Figure 47. When no PEG was present in the structure the section was made up of lamellar colonies of ice crystals as would be expected from the solidification of hexagonal ice [48,54]. When 2 wt% PEG was added to the sample the scale of the structure was decreased and evidence of more prominent secondary dendrite arms was seen as the primary lamellar crystals began to display small features at their edges.

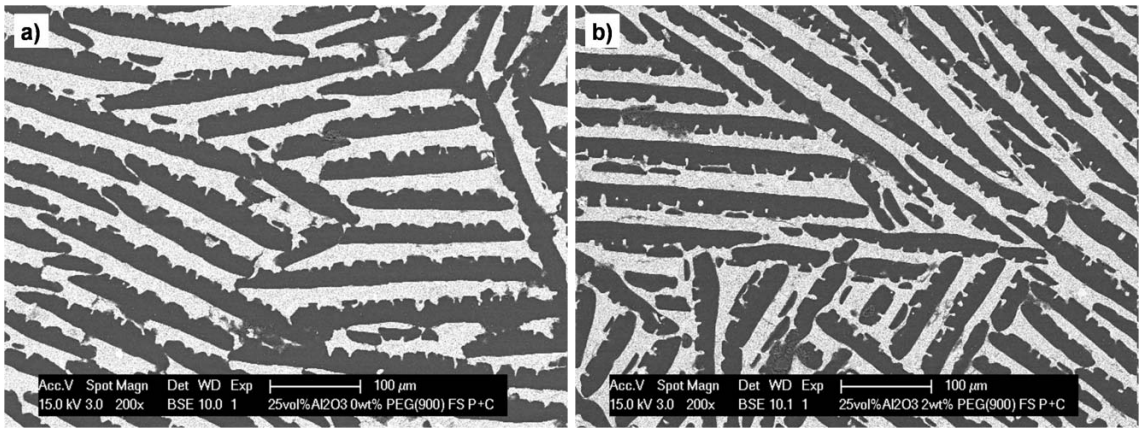

Figure 45. Micrographs taken from a section perpendicular to the freezing direction of samples containing 25 vol% Al_2O_3 and a) 0 wt% PEG (900 g/mol), b) 2 wt% PEG (900 g/mol) Magnifications of the micrographs are both 200x.

This agreed with what was observed in Figure 41b since the secondary dendrite arms did not extend far from the primary ice crystals. The addition of 5 wt% PEG to the sample once again caused the size of primary crystals to decrease. It was noted that the size of the oriented colonies seem to be getting smaller with increasing amounts of PEG. The sample containing 10 wt% PEG did not appear to display many differences from the 5 wt% sample with regard to the size of the ice crystals but did seem to show an increased amount of smaller features from secondary dendrite arms.

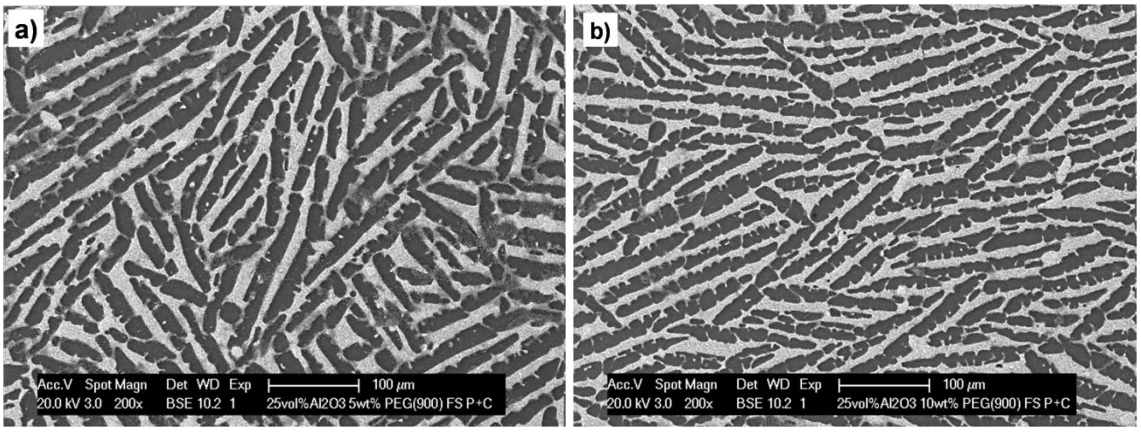

Figure 46. Micrographs taken from a section perpendicular to the freezing direction of samples containing 25 vol% Al_2O_3 and a) 5 wt% PEG (900 g/mol), b) 10 wt% PEG (900 g/mol) Magnifications of the micrographs are both 200x.

Upon increasing the PEG content to 15 wt% the sample showed a decrease in the scale of the structure, which was noted on the section parallel to the freezing direction, as well as a much more complicated structure that was a mixture of lamellar primary ice crystals and smaller sections from the finer secondary dendrite arms. The 15 wt% PEG sample also showed evidence of agglomerates in the structure that were not seen on the parallel sections for this sample. The microstructure of the 20 wt% PEG sample was much like the 15 wt% sample, and was comprised of a mixture of sections from primary and secondary dendrites, with the former having an increased amount of small features due to secondary arms. Once again there were a lot of agglomerates present on the section and it appears that the increasing polymer content had an effect on the dispersion of the particles in the slips. In all, observations of sections perpendicular to the freezing direction were consistent with what was observed on parallel sections for the respective samples.

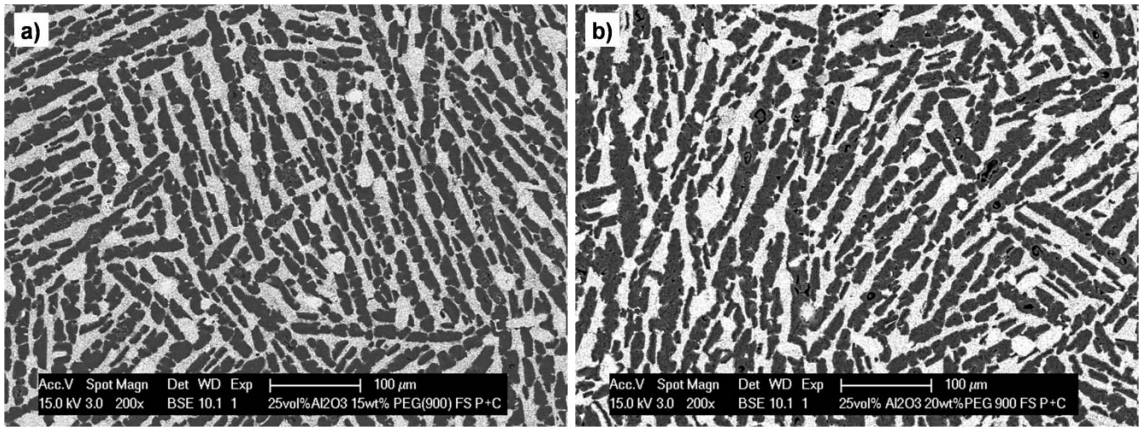

Figure 47. Micrographs taken from a section perpendicular to the freezing direction of samples containing 25 vol% Al_2O_3 and a) 15 wt% PEG (900 g/mol), b) 20 wt% PEG (900 g/mol) Magnifications of the micrographs are both 200x.

Figure 48 shows the results of pore size measurements from halfway up the height of the sample on sections parallel to the freezing direction. When no PEG was present the measured pore size was 25 μm, which was the largest value obtained for any of the samples. As soon as 2 wt% PEG was added a significant decrease in the pore size to 18 μm was observed. As the PEG content was increased to 5 and 10 wt% PEG no significant measurable change in the pore size was noted, given the size of the error bars on the data points. Eventually when the PEG content was increased to 15 and 20 wt% PEG the pore size decreased to 16 and 13 μm respectively. The samples displayed an overall decrease in the measured pore size from 25 μm to 13 μm which verifies what was qualitatively observed for these samples in the micrographs above. Based on solidification theory it would be expected that the addition of PEG would first cause a large decrease in the pore size and then a more gradual decrease as the polymer content is increased.

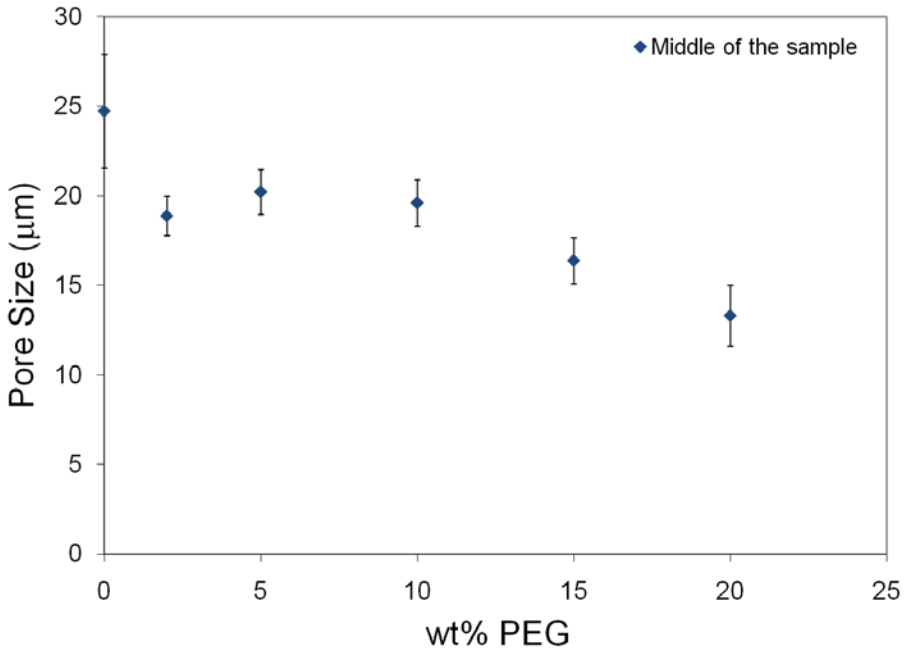

Figure 48. The effect of PEG content on the pore size midway up the sample measured on sections parallel to the freezing direction for samples containing 25 vol% Al_2O_3 and 0-20 wt% PEG (MW = 900 g/mol).

The results in Figure 48 are in agreement with this as the largest decrease in measured pore size occurred when the smallest amount of PEG was added to the slip, with a more gradual decrease noted as the amount of PEG was increased to 20 wt%. The theory behind this was discussed in more detail earlier in this section and it was noted that the effects of PEG on the interface would be weaker than that of the thermal gradient. It was observed in Figure 33 that samples cast with an LN_2 bath had significantly smaller pore sizes than samples cast with an EDI bath. Freezing with a colder bath gave larger overall changes in pore size than the gradual decrease observed in Figure 48 for increasing PEG content. This confirms that the effect of PEG is weaker than the effect of the thermal gradient, which agrees with what is expected from solidification theory.

The measured wall thickness values were obtained from the same images that were analyzed to gather the pore size values and can be seen in Figure 49.

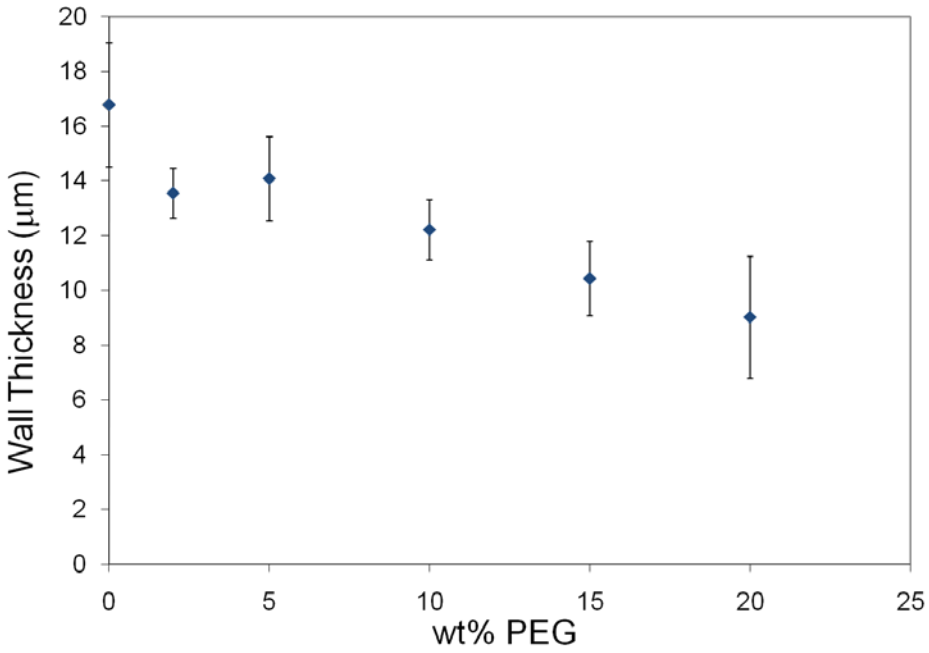

Figure 49. The effect of PEG on the pore wall thickness for sections parallel to the freezing direction containing 25 vol% Al_2O_3 and 0-20 wt% PEG (MW = 900 g/mol).

It can be seen that the pore wall thickness values displayed a trend that was similar to what was observed for the pore size values. When no PEG was present the wall thickness was 16.7 μm and this decreased to 13.5 μm for an addition of 2 wt% PEG. The wall thickness did not change significantly upon increasing the PEG content to 5 wt% and subsequently decreased to 12.2 μm for the sample with 10 wt% PEG. Finally the wall thickness values decreased to 10.4 μm and 9.0 μm for PEG contents of 15 and 20 wt%, respectively. It was noted that the 95% confidence intervals for the measured wall thickness values were larger than those for the

corresponding pore size values. This is thought to be due to the fact that the walls were increasingly broken up by secondary dendrite arms, especially as the PEG content was increased. Overall both the pore size and pore wall thickness measurements verify the gradual refinement of the microstructure that was observed for these samples on sections taken both parallel and perpendicular to the freezing direction.

The solid volume percent values that were obtained from the Archimedes method can are shown in Figure 50 and were found to range from 31% to 34% for samples with PEG contents ranging from 0 to 15 wt% PEG.

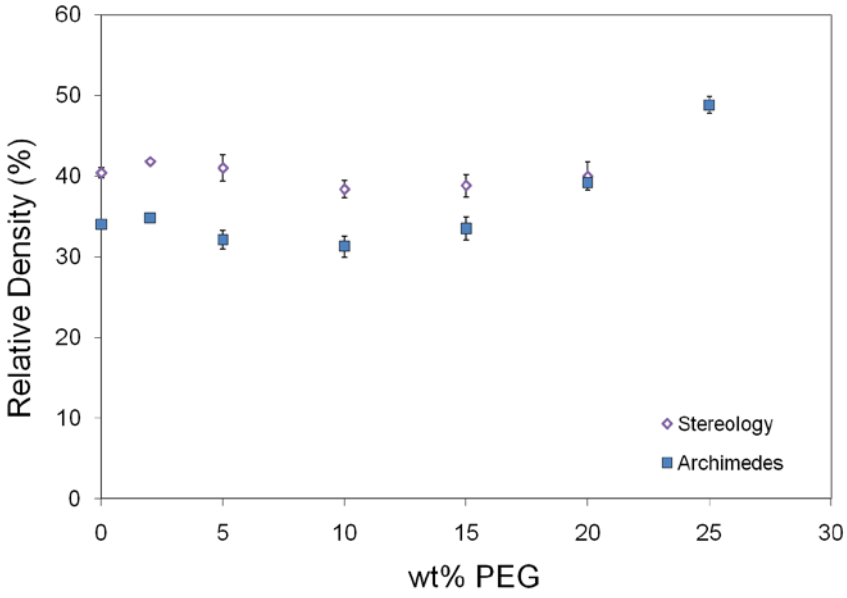

Figure 50. Comparison of the bulk densities measured by the Archimedes method and image analysis for samples containing 25 vol% Al_2O_3 and 0 – 25 wt% PEG.

These values are approximately 5 to 10% larger than the slip solid loading of 25 vol%. The sample that was processed with 20 wt% PEG had a somewhat higher solid volume fraction

value of almost 40% and the 25 wt% PEG sample gave an even higher value of 49%. The rather large solid volume fraction value for the 25 wt% sample is reasonable since the sample had some rather dense regions where fine porosity was likely lost during sintering. The loss of fine porosity in the pore walls is also a possible explanation for why the Archimedes value for the 20 wt% sample is somewhat higher than the other samples. Most of the samples had measured solid line fractions that were slightly higher than the values that were obtained for the Archimedes method. The reason for the larger values from image analysis is likely due to fine porosity in the pore walls that was not able to be seen at the magnifications used for image analysis. The 20 wt% PEG sample showed close agreement between the values obtained from both stereology and the Archimedes method. The lack of a solid volume fraction measurement for the sample containing 25 wt% PEG was due to the fact that the microstructure was not subject to image analysis since the large voids would have prohibited the proper application of measurement techniques.

Figure 51 shows the effect of increasing PEG content on the measured secondary dendrite arm spacing. It can be seen that the sample containing no PEG had a secondary spacing value of 22.6 μm, which was the smallest value for these samples.

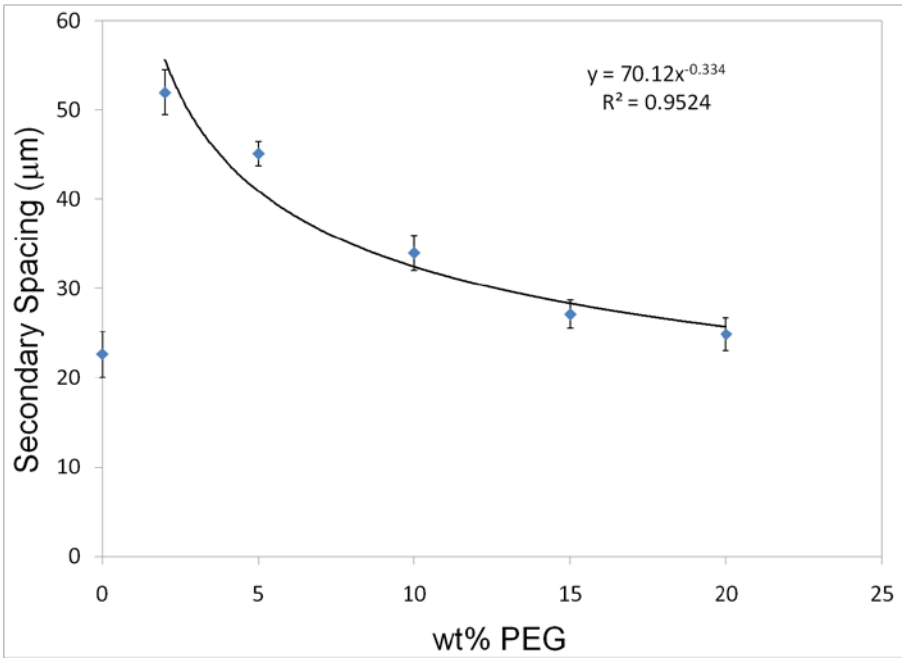

Figure 51. The effect of polyethylene glycol (PEG) content on the secondary dendrite arm spacing for slips containing 25 vol% Al_2O_3 solidified with an ethanol/dry ice bath.

When 2 wt% PEG was added the secondary spacing rose significantly to 51.9 μm. Further addition of 5 and 10 wt% PEG caused the spacing to decrease to 45.1 μm and 34 μm, respectively. A final decrease to 27.1 μm and 24.9 μm was noted for PEG contents of 15 and 20 wt%. It is not surprising that the addition of 2 wt% PEG caused such a large increase in the measured secondary dendrite arm spacing as this can be explained using solidification theory. At 2 wt% the samples have the largest supercooling value of all of the PEG contents that were tested, which gives a larger root to tip distance on the primary dendrite. This allows coarsening of the secondary dendrite arms to occur as they are in contact with the liquid for a longer time period. As the amount of supercooling decreases with increasing PEG composition it can be expected that the secondary spacing should diminish gradually. The dependence of secondary spacing on supercooling (ΔT_o) is given in equations 30-32 and is rather weak compared to that of

the thermal gradient or interfacial velocity. When the secondary spacing data for samples containing 2 – 20 wt% PEG were fit with a power law curve it was found that the values decayed with an exponent of -0.333, which agrees closely with the expected value of 1/3 from solidification theory in equation 30. As can be seen in figure 51 the R^2 value of 0.952 for the fit was quite good. These measurements support the qualitative observations made on sections parallel and perpendicular to the freezing direction and show that despite the complexity of the system the results are in agreement with what is expected from theory.

All of the measurements that have been discussed so far have been obtained from sections parallel to the freezing direction and midway up the height of the sample. As was seen for other samples (see Sections 5.1.3 and 5.2.1) that were freeze cast in similar molds it was expected that the interfacial velocity would decrease with time as heat must be extracted through an increasing amount of solidified material. Due to this it was expected that the values of measured quantities such as the pore size and wall thickness would vary from the bottom to the top of the sample. The pore size and wall thickness were measured near the bottom, at the centerline and near the top of each of the samples and the results can be seen below in Figure 52 and Figure 53.

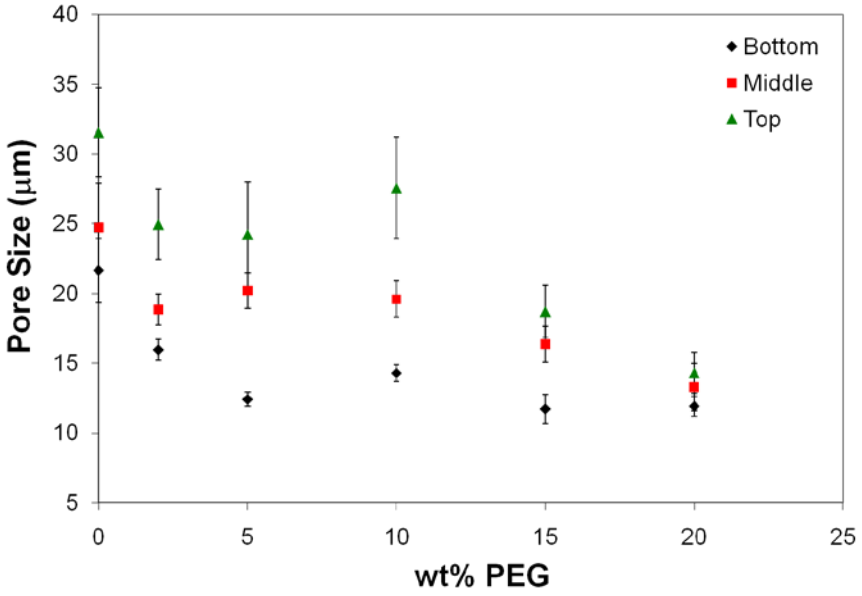

Figure 52. The effect of location on the measured pore size for freeze-cast samples containing 25 vol% Al_2O_3 and 0-20 wt% PEG.

It can be seen that for all of the samples the pore size was the smallest at the bottom of the sample and increased to a maximum near the top of the sample. The pore size for the sample containing 0 wt% PEG increased from 21 μm at the bottom to 31 μm at the top of the sample. The sample with 2 wt% PEG experienced a similar increment in pore size, rising from 15.9 μm to 24.9 μm from the bottom to the top of the sample. The coarsening in both of these samples was appreciable and significant given the confidence intervals that were calculated. These observations are consistent with what is expected as the interfacial velocity decreases and the overgrowth of more favorably oriented ice crystals causes the pore size to increase. The 5 and 10 wt% PEG samples experienced the greatest amount of coarsening with the pore size roughly doubling from 12.4 μm to 24.2 μm for the 5 wt% PEG sample and 14.3 μm to 27.5 μm for the 10 wt% PEG sample. These results were somewhat interesting as it was expected that the degree of coarsening would decrease as the structures became more broken down. The large coarsening

values for these two samples could possibly be attributed to some secondary dendrite arms becoming aligned with the direction of heat flow. The amount of coarsening present in the 15 wt% and 20 wt% PEG sample decreased significantly as the pore size rose from 11.7 μm to 18.7 μm and 9 μm to 11.6 μm, respectively. Based on the measured confidence intervals for the 20 wt% PEG sample it can be said that the coarsening in this sample was not significant. It is thought that the decrease in coarsening as the PEG content was raised from 10 wt% PEG to higher concentrations was due to the progressive breakdown of the structure. For all of the samples it was noted that the 95% confidence interval was smallest at the bottom of the sample and increased significantly towards the top of the sample, meaning that the variation between the measured images increased greatly due to coarsening. Regardless of the measurement position all of the samples showed the same general decrease in pore size that was discussed previously for measurements from the middle of the sample.

The variation in wall thickness with measurement location in the sample can be seen below in Figure 53.

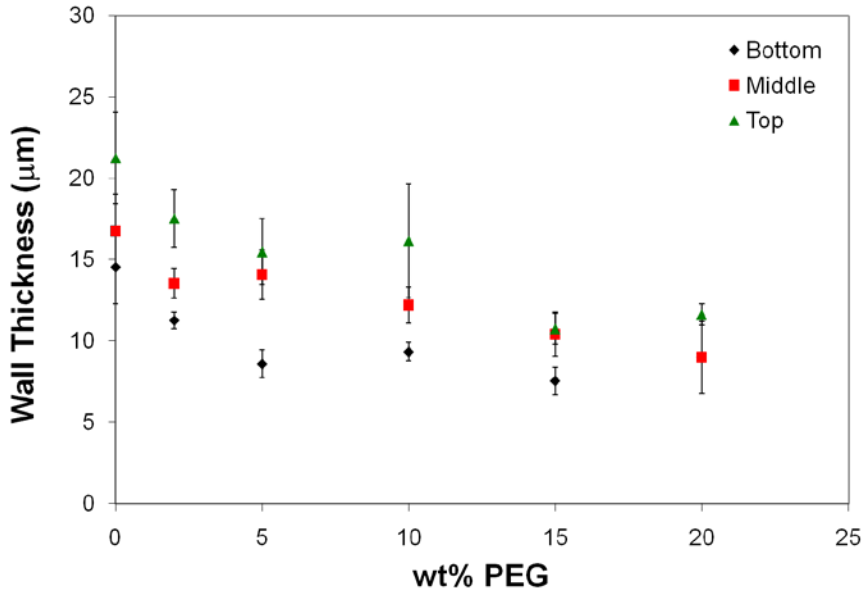

Figure 53. The effect of location on the measured wall thickness for freeze-cast samples containing 25 vol% Al_2O_3 and 0-20 wt% PEG.

The measured wall thickness values displayed behavior similar to the pore size values, as they increased in size from the bottom to the top of the sample. The degree to which the wall thickness increased along the height of the samples appeared to decrease somewhat as the polymer content was increased, with the 20 wt% PEG sample showing no measurable difference between the wall thickness at the bottom and top of the sample. This was likely due to the increased number of finer secondary dendrite arms that tend to break up the pore walls into smaller sections. Once again the 95% confidence intervals were largest for the measurements that were taken near the top of the sample, showing the effect of coarsening on the measurement techniques. Additionally, the measured values all decreased with increasing PEG content no matter where the measurement was performed on the sample.

5.1.5 Effect of PEG on Permeability

The permeability of the samples that contained 25 vol% Al_2O_3 and 0-20 wt% PEG was determined by using the Forchheimer equation (Equation 45), which is an extension of Darcy's law that accounts for non-Darcian effects from inertial flow in the sample. The use of this equation allows both the Darcian (k_1) and non-Darcian (k_2) permeabilities to be determined. Further details concerning the permeability test can be found in the experimental procedures (Section 4.3). The Darcian permeability values for these samples can be seen below in Figure 54.

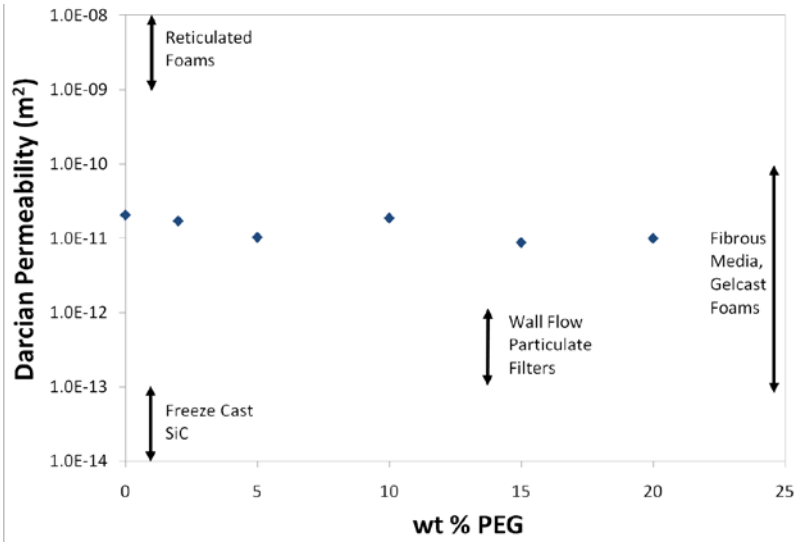

Figure 54. Measured Darcian permeability values for freeze cast samples containing 25 vol% Al_2O_3 and 0-20 wt% PEG. Ranges of measured permeability values from the literature for other common macroporous ceramics are included for comparison.

The experimental values fall in the wide range of values found in the literature for fibrous media and gelcast foams [153] and are somewhat higher than what has been reported for

through-wall diesel particulate filters [154]. Additionally the experimental values are roughly two orders of magnitude greater than what was determined for freeze cast SiC ceramics for cooling applications [138]. In general the Darcian permeability values appear to decrease from $2.05x10^{-11}$ to $9.92x10^{-12}$ m^2 as PEG was added in increasing amounts. This general decrease in permeability is not surprising as it was seen in Figure 48 that the pore size decreased steadily with increasing PEG content. Since the pore volume fraction for these samples was similar it can be expected that changes in pore size and pore morphology would be the primary variables that affect the measured permeability. The scatter in the experimental values is rather small compared to the range of permeabilities that exist in the literature for samples with similar pore size and total porosity. The only significant deviation from the observed trend with increasing PEG content occurs at 10 wt% PEG, where the measured permeability is almost equivalent to the value with no PEG present. This anomalously high value could be attributed to changes in the proportion of inertial or viscous flow in the sample due to the microstructural morphology or could simply be scatter in the data that inevitably arises during testing. The experimental non-Darcian permeability values for these samples can be seen below in Figure 55.

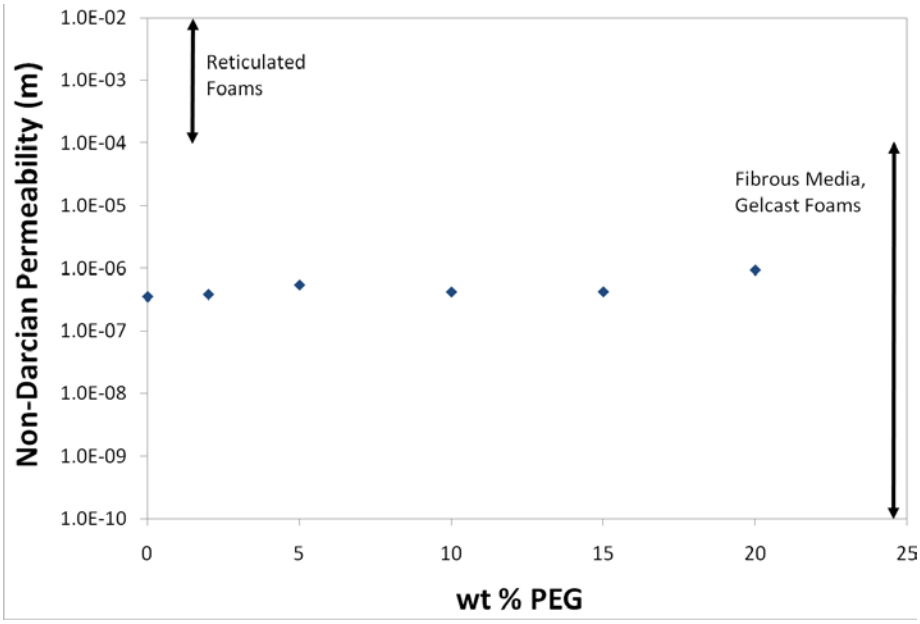

Figure 55. Measured non-Darcian permeability values for freeze cast samples containing 25 vol% Al_2O_3 and 0-20 wt% PEG. Ranges of measured permeability values from the literature for other common macroporous ceramics are included for comparison [153].

The non-Darcian permeability values showed a gradual increase from 3.52×10^{-7} to 9.36×10^{-7} m as the PEG content was changed from 0 to 20 wt%. The spread of the measured values is once again small and there appears to be no major deviations from the observed trend for any of the PEG contents. The values are smaller than what has been observed for reticulated ceramics, which have much larger pore sizes and lower solid loadings and are towards the high end of the broad range of values exhibited by fibrous media and gelcast foams [153]. No values of non-Darcian permeability were available in the literature for freeze-cast ceramic materials. The proportion of viscous (Darcian) flow can be calculated by using the Forchheimer number (Equation 46) and the results can be used to help interpret the permeability values. The effect of increasing PEG content on the amount of viscous flow in the samples can be seen below in Figure 56.

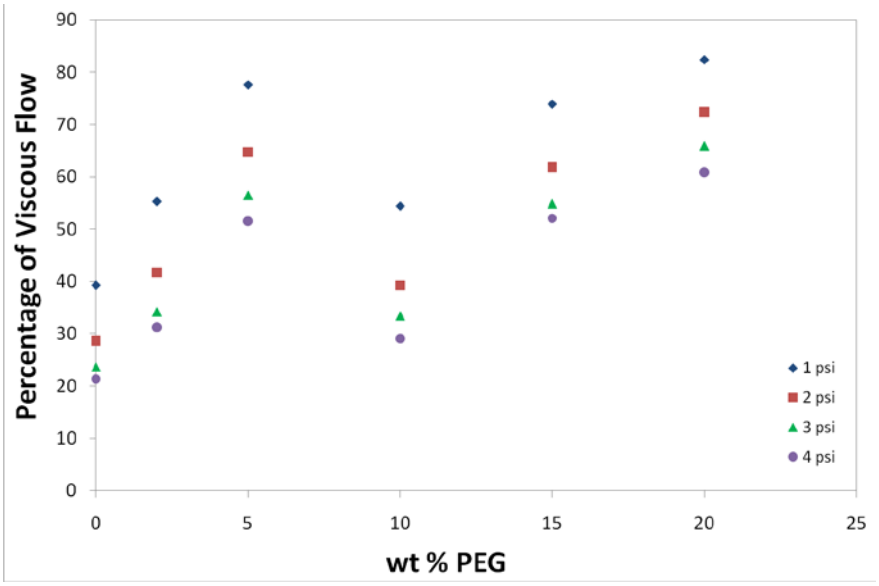

Figure 56. The effect of PEG content on the calculated fraction of viscous flow based on the Forchheimer number calculation.

There are four separate values plotted for each PEG content since the superficial velocity is a variable in the Forchheimer number equation and the samples were tested at four different pressures. Due to this the results were intentionally not averaged. It can be seen that there is significant variation between the fractions of viscous flow due to changes in gas pressure and that the amount of viscous flow decreased with increasing pressure for each individual sample. This result is logical considering that inertial effects become increasingly significant at higher fluid velocities. At a testing pressure of 1 psi the fraction of flow attributed to inertial effects was roughly 40% on average and this value increased to almost 60% for a pressure of 4 psi. It is clear that all of the samples showed a significant fraction of inertial flow, but no clear trend is evident. The large variation in the fraction of inertial flow could be attributed to changes in the

roughness of the pore walls and the size and extent of secondary branches in the microstructure. From these results it seems that the pore morphology, not just the pore size, affects the measured permeability values. More importantly these results suggest that inertial effects should not be neglected when measuring the permeability of freeze cast ceramics, thus justifying the use of the Forchheimer equation.

Overall the experimentally measured permeability values decreased with increasing PEG content and fell into the range of values for fibrous materials and gelcast ceramics. The values also were significantly larger than what has been reported in the literature so far for freeze cast materials. A more detailed discussion of how these values compare to the literature can be found in section 5.3.2.

5.1.6 Effect of PEG on Compressive Strength

The addition of increasing amounts of PEG to the slip caused significant changes in the microstructure and measured parameters such as the pore size and pore wall thickness. These changes were expected to have an effect on the measured properties of these materials. In the previous section it was found that the permeability of the samples generally decreased with increasing amounts of PEG. The compressive strength of freeze cast ceramics is also expected to be sensitive to changes in the microstructure so following permeability testing these samples were subjected to uniaxial compression testing. The compression strength of samples containing 25 vol% Al_2O_3 and 0 – 20 wt% PEG were measured on uniform samples with a diameter of 10 mm and a height of 5 mm. Further details concerning the testing can be found in the experimental procedures (Section 4.4).

The loading curves for the sample containing 5 wt% PEG can be seen below in Figure 57. These curves showed an initial elastic regime followed by a peak at the maximum compressive stress and finally a gradual failure regime. The maximum compressive stress occurred between 6% and 11% compressive strain, showing that these materials have good strain tolerance for highly porous ceramics, likely due to their aligned nature and rather dense pore walls.

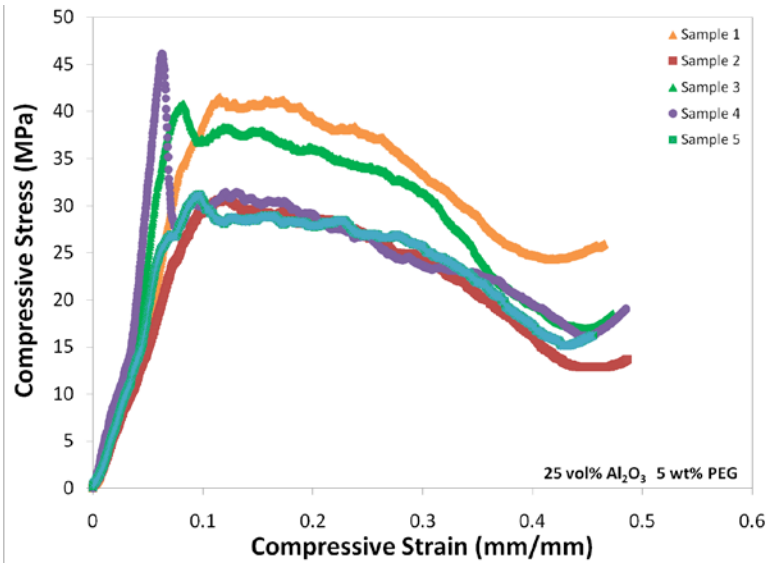

Figure 57. Loading curves obtained from uniaxial compression testing of 5 identical cylindrical samples containing 25 vol% Al_2O_3 and 5 wt% PEG at a strain rate of 1 mm/min.

For the majority of samples failure was gradual and occurred in a step-wise fashion. This was likely due to groups of similarly oriented lamellae failing and the load being transferred to the remainder of the sample by load transfer between the pore walls. This causes the compressive stress to either remain constant or rise until fracture of another group of lamellae occur. This process occurs repeatedly until the sample begins to compact after it has totally

failed, causing a rise in the measured compressive stress at higher compressive strain values. The failure regime can be thought of as the progressive failure of a series of columns. Sample 4 in this series displayed a much more drastic drop in the load bearing capability of the sample but eventually showed the gradual decay in the loading curve that was observed for the other samples. This large step in the curve could possibly be attributed to a defect in the sample that caused a large crack to be generated. The loading curves for the samples that contained 0, 2, 10 and 15 wt% PEG were similar in nature to those that were seen in Figure 35. The curves that resulted from the testing of the 20 wt% PEG samples were somewhat different and displayed well defined maximum compressive strength peaks that occurred at somewhat higher compressive strain values. The loading curves obtained from testing these samples can be seen below in Figure 58.

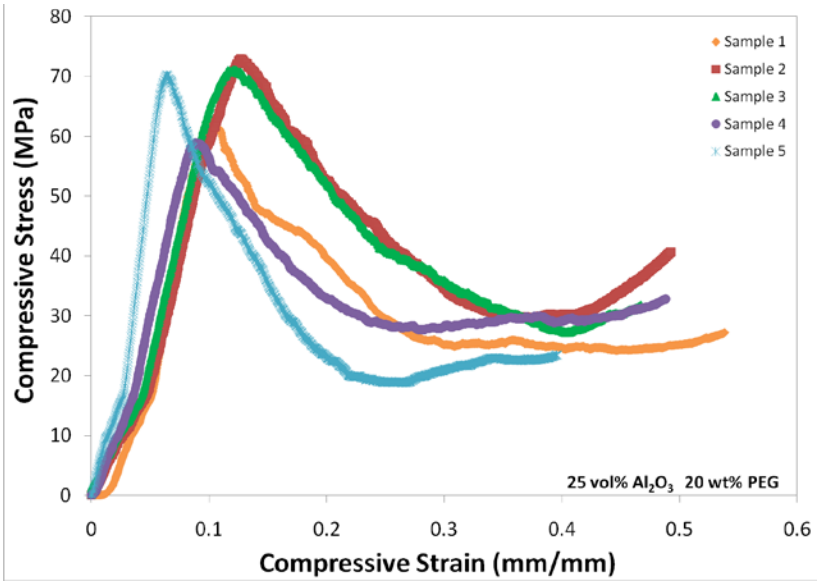

Figure 58. Loading curves obtained from uniaxial compression testing of 5 identical cylindrical samples containing 25 vol% Al_2O_3 and 20 wt% PEG at a strain rate of 1 mm/min.

The decay of the loading curves in the failure regime is not as gradual as was seen for the 5 wt% PEG sample but still shows evidence of the step-like failure due to progressive fracture of oriented ceramic lamellae. This behavior is similar to what was observed in Figure 36, where failure occurs and load transfer overwhelms a greater proportion of the pore walls, leading to a larger load drop. This could indicate that the lamellae are more laterally connected, thus behaving somewhat less like individual columns.

The measured uniaxial compressive strength values for samples containing 25 vol% Al_2O_3 and 0-20 wt% PEG can be seen below in Figure 59. The load was applied in an axial fashion for all of the samples as this was the preferred loading direction due to the directionality of the pore walls that resulted from directional solidification. Much like oriented composite materials the strength in the transverse direction would be expected to be extremely low due to the weak transverse connectivity between the lamellar and was not tested for this reason. Additionally, other studies have evaluated the strengths in the transverse direction [91,100,101,106] and found them to be at least 50% lower than the strengths in the axial direction.

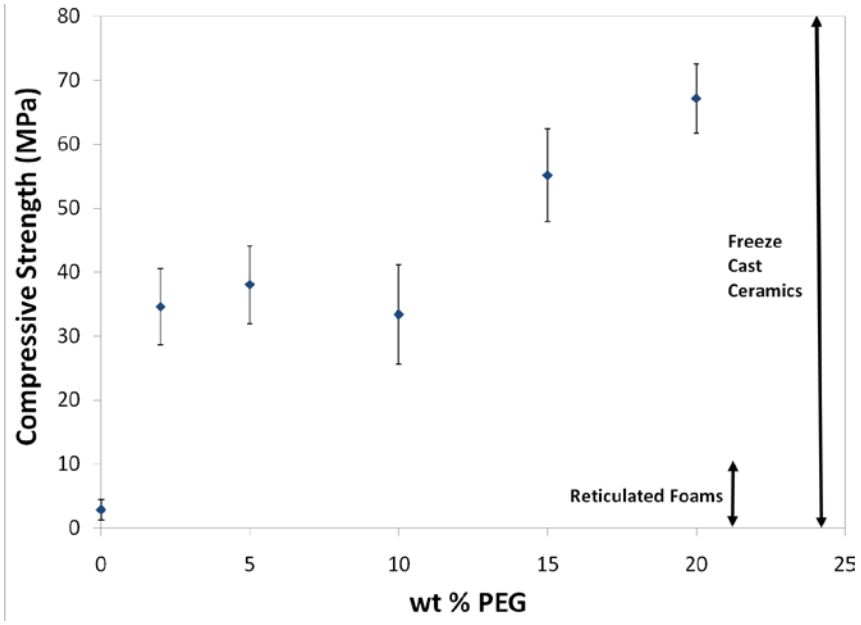

Figure 59. Uniaxial compressive strength values for samples containing 25 vol% Al_2O_3 and 0-20 wt% PEG. The load was applied to the samples axially at a strain rate of 1 mm/min. The arrows on the right represent the range of strength values found in the literature for different types of macroporous ceramics.

The samples displayed an overall increase in compressive strength as the PEG content in the slip was increased. The compressive strength increased from a value of 2.85±1.6 MPa at 0 wt% PEG to a value of 34.6±6 MPa when only 2 wt% PEG was added. This significant increase in strength was likely due to the effect of the binder on the integrity of the pore walls. The sample with no PEG had very cracked and discontinuous pore walls, as can be seen in Figure 41a which cause the sample to not be able to bear much load, giving a very low compressive strength. When 2 wt% PEG was added to the slip the integrity of the pore walls became greater and the strength was increased. When the PEG content was increased to 5 wt% the compressive strength increased to 38.07±6.09 MPa and then slightly decreased to 33.41±7.72 MPa for a content of 10 wt% PEG. These changes were not considered to be very significant given the measured 95% confidence intervals for these samples. The fact that little difference existed in

the compressive strength between the 2 wt%, 5 wt% and 10 wt% samples can be explained in part by the fact that their total porosities (calculated from the bulk density in Figure 50) and wall thickness values were very close. Any differences in the compressive strength between these samples could possibly be attributed to differences in lateral connectivity due to the extent of branching in the structures. When the PEG content was increased to 15 wt% the compressive strength increased significantly to 55.16±7.26 MPa. This increment in strength was likely due to an increased amount of branching that was present in this structure relative to the previous PEG contents, which, as mentioned before, could increase the connectivity of the lamellae and act as bridges that increase the overall strength of the material. Additionally the increased amount of polymer in the structure could have given higher strength due to the greater ability of the binder to dissipate the volume expansion of the ice and avoid cracking of the pore walls. Finally when the PEG content was increased to 20 wt% the compressive strength once again increased to 67.19±5.43 MPa. It was noted previously that the bulk density and solid volume fraction from stereology were approximately 5% higher for the 20 wt% PEG sample relative to all of the other PEG contents that were tested. This in turn gives a total porosity value that is approximately 5% lower than the other samples which would give an increase in strength of approximately 8% based on the change in load bearing area (Equation 48). Since the strength increased by approximately 22%, it is apparent that there are other factors to consider for this sample. Since this structure was the most broken down out of the PEG contents that were examined it is likely that the amount of connectivity between the lamellae was increased relative to lower PEG contents, which could help raise the strength significantly. On top of this, having such a large amount of polymer present during processing allows the pore walls to easily accommodate the volume expansion due to ice solidification, thus avoiding large cracks in the pore walls. A

combination of the above factors likely resulted in the high compressive strength that was reported for the 20 wt% PEG sample.

Figure 59 shows how the compressive strength measurements of this study compare to those that are found in the literature for other common porous ceramic materials, such as reticulated foams. It was found that with the exception of the sample with 0 wt% PEG that the values are significantly higher than those of reticulated foams [7,148]. It should be noted that the total porosity in these samples varied between 60 and 68% which is much lower than values for reticulated foams, which are often greater than 80%. The change in load bearing area alone does not account for the increase in strength values (~200%) between reticulated foams and the freeze cast samples in this study. The increased strengths are likely due to increased strut integrity for freeze cast samples, since reticulated foams often have cracks in their struts that are caused by thermal decomposition of the substructure that was replicated. These cracks make reticulated foams inherently weak. The combination of denser pore walls, aligned structure and lower porosity values give freeze cast ceramics higher strength than reticulated foams. The range of compressive strength values in the literature for freeze cast ceramics varies over a large range [15], as can be seen in Figure 59. Table 2 shows a summary of compressive strength values obtained from the literature for a variety of freeze cast ceramics with lamellar pore architectures and similar total porosity values to those that were examined in this study. The strength values obtained in this study are somewhat higher than a large number of the values reported by other authors in Table 2 and are in the range of those that were obtained by Han et al. who also worked with Al_2O_3 [95].

Table 2. Compressive strength values from the literature for freeze cast ceramics with a lamellar pore architecture and similar porosity values as were calculated for the samples with 0-20 wt% PEG.

Author	Porosity (%)	Compressive Strength (MPa)	Material	Reference Number
Deng et al.	69	1.67	TiO_2 coated glass	128
Deville et al.	68	16	Hydroxyapatite	97
Liu et al.	67	26	Alumina-Zirconia	127
Zuo et al.	66	28	YSZ	108
Han et al.	66.1 65.6	62.4 73.7	Alumina	95

In all the compressive strength values for the samples containing 25 vol% Al_2O_3 and 0-20 wt% PEG showed an overall increase as the PEG content was raised. This increase can be attributed largely to the PEG additions increasing the integrity of the pore walls but also to changes in the microstructure such as lateral connectivity that result from the effect of PEG on the solid-liquid interface during solidification. The reported compressive strength values are in the range that have been found for freeze cast ceramics and are somewhat higher than those with a lamellar pore architecture and similar total porosity.

5.1.7 Effect of Varying Molecular Weight of PEG on Microstructure

Freeze-casting presents a situation where heat is extracted through an increasing amount of solidified material, giving rise to a constantly decreasing interfacial velocity. This in turn causes appreciable ice crystal coarsening along the height of the sample. Evidence of this coarsening was presented for samples processed with both PEG (Table 1) and PVA (Table 5) binders in

varying proportions. To try and avoid this situation and achieve steady-state conditions a pseudo-Bridgman solidification apparatus was created where the samples were immersed into a freezing bath at a constant velocity. A tensile testing machine was used since it has a crosshead speed that was adjustable over a wide range of velocities. The details of this setup can be found in the experimental procedures (Section 4.1.4). Before any experiments could be performed it was necessary to find a range of velocities suitable for processing of the samples. The main criterion was that the amount of coarsening between the top and the bottom of the sample should be kept to a minimum. The details concerning the testing of the equipment and velocity optimization will not be presented here but can be found in Appendix B.

To investigate the effect of the molecular weight of PEG on the microstructure of freeze cast ceramics it was determined that a constant velocity of 55 μm/sec should be used (see Appendix B). The molecular weights were chosen such that PEG in a variety of physical states, ranging from liquid to a hard, flaky solid was tested. The slips all contained a fixed amount of alumina (25 vol%) and PEG relative to the water content (5 wt%) and were solidified under identical freezing conditions using the same bath (EDI, -73°C) and solidification velocity (55 μm/sec) for all samples. Further details concerning these tests can be found in the experimental procedures. The goal of using the pseudo-Bridgman solidification apparatus for these tests was to ensure that the molecular weight of PEG was the only dependent variable for the samples.

The lowest possible molecular weight that could be used for polyethylene glycol was its monomer, ethylene glycol (EG), which has a formula weight of 62 g/mol. When the sample containing EG was frozen using the pseudo Bridgman solidification apparatus the resulting structure was fine and dendritic in nature, as can be seen below in Figure 60 for a section parallel to the freezing direction. The secondary dendrite arms in this sample are relatively coarse and

appear to be of the same scale as the primary trunk that they originate from. When the molecular weight of PEG was increased to 400 g/mol the structure was again broken down and dendritic, but an overall decrease in the scale of the structure was noted. The primary and secondary dendrites seen below in Figure 60 for the 400 g/mol sample are visibly smaller than their counterparts from the sample containing EG as the additive.

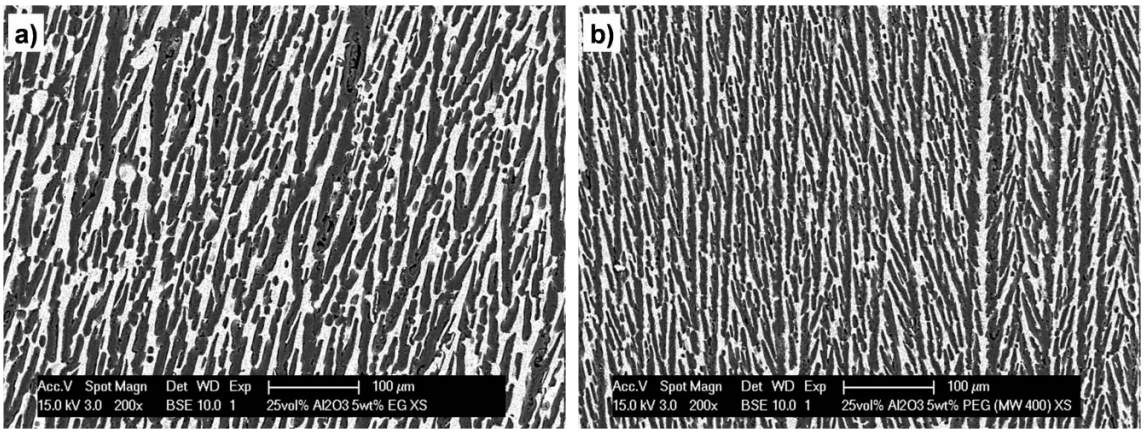

Figure 60. Micrographs taken from sections parallel to the freezing direction for samples containing 25 vol% alumina and a) 5 wt% of ethylene glycol and b) 400 g/mol Polyethylene glycol. The magnification of both micrographs is 200x.

Other than the change in scale the secondary branches in the 400 g/mol sample do not extend as far from the primary trunk, compared to those in the EG sample, before they terminate at particles that have accumulated against the next primary crystal. The branched nature of the structure is likely due to the polyethylene glycol destabilizing the solidification interface, as was seen for previous samples. When the molecular weight of polyethylene glycol was increased to 900 g/mol the changes observed in the structure were far less severe than was observed when going from EG to 400 g/mol as the molecular weight. The structure can be seen below in Figure

61 and is made up of fine primary and secondary dendrites that appear marginally smaller than those in the 400 g/mol sample. The secondary dendrite arms in the 900 g/mol sample are shorter and somewhat thicker than those that were observed in previous samples.

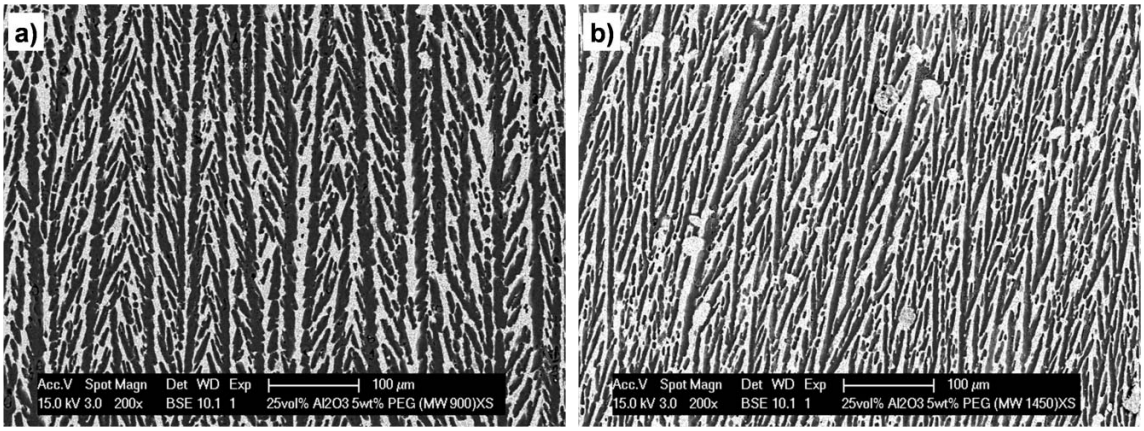

Figure 61. Micrographs taken from a section parallel to the freezing direction for samples containing 25 vol% alumina and a) 5 wt% of 900 g/mol and b) 1450 g/mol polyethylene glycol. The magnification for both micrographs is 200x.

The structure resulting from freezing with 1450 g/mol PEG can also be seen in Figure 61 and shows that the fine dendritic structure that was obtained during freezing followed the same trend as the other samples as the overall scale of the microstructure decreased. Both the primary and secondary dendrites appear to be finer than those that were seen in Figure 60 and the sample that was processed with 900 g/mol PEG. Additionally the secondary dendrite arms appear to be more constrained and begin to orient themselves in the direction of heat flow. It can also be seen that some agglomerates are present in the structure, which can possibly be attributed to particle dispersion problems due to the increased molecular weight of PEG that was used.

The structure resulting from processing with a molecular weight of 3350 g/mol can be seen below in Figure 62. The same trends that have been seen with earlier samples are again evident as the microstructure is somewhat finer in scale than the 1450 g/mol sample and much finer than the structures exhibited in Figure 60.

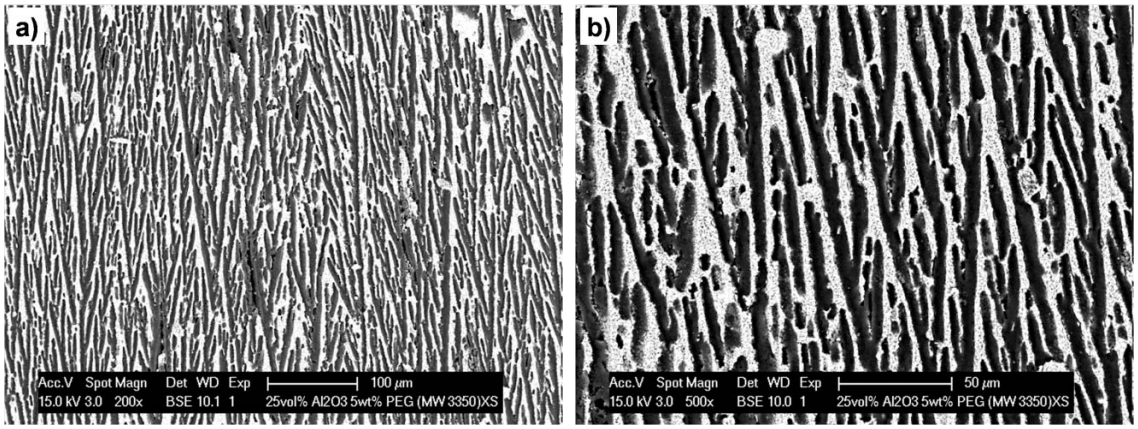

Figure 62. Micrographs taken from a section parallel to the freezing direction for a sample containing 25 vol% alumina and 5 wt% of 3350 g/mol polyethylene glycol. The higher magnification micrograph (b) shows detail of the branching in the microstructure. The magnifications of the micrographs are a) 200X and b) 500X (right).

A further refinement of the secondary dendrite arms was noted and the extent of branching makes the structure appear rather complicated at lower magnification. The higher magnification micrograph of this sample in Figure 62b shows that the branching is mostly limited to secondary arms that grow out from the primary trunk a slight distance before gradually orienting themselves more favorably with the direction of heat flow. The presence of agglomerates in the structure was once again noted.

Figure 63 – Figure 65 show sections taken from perpendicular to the freezing direction for the samples that were discussed above. All of the samples were taken from a height halfway

up the sample. The sample that was processed with ethylene glycol exhibits a mixture of lamellar ice crystals and sections through secondary dendrite arms. It is difficult to tell the difference between the two types of crystals due to the fact that they were similar in scale, as was seen in Figure 60. It was also noted that the ice crystals were oriented in lamellar colonies as was seen for other samples in the literature [44,45,54] and in other experiments (Sections 5.1.4 and 5.2.1).

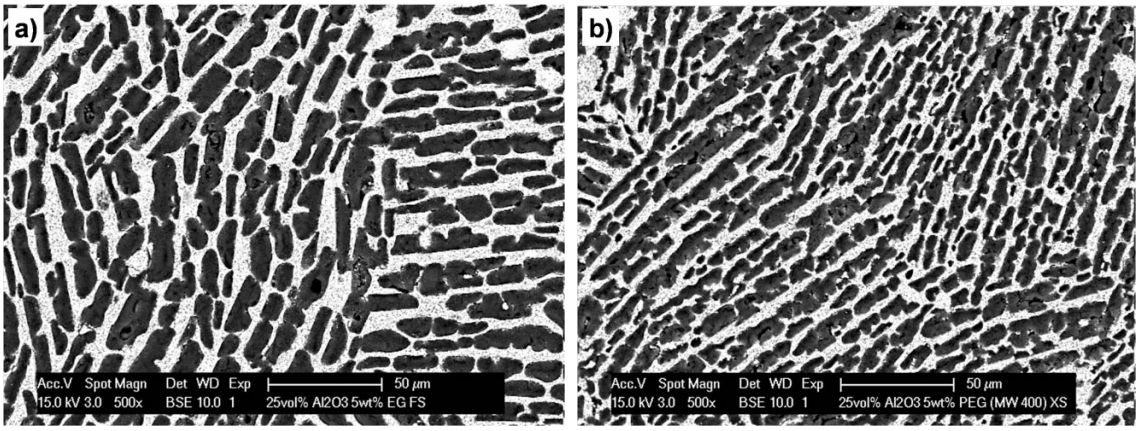

Figure 63. Micrographs taken on sections perpendicular to the freezing direction for samples containing 25 vol% Al_2O_3 and a) 5 wt% Ethylene glycol, b) 5 wt% 400 g/mol Poly(ethylene glycol). The magnifications of both micrographs are 500X.

When the molecular weight was increased to 400 g/mol the distinct change to a much finer microstructure that was seen in Figure 60 was once again evident. This section is made up of primary lamellar ice crystals that have finer features around them that are sections through the secondary dendrite arms. This differs from the sample processed with EG as the distinction between primary and secondary arms was unable to be made. It also appears that the sizes of the colonies in the 400 g/mol sample are somewhat smaller than those found in the EG sample. The

sample processed with 900 g/mol PEG does not display many differences from the one that was processed with 400 g/mol PEG. As can be seen in Figure 64a the structure is again a mixture of sections from primary and secondary crystals. The presence of agglomerates at this molecular weight was also noted. Agglomerates were not seen on parallel sections until higher molecular weights, however, the fact that they were present in this sample is likely due to the fact that there is a greater chance of viewing an agglomerate on perpendicular sections.

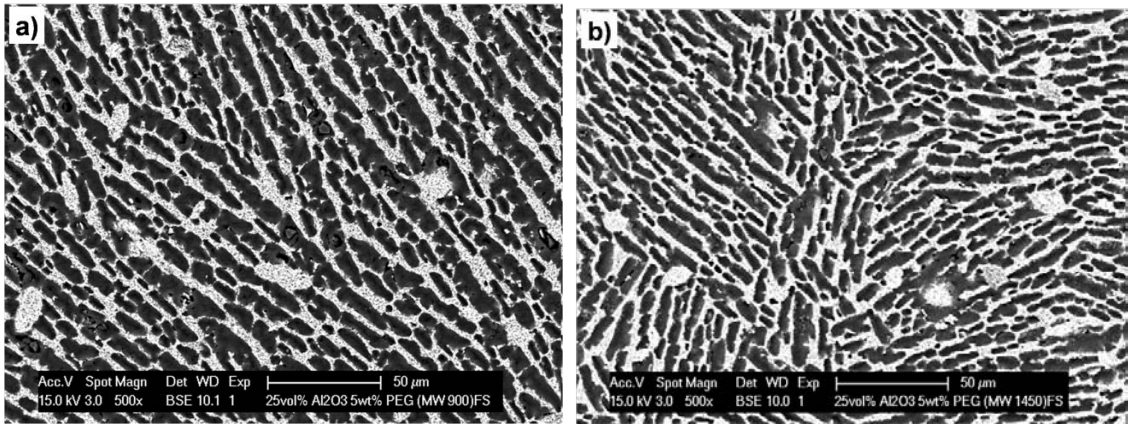

Figure 64. Micrographs taken on sections perpendicular to the freezing direction for samples containing 25 vol% Al_2O_3 and 5 wt% Poly(ethylene glycol) of molecular weight a) 900 g/mol and b) 1450 g/mol. The magnifications of both micrographs are 500x.

The 1450 g/mol sample, seen in Figure 64b, shows both a decrease in the pore size and the size of the colonies in the sample. These colonies are much more numerous and significantly smaller than those that were observed in Figure 63. As was seen with the other samples the microstructure was once again a mixture of sections from primary and secondary ice crystals. The sample processed with 3350 g/mol PEG (Figure 65) displayed little difference from the sample processed with 1450 g/mol PEG (Figure 64b) with regard to both the pore size and the

scale of the colonies of similarly oriented ice crystals. This is not surprising since the microstructures of these two samples on sections parallel to the freezing direction were of a similar scale.

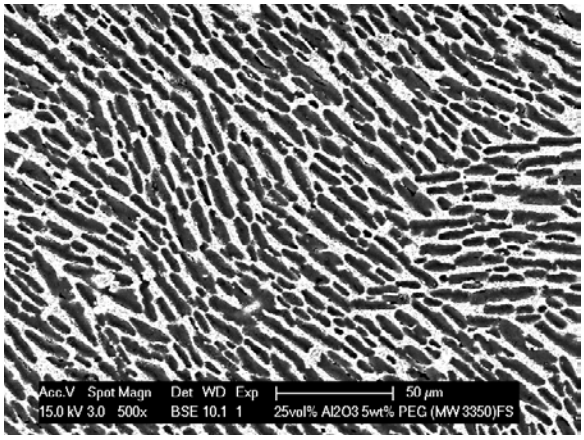

Figure 65. A micrograph taken on a section perpendicular to the freezing direction for a sample containing 25 vol% Al_2O_3 and 5 wt% Poly(ethylene glycol) of molecular weight 3350 g/mol. The magnification of the micrograph is 500x.

Despite the fact that it is difficult to tell the difference between primary and secondary dendrite arm sections on the sections taken perpendicular to the growth direction it does appear that the trends observed are consistent with those that were seen for sections taken parallel to the growth direction.

The pore size on sections parallel to the freezing direction was quantified by performing 200 individual measurements on each micrograph in a series of 5 micrographs, giving 1000 measurements per sample. The 95% confidence interval was calculated and reflected the variation in the average pore size between the 5 images that were used for measurement for each

sample. A plot of the measured pore size values against molecular weight can be seen in Figure 66.

Overall the trend in the measured pore size values reflected the gradual refinement of the structure with increasing molecular weight that was seen for sections parallel to the freezing direction in Figure 60-Figure 62. The pore size decreased from 10 μm for the sample containing 5 wt% ethylene glycol to 5.5 μm for the sample containing 5 wt% PEG with a molecular weight of 3350 g/mol. The error bars on the data points indicate the 95% confidence interval for each sample and show that the decrease in pore size was statistically significant.

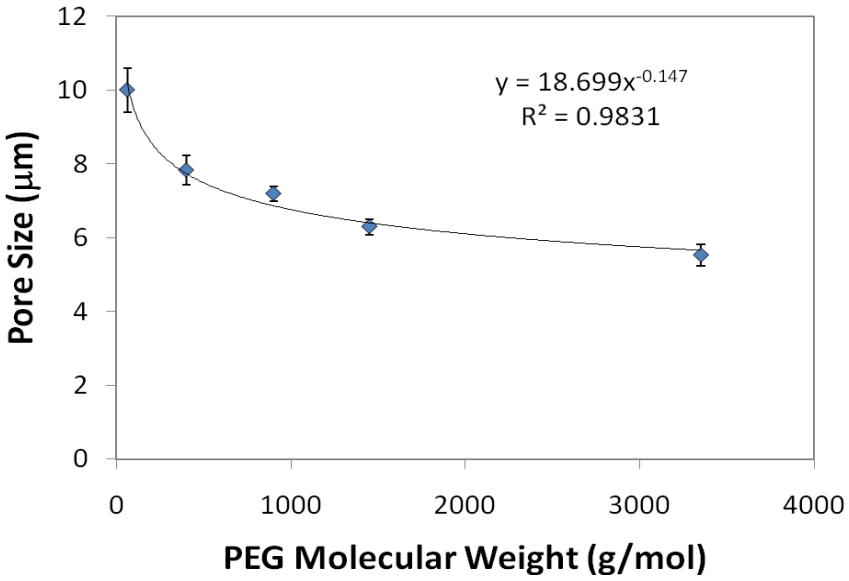

Figure 66. The effect of molecular weight of polyethylene glycol (PEG) on the pore size of freeze-cast ceramics prepared using the pseudo-Bridgman solidification mechanism. All measurements were performed on sections parallel to the freezing direction.

The general decrease in pore size is not surprising, as it can be expected based on traditional solidification theory. The equation for primary spacing of dendrites during directional

solidification of a binary alloy (Equation 29) shows that a number of variables can affect the expected spacing during steady state solidification. One of the primary reasons that the pseudo-Bridgman solidification setup was used was to provide an essentially constant solidification velocity, and hence conditions close to steady state. It was shown previously that increasing the thermal gradient (G) (Section 5.1.1) and varying the amount of constitutional supercooling (ΔT_o) (Section 5.1.4) can have an effect on the measured pore size in the samples. The conditions used during solidification with the pseudo-Bridgman apparatus presented a situation in which the interfacial velocity (v) and thermal gradient (G) were both held constant for all samples. If the changes in constitutional supercooling can are small then the ΔT_o quantity can be treated as a constant. A plot of the liquidus curves for a variety of molecular weights of PEG [155,156] can be seen below in Figure 67.

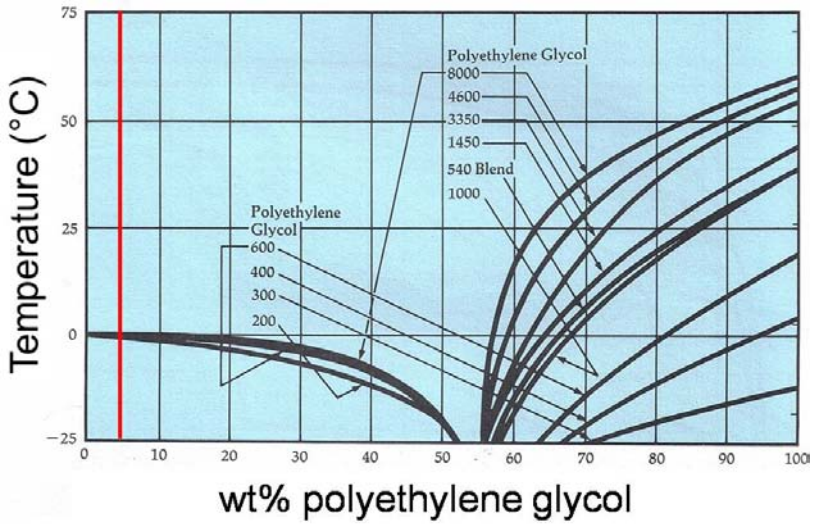

Figure 67. Liquidus curves for poly(ethylene glycol) solutions with molecular weights ranging from 200-8000 g/mol. Modified from [155,156] The composition of PEG used in given by the red line on the phase diagram.

This study used a 5 wt% aqueous solution of PEG as the liquid that the particles were dispersed in to create the ceramic slip. This composition is highlighted by the vertical red line in Figure 67 and it can be seen that at this point there is little difference in the liquidus curves for different molecular weights. Since the eutectic isotherm will be at a constant temperature the difference in ΔT_o (defined in Figure 2) for molecular weights ranging from 200 to 8,000 g/mol is negligible. Therefore it can be safely assumed that the supercooling variable in the primary spacing equation can be regarded as a constant under these experimental conditions. Since the velocity, thermal gradient and supercooling values are all constant during processing with the pseudo-Bridgman technique the only variable that remains in the primary spacing equation is the diffusion coefficient of PEG. This variable has a ¼ power dependence and like the supercooling variable that was discussed in section 5.1.4 was expected to have a weak effect on the primary spacing when compared to other variables such as the thermal gradient and interfacial velocity. When considering the diffusion of in aqueous PEG solutions it was expected that the molecular weight of the polymer should have some effect, with the expected trend being that increasing molecular weight should increase the viscosity of the solution and decrease the overall diffusivity of PEG in water. The kinematic viscosity, which is defined as the ratio of the dynamic viscosity to density, for PEG of various molecular weights can be seen in Table 3 [155,156]. These values are for 50 wt% PEG aqueous solutions at their freezing point and were chosen because this gives a value close to the eutectic composition of the PEG-H_2O binary system. This composition therefore is similar to the last liquid that freezes and is the highest viscosity that is encountered by the system during solidification.

Table 3. The kinematic viscosity at the freezing point of 50 wt% PEG solutions of varying molecular weight.

Molecular Weight (g/mol)	Kinematic Viscosity (centistoke)
400	150
900	290
1450	500
3350	800

It can be seen that the viscosity increased significantly with increasing molecular weight, as was expected. The increase in viscosity should in turn adversely affect the diffusivity in aqueous PEG solutions. In general the self-diffusion coefficient (D_o) of PEG in aqueous solution is governed by the Flory scaling law [157]

$$D_o = KM^{-a} \qquad (50)$$

where K and *a* are empirical constants with *a* varying between 0.5 for a poor solvent to 0.6 for a good solvent. An examination of the effect of the molecular weight of uniform oligomers of PEG on the self diffusion coefficient of dilute aqueous PEG solutions (0.3 wt% PEG) was performed by Shimada et al. [157]. The molecular weights examined in the study ranged from 62 to 1,603 g/mol and found that in general the self diffusion coefficient of PEG obeyed equation 50 with a value of *a* being determined as 0.43. The authors found that their diffusion coefficients were slightly higher than those found by Waggoner et. al., [158] who used 5 wt% PEG aqueous solutions. The slight differences were attributed to Waggoner using a higher PEG concentration and PEG compounds with a molecular weight distribution rather than oligomers with no distribution. The data from the Shimada study examined a larger amount of molecular weights

and hence this study was used to estimate values of the self diffusion coefficient for the pseudo Bridgman study. The calculated values can be seen below in Table 4.

Table 4. Estimated self-diffusion coefficients (D_o) for different molecular weights of polyethyelene glycol in aqueous solution.

PEG Molecular Weight (g/mol)	Do (m^2/sec)
62	1.03E-09
400	4.67E-10
900	3.31E-10
1450	2.70E-10
3350	1.89E-10

It can be seen that the effect of increasing the molecular weight in the solution does indeed decrease the diffusion coefficient of PEG. Returning to the primary spacing equation from solidification theory (Equation 29) it can be seen that if all other variables are held constant that the pore size in the sample should be proportional to $D^{1/4}$. As discussed previously the assumption that the solidification velocity, thermal gradient and constitutional supercooling are constant holds for the conditions of the pseudo-Bridgman solidification process. If the values of the diffusion coefficient of PEG from Table 4 are used it is found that the pore size decays according to a power law fit with an exponent of -0.107. The experimentally measured pore size data in Figure 66 was also able to be fit by a power law function with the exponent being calculated as -0.147 and the R^2 value being 0.983, implying a good fit. Obviously there is a difference between the exponents that were calculated from the experimental data and solidification theory. However, given the complexity of the structures and the error in the pore

size measurements it was felt that the two values agreed reasonably well. Therefore the effect of molecular weight on the primary spacing roughly agrees with what is expected from traditional solidification theory.

The secondary dendrite spacing in a binary alloy is given by equation 30 and is found to be dependent mainly upon the local solidification time, t_f, defined in equation 32. In general a longer local solidification time results in coarser secondary dendrite arms due to the fact that arms near the tip of the dendrite are exposed to the liquid for a longer period of time. The constant M in equation 30 is defined in equation 31.

It can be seen that for a particular composition of PEG that the only variable in this constant is the diffusion coefficient. Assuming that the local solidification time between the samples is similar due to the processing conditions it is reasonable to assume that a change in the diffusion coefficient will have an effect on the measured secondary spacing. Given the fact that the secondary spacing would be proportional to $D^{1/3}$ the expected effect would be weak, much like that that was found for the primary spacing values. The secondary spacing values were not directly measured for these samples but qualitative observation of Figure 60-Figure 62 shows that the secondary dendrite arms did become finer as the molecular weight of polyethylene glycol was increased. Table 4 showed that increasing the molecular weight decreased the diffusion coefficient of PEG so it could be expected that there should be an overall decrease in the secondary dendrite spacing. The most likely cause of the secondary dendrites becoming finer is the viscosity increasing with higher molecular weight values. As the viscosity increases it becomes more difficult for the secondary arms to grow and therefore their extent of growth out from the primary arm becomes more and more limited. The higher molecular weight samples seen in Figure 61 and Figure 62 show that some of the secondary arms begin to extend upwards

in the solidification direction rather than continue to grow outward from the primary crystal. The increased viscosity limiting the growth of the secondary arms could possibly promote tertiary dendrite arms to form, but these would most likely melt back into the liquid and act to coarsen the secondary dendrites. It does appear that the secondary dendrites seem to agree, at least qualitatively with what is expected from solidification theory.

In summary it appears that the effect of increasing the molecular weight of polyethylene glycol at a fixed composition tends to decrease both the primary and secondary dendrite spacing. This is likely due to the effect of increased viscosity on the diffusion coefficient of PEG in the solutions. The experimentally measured values also appear to correlate fairly well with what is expected from traditional solidification theory of binary alloys. The pseudo-Bridgman solidification apparatus provided a unique way to control the solidification velocity and thermal gradient such that the effect of the molecular weight of PEG could be elucidated.

5.2 SAMPLES FREEZE-CAST WITH POLYVINYL ALCOHOL (PVA)

Polyvinyl alcohol (PVA) is a water soluble polymer that, like PEG, is commonly added to ceramics to give the green body increased strength. Previous studies have shown that PVA has the ability to affect the growth morphology of ice by adsorbing to rapidly growing facets and inhibiting growth on these planes [68]. For this reason it was decided to examine the effect of varying the amount of PVA present in the slip and determine the effects it has on the microstructure and properties of freeze cast alumina ceramics. The samples that were examined contained 25 vol% Al_2O_3 with PVA contents ranging from 0 to 20 wt% relative to the alumina

content and were frozen using an ethanol-dry ice bath that gave a chill block temperature of -75°C.

5.2.1 Effect of PVA on Microstructure

As can be seen below in Figure 68 and Figure 69 the PVA had a significant effect on the observed microstructures. With no polyvinyl alcohol present in the slip the pores in the sample are generally continuous and extend from one side of the micrograph to the other. The presence of small secondary dendrite arms extending from the primary ice crystals are also noted and give the pore walls a serrated morphology. According to solidification theory once a solute is introduced, constitutional supercooling of the growing crystals will occur provided the solute is rejected in front of the growing solid-liquid interface. This is indeed the case as the growing ice crystals have very low tolerance for solute and the PVA is rejected from the growing interface. Therefore upon addition of the lowest amount of PVA, in this case 5 wt%, the maximum supercooling should occur. The addition of 5 wt% PVA appears to give finer primary ice dendrites and coarser secondary arms. This agrees with solidification theory since at the largest value of supercooling the greatest distance between the root and tip of the dendrite will be present, allowing dendrite arms near the tip to experience longer periods of time in contact with the liquid, giving way to coarsening. It is also noted that upon the addition of 5 wt% PVA that there are many more pore terminations present. This can most likely be explained by the fact that some of the primary ice crystals are being overgrown by secondary dendrite arms that have coarsened and are more favorably aligned with the direction of heat flow.

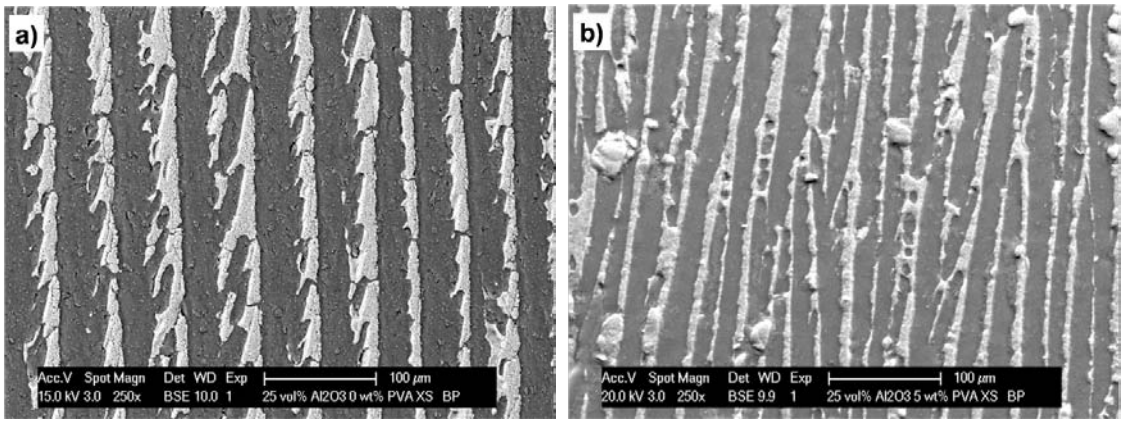

Figure 68. SEM micrographs of sections parallel to the freezing direction for samples containing 25 vol% Al_2O_3 and a) 0 wt% PVA and b) 5 wt% PVA. The magnifications of both micrographs are 250x.

When the amount of PVA was increased to 15 wt% it is noted that both the primary and secondary dendrites become finer and the structure has very thin and irregular pore walls. This can be explained by the increased amount of PVA that was added to the slip. As the amount of solute is increased further the amount of constitutional supercooling decreases. This is expected to give finer primary dendrites and secondary dendrites since the root to tip distance is now much smaller, thus giving the secondary arms less time to coarsen. Finally the sample containing 20 wt% PVA exhibited a structure with extremely fine primary and secondary dendrites. Once again this agrees with what is expected from solidification theory due to the decreased amount of supercooling.

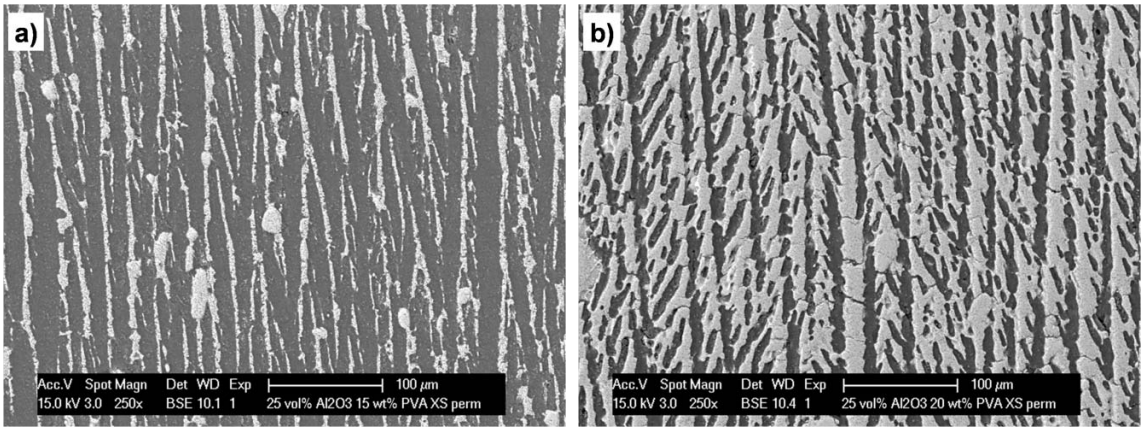

Figure 69. SEM micrographs of sections parallel to the freezing direction for samples containing 25 vol% Al_2O_3 and a) 15 wt% PVA and b) 20 wt% PVA. The magnification of both micrographs is 250x.

Figure 70 and Figure 71 show polished sections taken from a direction perpendicular to the solidification direction for the same samples that were discussed previously. Each of the sections was obtained from halfway up the height of the sample. For the sample containing no PVA, lamellar colonies that are typical of the growth of hexagonal ice under these conditions can be seen.

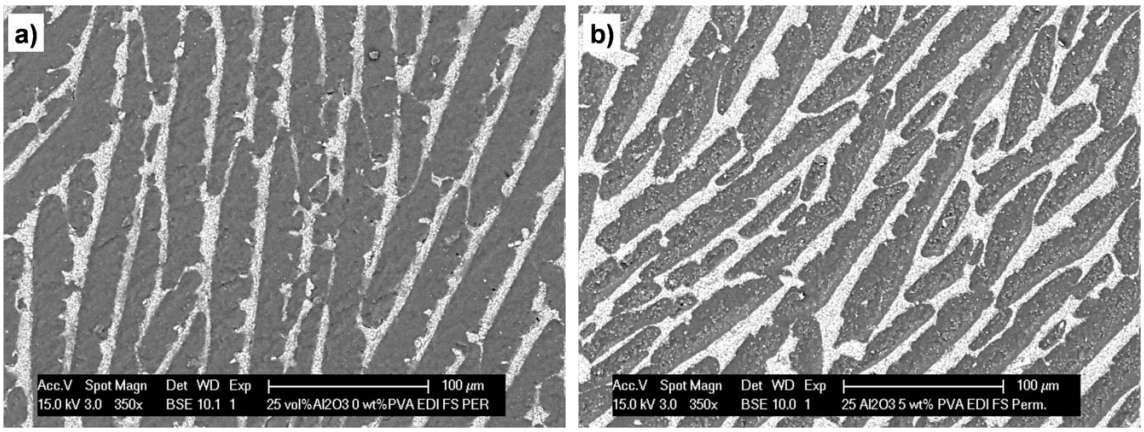

Figure 70. SEM micrographs of sections perpendicular to the freezing direction for samples containing 25 vol% Al_2O_3 and a) 0 wt% PVA and b) 5 wt% PVA. The magnification of both micrographs is 350x.

When 5 wt% PVA was added the transverse sections showed lamellar primary crystals that are often surrounded by smaller pore sections. These smaller pore sections are most likely due to the presence of secondary dendrite arms that have coarsened and become aligned with the direction of solidification, as was noted in the section from parallel to the freezing direction in Figure 68. The small pore sections also seem to be aligned, which would support the fact that they are secondary dendrites that grew from the same primary dendrite. Figure 71 shows a perpendicular section from a sample that contains 15 wt% PVA. For this sample the number of features surrounding the lamellar pores has increased in number.

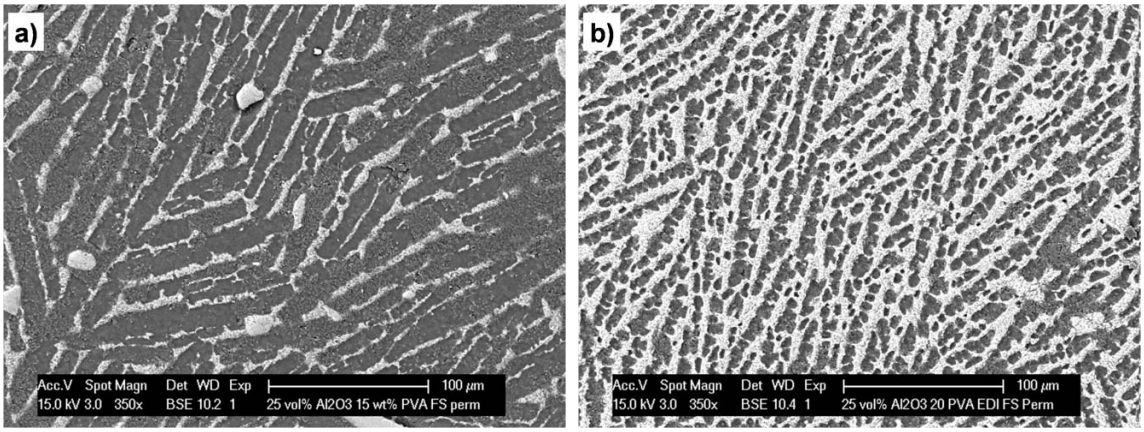

Figure 71. SEM micrographs of sections perpendicular to the freezing direction for samples containing 25 vol% Al_2O_3 and a) 15 wt% and b) 20 wt% PVA. The magnification of both micrographs is 350x.

The sample containing 20 wt% PVA shows very fine lamellae from the primary dendrites that are surrounded by very fine features from the secondary dendrite arms, which is in agreement with the section taken parallel to the freezing direction.

Overall the general changes observed in the microstructure of the samples as the PVA content increases appear to be qualitatively consistent with the expected effects of constitutional supercooling on the growth habit of ice crystals. There is a decrease in the primary dendrite spacing upon addition of PVA and the secondary dendrite arms appear to first coarsen and then become finer as the amount of supercooling decreases with increasing PVA content.

Figure 72 shows the results of pore size measurements from sections both parallel and perpendicular to the casting direction as a function of PVA content.

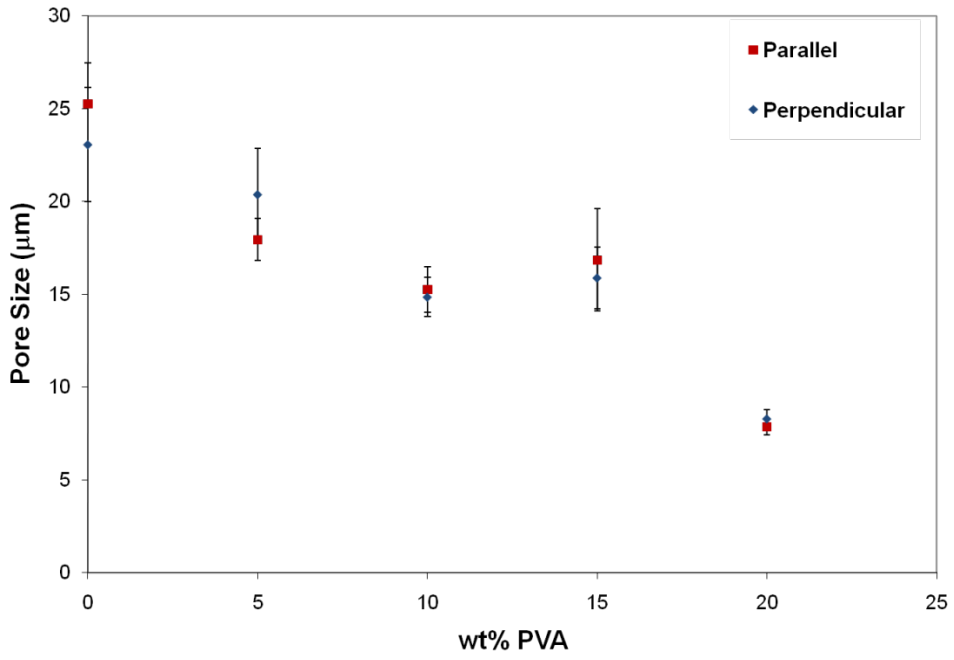

Figure 72. Effect of PVA content on pore size measured on sections parallel to the casting direction and perpendicular to the casting direction.

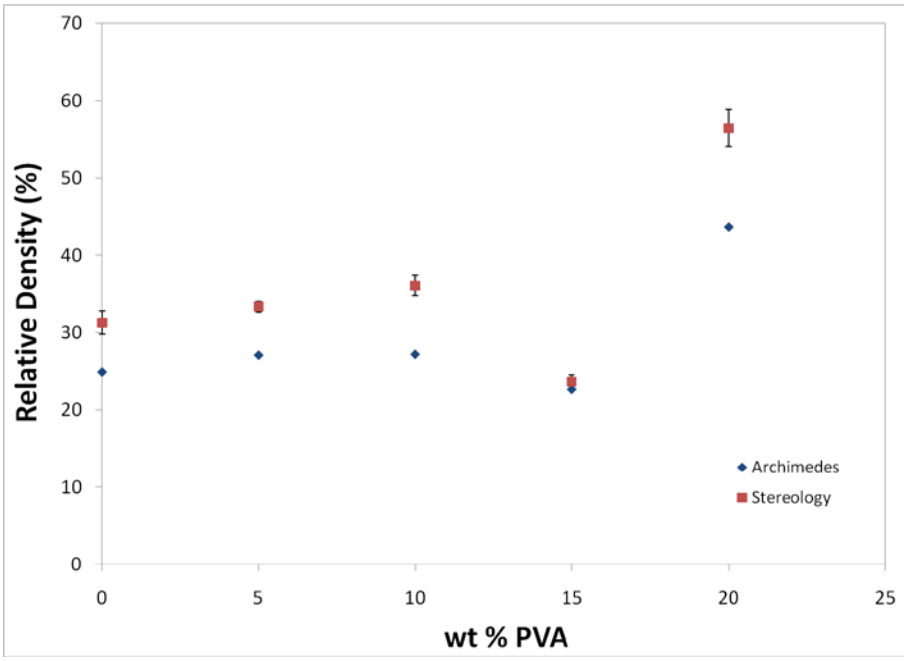

Figure 73. Comparison of the bulk densities of samples with 25 vol% Al_2O_3 and 0 – 20 wt% PVA as measured by the Archimedes method and image analysis.

It should be noted that the agreement between the measurements from both sections are quite good. The pore size, which was measured perpendicular to the pore channel axis decreased from 25μm for the sample containing no PVA to 18 μm for the sample containing 5 wt% PVA. There was another small decrease in pore size as the PVA content was increased to 15 wt% followed by a significant decrease to 8 μm for the sample containing 20 wt% PVA. These measurements verify what was qualitatively observed for these samples above. The solid volume fractions obtained from the Archimedes method presented in Figure 73 ranged between 0.23 and 0.27 which is in close agreement with the slip solid loading of 25 vol%. The sample containing 20 wt% PVA had a significantly higher solid volume fraction of 0.44. For most of the samples the measured solid line fractions are approximately 5 vol% higher than the solid

volume fraction measured using the Archimedes method. This is most likely due to fine porosity in the pore walls that was not able to be detected at the magnifications used in image analysis. The image analysis measurements for the 20 wt% PVA sample gave higher measured solid volume fractions, in agreement with the result from the Archimedes method. This is most probably due to the porosity in the pore walls created by the fine secondary dendrites. It is thought that a significant fraction of this porosity was removed in sintering and resulted in the thick pore walls observed in Figure 69 and Figure 71.

The measured pore wall thickness for both parallel and perpendicular sections can be seen below in Figure 74.

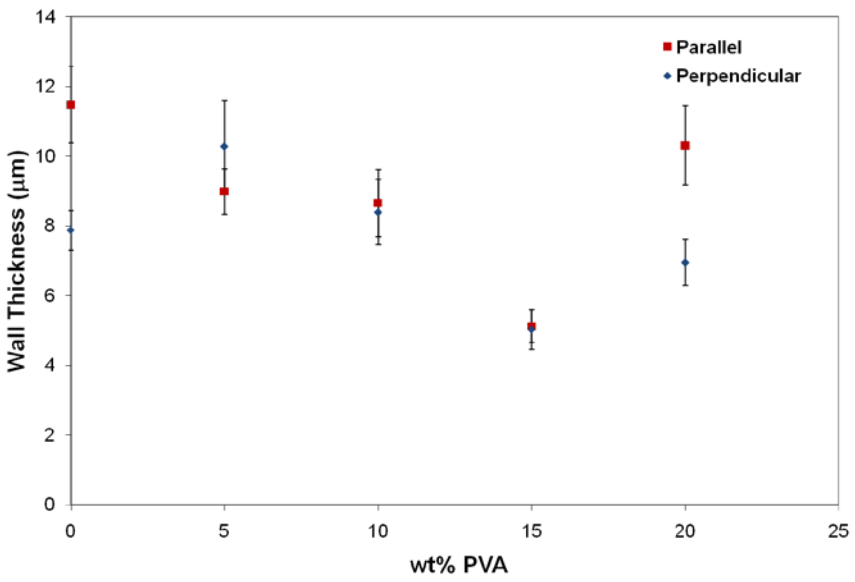

Figure 74. Effect of PVA content on pore wall thickness measured on sections parallel to the casting direction and perpendicular to the casting direction.

It was noted that the wall thickness values reflected the trend in the measured pore size to some extent. When no PVA was present the wall thickness was 11.5 μm which subsequently decreased to 9 μm and 8.7 μm for 5 wt% PVA and 10 wt% PVA. The pore wall thickness of the 15 wt% PVA sample decreased to 5 μm. Finally the pore wall thickness of the 20 vol% increased to 10 μm, which is consistent with the decrease in pore size and increased solid volume fraction noted above. Once again the agreement between the measurements on sections parallel and perpendicular to the freezing direction was quite good.

Due to the nature of the decelerating solid-liquid interface and decreasing thermal gradient that is encountering during freeze casting, one might expect that there will be differences in the pore size between the top and bottom of the sample. Due to this the pore size was measured using image analysis on sections parallel to the freezing direction taken from areas near the top and bottom of the sample. The results of these measurements can be seen below in Table 5.

Table 5. Pore size measurements from the top and bottom of the samples for sections parallel to the freezing direction.

wt% PVA	Location in sample	λ_p (μm)	λ_p standard deviation (μm)
0	top	27.8	5.3
0	bottom	23.9	3.6
5	top	22.7	4.1
5	bottom	13.8	2.6
10	top	21.1	4.8
10	bottom	13.6	3.6
15	top	17.5	4.0
15	bottom	14.6	3.0
20	top	12.2	2.3
20	bottom	9.7	2.8

For the sample containing 0 wt% PVA it is noted that there is very little difference in the measured pore size between the top and the bottom of the sample, which suggests that the interfacial velocity was relatively constant during solidification. The samples containing 5 and 10 wt% PVA showed a significant increase in pore size from the bottom to the top of the sample as both increased from roughly 14 μm to approximately 21-22 μm. This observation supports the idea that there was a significant amount of overgrowth of less favorably oriented ice crystals taking place, as can be seen in Figure 68 and Figure 69. If indeed the secondary dendrite arms were able to coarsen to an appreciable amount to where they could overtake less favorably oriented ice crystals then this could help explain the observed increase in pore size along the length of the sample. As the PVA content is further increased it was speculated that the secondary dendrites would become finer since the amount of supercooling is decreasing. This was indeed the case and can be seen in Figure 69 and Figure 71. The measured pore size for these samples did not increase significantly given the measured confidence interval which may suggest that the finer secondary dendrites were not able to overtake the primary ice crystals, thus resulting in less measurable coarsening. Finally, the small increase in pore size for the 15 and 20 wt% PVA samples suggests that, much like the 0 wt% PVA sample, the interfacial velocity was relatively constant during solidification.

5.2.2 Effect of PVA on Permeability

The permeability of the samples that contained 25 vol% Al_2O_3 and 0 – 20 wt% PVA was determined using the Forchheimer correction to Darcy's law, which takes into account non-

Darcian effects due to inertial flow. By using the Forchheimer relation both the Darcian and non-Darcian permeabilities were able to be calculated for these materials. Further details concerning the measurement of permeability can be found in the experimental procedures (Section 4.3). The results for the Darcian permeability can be seen below in Figure 75.

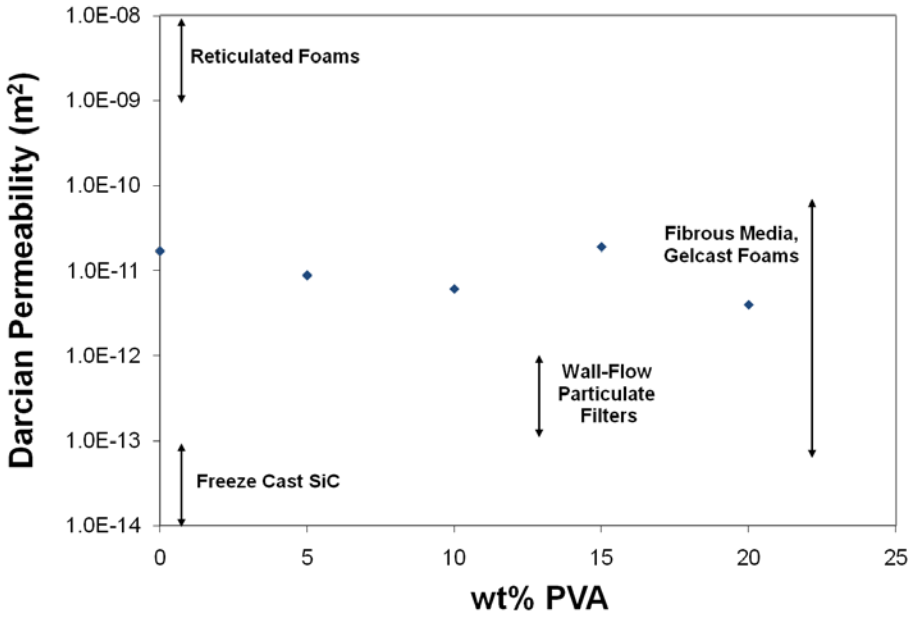

Figure 75. Measured Darcian permeability values for freeze cast samples containing 25 vol% Al_2O_3 and 0-20 wt% PVA. Ranges of measured permeability values from the literature for other common macroporous ceramics are included for comparison.

The calculated permeability values are somewhat higher than what is reported for ceramic through-wall diesel particulate filters [154] and lie in broad range of values exhibited by fibrous media and gelcast foams [153]. The results also suggest that freeze cast ceramics are somewhat less permeable than reticulated foams, which commonly have much lower solid volume fractions and more importantly significantly larger pore sizes. In general the Darcian

permeabilities seem to decrease from $1.7x10^{-11}$ to $3.9x10^{-12}$ m^2 as the PVA content is increased as one would expect given the observed decrease in pore size in Figure 72. It was also noted that the variation in permeability is small compared to the range over which values vary in the literature. A rather significant decrease in permeability was noted for the 20 wt% PVA sample. This can be attributed not only to the very fine pore, but also to the increased solid volume fraction in the sample that resulted from the loss of fine porosity during sintering. The 15 wt% PVA sample showed significant deviations from the observed trends in Figure 75 and exhibited permeability higher than that of the sample containing no PVA. Figure 76 shows the results for the non-Darcian permeability with varying PVA content.

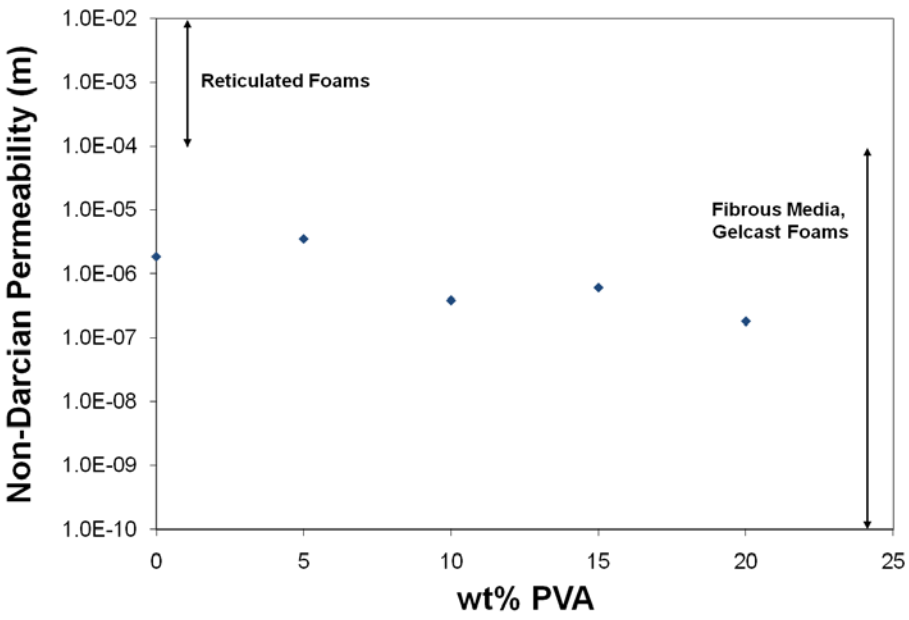

Figure 76. Measured non-Darcian permeability values for freeze cast samples containing 25 vol% Al_2O_3 and 0-20 wt% PVA. Ranges of measured permeability values from the literature for other common macroporous ceramics are included for comparison [153].

It can be seen from this plot that in general the overall permeability once again decreases, but a significant deviation occurs from the observed trends, this time for the 5 wt% PVA sample. The deviations that are observed in Figure 75 and Figure 76 may be able to be explained by changes in amount of Darcian flow experienced as the pore morphology changes in the samples. The percentage of Darcian flow with varying PVA content can be seen below in Figure 77.

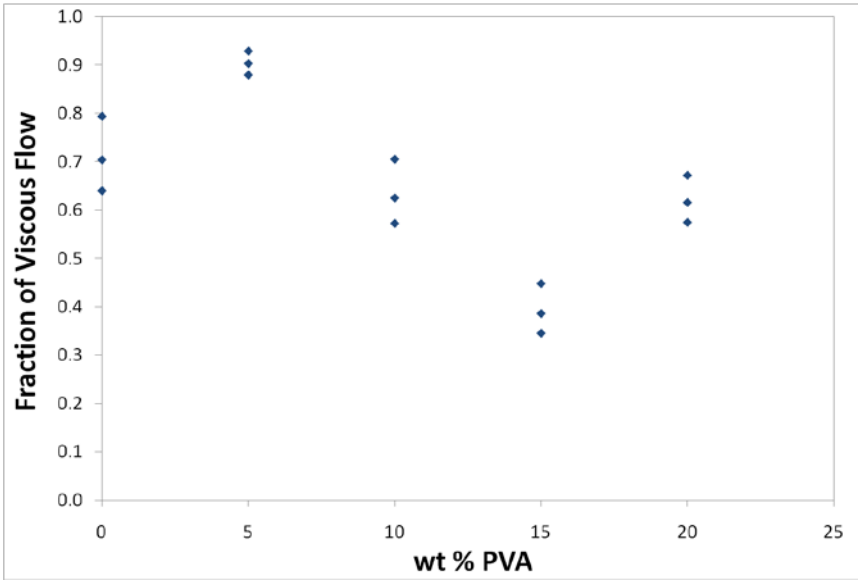

Figure 77. Plot of the fraction of Darcian (viscous) flow with varying PVA content.

In this plot there are 3 data points for each PVA content due to the fact that the samples were tested at 3 different gas pressures, each of which yielded a different superficial velocity, which is a variable in the determination of the Forchheimer number. It should also be noted that the variation in the amount of viscous flow due to a change in gas pressure during testing was small compared to the variation between samples processed with different PVA contents. Due to

this the changes in permeability as the PVA is increased can be interpreted in terms of the effect of microstructural changes on the fraction of viscous flow. For the majority of the samples the amount of Darcian flow was significant, showing values greater than 60%. The exception is the 15 wt% PVA sample, which had a Darcian contribution that was less than 50%. As mentioned previously this is also the PVA content that exhibited the anomalously high value of Darcian permeability in Figure 75. The large inertial flow contribution could be due to the thin convoluted pore walls observed in Figure 69. The fact that the 15 wt% sample exhibited a lower percentage of viscous flow than the other samples could be the reason that the Darcian permeability is so anomalously high. On the other hand the 5 wt% sample showed a very small percentage of inertial flow, which could explain why it exhibited the highest non-Darcian permeability in Figure 76.

5.2.3 Effect of PVA on Compressive Strength

It was observed above that the concentration of PVA binder that is added to the slip during processing has an effect on the observed microstructure and consequently the measured permeability values for freeze cast samples processed with 25 vol% Al_2O_3. Another property that is dependent upon the observed microstructure is the uniaxial compressive strength, which has been accepted in the literature as a method by which to characterize the strength of macroporous ceramics. The compression strength of samples containing 25 vol% Al_2O_3 and 0 – 20 wt% PVA were measured on uniform samples with a diameter of 10 mm and a height of 5 mm. The samples that were tested were also used for permeability measurements and were from the same location on the samples where the microstructural measurements were performed. Further detail concerning these tests can be found in the experimental procedures (Section 4.4).

The loading curves that resulted from testing samples containing 5 wt% PVA can be seen below in Figure 78.

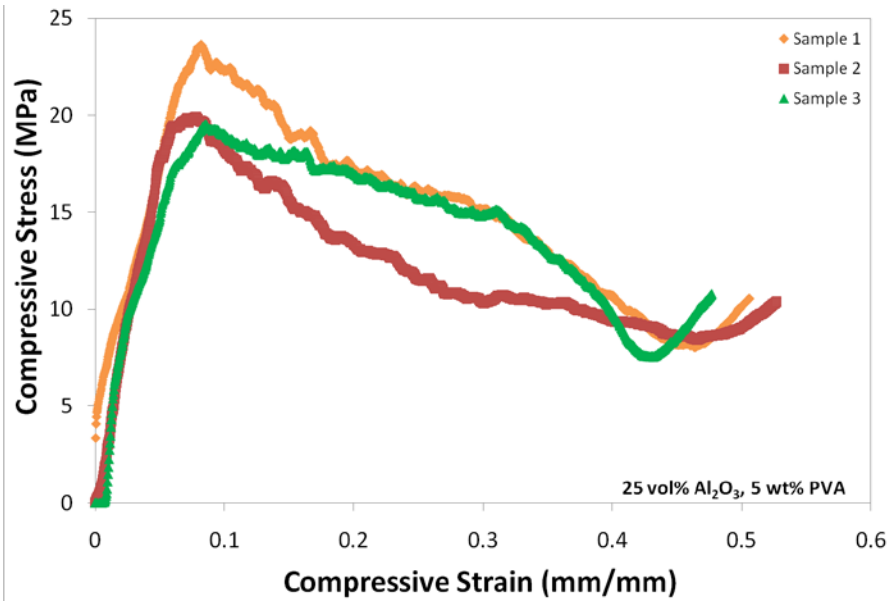

Figure 78. Loading curves obtained from uniaxial compression testing of three identical cylindrical samples containing 25 vol% Al_2O_3 and 5 wt% PVA at a strain rate of 1 mm/min.

It can be seen that these samples behaved quite well under compression, especially for a ceramic material with approximately 70% total porosity. The loading curves in this case consisted of an elastic region followed by a plateau where the maximum compressive strength was reached. This plateau occurred at a value of 8-9% compressive strain, showing that these materials have good strain tolerance for a ceramic material. Once the maximum value was reached the loading curve showed evidence of failure as the load bearing capability of the sample was decreased. None of the samples that were tested failed in a catastrophic manner. Instead the samples appeared to display a gradual fracture path as the loading curve displayed a series of

steps in it in the failure regime. This trait can likely be attributed to the failure of groups of lamellae followed by load transfer to the remainder of the sample. Once a group of lamellae fail the compressive strength either remains constant or begins to increase until the next failure occurs. The test was stopped when the compressive stress started to increase at higher compressive strain values as this was a result of the crushed sample being compacted by the compression platens. This behavior was very similar to what was observed in Figure 35 and Figure 57 for samples processed with PEG. Samples containing 0, 10 and 15 wt% PVA exhibited loading curves that were similar to what was seen above for the 5 wt% PVA sample. The loading curves for samples with 20 wt% PVA were somewhat different and displayed very well defined maximum compressive stress peaks that occurred at somewhat higher compressive strain values. These loading curves can be seen below in Figure 79.

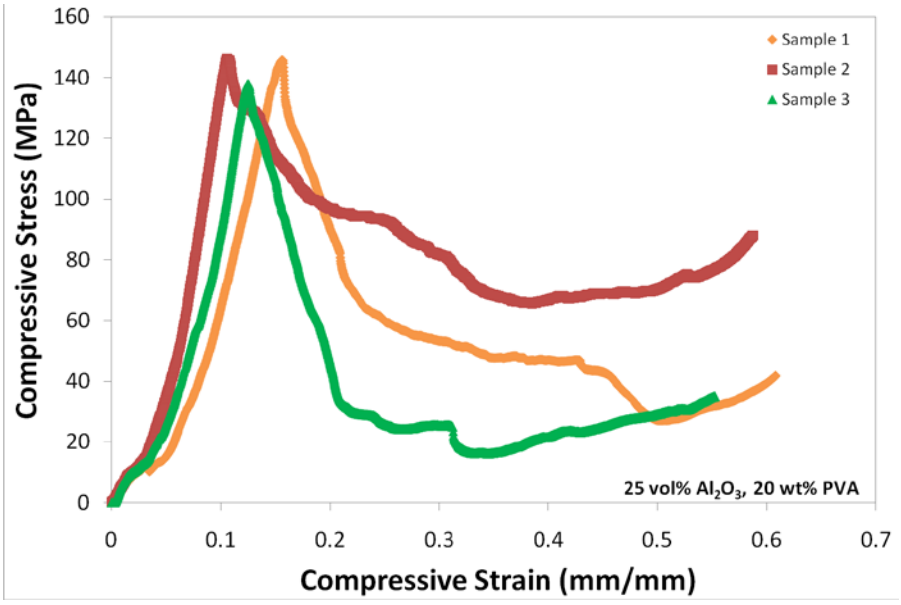

Figure 79. Loading curves obtained from uniaxial compression testing of three identical cylindrical samples containing 25 vol% Al_2O_3 and 20 wt% PVA at a strain rate of 1 mm/min.

Unlike the previous samples once the maximum compressive stress is reached the loading curves decay very quickly in the failure regime and do not show as much of the more gradual step-like decay that was observed in Figure 78. This was similar to what was seen for higher solid loadings and PEG contents in Figure 36 and Figure 58, respectively. The rapid drop was likely due to better transverse connectivity between the lamellae due to ceramic bridges created by dendritic branching. Once failure of the sample takes place, load transfer overwhelms a larger percentage of the pore walls and causes a large drop in the curve. Despite the differences between the loading curves seen in Figure 78 and Figure 79 all of the samples processed with PVA displayed an elastic region, maximum compressive strength plateau and a failure region and showed rather good compressive strain tolerance for macroporous ceramic materials.

The measured uniaxial compressive strength values for samples containing 25 vol% Al_2O_3 and 0-20 wt% PVA can be seen below in Figure 80. These values were obtained by applying the compressive load parallel to the ice crystal growth direction (axially), which is the desired loading direction. The samples were not tested in the transverse direction but it can be expected that the strengths will be significantly lower than the axial value as was found for lamellar alumina [91] and hydroxyapatite [100,101] freeze cast ceramics.

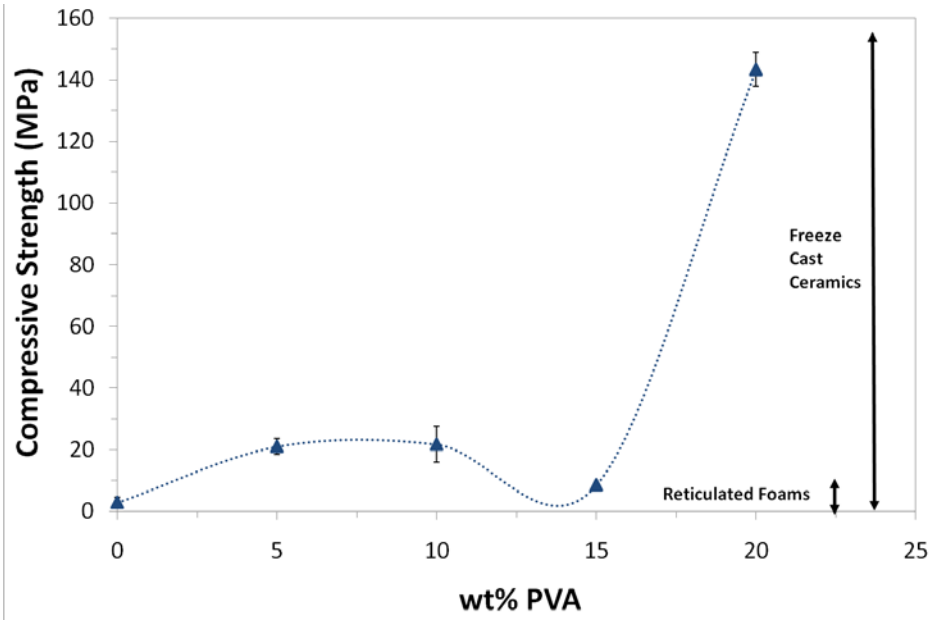

Figure 80. Uniaxial compressive strength values for samples containing 25 vol% Al_2O_3 and 0-20 wt% PVA. The load was applied to the samples axially at a strain rate of 1 mm/min. The dotted line in the figure does not reflect fitting of the data set but is present to highlight the changes between samples. The arrows on the right represent the range of strength values found in the literature for different types of macroporous ceramics.

It was noted that the samples displayed a general increase in the compressive strength with increasing PVA content and that the variability in the measured values was rather small. The compressive strength increased from a value of 2.85±1.6 MPa when no PVA was present to 21±2.6 MPa when 5 wt% PVA was added. It is not surprising that an increase in the strength was noted when PVA was added to the slip. The compressive strength of a macroporous ceramic will be sensitive of the integrity of the walls that bear the applied load. In the case of the sample with no PVA the pore walls were thick but also had large cracks in them as can be seen in the micrograph in Figure 81. These cracks are large defects which affect the integrity of the sample and cause it to be very delicate, even after sintering at high temperature, resulting in a low compressive strength. When 5 wt% PVA was added to the slip the pore walls became more continuous and did not show significant cracking as the PVA acted as a binder that more easily

accommodated the volume expansion that takes place during the solidification of ice. The structure of the 5 wt% PVA sample was much more broken down than the 0 wt% sample and gave a lower measured wall thickness. The increase in strength for the 5 wt% PVA sample can largely be attributed to the stronger pore walls but could also be due somewhat to better connectivity between lamellae or the refinement in wall size, as seen by Munch et al [91].

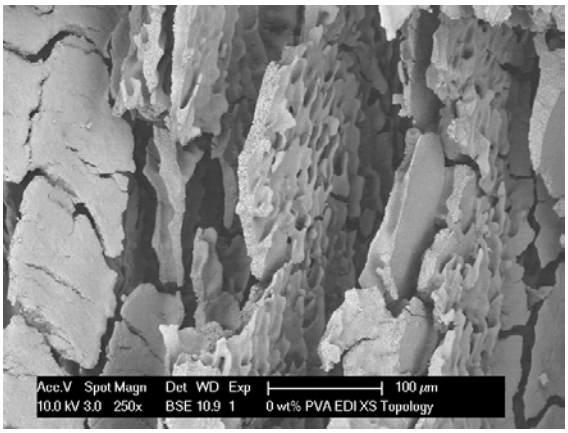

Figure 81. A SEM micrograph of a sample containing 25 vol% Al_2O_3 and 0 wt% PVA that shows the extensive amount of cracking in the pore walls that resulted from the lack of a polymeric binder during processing. The magnification of the micrograph is 250x.

The strength of the 10 wt% PVA sample did not differ greatly from the 5 wt% sample, which was not surprising as both structures were significantly broken down and showed no significant changes in the measured wall thickness. On top of this the measured solid fraction values and hence the amount of porosity in the samples was similar, as seen in Figure 73. Upon addition of 15 wt% PVA the compressive strength dropped significantly to a value of 8.59±0.05 MPa. This decrease in strength was likely due to the fact that the 15 wt% sample had very thin and irregular pore walls with many discontinuities that lowered the ability of the sample to bear a

compressive load. Additionally the measured solid volume fraction for this sample was somewhat lower than for the other samples, giving an increase in the amount of porosity in the sample, which could be expected to decrease the maximum compressive strength. The sample containing 20 wt% PVA gave a maximum compressive strength of 143.3±5.47, which is roughly 7 times greater than any other sample tested in this series. It was seen in Figure 69 and Figure 71 that the microstructure of this sample consisted of very fine dendrites that were surrounded by rather thick and dense pore walls. The thick pore walls were likely due to the loss of fine porosity during sintering, which was supported by the fact that the measured solid volume fraction in Figure 73 increased significantly at 20 wt% PVA. The measured porosity for the 20 wt% sample was 43.6% which is significantly lower than the other samples, which ranged from 63.9% to 76.3%. It should be noted that the strength increase from 10 wt% PVA to 20 wt% PVA was greater than 500%, where the increase based on the change in load bearing area was calculated to be only 35%. Additionally this sample showed very prevalent branching which likely gave a high degree of interconnectivity that strengthened the sample. The decreases in total porosity combined with the increased wall integrity and connectivity between lamellae were likely what gave the 20 wt% PVA sample such an increase in strength.

The measured compressive strength values for these samples are certainly within the range of experimental values found in the literature for other freeze cast ceramics [138] and are somewhat higher than those that are found for reticulated foams [7,148], where the low solid volume fraction and defects present on the struts tend to limit the strength to values less than 10 MPa. Further discussion of how these values compare to those found in the literature can be found in section 5.3.3. Overall it was noted that the addition of PVA significantly increased the

strength of freeze cast ceramics relative to the case where no PVA was present and that large amounts of PVA gave samples with very high compressive strength.

5.2.4 PVA Gelation Studies

When certain types of polymers are in solution a change in temperature, solvent loss, an increase in the concentration of the polymer or addition of certain chemicals can cause the molecules to crosslink and form a gel. The gel can consist of physical or chemical bonds, with physical gels often being reversible and chemical gels being practically irreversible. Some authors have used gel formation in the field of freeze casting by adding colloidal silica to the slip, which gels upon freezing [82,112,113]. Polyvinyl alcohol is a water soluble polymer that has the ability to form a gel while in solution [159].

During preliminary experiments with samples containing 25 vol% Al_2O_3 and 20 wt% PVA a rather different microstructure was observed compared to the samples in section 5.2.1. The changes were likely due to the fact that the slip in the preliminary study was allowed to rest overnight before casting. This period of rest allowed the PVA to gel, creating a high viscosity slip that was difficult stir and pour. The microstructure of this sample can be seen in Figure 82 and is extremely broken down and contains a significant amount of large bubbles that were trapped in the sample during solidification, likely because of the high viscosity. Additionally, it was noted that the dense, thick walls seen in Figure 69b were not present in Figure 82.

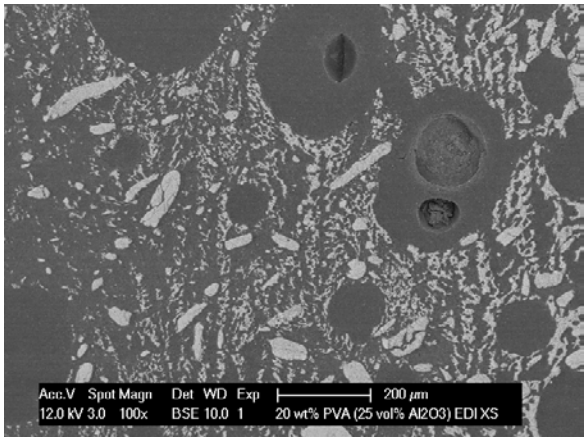

Figure 82. SEM micrograph of a section parallel to the freezing direction for a sample containing 25 vol% Al_2O_3 and 20 wt% PVA. The magnification of the micrograph is 200x.

The above observation showed that allowing PVA to dwell can lead to the formation of a gel and have a profound effect on the final microstructure that is obtained. In particular, freezing through gelled slips could create freeze cast samples that do not require freeze drying. This can only be accomplished if the gel that is formed is strong enough to allow the water to evaporate from the sample while it warms up. If the gel is not strong enough the PVA will go back into solution and the sample will eventually melt. Removal of the freeze drying step would be useful, especially from an industrial standpoint since this step is the most time-consuming part of the entire freeze casting process. This prompted a systematic study of the effect of dwell time on the ability of the samples to withstand melting.

The amount of PVA chosen for the experiment was 20 wt% relative to the alumina content (23 vol%) since this was the composition that gave the most pronounced change in both viscosity and microstructure in the preliminary experiments. The slips were allowed to dwell at room temperature (23°C) or 60°C and then solidified using an EDI bath (-73°C) at different time intervals. Following removal from the mold the behavior of the sample while it warmed to room

temperature was observed and digital photographs were captured at 5 minute intervals. It was expected that greater dwell times and temperatures would create stronger gels that would resist water absorption as the sample thawed, allowing the ice to slowly melt out of the sample while retaining a net shape.

A series of slips were allowed to dwell at room temperature for time periods of 0, 2, 4, 23 and 98 hours before being solidified and observed while returning to room temperature. It was noted that all of the samples that were subject to a room temperature dwell began to show signs of melting 20 minutes after being removed from the mold. The samples generally began to deform significantly after 30 minutes and were completely melted after 50-60 minutes. The only notable difference in behavior was the amount of time that it took for the sample to completely melt, which was deemed relatively insignificant given the small differences that were noted. An example of the melting behavior that was typical of the samples aged at room temperature can be seen in Figure 83 for a sample that was aged for 23 hours before being frozen. Further information on these samples can be found in Appendix C.

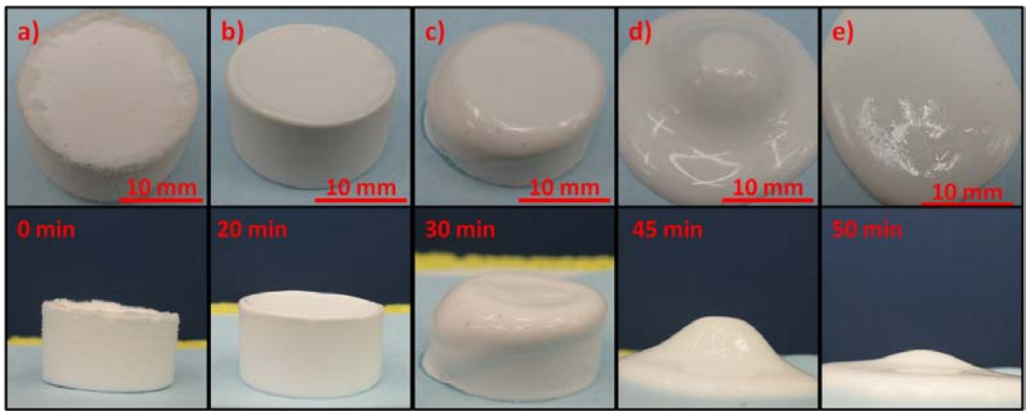

Figure 83. Time lapse sequence of the melting behavior of a sample containing 23 vol% Al_2O_3 and 20 wt% PVA that was allowed to age for 23 hours at 23°C prior to freezing. The lower images are profile views of the sample at a specified time since removal from the mold and correspond to the image that is directly above it.

Gel formation is a process that can occur more rapidly at higher temperatures. The next series of samples were allowed to dwell for time periods of 24 and 98 hours at 60°C to see if any improvements were noted. It was found that neither of the two dwell periods that were examined created a stable enough gel to resist complete melting of the sample. The samples behaved in a fashion that was very similar to the samples that were aged for different time periods at room temperature as they began to show signs of melting at 20 minutes, visibly deformed by 30 minutes and were completely melted by 50-60 minutes. Based on these results it appears that the dwell temperature did not have a significant effect on the gel formation. Further information on these samples can be found in Appendix C.

For slips containing PVA there was little improvement in the resistance to melting regardless of the aging temperature or dwell time. It is possible that a longer time period could be required for a strong enough gel to form, but a dwell time of 98 hours is already a very long time and it is more likely that the physical gel formed by PVA is thermoreversible and simply cannot hold up during the warming of the sample. Another type of gelling agent was tested and the results of this trial can be found in Appendix C.

5.3 COMPARISON OF PEG AND PVA ADDITION ON FREEZE-CAST CERAMICS

The effects of two different water soluble polymers, namely poly(ethylene glycol) (PEG) and poly(vinyl alcohol) (PVA), on the microstructure and properties of freeze cast ceramics were the a large part of this research. PEG was chosen mainly because it was present as a binder in early

processing runs, while PVA was investigated based on evidence in the literature [68] that it could modify the growth habit of hexagonal ice. The effects of PEG and PVA on freeze cast ceramics have already been discussed in detail in sections 5.1.4 – 5.1.7 and 5.2.1– 5.2.3 The aim of this section is to summarize and compare the results that were obtained for these two polymers in an effort to highlight any differences that exist between them, as well as to provide a more thorough comparison of the property measurements with what has been seen in the literature for other macroporous ceramics, particularly reticulated and direct foams.

5.3.1 Comparison of the Effects of PEG and PVA on Microstructure

The studies of the effects of PEG and PVA on the microstructure of freeze cast ceramics that were discussed in previous sections were performed under identical conditions. The slips that were created had the same solid loading and range of polymer contents, while the samples were frozen in identical molds using the same freezing bath temperature. Afterwards the samples were all freeze dried and sintered using identical protocols. By keeping all of these conditions the same the only variable between the two sets of samples is the type of water soluble polymer that was used as a binder. Therefore any significant differences observed in the microstructure or properties for these sets of samples could be attributed to the type of polymer that was used in the initial slip.

Micrographs of sections parallel to the freezing direction for samples containing 0 – 20 wt% of either PEG or PVA were seen in Figures 41 – 43 and Figures 68 – 69, respectively. Additionally, the trends observed in these microstructures with increasing polymer content were discussed in detail in section 5.1.4 for PEG and 5.2.1 for PVA. In general the observations on such sections suggested a progressive refinement of the structure with increasing polymer

content that was consistent with what was expected from solidification theory. The primary and secondary dendrite arm spacing in these structures appeared to be refined for both sets of samples with PVA having microstructures that were finer and considerably more broken down than the corresponding PEG samples. Micrographs of sections perpendicular to the freezing direction were presented in Figures 45 – 47 and Figures 70 – 71 for PEG and PVA, respectively. Analysis of these sections showed that they agreed quite well with what was observed on sections parallel to the freezing direction as once again a progressive refinement of the microstructure was seen.

The pore size values, measured on sections parallel to the freezing direction, for samples containing PEG and PVA can be seen in Figure 84.

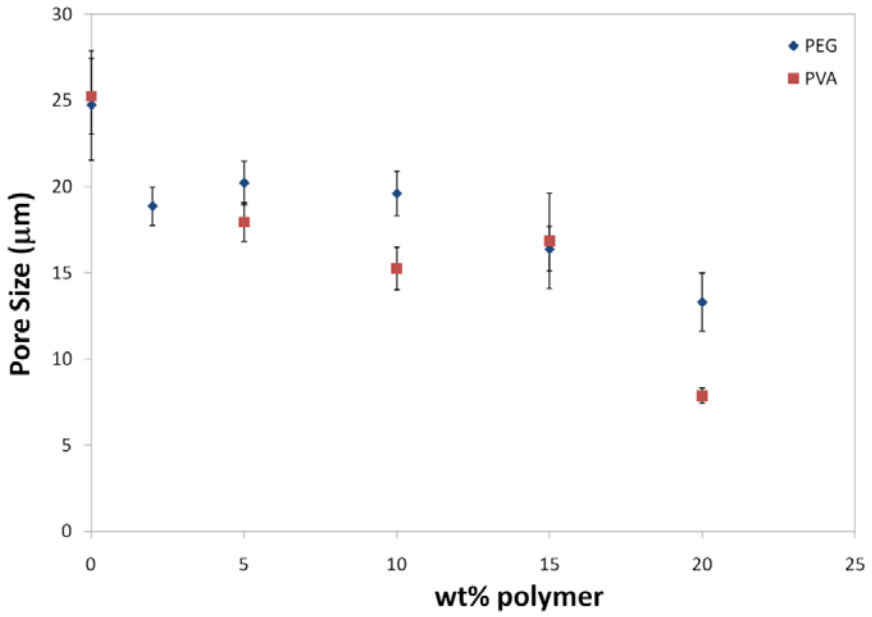

Figure 84. The effect of polymer content on the pore size for samples containing 25 vol% Al_2O_3 and 0-20 wt% PEG or PVA. The measurements were performed on sections parallel to the freezing direction.

It was noted that a general decrease in the pore size was observed with increasing polymer content, regardless of whether PEG or PVA was used. A small addition of either PEG or PVA caused the pore size to decrease significantly (relative to the case with no polymer added) and was followed by a more gradual decrease with increasing polymer content. As stated previously this decrease is consistent with what is expected based on constitutional supercooling from solutes and its consequent effect on the solid-liquid interface. For the most part the type of polymer used in the slip did not cause a significant difference in the measured pore size as the measured values for samples containing PEG and PVA agreed quite well. A significant deviation in the measured values occurs at 20 wt% due to the fact that a significant fraction of fine porosity was lost during the sintering of the 20 wt% PVA sample, resulting in thick, dense walls and very fine dendritic pores.

A comparison of the measured pore wall thickness values on sections parallel to the freezing direction for samples created with PVA or PEG can be seen below in Figure 85.

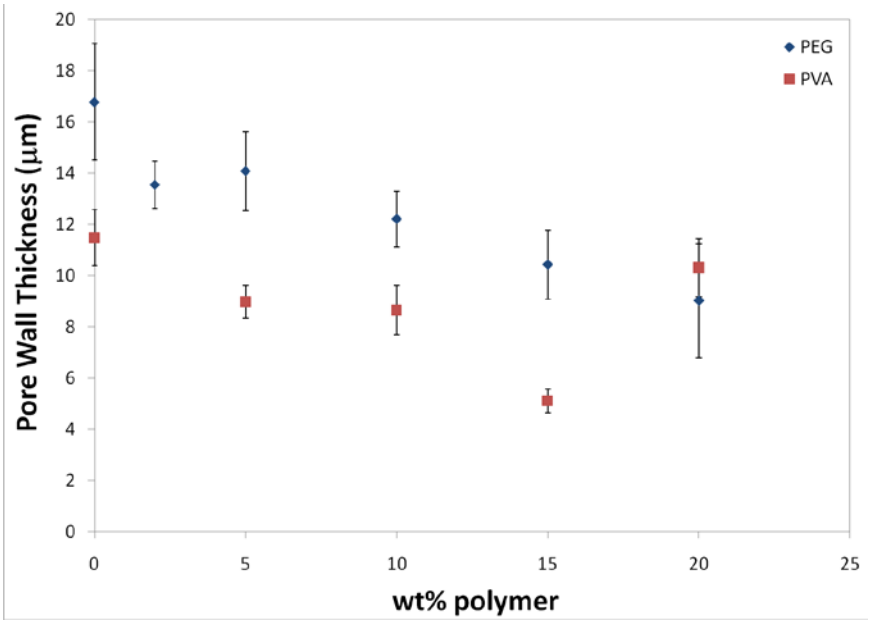

Figure 85. The effect of polymer content on the pore wall thickness for samples containing 25 vol% Al_2O_3 and 0-20 wt% PEG or PVA. The measurements were performed on sections parallel to the freezing direction.

The measured wall thickness values differed somewhat depending on the type of polymer that was used in the slip. In general the samples that were made with PVA gave smaller wall thickness values than those with PEG. Additionally, both types of samples showed a general decrease in wall thickness that was consistent with the refinement of the structure and reflected the changes in pore size to some extent. The only major deviation from this trend was for the 20 wt% PVA sample, which had a pore wall thickness that was greater than that of the 20 wt% PEG sample. As explained previously this was due to the thicker walls that resulted from the loss of fine porosity during sintering.

In general the qualitative and quantitative comparison of the microstructure of samples prepared with PEG or PVA showed that the type of polymer used did not have a large effect on the measured pore size until higher polymer contents and that samples made with PVA generally had thinner pore walls. Samples that were processed with PEG and PVA agreed qualitatively

with what was expected from constitutional supercooling as a progressive refinement of the structure was noted, with the degree of refinement being much greater for samples that contained PVA. It appears that PVA is more effective at refining the microstructure, which could possibly be due to the polymer inhibiting growth on the prismatic planes of the hexagonal ice crystals, however further studies would have to be done to prove that this is the case.

5.3.2 Comparison of the Effect of PEG and PVA on Permeability

It was seen in sections 5.1.5 and 5.2.2 that the changes that occurred in the microstructure with increasing polymer content had an effect on the measured permeability values for samples that were made with varying amounts of either PEG or PVA. The permeability of the samples was affected by changes in the pore size as well as the pore morphology and porosity in the samples. Previous sections presented permeability results for these samples individually with a brief comparison to values found in the literature. In this section the results of permeability for PEG and PVA will be compared to each other and a more comprehensive comparison to values for other types of macroporous ceramics will be presented.

The measured Darcian and non-Darcian permeability values calculated from the Forchheimer equation for samples containing 25 vol% Al_2O_3 and 0 – 20 wt% of either PEG or PVA are presented below in Figures 86 and 87.

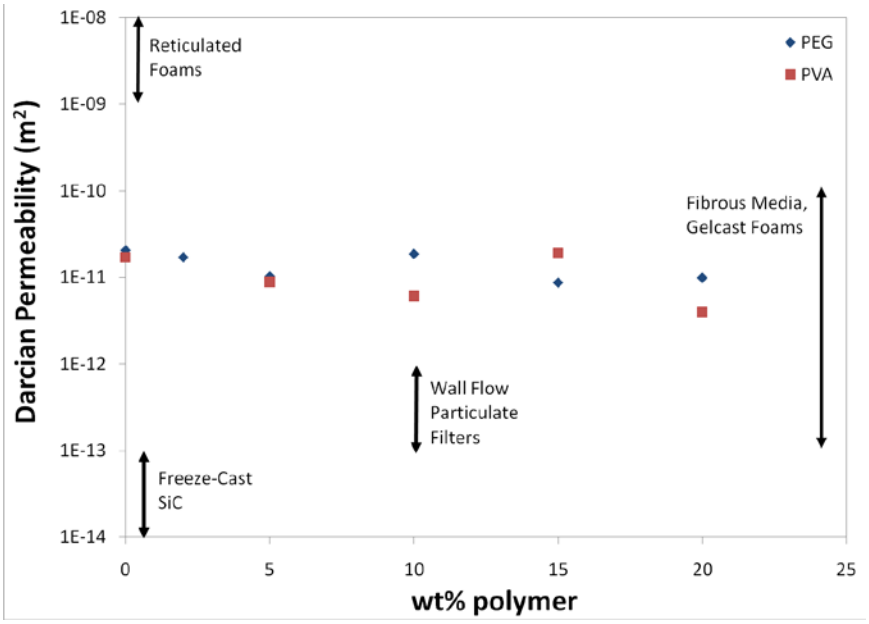

Figure 86. Darcian permeability values for freeze cast samples containing 25 vol% Al_2O_3 and 0-20 wt% of either PEG or PVA. Ranges of measured permeability values from the literature for other common macroporous ceramics are included for comparison.

With the exception of the 15 wt% sample it can be seen that the PEG samples generally had somewhat higher Darican permeability values than PVA samples with similar polymer contents. This was likely due to the fact that the microstructures of the PEG samples were commonly less highly branched and had slightly larger pore sizes. In general it was noted that the Darcian permeabilities of ceramics with either PEG or PVA as the additive decreased as the polymer content was increased. This overall decrease made sense given the decrease in pore size that was noted for the samples in Figure 84 and the increasingly dendritic nature of the samples as the amount of PEG or PVA was increased.

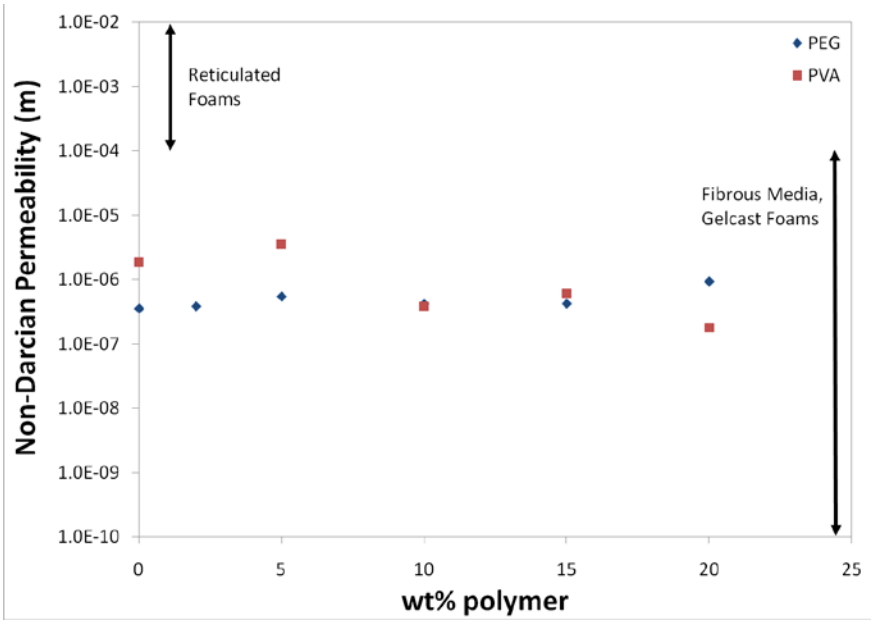

Figure 87. Non-Darcian permeability values for freeze cast samples containing 25 vol% Al_2O_3 and 0-20 wt% of either PEG or PVA. Ranges of measured permeability values from the literature for other common macroporous ceramics are included for comparison.

These permeability values are higher than what was reported in the literature for wall-flow diesel particulate filters [154] and fall in the broad range exhibited by fibrous media and gelcast foams [150,153,160-163]. The permeability results also suggest that these freeze cast materials are less permeable than reticulated ceramic foams [153,160,164-166]. However, it must be remembered that the solid volume fraction in reticulated foams is much lower and more importantly the pore sizes are significantly larger than those of freeze cast ceramics. For these reasons it is not surprising that permeability values for these foams are often two to three orders of magnitude greater than those of freeze cast ceramics. An isolated study on freeze-cast SiC [138] with pore sizes between 10 and 70 μm and porosities of 10 – 30% yielded significantly lower permeability values than those that were found for freeze cast alumina in this study. At the current time, no further data in the literature concerning the permeability of freeze cast ceramic

materials exists. As mentioned earlier the range of permeabilities for the freeze cast ceramics in this study fell well within the range exhibited by open cell gelcast foams. One reason why gelcast foams exhibit such a wide range of permeability values is due to the large variety of pore sizes and porosity values that can be attained using this method. Ortega et al. [161] examined the permeability of open cell gelcast alumina foams of a variety of pore sizes and solid volume fractions and their results provide a good basis upon which to compare the values determined in this study for freeze cast alumina. The results from Ortega for measured Darcian permeability values of gelcast foams can be seen below in Figure 88.

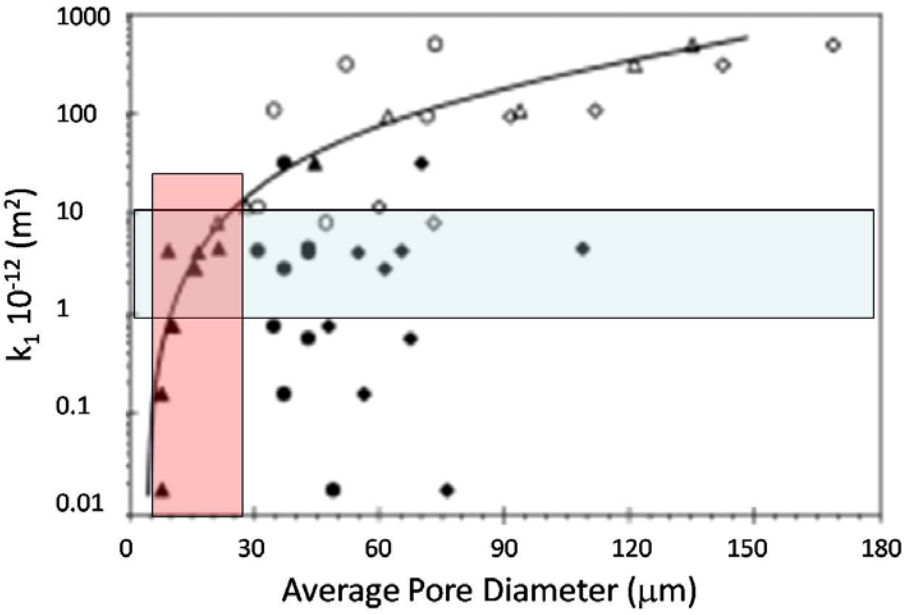

Figure 88. The effect of average pore diameter on the Darcian permeability of alumina gelcast foams as determined by Ortega et al. [161] The range of Darcian permeability values for freeze cast ceramics from this study are highlighted in blue and the range of pore sizes are highlighted in red.

The blue and red shaded regions in Figure 88 are representative of the range of Darcian permeability values and pore sizes that were found for freeze cast alumina ceramics processed with varying amounts of PEG or PVA. It can be seen that these permeabilities are attainable for gelcast foams exhibiting a wide range of pore sizes. However, if the range of pore sizes is limited strictly to those for freeze cast ceramics (the red shaded area) it can be seen that the permeability values attainable by gelcast foams do not exceed those that are achievable with freeze cast alumina ceramics. It is clear that the wide range of permeabilities in Figure 88 were largely due to the variety of pore sizes that were examined. However it should be noted that in some cases there are multiple permeability values for a single pore size, illustrating why the range of values in the literature for gelcast foams often span a few orders of magnitude. The variation in permeability for a single pore size is usually attributed to differences in the amount of open porosity in the sample. Figure 89 presents a summary of Darcian and non-Darcian values obtained by Ortega et al. [161] as a function of relative density of gelcast alumina foams.

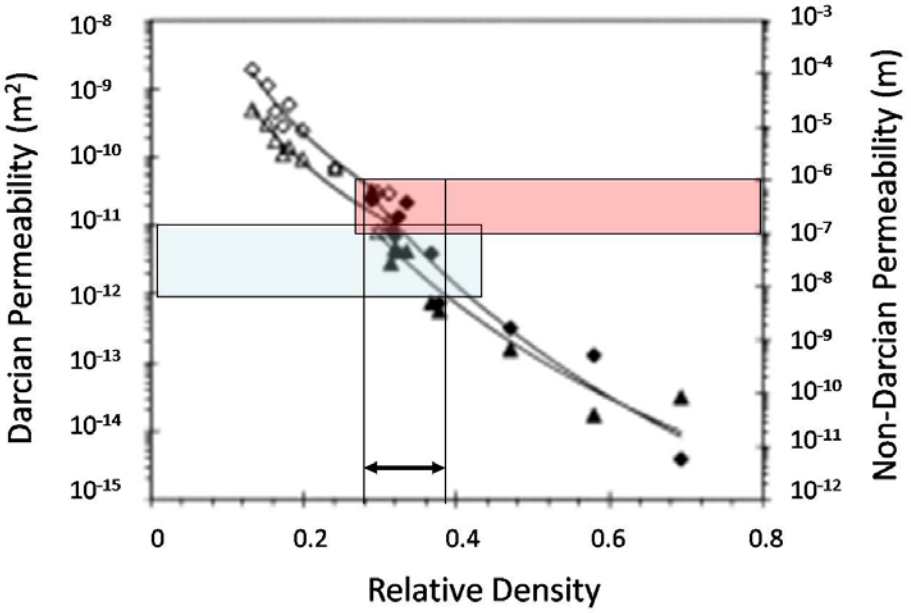

Figure 89. Darcian and non-Darcian permeability values of gelcast alumina foams as a function of relative density. The values on the plot are taken from Ortega et al. [161] while the red and blue shaded regions represent Darcian and non-Darcian permeability ranges found for freeze cast alumina ceramics with 25 vol% Al_2O_3 and 0 – 20 wt% of PEG or PVA.

When the permeability ranges for freeze cast alumina ceramics discussed previously were superimposed on the plot it can be seen that the relative density of gelcast foams with similar values range from approximately 28% to 36% which are close to the densities that were obtained for the freeze cast materials. It can also be seen that higher relative density values cause the permeability to decrease due to the amount of porosity in the sample decreasing. Although the porosity values of the alumina samples processed with different amounts of PEG and PVA were relatively similar (66 – 68%) it was noted that a significant decrease in Darcian permeability was observed for the 20 wt% PVA sample, which had a significantly lower porosity of only 43%. A comparison of the Darcian and non-Darcian values for ceramic materials is shown in Figure 90.

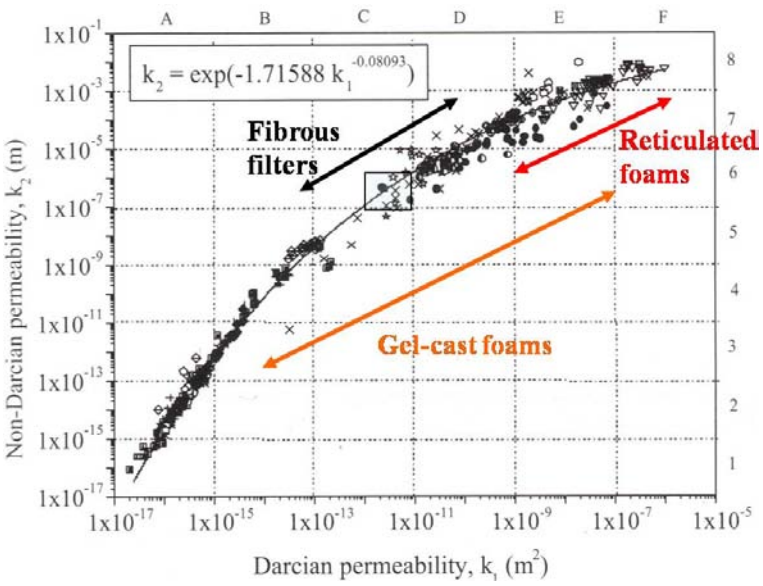

Figure 90. Darcian and non-Darcian permeability data gathered from the literature for a wide variety of porous materials. The ranges for common macroporous materials have been added for clarity. The experimentally determined values for samples containing 25 vol% Al_2O_3 and 0 – 20 wt% PEG or PVA are highlighted in the light blue square. Modified from [153].

The above figure represents a large collection of Darcian and non-Darcian permeability values from the literature for a wide range of ceramic materials, including macroporous ceramics such as gel-cast foams, reticulated foams and fibrous filters. Freeze cast ceramics were not included on the plot due to the sparse amount of information that exists on them in the literature. The values for freeze cast alumina that were obtained in this study are highlighted in light blue on the plot. It was found that the experimental values agreed quite well with the literature and further supported the findings that the freeze cast materials exhibit permeabilites that are in the range of gel-cast foams and fibrous filters.

5.3.3 Comparison of the Effect of PEG and PVA on Compressive Strength

In sections 5.1.2, 5.1.6 and 5.2.3 it was noted that changes in the microstructure with increasing polymer content had a significant effect on the measured compressive strength values for samples that were made with varying amounts of either PEG or PVA. The strength values of the samples were affected by changes in a number of variables such as the porosity, pore wall thickness, pore wall integrity, degree of connectivity between lamellae and the pore morphology. Previous sections presented strength results for these samples individually with a brief comparison to values found in the literature. In this section compressive strength values obtained for samples prepared with PEG and PVA will be compared to each other and a more comprehensive comparison to values for other types of macroporous ceramics will be presented.

A comparison of the compressive strength values that were obtained for samples containing 25 vol% Al_2O_3 and 0 – 20 wt% of either PEG or PVA is presented below in Figure 91.

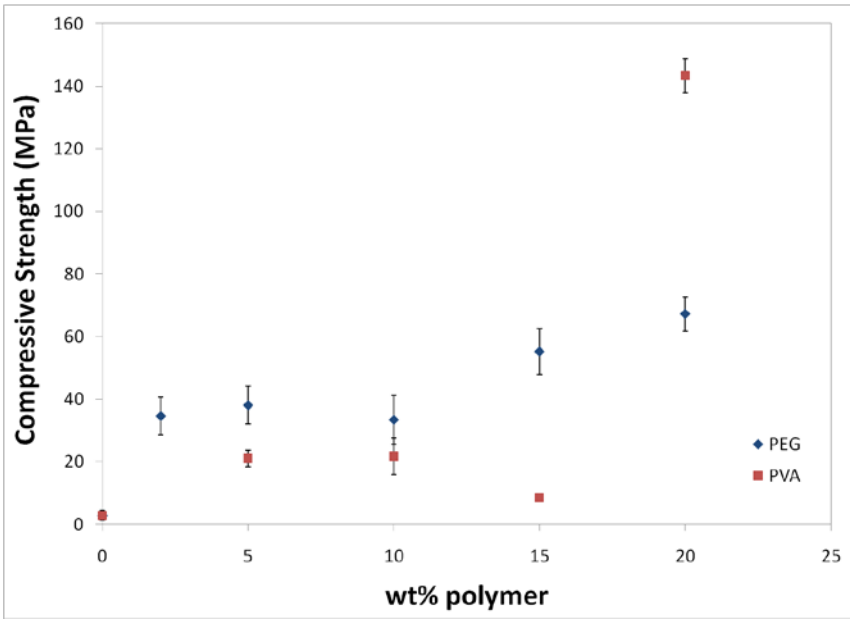

Figure 91. The effect of polymer content on the compressive strength of freeze cast ceramics containing 25 vol% Al_2O_3 and 0 – 20 wt% of either PEG or PVA. The compressive load was applied to the samples axially at a strain rate of 1 mm/min.

As was noted in previous sections the compressive strength of freeze cast ceramics generally became much greater as the amount of PEG or PVA in the original slip was raised. Samples that did not have any PEG or PVA present exhibited very low compressive strength values due to the heavily cracked pore walls that were a result of not having a polymeric binder present to accommodate the volume change during freezing. Addition of a small amount of PEG or PVA caused the compressive strength to increase by more than tenfold for samples containing PVA and by approximately 15 times the value with no binder for samples containing PEG. In general the samples that were processed with varying amounts of PEG gave higher compressive strength values compared to similar samples that contained PVA. This is thought to be due to the fact that the samples that contained PEG had pore volume fractions that were 10% lower than the samples that contained PVA as the binder. The 20 wt% PVA sample exhibited a

compressive strength that was more than double the value that was obtained for a similar sample that contained 20 wt% PEG. This increase in strength was greater than 100% and was significantly higher than would be expected based solely off of the change in load bearing area (6%). This large difference was likely due to the very dense walls and highly broken down structures that were observed in Figure 69 and Figure 71 as well as the increased solid volume fraction that was seen in Figure 73 for the 20 wt% PVA sample. It appears that PEG gives better compressive strength values for a wider range of polymer compositions (2-15 wt%) but the highest measured value was for the 20 wt% PVA sample.

The uniaxial compressive strength is a well accepted measure of the strength of macroporous ceramics. This test is often chosen because these materials are not amenable to three-point bend tests due to the presence of large voids throughout the structure. Additionally the strength of macroporous ceramics is a topic that is of great interest and has received a lot of attention in the literature. An abundance of compressive strength data exists for replicated foams [7,148,149], gelcast foams [7,70,72,150,151,162] and freeze-cast ceramic materials [84,88,94,95,97,98,100-103,106,108,119,124-128]. Figure 92 presents a collection of compressive strengths obtained from the literature for a freeze-cast ceramics.

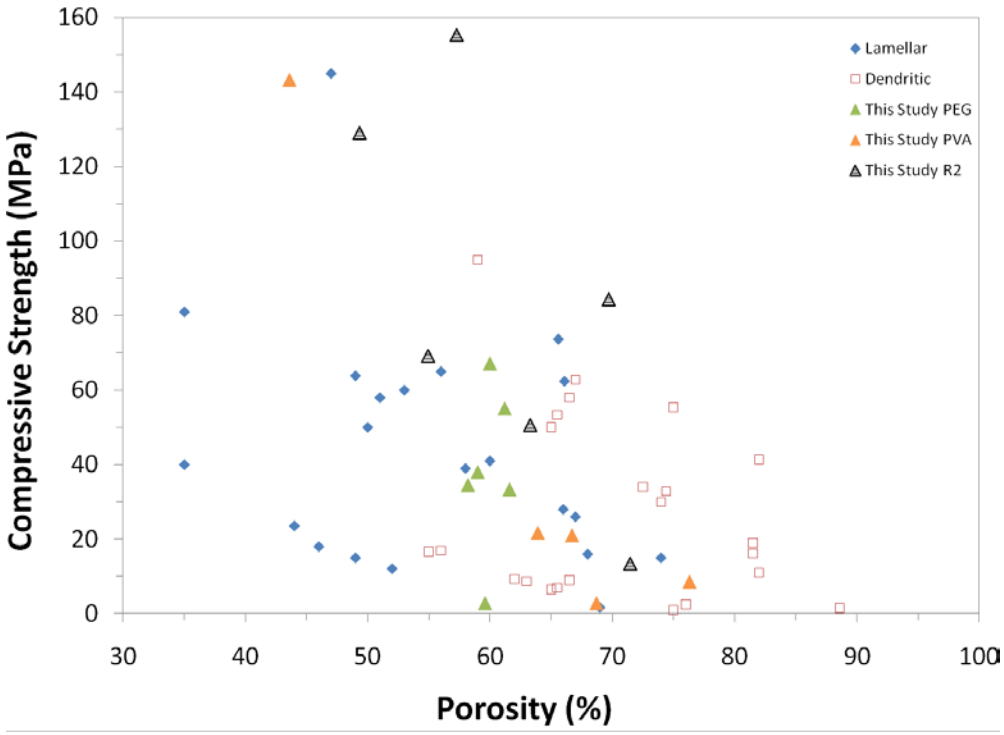

Figure 92. Compressive strength values collected from the literature for freeze cast ceramics. The data is separated by pore morphology and includes values from this study, which are represented by triangles in the plot.

The range of strength values for freeze cast ceramics is quite large, spanning from a few MPa to almost 160 MPa. The compressive strength of freeze cast ceramics is very sensitive to the total porosity in the sample. It is generally expected that as the amount of porosity increases that the compressive strength will decrease due to the smaller amount of solid present in the sample. Some evidence of this trend can be seen in Figure 92. This figure also shows that large variations in reported strength values have been found for similar total porosity values. This is due to the fact that other factors such as pore wall thickness, pore wall density and the pore morphology can affect the measured compressive strength. Figure 92 presents the data in groups separated by pore morphology to see if any clear trends were evident. It should be noted that all data points in this figure that are from the current study have lamellar pore architectures. It

appeared that for a reasonably large range of porosity values (55 to 75%) that the structures with lamellar pore architectures gave consistently higher strengths than those from completely dendritic structures, such as are generated when using camphene-based freeze casting. It should be noted that most freeze cast samples with total porosity greater than 70% had dendritic pores. The lamellar structures likely have larger compressive strength values due to the anisotropy of the structure in the loading direction. The values obtained in this study from the testing of samples containing 25 vol% solids and 0 – 20 wt% of either PEG or PVA agree well with what has been found in the literature for freeze cast ceramics. The samples processed with PVA are on the lower end of the range found for lamellar pore architectures while the samples processed with PEG display values that are higher than were obtained for lamellar structures with significantly lower amounts of porosity. It should be noted that the 20 wt% PVA sample gave one of the higher recorded values due to lower pore volume fraction, increased lamellar connectivity and very dense walls. The compressive strengths of the samples that contained 20 – 40 vol% alumina and 4 wt% PEG from Section 5.1.2 (represented by gray triangles in Figure 92) agreed well with the literature and also gave two of the highest compressive strength values on the plot.

Figure 93 presents a collection of compressive strength values from the literature for a variety of macroporous ceramic materials.

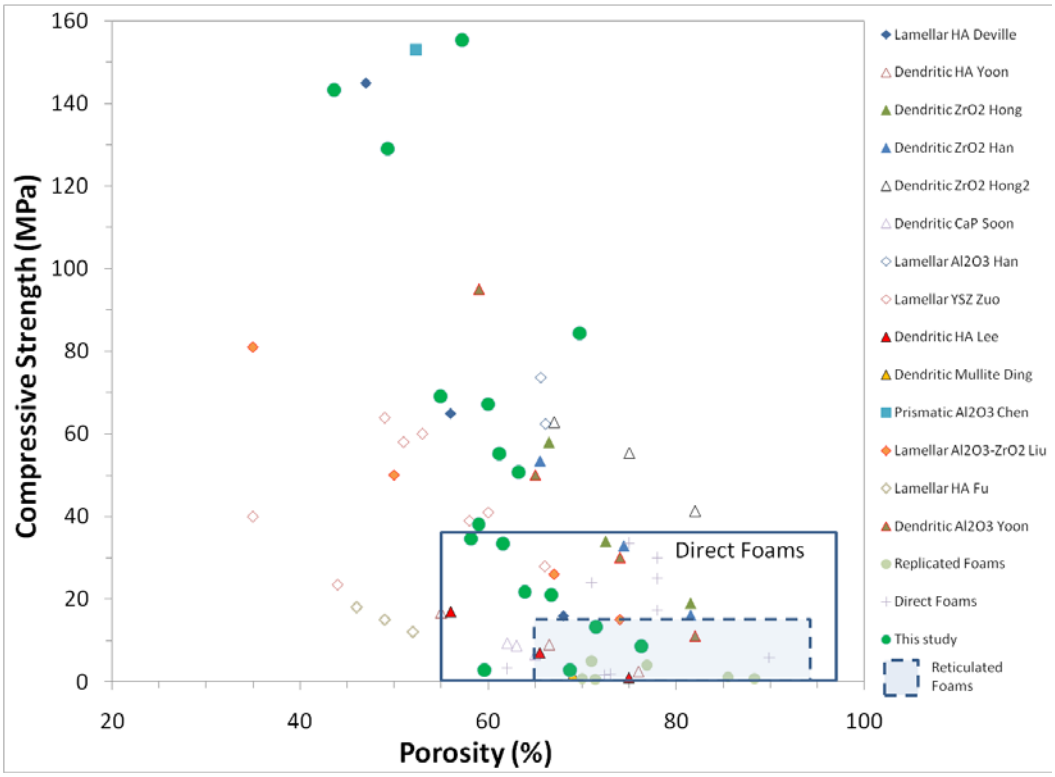

Figure 93. Compressive strength values as a function of total porosity for a variety of macroporous ceramic materials. The porosity and compressive strength ranges found in the literature for direct foams and reticulated foams are added for comparison. The data is also classified by pore morphology with diamonds representing lamellar pores and triangles representing dendritic pores.

It can be seen that some of the compressive strength values that were obtained for the freeze cast samples in this study were within the range exhibited by ceramic direct foams and were significantly larger than what has been reported for reticulated ceramic foams. Reticulated ceramic foams commonly have pore volume fractions that are much larger than what is typically found for freeze cast ceramics. On top of this reticulated ceramics generally have defects on their struts that are a result of burning out the polymeric foam that was used as a template for the structure. Direct foams on the other hand exhibit a somewhat larger range of pore volume fractions and compressive strength values than reticulated ceramics. Despite this a large fraction of the reported compressive strengths for freeze cast materials are significantly higher than those

of direct foams. Possible explanations for this are that there are often cracks in the direct foams and the struts that make up the foams are commonly not dense. There have been significant improvements in the processing of these foams [70-72] that have given markedly increased strength values but in general direct foams are much weaker than freeze cast ceramics. Overall it can be seen that freeze cast ceramics exhibit a range of strength values that are able to be tuned by adjusting both the porosity and pore morphology. The aligned nature of the pore walls tends to give freeze cast ceramics significantly higher strengths than what is reported for reticulated and direct foams. Additionally, the range of strength values found for freeze cast alumina ceramics in this study varied significantly but gave some of the highest reported values to date.

6.0 CONCLUSIONS

1. Freeze cast alumina ceramics have been produced using solid loadings ranging from 20-40 vol% with polymer additions of 0-20 wt% relative to the water content using freezing temperatures that varied from -16°C to -196°C. As a result ceramics with wide ranging microstructures were able to be created.
2. The porosity of the freeze cast bodies was able to be tuned by adjusting the initial solid loading with the final porosity value being linearly dependent upon the solid content. The overall scale of the structure was also highly sensitive to the freezing bath temperature, with colder temperatures giving a large reduction in the measured pore size and pore wall thickness values. Importantly, the effect of increasing solid loading only gave a decrease in measured pore size for samples that were frozen using an ethanol-dry ice bath. At liquid nitrogen temperature (-196°C) the freezing kinetics dominated structure formation and little difference in pore size was noted as the solid loading was increased.
3. The addition of water-soluble polymers to the slip caused a refinement in the structure with increasing polymer content, regardless of the type of polymer that was present. It was shown that the addition of either polyethylene glycol (PEG) or polyvinyl alcohol (PVA) caused the measured pore size and pore wall thickness to decrease for samples with a constant solid loading. The refinement in structure was shown to be qualitatively

consistent with the effects of constitutional supercooling theory. While both polymers progressively refined the structure it was found that PVA was somewhat more effective at this, giving an extremely fine dendritic structure at a content of 20 wt%.

4. Varying the molecular weight of PEG that was added to the slip had an effect on the morphology of the microstructures that were obtained after sintering. In general the structures became increasingly refined as the molecular weight of polymer was increased. The effect of increasing molecular weight was found to be consistent with the effect of increasing molecular weight on diffusivity and the resulting primary and secondary dendrite spacing in the final material.
5. The permeability of the freeze cast samples was found to depend primarily on the pore size in the final sample but was also influenced by the relative roughness of the pore walls as all samples showed evidence of inertial flow. The reported permeability values were in the range of other common filtration media and significantly higher than values in the literature for other freeze cast materials. The type of polymeric additive did not appear to affect the measured permeability values markedly as both series of samples displayed similar values that generally decreased with increasing polymer content.
6. Compressive strength values for the freeze cast materials were dependent not only upon the porosity in the sample but also upon the degree to which the structure was broken down. It was found that the more broken down structures exhibited compressive strength values that were significantly higher than structures with a lesser degree of branching. Highly aligned and dense pore walls were created as a result of the presence of a polymeric binder that was able to accommodate the volume change during solidification. Consequently the reported strength values were significantly larger than what has been

found in the literature for other types of macroporous ceramics such as direct and reticulated foams, where cracks in the solid struts are often present.

In closing, we have generated very strong, highly porous ceramic materials with very good permeabilities that could potentially be useful in filtration applications. The microstructure and properties of these ceramics can be easily modified by changing a number of variables such as the solid content, freezing temperature and polymer content. Most importantly a wide range of properties are attainable by simply altering the polymer content while keeping all of the other processing conditions the same.

7.0 SUGGESTIONS FOR FUTURE WORK

The conclusions arrived at by this study showed that the microstructure and properties of freeze cast ceramics can be easily modified by simply changing the amount of water-soluble polymer that was present in the initial slip. Some possible future directions for continued research of this project are outlined below.

1. The lowest solid loading that was used in this study was 20 vol% Al_2O_3. It was found that the porosity in these structures was linearly dependent upon the solid loading. Due to this, materials with very high porosity could be obtained by decreasing the solid loading below 20 vol%. To aid with the increasingly fragile nature of the green bodies higher polymer contents could be used to provide strength until the materials are sintered. Suggestions would be to use solid loadings ranging from 2-10 vol% with 10 wt% or more polymer relative to the water content. This should give ultrahigh porosity ceramics with a fine and highly broken down pore structure.
2. Permeability measurements were performed on samples with 25 vol% solids and 0-20 wt% PEG or PVA. No permeability measurements were performed on the varying solid loading samples, which displayed some of the highest strength values to date for freeze cast ceramics. It would be interesting to find out what the permeability of these structures are to assess whether or not the stronger structures would be useful in any of the suggested applications.

3. The experiments that dealt with trying to enter the coupled zone for the PEG-H_2O binary system were not successful due to problems with the samples melting and exploding during the freeze drying process. This was attributed to a lack of temperature control during the freeze drying operation. The experiments could be repeated using a freeze dryer that has temperature controlled shelves to see if the samples are able to be successfully created. If the samples are able to be freeze dried successfully they can then be sintered and examined using the methods that were outlined in this study to see if the extremely fine porosity that was expected was actually created.
4. The removal of the time consuming freeze drying step would make freeze casting much more appealing from a technological standpoint. Samples that did not melt after 48 hours at room temperature were successfully made in this study using agar as a gelling agent. After further inspection of the samples it was noted that the directional nature of the samples was completely lost. The directional nature of the pores in freeze casting is largely responsible for the improved permeability and compressive strength values relative to other types of macroporous ceramics. Due to this further study with agar as a gelling agent could be performed with the goal of retaining unidirectional porosity and avoiding freeze drying. Suggestions would include decreasing the amount of agar present and carefully controlling the viscosity of the slip to allow the ice crystals to easily grow.
5. X-ray tomography of two freeze cast samples was performed in this study but the results were not presented as since a complete series of samples was not examined. Tomography gives a 3-D representation of the sample and allows interactive analysis of selected areas. On top of this the data is made up of thousands of 2-D slices of the

sample. The evolution of the microstructure on both parallel and perpendicular sections can be more carefully be examined using these sections combined with the stereological methods employed in this study. Such quantities that could be observed along the height of the sample are colony size, pore morphology, wall thickness and degree of branching. The sections could also be processed using conventional image analysis software to unearth a wealth of information about the microstructure.

The materials that were created in this study behave much like composites in their mechanical response under uniaxial compression. It would be interesting to make these true composite materials by infiltrating them with a second phase such as a polymer or a metal. This could result in composite structures with very high strength and toughness.

APPENDIX A

COUPLED ZONE EXPERIMENTS WITH POLYETHYLENE GLYCOL BINDER

Polyethylene glycol (PEG) is a water soluble polymer that forms a simple binary eutectic when mixed with water. Due to this is was thought that if PEG concentrations close to the eutectic composition were chosen that extremely fine structures could be created as a result of coupled growth. Such structures would be particularly well suited for filtration applications given the fact that small pores would be expected in the final structure. The binary eutectic phase diagram of PEG has been experimentally determined through differential scanning calorimetry experiments by Huang and Nishinari [152] and can be seen below in Figure 94.

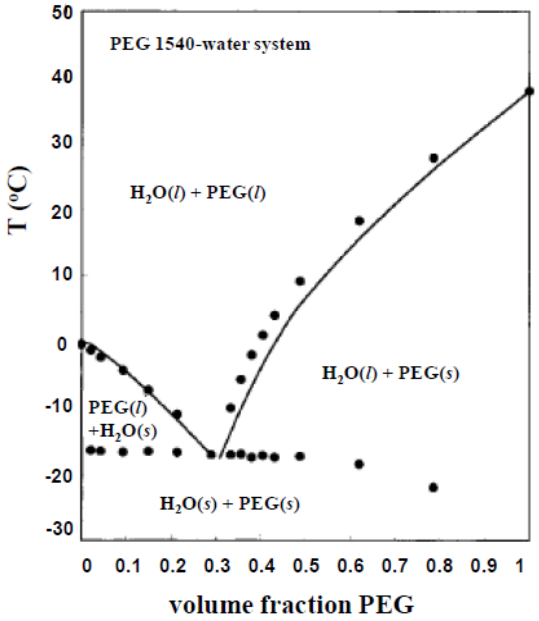

Figure 94. The binary eutectic phase diagram for the PEG-H_2O system. The molecular weight of PEG used in the study was 1540 g/mol. Modified from [152].

From this figure it can be seen that the eutectic isotherm is located at -17°C and the eutectic composition is approximately 30 vol% PEG, which is equivalent to 50 wt% PEG relative to the water content. While this information is for a 1540 g/mol PEG, the composition and temperature of the eutectic point does not shift much for 900 g/mol PEG. Based on this information three PEG (MW = 900) compositions, namely 40, 45 and 47.5 wt% relative to water, were chosen for the coupled zone trials.

The first group of samples that were created contained 25 vol% alumina and the concentrations of PEG that were listed above. Even with the high polymer concentrations present in the slips the particles were well dispersed and the fluid flowed easily while filling the solidification mold. These samples were frozen using an ethanol-dry ice freezing bath (-73°C) and took around 15 minutes to completely solidify.

Once the samples were frozen, some difficulties were encountered when trying to remove them from the two-part polymeric mold. The large amount of polymer present in the samples caused them to either split down the centerline while separating the two halves of the mold or deform when pressure was applied to remove them from the mold wall. To attempt to avoid this, the samples were quenched into liquid nitrogen (-196°C) with the goal of causing the polymer to become rigid long enough to facilitate sample removal. The rapid quench caused some of the samples to crack down the centerline of the mold which led to the sample splitting into two pieces. Some pieces of the samples for each of the three polymer contents were retained and freeze dried for analysis. Further difficulties were encountered when all of the samples melted, either partially or wholly, during the freeze drying procedure. Some of the samples even showed evidence of exploding, as the chamber of the freeze dryer was spattered with alumina. A picture of the samples after freeze drying was completed can be seen below in Figure 95.

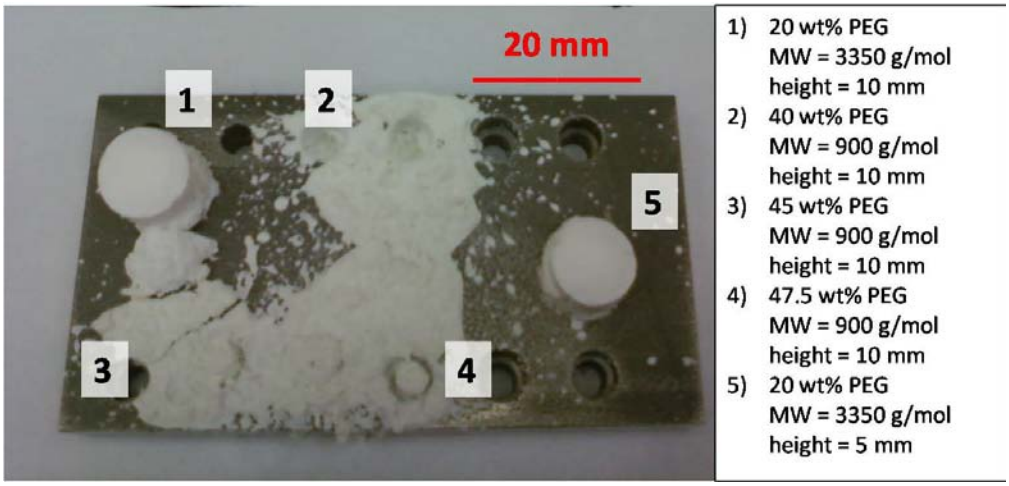

Figure 95. Coupled zone samples containing 40-47.5 wt% PEG (900 g/mol) and 20 wt% PEG (1450 g/mol). All samples contained 25 vol% Al_2O_3. The 900 MW samples showed evidence of melting and exploding while the 3350 MW samples appeared to retain their shape after freeze drying.

The most likely explanation for the samples melting and exploding can be explained by the PEG starting to flow under its own weight as the sample begins to warm up during the freeze drying process. This occurs because the only temperature control during freeze drying is from the block that the samples are placed on, which is initially at liquid nitrogen temperature. As the block warms up the samples also warm up and the polymer begins to flow, which causes the samples to lose shape and consequently many of the pores near the sample surface that serve as an exit for the water vapor generated during sublimation become blocked. Depending on the amount of pores which become closed the water vapor removal can be severely impeded and a pressure builds up in the sample, eventually leading to an explosion.

Part of the problem with the first set of samples could have been the molecular weight of PEG that was used. Since PEG with a molecular weight of 900 g/mol is a waxy solid at room temperature it was decided to use a higher molecular weight PEG that is a solid at room temperature, which could resist flowing as the block begins to warm, thus avoiding the problems encountered with the 900 g/mol samples.

A higher molecular weight of 3350 g/mol was selected and a slip containing 25 vol% Al_2O_3 and 20 wt% PEG (relative to water content) was created. The higher molecular weight presented no problems during slip preparation and the resulting colloid was well dispersed and flowed readily. Samples were frozen using the same mold and bath as for the first trials with the lower molecular weight PEG. Complete freezing of the samples took 15 minutes and due to the lower polymer content no problems were encountered when removing the samples from the mold. The samples were then transferred to the freeze dryer and observed periodically during the first few hours of the process. The samples started to develop cracks once the block started

to warm up and eventually shattered into a few pieces. Despite the samples breaking into multiple pieces none of them showed any evidence of melting and sizable fragments remained for firing. After the samples were subjected to a pre-firing process to burn out the PEG and subsequently sintered they were extremely cracked and delicate. A micrograph of one of these samples can be seen below in Figure 96.

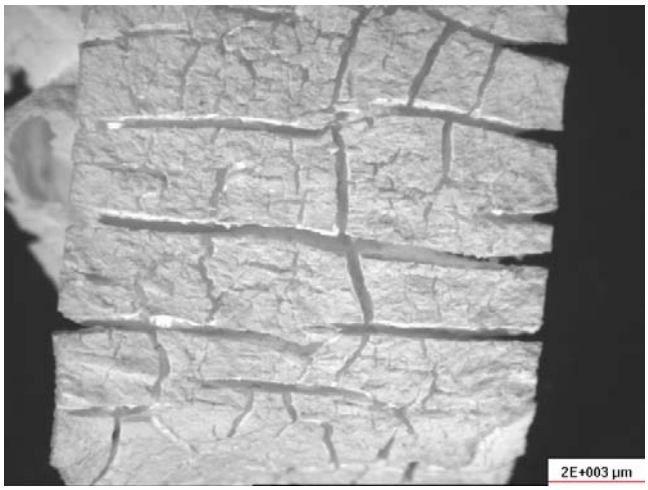

Figure 96. Low-power optical micrograph of a sample containing 25 vol% Al_2O_3 and 20 wt% PEG with a molecular weight of 3350 g/mol. The sample was sintered at 1400°C for one hour and became heavily cracked. Scale bar = 2mm.

As can be seen the end state of the sintered samples is less than desirable and while the increased molecular weight avoided the slumping and melting of the samples, the problem of cracking and exploding is still present. A possible explanation could be that the pores which are created during solidification are extremely fine and this is limiting the vapor transport during the sublimation step in freeze drying. It also is still possible that the polymer could be starting to flow as the block warms up, leading to similar problems as were encountered with the 900 g/mol

samples. Regardless of what is happening the solution to the problem was not entirely solved by using a higher molecular weight of PEG.

Another variable that could be contributing to the samples not freeze drying properly is the height of the samples. It can be expected that taller samples have a greater chance of melting since a larger thermal gradient is present across the samples from the chill block to the top of the sample. To investigate this samples ranging in height from 5 to 10 mm were created. A molecular weight of 1450 g/mol was used as a balance between the samples which entirely melted (900 g/mol PEG) and the ones that cracked during freeze drying (3350 g/mol PEG). In addition two 5 mm tall samples were created using 900 g/mol PEG to see if smaller samples could be processed without deforming or melting. The freeze-dried samples can be seen below in Figure 97.

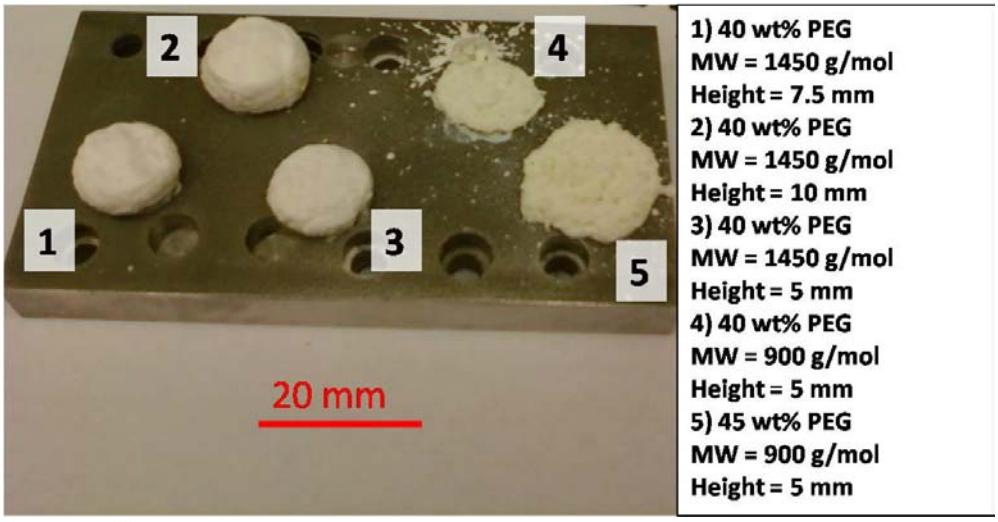

Figure 97. Coupled zone samples containing 40-45 wt% PEG of molecular weights 900 and 1450 g/mol. The samples showed evidence of melting, deformation and exploding during freeze drying regardless of the sample height.

As can be seen above all of the samples showed some evidence of melting or deformation. The samples processed with 900 g/mol PEG still melted despite the small sample height of 5 mm. It appears that samples with large amounts (greater than 40 wt%) of 900 g/mol PEG cannot be successfully processed using the current methods. The samples that were processed using 1450 g/mol PEG generally became distorted and somewhat bloated, regardless of the height of the sample. This is once again most likely due to a combination of the polymer beginning to flow as the chill block warms up and difficulties in removed the water vapor that is generated during sublimation of the ice crystals.

All of the above trials seem to have one central theme: the freeze drying step is problematic and is causing the samples to melt or crack. These problems can likely be attributed to inhomogeneous gas evolution during the freeze drying step. A final set of samples was created with 20, 25 and 30 wt % PEG (relative to the water content) with a molecular weight of 900 g/mol. These samples were frozen, brought to liquid nitrogen temperature on a chill block and then placed into the chamber of the freeze dryer. All of the samples were placed on their side to minimize the thermal gradient across the sample. Visual observation of the condition of the samples and the pressure of the chamber were recorded during the freeze drying process. A plot of the variation in chamber pressure with time can be seen below in Figure 98.

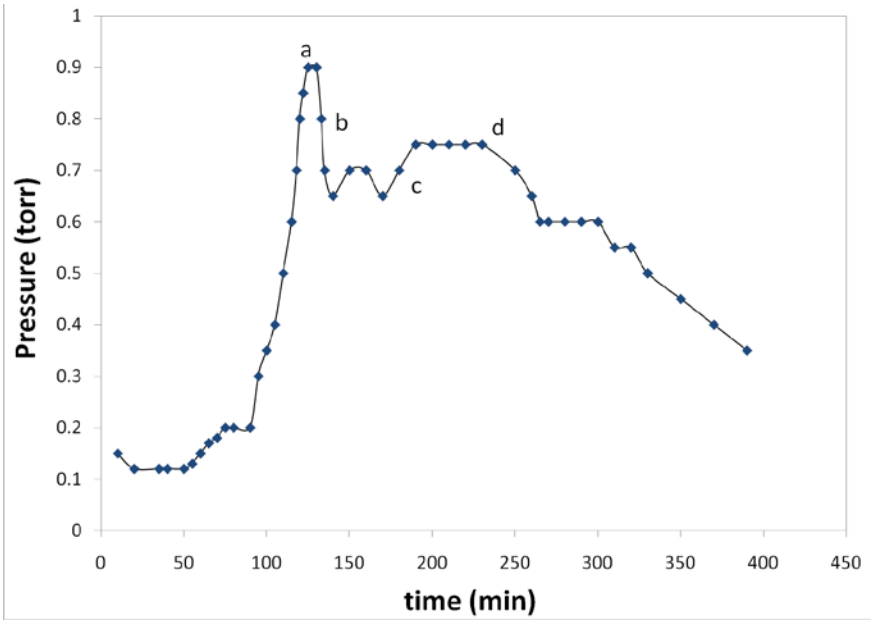

Figure 98. The variation in freeze dryer chamber pressure with time for the freeze drying of samples containing 25 vol% Al_2O_3 and 20 – 30 wt% PEG (900g/mol).

During the course of freeze drying not much happened during the first 100 minutes other than a slight increase in the pressure in the chamber. This rise in pressure occurred while the block and samples slowly defrosted, and one could expect the vapor pressure in the chamber to increase because of this. Just after this the pressure in the chamber begins to rise dramatically from approximately 0.2 torr at 100 minutes to 0.9 torr at 125 minutes (labeled as point 'a' in Figure 98). Coincidently at this point both the 25 and 30 wt% PEG samples begin to crack due to the large amount of water vapor that is being released into the chamber. Over the next few minutes the 30 wt% PEG sample continued to crack very severely and eventually developed a large radial crack at point 'b'. The pressure in the chamber then started to decrease and eventually started to increase again at point 'c', at which point the 20 wt% PEG sample started to crack, the 25 wt% PEG sample continued to crack and the 30 wt% PEG sample started to show signs of deformation. At this point the block and samples must be sufficiently warm such that

the outer edges of the 30 wt% PEG sample can start to flow. From points ‘c’ to ‘d’ in Figure 98 the pressure is holding steady, which can likely be attributed to a constant rate of out-gassing by the samples. Also in this interval the 30 wt% PEG sample continues to deform more significantly. By point ‘d’ the 25 wt% PEG sample had developed a large circumferential crack which continued to grow as the freeze drying procedure continues. From 300 minutes onward to pressure in the chamber steadily decreases, which indicates that a large fraction of the ice has sublimated and the remaining water vapor is being removed much more easily. There is still, however, a continuation of the cracking of both the 20 and 25 wt% PEG samples and deformation of the 30 wt% PEG sample. At 400 minutes it was assumed that most of the sublimation of the samples had finished since the pressure steadily was decreasing so monitoring of the pressure was discontinued and the freeze dryer was allowed to run overnight. The samples were again inspected at 19 hours, at which point the chamber pressure was 0.12 torr and there was no visible change in the state of any of the samples.

Overall during the freeze drying operation of the 20, 25 and 30 wt% PEG samples there was significant cracking observed that appeared to correlate with spikes in vapor pressure during sublimation of the ice crystals at reduced pressure. Also it was noted that using amounts of 900 g/mol PEG equivalent to or greater than 30 wt% relative to water content would cause partial to complete melting of the sample using the freeze drying apparatus. These problems are directly related to the fact that the freeze drying apparatus that was used in this study does not have temperature control over the block or the samples. If the temperature in the chamber were able to be controlled then processing of samples with higher amounts of PEG could potentially be accomplished. However, given the limitations of the freeze drying apparatus no further

experimentation on the coupled zone was performed and hence no firm conclusions could be made regarding the pore structures that could potentially be generated.

Based on the results of these experiments and the those found in section 5.1.4 it was determined that using the current freeze drying setup limits the addition of PEG to a maximum of 20 wt% (relative to the water content) before the detrimental effects of partial melting and inhomogeneous gas evolution destroy the microstructure.

APPENDIX B

PSEUDO-BRIDGMAN VELOCITY OPTIMIZATION EXPERIMENTS

As mentioned previously, during freeze-casting a situation exists where heat is extracted through an increasing amount of solidified material. This in turn leads to a constantly decreasing interfacial velocity and hence appreciable coarsening of the ice crystals. Evidence of this coarsening was presented for samples processed with both PEG (Table 1) and PVA (Table 5) binders in varying proportions. To try and avoid this situation and achieve steady-state conditions a pseudo-Bridgman solidification technique was tested where the samples were immersed into a freezing bath at a constant velocity. A tensile testing machine was used since it has a crosshead speed that was adjustable over a wide range of velocities. The details of this setup can be found in the experimental procedures section. Before any experiments could be performed it was necessary to first test the apparatus and identify a range of velocities that would be suitable for processing of the samples. The criterion that had to be met for a velocity to be viable was that there should be little difference between the measured pore size at the top and bottom of the sintered sample.

Velocity optimization experiments were performed with slips that contained 25 vol% Al_2O_3 and 5 wt% PEG relative to the solid loading. This slip formulation was investigated since

it was chosen as the composition to be used in future experiments on the effect of the molecular weight of PEG on the microstructure of freeze cast ceramics. The solidification velocity was varied between 20 and 90 μm/sec such that a range of velocities comparable to those used by other authors to process freeze cast ceramics were tested [54].

The first sample was frozen at a rate of 20 μm/sec and yielded a microstructure that was directionally oriented and dendritic in nature. During the test it was observed that the sample was completely solidified before half of the sample had entered the freezing bath. This presented a situation that was similar to freeze casting using a mold on a chill block and hence measureable coarsening was expected. Representative SEM micrographs from sections parallel to the freezing direction can be seen below in Figure 99.

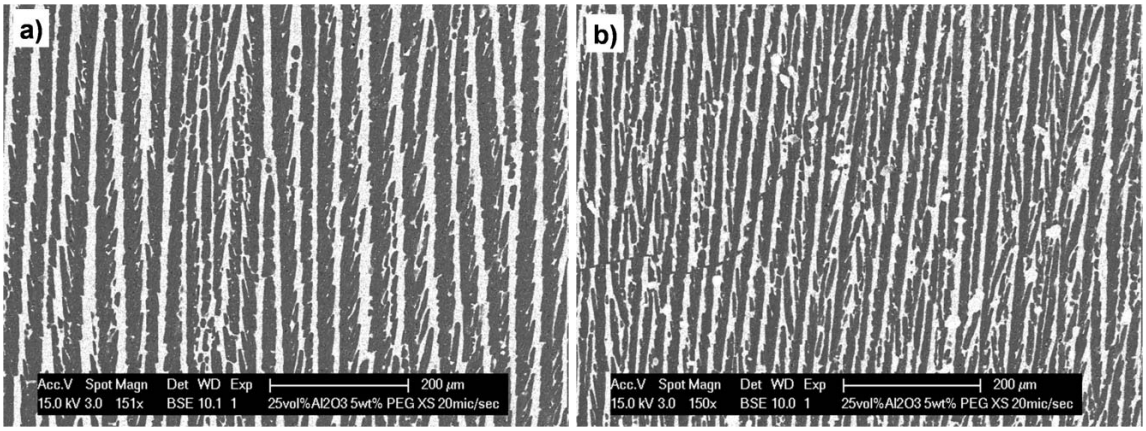

Figure 99. SEM micrographs taken from a section parallel to the freezing direction of a sample frozen at 20 μm/sec illustrating the difference in pore size between a) the top and b) the bottom of the sample. Both micrographs were captured at 150x.

Upon visual inspection of the micrographs in Figure 99 it is clear that there is a difference in the pore size between the top and bottom of the sample. The pore size for this sample was

quantified using an image analysis program and it was determined that the pore size at the bottom of the sample was 12.7±1.6μm and increased to 20.6±0.95 μm at the top of the sample.

The second solidification velocity that was tested was 40 μm/sec and the microstructure of the sample was once again dendritic in nature. During most of the immersion process the solid-liquid interface remained a small (approximately 1 mm) distance ahead of the freezing bath. Despite this the sample completely froze by the time that approximately 75% of the sample was immersed into the freezing bath. SEM micrographs of the top and bottom of the sample that were taken from a section parallel to the freezing direction can be seen below in Figure 100.

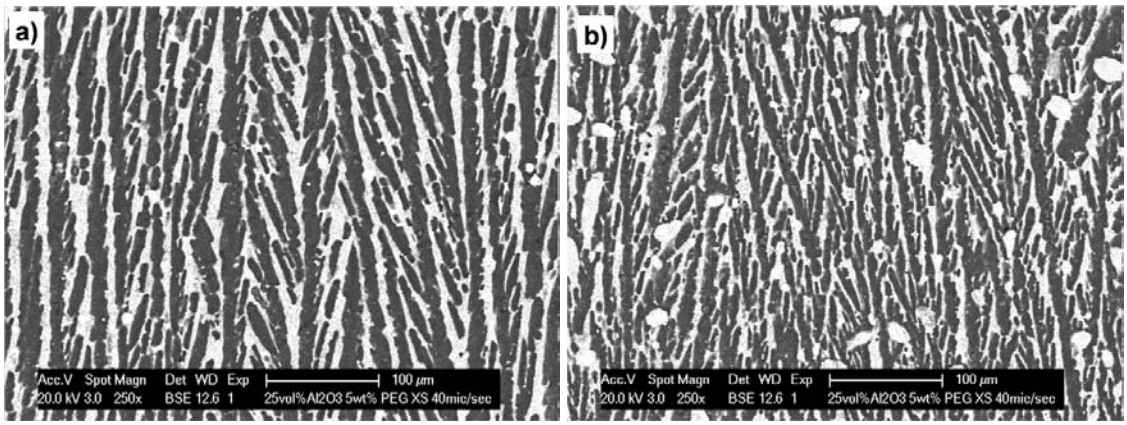

Figure 100. SEM micrographs taken from a section parallel to the freezing direction of a sample frozen at 40 μm/sec showing the difference in pore size between a) the top and b) the bottom of the sample. Both micrographs were captured at 250x.

It was expected that there could have been some coarsening of the ice crystals during solidification since the sample was completely frozen before the entire sample was immersed into the bath. In true steady state conditions the solid-liquid interface would remain at a fixed

distance ahead of the freezing bath and the sample would finish solidifying just before the sample is completely immersed. The measured pore size was found to be 11.49±0.46 μm at the bottom of the sample and 15.89±1.46 μm at the top of the sample. Based on these measurements it was found that coarsening still occurred, although on a much smaller scale than the sample that was frozen at 20 μm/sec. This sample also displayed ice crystal growth from the walls of the vial that held the slip, which was a feature that was not present in the 20 μm/sec sample. A micrograph from a section parallel to the freezing direction that exhibits such growth can be seen below in Figure 101.

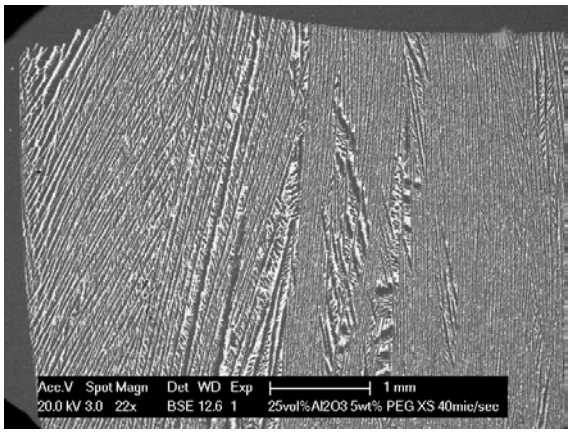

Figure 101. SEM micrograph of a section parallel to the freezing direction for a sample containing 25 vol% Al_2O_3 and 5 wt% PEG that shows evidence of ice crystal growth from the mold wall. The solidification velocity for this sample was 40μm/sec. (Magnification 22x)

It can be seen that even though there is growth of ice crystals from the side of the mold wall, they were eventually overgrown by crystals that were more favorably aligned to the direction of heat flow. The reason that ice crystals can grow from the side is due to the fact that the thin glass vial is cooled rapidly as it is immersed into the freezing bath and hence ice crystals

nucleate on the cooled surface and begin to grow inward at a slower rate. Since the vial for the first sample (20 μm/sec) was not fully immersed into the bath this type of growth was not observed. It was expected that faster immersion velocities would result in more pronounced growth from the sides.

The next velocity that was examined was 55 μm/sec. Once again during solidification the solid-liquid interface remained at a small (1mm) distance ahead of the freezing bath and the sample completed freezing just before full immersion was completed. These observations gave hope that there was minimal coarsening of the ice crystals during solidification. Micrographs from sections parallel to the freezing direction can be seen below in Figure 102 for heights close to the top and bottom of the sample.

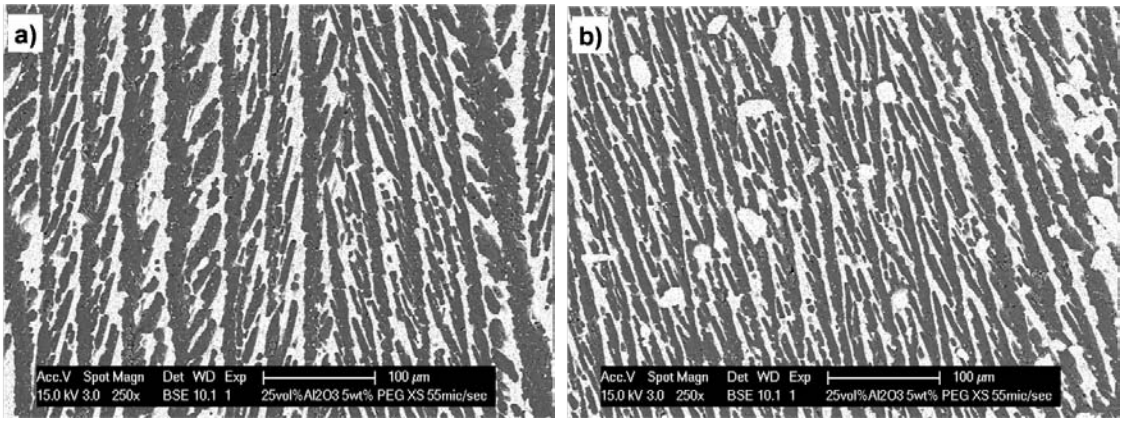

Figure 102. SEM micrographs taken from a section parallel to the freezing direction of a sample frozen at 55 μm/sec comparing the pore size between a) the top and b) the bottom of the sample. Both micrographs were captured at 250x.

Upon visual inspection of these micrographs it appears that the pore size at the top of the sample is larger than at the bottom. Measurements performed on images yielded pore size values

of 13.51±0.25 μm and 12.64±0.14 μm for the top and bottom of the sample, respectively. These measurements do validate that a small amount of coarsening was present in the sample. The most likely reason for the top of the sample looking significantly larger than the bottom is some of the dendrites were not properly oriented when the sample was sectioned, thus giving them a larger cross section. Of the velocities tested so far this sample has shown the smallest amount of coarsening with a difference of roughly 1 μm between the top and bottom of the sample. The only negative aspect of this sample was that it showed an increased amount of ice crystal growth from the sides of the vial, which can be seen below in Figure 103.

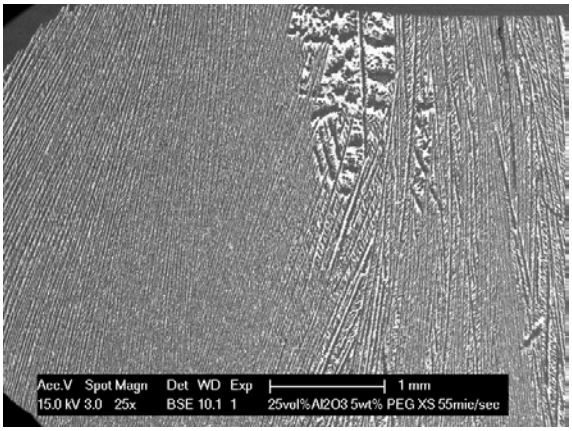

Figure 103. SEM micrograph of a section parallel to the freezing direction for a sample containing 25 vol% Al_2O_3 and 5 wt% PEG that was solidified at a rate of 55 μm/sec and shows evidence of prominent ice crystal growth from the mold wall. (Magnification 25x)

Comparison of Figure 101 and Figure 103 confirms that the amount of growth from the side of the mold is more prominent than was encountered for the sample that was solidified at 40 μm/sec, and shows that even though this growth is more pronounced these crystals are still being

overgrown by more favorably oriented ones. On top of this the sample is still largely oriented in the preferred direction and exhibited very little coarsening.

The solidification velocity was increased to 65 μm/sec for the next sample and micrographs from the top and bottom of the sample for sections parallel to the freezing direction can be seen below in Figure 104.

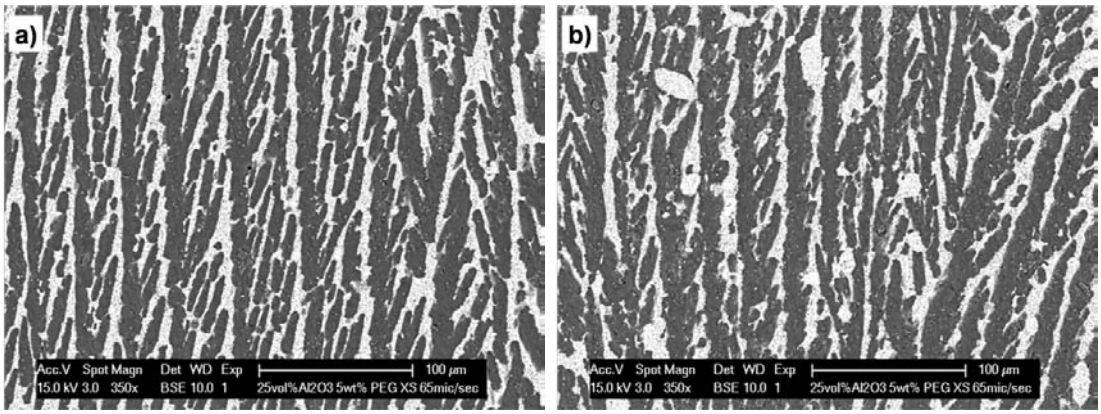

Figure 104. SEM micrographs taken from a section parallel to the freezing direction of a sample frozen at 65 μm/sec comparing the pore size between a) the top and b) the bottom of the sample. Both micrographs were captured at 250x.

The micrographs seen in the above figure show little difference in the size of the pores between the top and bottom of the sample. It can be seen that the secondary branches have become more regular and prominent by the time they reach the top of the sample, which is consistent with what is expected from solidification theory, as more favorably oriented ice crystals will overtake others and give a regular structure. The pore size values from image analysis were determined to be 11.02±0.12 μm and 10.99±0.55 μm for the top and bottom of the sample, respectively, confirming that no significant coarsening of the ice crystals occurred

during solidification of these samples. As expected the amount of ice crystal growth from the side of the mold was increased and the percentage of the sample that was favorably oriented was decreased somewhat compared to the previous sample. Evidence of the increased amount of ice crystal growth from the side of the sample can be seen below in Figure 105.

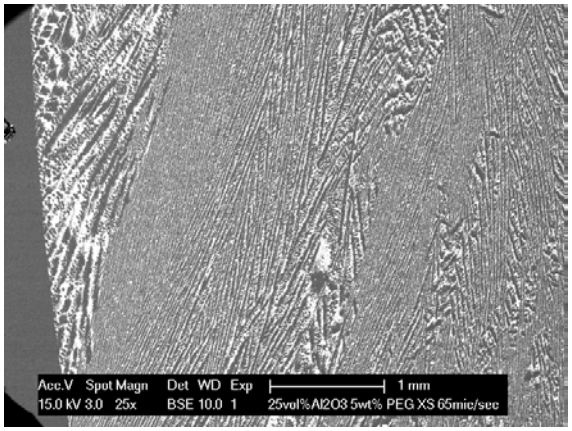

Figure 105. SEM micrograph of a section parallel to the freezing direction for a sample containing 25 vol% Al_2O_3 and 5 wt% PEG that was solidified at a rate of 65 μm/sec and shows evidence of prominent ice crystal growth from the mold wall. (Magnification 25x)

Overall a significant portion (at least 50%) of the sample was still favorably oriented and no measurable difference in pore size between the top and bottom of the sample was present.

When the solidification velocity was increased to 75 μm/sec many of the same trends that were present for the previous sample (65 μm/sec) were again present. It can be seen below in Figure 106 that there does not appear to be a large difference in the size of the pores between the top and bottom sections of the sample. Once again the sample becomes more regular and the secondary dendrite arms become more prominent on the top section compared to the bottom section, which could be due to a decelerating interface allowing them more time to coarsen.

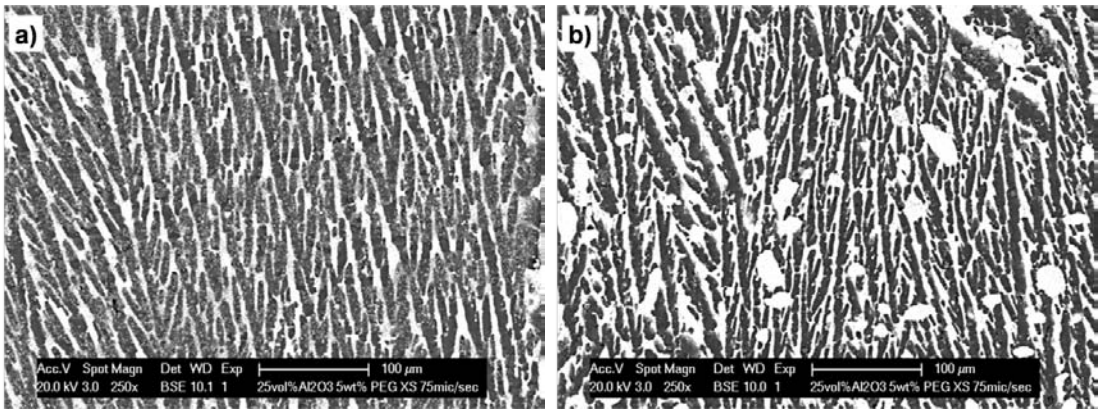

Figure 106. SEM micrographs taken from a section parallel to the freezing direction of a sample frozen at 75 µm/sec comparing the pore size between a) the top and b) the bottom of the sample. Both micrographs were captured at 250x.

The pore size values from image analysis were measured as 9.73±0.87 µm on the top section and 8.93±1.34 µm on the bottom section, confirming that little measurable coarsening occurred during solidification. When this sample was being frozen a situation arose where the vial was completely submerged before the sample was completely solid. Due to this it was expected that the amount of growth from the sides of the mold would be much more pronounced than for any of the samples that were previously discussed. It can be seen below in Figure 107 that a large portion of the sample is made up of crystals that are not oriented with the main direction of heat flow. Instead these crystals grow out from the side of the vial where it is being rapidly chilled due to immersion in the freezing bath and thus providing a secondary heat flow direction that crystals can grow along. A small section towards the middle of the sample was noted to still be oriented in the preferred direction (bottom to the top of the sample) but this comprised less than 50% of the section taken parallel to the freezing direction.

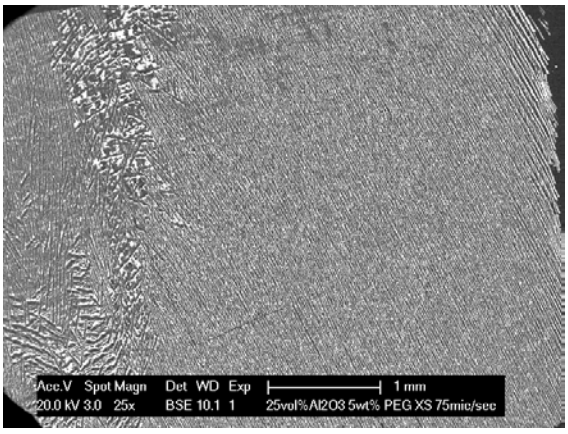

Figure 107. SEM micrograph of a section parallel to the freezing direction for a sample containing 25 vol% Al_2O_3 and 5 wt% PEG that was solidified at a rate of 75 μm/sec and shows evidence of signifcant ice crystal growth from the mold wall that accounts for a large percentage of the sample. (Magnification 25x)

Overall for the sample that was solidified at 75 μm/sec there was little measurable coarsening during solidification but the percentage of the sample that was oriented in a favorable direction was less than desirable.

The final velocity that was tested for the velocity optimization experiments was 90 μm/sec. Based on the findings for the previous samples it was not expected that this velocity would create a satisfactory sample, however, it was examined to ensure that a range of velocities that were encountered in the literature were tested. As was expected, during the solidification of the sample the vial was fully immersed into the freezing bath well before the sample was solidified. Figure 108 shows a micrograph that was taken from a section parallel to the freezing direction.

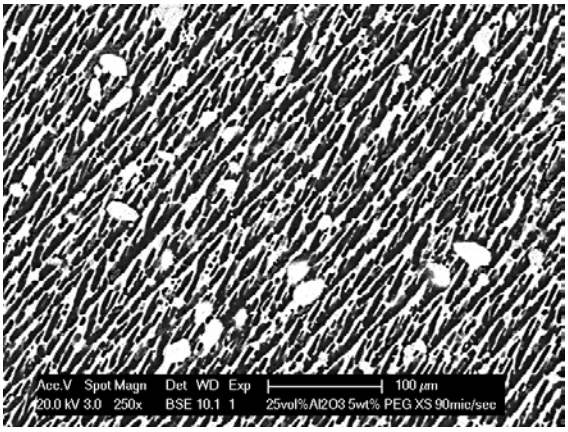

Figure 108. SEM micrograph of a section parallel to the freezing direction for a sample containing 25 vol% Al_2O_3 and 5 wt% PEG that was solidified at a rate of 95 μm/sec. This micrograph is from the middle of the sample and illustrates how growth from the side of the mold comprises most of the sample. (Magnification 25x)

This micrograph shows that the ice crystals are no longer oriented from the bottom to the top of the sample, but are rather extend at a 45 degree angle from the side of the vial and extend in towards the middle of the sample. The growth from both sides of the vial extended inwards toward the middle of the sample where there was a very small section that was oriented from the top to the bottom of the sample. Therefore it was decided that this velocity was too fast since the desired directionality was not present due to the large amount of growth from the sides of the vial. Given the current pseudo-Bridgman setup it was determined that the problem of growth from the sides of the mold was unavoidable, but able to be minimized by solidifying at lower interfacial velocities.

As can be seen in Table 6 it was found that as the solidification velocity was increased that both the pore size and the degree of ice crystal coarsening were decreased. In general, velocities from 40-75 μm/sec were reasonably well suited for processing of samples with small degrees of ice crystal coarsening.

Table 6. A summary of the pore size at the top and bottom of the sample for different solidification velocities that were tested using the pseudo-Bridgman solidification apparatus.

Velocity (μm/sec)	Pore Size (μm)	
	Top	Bottom
20	20.63±0.95	12.70±1.60
40	15.89±1.46	11.49±0.46
55	13.51±0.25	12.64±0.14
65	11.02±0.12	10.99±0.55
75	9.73±0.87	8.93±1.34

It was also noted that the amount of ice crystal growth from the sides of the vial increased steadily with increasing velocity until the entire sample was comprised of such growth. As the goal of these trials was to find a suitable velocity for further experimentation it was decided that 55 μm/sec was the optimum velocity to use for further processing. This velocity was selected mainly because of the fact that it was the first velocity to show relatively little coarsening. As the velocities were increased the amount of coarsening did not change much, but the percentage of the sample that was made up of growth from the sides of the vial increased significantly. The 55 μm/sec sample was the lowest velocity to display a combination of both minimal coarsening and growth from the sides of the mold, and was therefore chosen as the velocity for all future pseudo-Bridgman experiments.

APPENDIX C

GELATION STUDIES – ADDITIONAL INFORMATION

Results for many of the samples that were allowed to dwell at room temperature and 60°C for the gelation studies in section 5.2.4 were not presented since the results were similar. All of the information for these samples and their behavior while returning to room temperature are presented in this appendix for completeness. Further details concerning the setup of the experiments can be found in the experimental procedures.

C.1 SAMPLES AGED AT ROOM TEMPERATURE

Figure 109 shows a time lapse sequence of a sample that was frozen immediately after the slip was taken off of the ball mill.

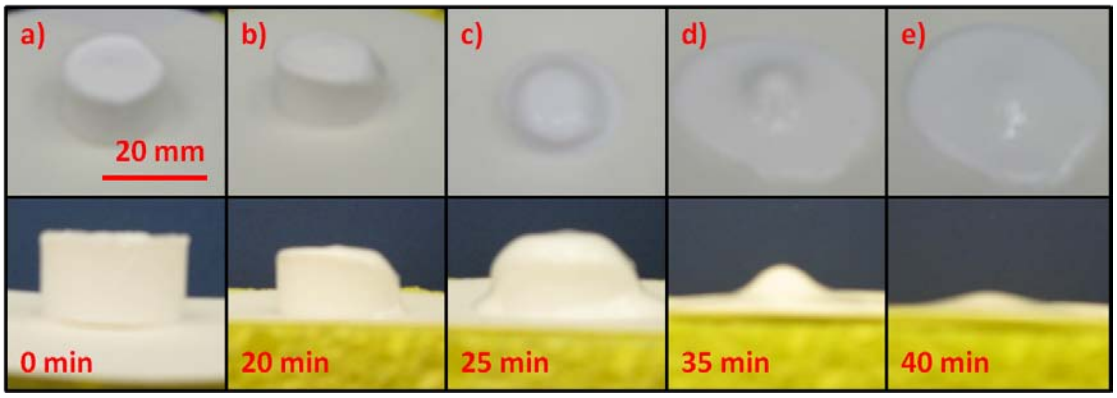

Figure 109. Time lapse sequence of the melting behavior of a sample containing 23 vol% Al_2O_3 and 20 wt% PVA that was frozen immediately after removal from the ball mill (no dwell time). The lower images are profile views of the sample at a specified time since removal from the mold and correspond to the image that is directly above it.

The sample first started to show signs of melting at 15 minutes and was visibly melting by 20 minutes. Following this the sample progressively melted and was completely liquid 45 minutes after being removed from the mold. It was not surprising that this sample completely melted, as the sample had no dwell time to allow a gel network to form in the liquid.

The next sample that was solidified was allowed to dwell for 2 hours at room temperature before solidification. The state of the sample as it returned to room temperature can be seen in Figure 110. This sample showed the first evidence of melting by 17 minutes and shows definite signs of melting at 20 minutes. As was the case with the sample that had no dwell time this sample progressively melted and completely turned to liquid after 50 minutes at room temperature. The only difference noted between the sample with no dwell time and the 2 hour dwell sample was a 5 minute difference in the amount of time required for the sample to completely melt. This marginal increase is not surprising since 2 hours is a relatively short amount of time to expect a strong gel network to build up that would allow the sample to resist melting while warming back to room temperature.

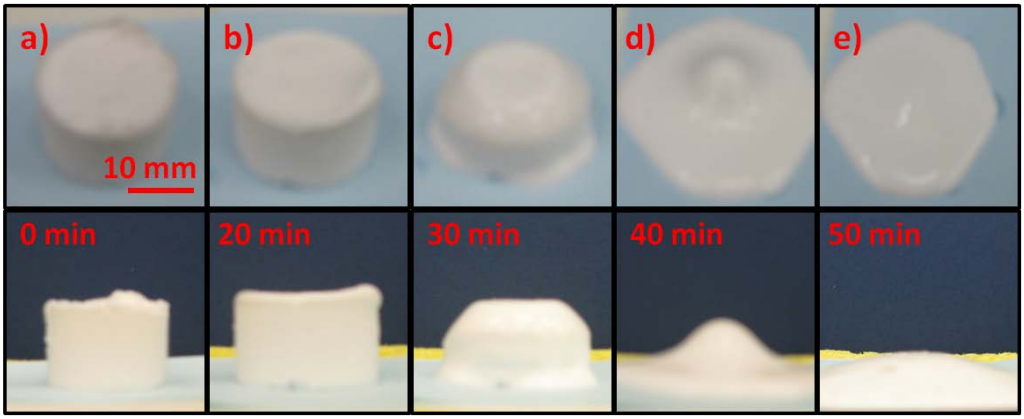

Figure 110. Time lapse sequence of the melting behavior of a sample containing 23 vol% Al_2O_3 and 20 wt% PVA that was allowed to age for 2 hours at room temperature prior to freezing. The lower images are profile views of the sample at a specified time since removal from the mold and correspond to the image that is directly above it.

Figure 111 shows a time lapse sequence of a sample containing 23 vol% Al_2O_3 and 20 wt% PVA that was allowed to age for 4 hours at room temperature (23°C). This sample showed very little difference from the sample that was aged for 2 hours at room temperature, as it showed signs of initial melting around 20 minutes and progressively melted over the next 30 minutes, showing complete melting after 50 minutes at room temperature. Since no improvement was seen for the samples for short dwell times the next group of samples was allowed to dwell overnight before freezing, as it was thought that the gel network might take a significant period of time to form while resting at room temperature.

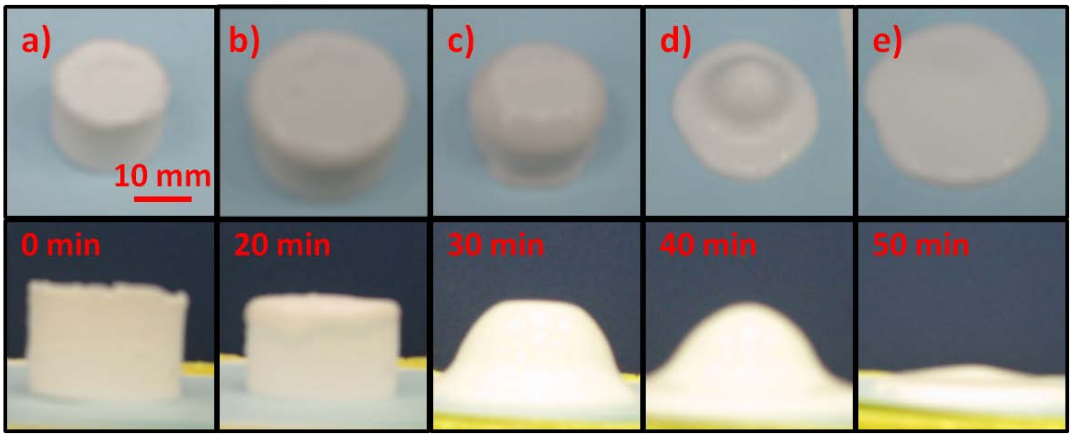

Figure 111. Time lapse sequence of the melting behavior of a sample containing 23 vol% Al_2O_3 and 20 wt% PVA that was allowed to age for 4 hours at room temperature prior to freezing. The lower images are profile views of the sample at a specified time since removal from the mold and correspond to the image that is directly above it.

The time lapse sequence for the sample that was aged for 23 hours at room temperature before being frozen was presented in section 5.2.4 and will not be repeated here. It was noted that the sample began to melt after 20 minutes at room temperature, was visibly deformed by 30 minutes and completely melted by the time 50 minutes had elapsed. The results of an overnight dwell did not show any measurable improvement in the melt resistance of the samples. It is possible that more time is required to form a stable gel, but the more likely scenario is that the physical gel that is formed by PVA is simply not strong enough to resist being rehydrated by water once the sample begins to warm up.

C.2 SAMPLES AGED AT 60°C

The formation of a gel is a kinetic process that can be sped up by aging at a higher temperature. Therefore the next sample that was investigated was subject to a dwell time of 24

hours in a 60°C oven before solidification was initiated. The time-lapse melting behavior of the sample as it returns to room temperature can be seen below in Figure 112.

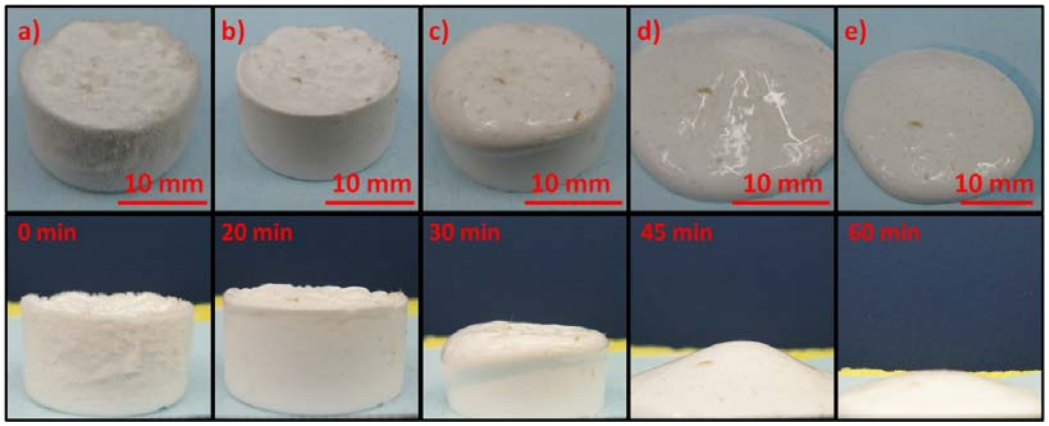

Figure 112. Time lapse sequence of the melting behavior of a sample containing 23 vol% Al_2O_3 and 20 wt% PVA that was allowed to age for 24 hours at 60°C prior to freezing. The lower images are profile views of the sample at a specified time since removal from the mold and correspond to the image that is directly above it.

Despite having an overnight dwell at a temperature roughly three times greater than the other samples were aged at this sample started to melt around the outer edges at about 20 minutes, as can be seen above. After 30 minutes the sample was visibly deforming and this trend continued until the sample was completely melted at 60 minutes. The only noticeable differences between this sample and the samples that were aged at room temperature were that it took a slightly longer time period for the sample to melt and there was a readily observable ring of moisture at the base of the sample. It appears that the longer dwell time at 60°C is somewhat more effective at removing water from the sample, but the end result is still complete melting.

After no noticeable improvement was noted for a 24 hour dwell time at either room temperature or 60°C it was decided to let the samples age for a considerable period of time

before the next set was tested. Samples were allowed to age at room temperature and 60°C for 98 hours before being solidified. This time was chosen because the gel network should have more than sufficient time to develop at either of the aging temperatures that were tested. Figure 113 shows the results for the sample that was aged for 98 hours at room temperature.

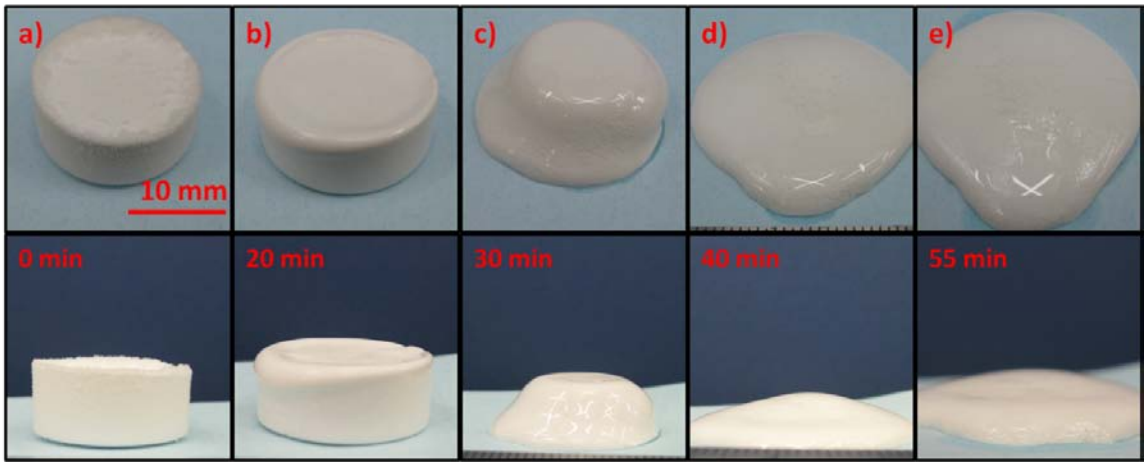

Figure 113. Time lapse sequence of the melting behavior of a sample containing 23 vol% Al_2O_3 and 20 wt% PVA that was allowed to age for 98 hours at room temperature prior to freezing. The lower images are profile views of the sample at a specified time since removal from the mold and correspond to the image that is directly above it.

As was seen for all of the previous samples that were aged at room temperature the sample started to melt around the top edges after 20 minutes had elapsed. By 25 minutes the sample began to show visible deformation and at 30 minutes the sample had a visible sheen to it as well as a ring of moisture at the sample base. The fact that the liquid coating the sample had a visible sheen to it was most likely due to the fact that it contained PVA. As the sample started to warm up and the ice turns into water some of the PVA is going back into solution and is removed from the sample. The sample continues to deform and is once again fully melted by 55

minutes, showing only a minor improvement over the other samples that were aged at room temperature.

The time lapse behavior of a sample that was aged at 60°C for 98 hours can be seen below in Figure 114. This combination of aging temperature and dwell time should provide the strongest gel out of all of the conditions that were tested.

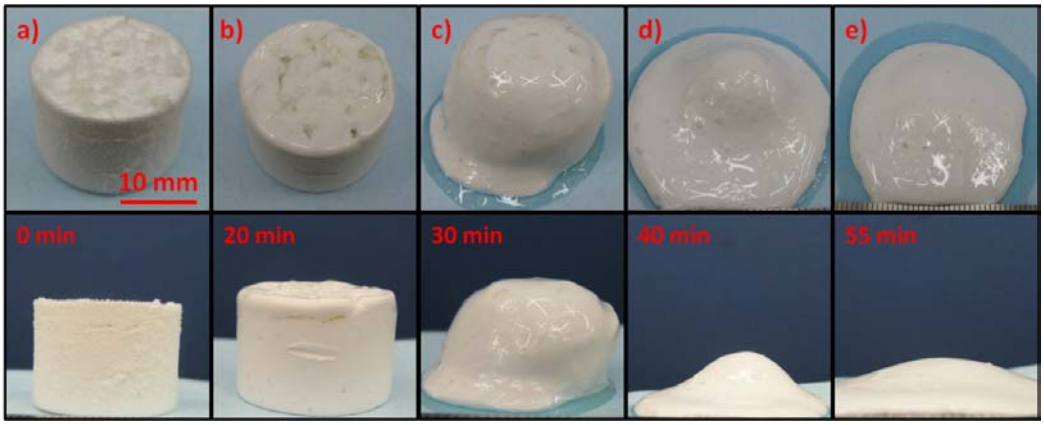

Figure 114. Time lapse sequence of the melting behavior of a sample containing 23 vol% Al_2O_3 and 20 wt% PVA that was allowed to age for 98 hours at 60 °C prior to freezing. The lower images are profile views of the sample at a specified time since removal from the mold and correspond to the image that is directly above it.

As this sample aged in the oven air bubbles slowly rose up out of the slip and collected at the surface, causing some of the oil that was placed on top of the slip to prevent evaporation to form pockets in the top millimeter of the slip. This can be seen below in Figure 115, which is a view down into the vial that is holding the aged slip.

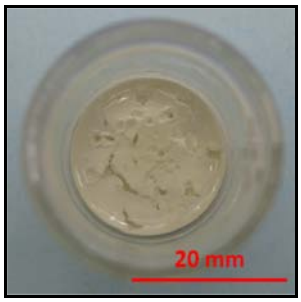

Figure 115. Pockets of oil that arose due to air bubble coalescence during aging of a sample containing 23 vol% Al2O3 and 20 wt% PVA for 98 hours at a temperature of 60 °C.

As can be seen in the time lapse series in Figure 114 the sample appears to start melting at 10 minutes. It should be noted, however, that this is not the sample melting, but is some of the pockets of oil that were trapped in the slip during freezing. Generally when the samples were solidified the oil was easily separated from the frozen body. In this case due to the topography of the top surface of the slip some of the oil was not able to be removed and gave the appearance that the sample started to melt at 10 minutes. True melting of the sample started at 20 minutes, as the edges once again were the first to deform. By 25 minutes the sample is visibly flowing, resulting in deformation. After 30 minutes have elapsed the sample has melted significantly and is once again releasing the PVA solution, resulting in a glistening coating on the sample. After 40 minutes at room temperature the ring of moisture at the bottom of the sample is becoming rather prominent. This ring continues to expand as the sample progressively deforms and eventually melting of the entire sample is completed at 55 minutes.

Overall there was little improvement in the resistance of the samples to melting regardless of the aging temperature or dwell time for samples containing 23 vol% alumina and 20 wt% PVA relative to solids. All of the samples started to show some signs of melting after 20 minutes at room temperature and the time required for complete melting varied from 45 to 55

minutes. None of the trials were successful at retaining the shape of the frozen body while allowing the water to be removed, which is most likely due to the fact that the physical gel created by aging the PVA slips is simply not strong enough to resist going back into solution with the water that is created when the ice crystals melt. It is possible that aging at a higher temperature for a longer time period could delay the time required for complete melting, but it appears unlikely to be a feasible route for removing the freeze drying step based on the experimentation that was performed.

C.3 GELATION STUDY WITH AGAR

Based on the results of the gelation experiments with PVA that were discussed in the previous section, it was decided to try to find a compound that forms a stronger gel during solidification. It was found that agar, which is a natural seaweed derivative forms a very strong and irreversible gel upon cooling below 30°C. Agar has been used as a binder in the processing of a variety of ceramics and has also been used as a gelling agent during the processing of ceramic direct foams. The slip that was formulated contained 25 vol% alumina and 6.3 wt% agar relative to the solid content. The slip was aged at 80°C for 30 minutes to ensure that all of the agar was dissolved in the water and was then cooled to room temperature before freezing using an EDI bath (-73°C). After removal from the mold the behavior of the sample as it returned to room temperature was observed. A time lapse sequence of digital photographs of the sample can be seen below in Figure 116.

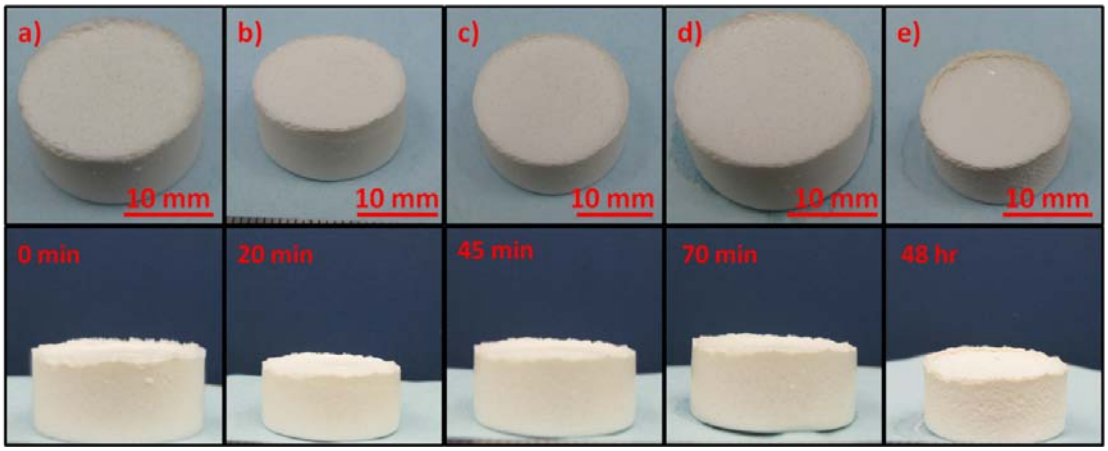

Figure 116. Time lapse behavior of a sample containing 23 vol% Al_2O_3 and 6 wt% agar that was allowed to age for 30 minutes at 80 °C prior to freezing. The lower images are profile views of the sample at a specified time since removal from the mold and correspond to the image that is directly above it.

Unlike the samples that contained PVA binder, which started to show signs of melting after 20 minutes at room temperature, the sample containing agar binder showed no visible changes. As can be seen in Figure 116 the sample did not appear to deform or melt at all and remained unchanged after a full 70 minutes at room temperature, at which point all of the samples containing PVA had long since completely melted. At approximately 45 minutes a ring of moisture can be seen at the base of the sample which gradually grows as time progresses. The sample was allowed to dry for 48 hours and room temperature and showed no changes. Once the sample was dried it was sintered at 1400°C for 1 hour using a heating rate of 3°C/min to slowly burn out the agar and a cooling rate of 10°C/min. The relative bulk and apparent densities of the sample were calculated to be 57.7% and 97%, respectively. The relative bulk density value is somewhat higher than values that were found for samples that were processed with PEG and PVA. The sample that was processed with 20 wt% PVA (Figure 69) displayed a relative bulk density value around 50%, which was explained by significant densification of the pore walls. Therefore it is likely that significant densification of the structure occurred during the sintering

of the sample. The relative apparent density value is in close agreement with values that were calculated for samples processed with both PEG and PVA binders and is suggestive of the fact that a large majority of the porosity in the samples is open.

After firing the sample was sectioned and polished for microscopy to determine if the porosity in the sample was unidirectional. SEM micrographs of the sample from a section taken parallel to the ice growth direction can be seen below in Figure 117.

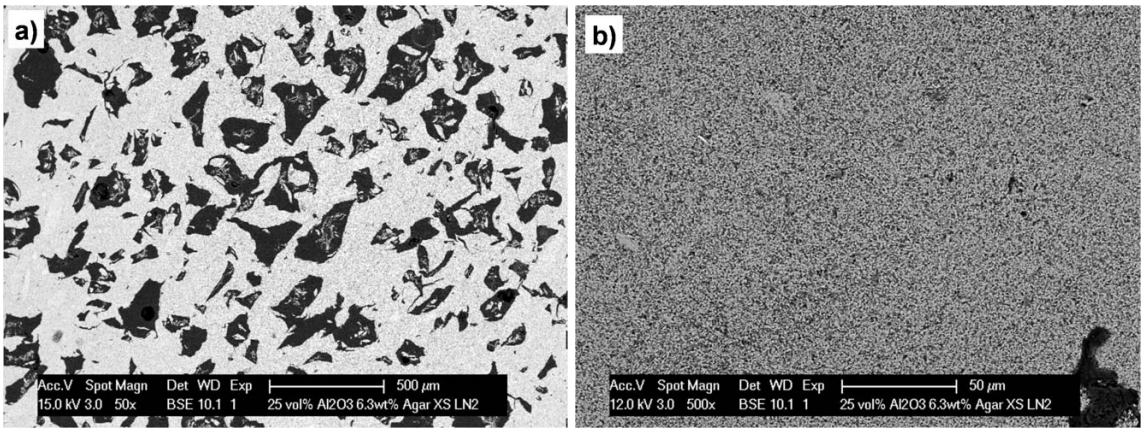

Figure 117. Micrographs of a sample containing 25 vol% Al_2O_3 and 6.3 wt% agar relative to the solid content. Magnifications are a) 50x and b) 500x.

It can clearly be seen from the above micrographs ice crystals did not solidify unidirectionally in these samples. The large voids seen in Figure 117 most likely resulted from undissolved agar that was burnt out during the sintering operation as ice crystals do not adopt such morphologies. Upon inspection at higher magnification it appears that any porosity contained in the sample porosity is very fine, and that the ice crystals formed homogeneously throughout the entire sample. This could have been due to the fact that the agar was able to fully

gel while cooling to room temperature and the ice crystals could not force their way through the gelled slip due to the increased viscosity that was present.

In summation, the tests using agar as a gelling agent were partially successful, as the sample was able to be processed without freeze drying. The lack of directionality in the samples and the lack of pores on the order of tens of micrometers are undesirable as these are features that make freeze cast ceramics desirable for a number of potential applications. Further experimentation would be required to assess the feasibility of obtaining directional pores in these samples.

BIBLIOGRAPHY

1. K.S.W. Sing, D.H. Everett, R.A.W. Haul, L. Moscou, R.A. Pierotti, J. Rouquerol and T. Siemieniewska, "Reporting Physisorption Data for Gas Solid Systems with Special Reference to the Determination of Surface-Area and Porosity (Recommendations 1984)," *Pure Appl. Chem.*, **57** [4] 603-19 (1985).

2. I. Nettleship, "Applications of Porous Ceramics," *Key Eng. Mater.*, **122-124**, 305-324 (1996).

3. J. Saggio-Woyansky, C.E. Scott and W.P. Minnear, "Processing of Porous Ceramics," *Am. Ceram. Soc. Bull.*, **71** [11] 1674-1682 (1992).

4. D. Fino and G. Saracco, "Gas (Particulate) Filter"; pp. 416-436 in *Cellular Ceramics: Structure, Manufacturing, Properties and Applications*, Edited by M. Scheffler and P. Colombo. Wiley-VCH Verlag GmbH & Co., Weinheim, 2005.

5. F. Scheffler, P. Claus, S. Schimpf, M. Lucas and M. Scheffler, "Heterogeneously Catalyzed Processes with Porous Cellular Ceramic Monoliths"; pp. 454-483 in *Cellular Ceramics: Structure, Manufacturing, Properties and Applications*, Edited by M. Scheffler and P. Colombo. Wiley-VCH Verlag GmbH & Co., Weinheim, 2005.

6. J.R. Jones and A.R. Boccaccini, "Biomedical Applications: Tissue Engineering"; pp. 547-570 in *Cellular Ceramics: Structure, Manufacturing, Properties and Applications,* Edited by M. Scheffler and P. Colombo. Wiley-VCH Verlag GmbH & Co., Weinheim, 2005.

7. A.R. Studart, U.T. Gonzenbach, E. Tervoort and L.J. Gauckler, "Processing Routes to Macroporous Ceramics: A Review," *J. Am. Ceram. Soc.*, **89** [6] 1771-1789 (2006).

8. K. Schwartzwalder and A.V. Somers, Method of Making Porous Ceramic Articles, US Pat. No. 3090094, May 21, 1963.

9. L.J. Gauckler, M.M. Waeber, C. Conti and M. Jacobduliere, "Ceramic Foam for Molten-Metal Filtration," *J. Metals*, **37** [9] 47-50 (1985).

10. L. Montanaro, Y. Jorand, G. Fantozzi and A. Negro, "Ceramic Foams by Powder Processing," *J. Eur. Ceram. Soc.*, **18** 1339-1350 (1998).

11. A. Herzog, R. Klingner, U. Vogt and T. Graule, "Wood-Derived Porous SiC Ceramics by Sol Infiltration and Carbothermal Reduction," *J. Am. Ceram. Soc.*, **87** [5] 784-793 (2004).

12. J. Cao, C.R. Rambo and H. Sieber, "Preparation of Porous Al_2O_3-Ceramics by Biotemplating of Wood," *J. Porous Mat.*, **11** 163-172 (2004).

13. G-J Zhang, J-F Yang and T. Ohji, "Fabrication of Porous Ceramics with Unidirectionally Aligned Continuous Pores," *J. Am. Ceram. Soc.*, **84** [6] 1395-1397 (2001).

14. Y. Hotta, P.C.A. Alberius and L. Bergstrom, "Coated Polystyrene Particles as Templates for Ordered Macroporous Silica Structures with Controlled Wall Thickness," *J. Mater. Chem.*, **13** [3] 496-501 (2003).

15. S. Deville, "Freeze-Casting of Porous Ceramics: A Review of Current Achievements and Issues," *Adv. Eng. Mater.*, **10** [3] 155-169 (2008).

16. W. Kurz and D.J. Fisher "Fundamentals of Solidification - Fourth Revised Edition" Trans Tech Publications LTD Switzerland 1998.

17. K.A. Jackson, "Mechanism of Growth," in *Liquid Metals and Solidification*, American Society of Metals p. 174-186 (1958).

18. W.A. Tiller, K.A. Jackson, J.W. Rutter and B. Chalmers, "The Redistribution of Solute Atoms During the Solidification of Metals," *Acta Met.*, **1** 428-437 (1953).

19. J.W. Rutter and B. Chalmers, "A Prismatic Substructure Formed During Solidification of Metals," *Can. J. Phys.*, **31** 15-39 (1953).

20. W.W. Mullins and R.F. Sekerka, "Stability of a Planar Interface During Solidification of a Dilute Binary Alloy," *J. Appl. Phys.*, **35** 444-451 (1964).

21. B. Rubinsky, "Solidification Processes in Saline Solutions," *J. Cryst. Growth*, **62** 513-522 (1983).

22. W. Kurz and D.J. Fisher, "Dendrite Growth at the Limit of Stability: Tip Radius and Spacing," *Acta Met.*, **29** 11-20 (1981).

23. R. Trivedi, "Interdendritic Spacing II: A Comparison of Theory and Experiments," *Metallurgical Transactions*, **15A** 977-982 (1984).

24. J.D. Hunt, in *Solidification and Casting of Metals*, The Met. Soc., London, 1979, p.1.

25. J.A. Warren and J.S. Langer, "Predictions of Dendritic Spacings in a Directional-Solidification Experiment," *Phys. Rev.*, **47E** 2702-2712 (1993).

26. T.Z. Kattamis and M.C. Flemings, "Dendrite Morphology, Microsegregation and Homogenisation of Low Alloy Steels," *Trans. Metall. Soc. AIME*, **233** 992-999 (1965).

27. T.Z. Kattamis, J.C. Coughlin and M.C. Flemings, "Influence of Coarsening on Dendrite Arm Spacing of Aluminum-Copper Alloys," *Trans. Metall. Soc. AIME*, **239** 1504-1511 (1967).

28. D.R. Uhlmann, B. Chalmers and K.A. Jackson, "Interaction Between Particles and a Solid-Liquid Interface," *J. Appl. Phys.*, **35** [10] 2986-2993 (1964).

29. Ch. Körber, G. Rau, M.D. Cosman and E.G. Cravalho, "Interaction of Particles and a Moving Ice-Liquid Interface," *J. Cryst. Growth*, **72** 649-662 (1985).

30. G. Lipp and C. Körber, "On the Engulfment of Spherical Particles by a Moving Ice-Liquid Interface," *J. Cryst. Growth*, **130** 475-489 (1993).

31. J. Pötschke and V. Rogge, "On the Behaviour of Foreign Particles at an Advancing Solid-Liquid Interface," *J. Cryst. Growth*, **94** 726-738 (1989).

32. A.W. Rempel and M.G. Worster, "The Interaction Between a Particle and an Advancing Solidification Front," *J. Cryst. Growth*, **205** 427-440 (1999).

33. G.F. Bolling and J. Cissé, "A Theory for the Interaction of Particles with a Solidifying Front," *J. Cryst. Growth*, **10** 56-66 (1971).

34. G.F. Bolling and J. Cissé, "A Study of the Trapping and Rejection of Insoluble Particles During the Freezing of Water," *J. Cryst. Growth*, **10** 67-76 (1971).

35. R. Asthana and S.N. Tewari, "The Engulfment of Foreign Particles by a Freezing Interface," *J. Mat. Sci.*, **28** 5414-5425 (1993).

36. S. Sen, W.F. Kaukler, P. Curreri and D.M. Stefanescu, "Dynamics of Solid/Liquid Interface Shape Evolution Near an Insoluble Particle - An X-Ray Transmission Microscopy Investigation," *Met. Trans. A*, **28** 2129-2135 (1997).

37. J.A. Sekhar and R. Trivedi, "Solidification Microstructure Evolution in the Presence of Inert Particles," *Mater. Sci. Eng. A*, **147** 9-21 (1991).

38. L. Hadji, "Morphological Instability Prior to Particle Engulfment by a Solidifying Interface," *Scripta Mat.* **48** 665-669 (2003).

39. L. Hadji, "Morphological Instability Induced by the Interaction of a Particle with a Solid-Liquid Interface," *Eur. Phys. J. B* **37** 85-89 (2004).

40. N.O. Shanti, K. Araki and J.W. Halloran, "Particle Redistribution During Dendritic Solidification of Particle Suspensions," *J. Am. Ceram. Soc.*, **89** [8] 2444-2447 (2006).

41. S.S.L. Peppin, J.A.W. Elliott and M.G. Worster, "Solidification of Colloidal Suspensions," *J. Fluid Mech.*, **554** 147-66 (2006).

42. S.S.L. Peppin, M.G. Worster and J.S. Wettlaufer, "Morphological Instability in Freezing Colloidal Suspensions," *Proc. R. Soc. A*, **463** 723-33 (2007).

43. S.S.L. Peppin, J.S. Wettlaufer and M.G. Worster, "Experimental Verification of Morphological Instability in Freezing Aqueous Colloidal Suspensions," *Phys. Rev. Lett.*, **100** [23] art. no. 238301 (2008).

44. S. Deville, E. Maire, A. Lasalle, A. Bogner, C. Gauthier, J. Leloup and C. Guizard, "*In Situ* X-Ray Radiography and Tomography Observations of the Solidification of Aqueous Alumina Particle Suspensions. Part I: Initial Instants," *J. Am. Ceram. Soc.*, **92** [11] 2489-96 (2009).

45. S. Deville, E. Maire, A. Lasalle, A. Bogner, C. Gauthier, J. Leloup and C. Guizard, "*In Situ* X-Ray Radiography and Tomography Observations of the Solidification of Aqueous Alumina Particles Suspensions. Part II: Steady State," *J. Am.Ceram. Soc.*, **92** [11] 2497-2503 (2009).

46. S. Deville, E. Maire, G. Bernard-Granger, A. Lasalle, A. Bogner, C. Gauthier, J. Leloup and C. Guizard, "Metastable and Unstable Cellular Solidification of Colloidal Suspensions," *Nat. Mater.*, **8** [12] 966-72 (2009).

47. P.V. Hobbs, "Ice Physics" Clarendon Press, Oxford 1974.

48. V.F. Petrenko and R.W. Whitworth "Physics of Ice" Oxford University Press, New York 1999.

49. K.A. Jackson, D.R. Uhlmann and J.D. Hunt, "On the Nature of Crystal Growth From the Melt," *J. Cryst. Growth*, **1** 1-36 (1967).

50. W.M. Ketcham and P.V. Hobbs, "The Preferred Orientation in the Growth of Ice from the Melt," *J. Cryst. Growth*, **1** 263-270 (1967).

51. J.S. Wettlaufer, "Dynamics of Ice Surfaces," *Interface Sci.*, **9** 117-29 (2001).

52. H. Nada and Y. Furukawa, "Anisotropy in Molecular-Scaled Growth Kinetics at Ice-Water Interfaces," *J. Phys. Chem B*, **101** 6163-6166 (1997).

53. R.W. Powell, "Thermal Conductivities and Expansion Coefficients of Water and Ice," *Adv. Phys.*, **7** 276-297 (1958).

54. S. Deville, E. Saiz and A.P. Tomsia, "Ice-Templated Porous Alumina Structures," *Acta Mat.*, **55** 1965-1974 (2007).

55. F.G.J. Perey and E.R. Pounder, "Crystal Orientation in Ice Sheets," *Can. J. Phys.*, **36** 494-502 (1958).

56. J.D. Harrison and W.A. Tiller, "Ice Interface Morphology and Texture Developed during Freezing," *J. Appl. Phys.*, **34** [11] 3349-3355 (1963).

57. G. Kvajic, V. Brajovic, M. Milosevic-Kvajic and E.R. Pounder, "Selective Growth of Ice Crystals from Dilute Water Solution," in *Physics and Chemistry of Ice*, E. Whalley, ed., Royal Society of Canada, Ottawa p. 251-255 (1973).

58. M.G. Worster and J.S. Wettlaufer, "Natural Convection, Solute Trapping and Channel Formation during Solidification of Saltwater," *J. Phys. Chem B*, **101** 6132-6136 (1997).

59. J.S. Wettlaufer, M.G. Worster and H.E. Huppert, "The Phase Evolution of Young Sea Ice," *Geophys. Res. Lett.*, **24** [10] 1251-1254 (1997).

60. Ch. Körber and M.W. Scheiwe, "Observations on the Non-Planar Freezing of Aqueous Salt Solutions," *J. Cryst. Growth*, **61** 307-316 (1983).

61. H.C. Simpson, G.C. Beggs, J. Nakamura and A. Baxter, "The C-Axis Growth Rate of Ice Crystals," *Desalination*, **18** 219-230 (1976).

62. E.F. Janzow and B.T. Chao, "Induced Crystallization of Large Free Ice Crystals in Slowly Flowing Brine," *Desalination*, **12** 163-175 (1973).

63. C. Körber, "Phenomena at the Advancing Ice-liquid Interface: Solutes, Particles and Biological Cells," *Quart. Rev. Biophys.*, **21** [2] 229-298 (1988).

64. Ch. Körber, M.W. Scheiwe and K. Wollhöver, "Solute Polarization During Planar Freezing of Aqueous Salt Solutions," *Int. J. Heat Mass Transfer*, **26** [8] 1241-1253 (1983).

65. J.A. Raymond and A.L. DeVries, "Adsorption Inhibition as a Mechanism of Freezing Resistance in Polar Fishes," *Proc. Natl. Acad. Sci. USA*, **74** [6] 2589-2593 (1977).

66. J.A. Raymond, P. Wilson and A.L. DeVries, "Inhibition of Growth of Nonbasal Planes in Ice by Fish Antifreezes," *Proc. Natl. Acad. Sci. USA*, **86** 881-885 (1989).

67. B. Rubinsky, R. Coger, K.V. Ewart and G.L. Fletcher, "Ice-crystal Growth and Lectins," *Nature*, **360** 113-114 (1992).

68. C. Budke and T. Koop, "Ice Recrystallization Inhibition and Molecular Recognition of Ice Faces by Poly(vinyl alcohol)," *ChemPhysChem*, **7** 2601-2606 (2006).

69. Q.Z. Chen, I.D. Thompson, A.R. Boccaccini, "45S5 Bioglass ® -Derived Glass-Ceramic Scaffolds for Bone Tissue Engineering," *Biomaterials*, **27** 2414-2425 (2006).

70. U.T. Gonzenbach, A.R. Studart, D. Steinlin, E. Tervoort and L.J. Gauckler, "Processing of Particle-Stabilized Wet Foams into Porous Ceramics," *J. Am. Ceram. Soc.* **90** [11] 3407-3414 (2007).

71. A.R. Studart, U.T. Gonzenbach, I. Akartuna, E. Tervoort and L.J. Gauckler, "Materials from Foams and Emulsions Stabilized by Colloidal Particles," *J. Mater. Chem.*, **17** 3283-9 (2007).

72. U.T. Gonzenbach, A.R. Studart, E. Tervoort and L.J. Gauckler, "Macroporous Ceramics from Particle-Stabilized Wet Foams," *J. Am. Ceram. Soc.*, **90** [1] 16-22 (2007).

73. P.C. Hiemenz and R. Rajagopalan, "Principles of Colloid and Surface Chemistry 3rd Edition" Marcel Dekker, New York (1997).

74. J.S. Reed, "Principles of Ceramics Processing – Second Edition" Wiley, New York.

75. W. Mahler and M.F. Bechtold, "Freeze-Formed Silica Fibres," *Nature*, **285** 27-28 (1980).

76. W. Mahler and U. Chowdhry, "Morphological Consequences of Freezing Gels"; pp. 207-218 in Ultrastructure Processing of Ceramics, Glasses and Composites. John Wiley and Sons, New York, 1984.

77. A. Twitty, R.S. Russell-Floyd, R.G. Cooke and B. Harris, "Thermal Shock Resistance of Nextel/Silica-Zirconia Ceramic-Matrix Composites Manufactured by Freeze-Gelation," *J. Eur. Ceram. Soc.*, **15** 455-461 (1995).

78. M.J. Statham, F. Hammett, B. Harris, R.G. Cooke, R.M. Jordan and A. Roche, "Net-Shape Manufacture of Low-Cost Ceramic Shapes by Freeze-Gelation," *J. Sol-Gel Sci. Technol.*, **13** 171-175 (1998).

79. S.W. Sofie and F. Dogan, "Freeze Casting of Aqueous Alumina Slurries with Glycerol," *J. Am. Ceram. Soc.*, **84** [7] 1459-1464 (2001).

80. T. Fukasawa, Z-Y. Deng, M. Ando, T. Ohji and Y. Goto, "Pore Structure of Porous Ceramics Synthesized from Water-Based Slurry by Freeze-Dry Process," *J. Mater. Sci.*, **36** 2523-2527 (2001).

81. T. Fukasawa, M. Ando, T. Ohji and S. Kanzaki, "Synthesis of Porous Ceramics with Complex Pore Structure by Freeze-Dry Processing," *J. Am. Ceram. Soc.*, **84** [1] 230-232 (2001).

82. D. Koch, L. Andresen, T. Schmedders and G. Grathwohl, "Evolution of Porosity by Freeze Casting and Sintering of Sol-Gel Derived Ceramics," *J. Sol-Gel Sci. Technol.*, **26** 149-152 (2003).

83. K. Araki and J.W. Halloran, "Porous Ceramic Bodies with Interconnected Pore Channels by a Novel Freeze Casting Technique," *J. Am. Ceram. Soc.*, **88** [5] 1108-1114 (2005).

84. S. Deville, E. Saiz, R.K. Nalla and A.P. Tomsia, "Freezing as a Path to Build Complex Composites," *Science* **311** 515-518 (2006).

85. Y-H Koh, E-J Lee, B-H Yoon, J-H Song, H-E Kim and H-W Kim, "Effect of Polystyrene Addition on Freeze Casting of Ceramic/Camphene Slurry for Ultra-High Porosity Ceramics with Aligned Pore Channels," *J. Am. Ceram. Soc.*, **89** [12] 3646-3653 (2006).

86. Y-H Koh, J-H Song, E-J Lee and H-E Kim, "Freezing Dilute Ceramic/Camphene Slurry for Ultra-High Porosity Ceramics with Completely Interconnected Pore Networks," *J. Am. Ceram. Soc.*, **89** [10] 3089-3093 (2006).

87. K. Araki and J.W. Halloran, "Room-Temperature Freeze Casting for Ceramics with Nonaqueous Sublimable Vehicles in the Naphthalene-Camphor Eutectic System," *J. Am. Ceram. Soc.*, **87** [11] 2014-2019 (2004).

88. R. Chen, C-A Wang, Y. Huang, L. Ma and W. Lin, "Ceramics with Special Porous Structures Fabricated by Freeze-Gelcasting: Using tert-Butyl Alcohol as a Template," *J. Am. Ceram. Soc.*, **90** [11] 3478-3484 (2007).

89. C.M. Pekor, P. Kisa and I. Nettleship, "Effect of Polyethylene Glycol on the Microstructure of Freeze-Cast Alumina," *J. Am. Ceram. Soc.*, **91** [10] 3185-3190 (2008).

90. C. Pekor, B. Groth and I. Nettleship, "The Effect of Polyvinyl Alcohol on the Microstructure and Permeability of Freeze-Cast Alumina," *J. Am. Ceram. Soc.*, **93** [1] 115-120 (2010).

91. E. Munch, E. Saiz, A.P. Tomsia and S. Deville, "Architectural Control of Freeze-Cast Ceramics Through Additives and Templating," *J. Am. Ceram. Soc.*, **92** [7] 1534-1539 (2009).

92. Y. Zhang, L. Hu and I. Han, "Preparation of a Dense/Porous Bilayered Ceramic by Applying an Electric Field during Freeze-Casting," *J. Am. Ceram. Soc.*, **92** [8] 1874-6 (2009).

93. K. Araki and J.W. Halloran, "New Freeze-Casting Technique for Ceramics with Sublimable Vehicles," *J. Am. Ceram. Soc.*, **87** [10] 1859-1863 (2004).

94. B-H. Yoon, W-Y. Choi, H-E. Kim, J-H. Kim and Y-H. Koh, "Aligned Porous Alumina Ceramics with High Compressive Strengths for Bone Tissue Engineering," *Scripta Mat.*, **58** 537-540 (2008).

95. J. Han, L. Hu, Y. Zhang and Y. Zhou, "Fabrication of Ceramics with Complex Porous Structures by the Impregnate-Freeze-Casting Process," *J. Am. Ceram. Soc.*, **92** [9] 2165-67 (2009).

96. T. Fukasawa, Z-Y Deng, M. Ando, T. Ohji and S. Kanzaki, "Synthesis of Porous Silicon Nitride with Unidirectionally Aligned Channels Using Freeze-Drying Process," *J. Am. Ceram. Soc.*, **85** [9] 2151-2155 (2002).

97. S. Deville, E. Saiz and A. Tomsia, "Freeze Casting of Hydroxyapatite Scaffolds for Bone Tissue Engineering," *Biomaterials*, **27** 5480-5489 (2006).

98. E-J Lee, Y-H Koh, B-H Yoon, H-E Kim and H-W Kim, "Highly Porous Hydroxyapatite Bioceramics with Interconnected Pore Channels using Camphene-Based Freeze Casting," *Mater. Lett.*, **61** 2270-2273 (2007).

99. Q. Fu, M.N. Rahaman, F. Dogan and B.S. Bal, "Freeze Casting of Porous Hydroxyapatite Scaffolds. 1. Processing and General Microstructure," *J. Biomed. Mater. Res. Part B: Appl. Biomater.*, **86** 125-135 (2008).

100. Q. Fu, M.N. Rahaman, F. Dogan and B.S. Bal, "Freeze Casting of Porous Hydroxyapatite Scaffolds. II. Sintering, Microstructure, and Mechanical Behavior," *Biomed. Mater. Res. Part B: Appl. Biomater.*, **86B** 514-22 (2008).

101. Q. Fu, M.N. Rahaman, F. Dogan and B.S. Bal, "Freeze-cast Hydroxyapatite Scaffolds for Bone Tissue Engineering Applications," *Biomed. Mater.*, **3** 1-7 (2008).

102. B-H Yoon, C-S Park, H-E Kim and Y-H Koh, "*In Situ* Fabrication of Porous Hydroxyapatite (HA) Scaffolds with Dense Shells by Freezing HA/Camphene Slurry," *Mater. Lett.*, **62** 1700-1703 (2008).

103. B-H Yoon, Y-H Koh, C-S Park and H-E Kim, "Generation of Large Pore Channels for Bone Tissue Engineering Using Camphene-Based Freeze Casting," *J. Am. Ceram. Soc.*, **90** [6] 1744-1752 (2007).

104. T. Moritz and H-J Richter, "Ice-mould Freeze Casting of Porous Ceramic Components," *J. Eur. Ceram. Soc.*, **27** 4595-4601 (2007).

105. Y. Zhang, K. Zuo and Y-P. Zeng, "Effects of Gelatin Addition on the Microstructure of Freeze-Cast Porous Hydroxyapatite Ceramics," *Ceram. Int.*, **35** 2151-4 (2009).

106. Y-M. Soon, K-H. Shin, Y-H. Koh, J-H. Lee and H-E. Kim, "Compressive Strength and Processing of Camphene-based Freeze Cast Calcium Phosphate Scaffolds with Aligned Pores," *Mater. Lett.*, **63** 1548-50 (2009).

107. Y-H Koh, I-K Jun, J-J Sun and H-E Kim, "*In Situ* Fabrication of a Dense/Porous Bi-layered Ceramic Composite using Freeze Casting of a Ceramic-Camphene Slurry," *J. Am. Ceram. Soc.*, **89** [2] 763-766 (2006).

108. K.H. Zuo, Y-P. Zeng and D. Jiang, "Properties of Microstructure-Controllable Porous Yttria-Stabilized Zirconia Ceramics Fabricated by Freeze Casting," *Int. J. Appl. Ceram. Technol.*, **5** 198-203 (2008).

109. S.W. Sofie, "Fabrication of Functionally Graded and Aligned Porosity in Thin Ceramic Substrates With the Novel Freeze-Tape-Casting Process," *J. Am. Ceram. Soc.*, **90** [7] 2024-2031 (2007).

110. P. Kisa, P. Fisher, A. Olszewski, I. Nettleship and N.G. Eror, "Synthesis of Porous Ceramics Through Directional Solidification and Freeze-Drying," *Proc. Mater. Res. Soc.* **788** (2004).

111. C. McKee and J.Y. Walz, "Effects of Clay on the Properties of Freeze-Casted Composites of Silica Nanoparticles," *J. Am. Ceram. Soc.*, **92** [4] 916-21 (2009).

112. H. Nishihara, S.R. Mukai, D. Yamashita and H. Tamon, "Ordered Macroporous Silica by Ice Templating," *Chem. Mater.*, **17** 683-9 (2005).

113. H. Nishihara, S.R. Mukai, Y. Fujii, T. Tago, T. Masuda and H. Tamon, "Preparation of Monolithic SiO_2-Al_2O_3 Cryogels with Inter-connected Macropores through Ice Templating," *J. Mater. Chem.*, **16** 3231-3236 (2006).

114. L. Ren, Y-P Zeng and D. Jiang, "Fabrication of Gradient Pore TiO_2 Sheets by a Novel Freeze-Tape-Casting Process," *J. Am. Ceram. Soc.*, **90** [9] 3001-3004 (2007).

115. L. Ren, Y-P Zeng and D. Jiang, "Preparation of porous TiO_2 by a novel freeze casting," *Ceramics Int.*, **35** 1267-70 (2009).

116. J-W Moon, H-J Hwang, M. Awano and K. Maeda, "Preparation of NiO-YSZ Tubular Support with Radially Aligned Pore Channels," *Mater. Lett.*, **57** 1428-1434 (2003).

117. Y-H Koh, J-J Sun and H-E Kim, "Freeze Casting of Porous Ni-YSZ Cermets," *Materials Letters*, **61** 1283-1287 (2007).

118. S-H Lee, S-H Jun, H-E Kim and Y-H Koh, "Fabrication of Porous PZT-PZN Piezoelectric Ceramics With High Hydrostatic Figure of Merits Using Camphene-Based Freeze Casting," *J. Am. Ceram. Soc.*, **90** [9] 2807-2813 (2007).

119. S. Ding, Y-P Zeng and D. Jiang, "Fabrication of Mullite Ceramics With Ultrahigh Porosity by Gel Freeze Drying," *J. Am. Ceram. Soc.*, **90** [7] 2276-2279 (2007).

120. B-H. Yoon, E-J. Lee, H-E. Kim and Y-H. Koh, "Highly Aligned Porous Silicon Carbide Ceramics by Freezing Polycarbosilane/Camphene Solution," *J. Am. Ceram. Soc.*, **90** [6] 1753-1759 (2007).

121. B-H. Yoon, C-S. Park, H-E. Kim and Y-H Koh, "*In Situ* Synthesis of Porous Silicon Carbide (SiC) Ceramics Decorated with SiC Nanowires," *J. Am. Ceram. Soc.*, **90** [12] 3759-3766 (2007).

122. J-H. Song, Y-H Koh, H-E Kim, L-H Li and H-J Bahn, "Fabrication of a Porous Bioactive Glass-Ceramic Using Room-Temperature Freeze Casting," *J. Am. Ceram. Soc.*, **89** [8] 2649-2653 (2006).

123. K. Mallick, "Freeze Casting of Porous Bioactive Glass and Bioceramics," *J. Am. Ceram. Soc.*, **92** [S1] S85-S94 (2009).

124. C. Hong, X. Zhang, J. Han, J. Du and W. Zhang, "Camphene based Freeze Cast ZrO_2 Foam with High Compressive Strength," *Mater. Chem. Phys.*, **119** [3] 359-62 (2010).

125. J. Han, C. Hong, X. Zhang, J. Du and W. Zhang, "Highly porous ZrO_2 ceramics fabricated by a camphene-based freeze-casting route: Microstructure and Properties," *J. Eur. Ceram. Soc.*, **30** 53-60 (2010).

126. C. Hong, X. Zhang, J. Han, J. Du and W. Han, "Ultra-high-porosity zirconia ceramics fabricated by novel room-temperature freeze-casting," *Scripta Mat.*, **60** 563-6 (2009).

127. G. Liu, D. Zhang, C. Meggs and T.W. Button, "Porous Al_2O_3-ZrO_2 composites fabricated by an ice template method," *Scripta Mat.*, **62** 466-8 (2010).

128. Z-Y Deng, H.R. Fernandes, J.M. Ventura, S. Kannan and J.M.F. Ferreira, "Nano-TiO_2-Coated Unidirectional Porous Glass Structure Prepared by Freeze Drying and Solution Infiltration," *J. Am. Ceram. Soc.*, **90** [4] 1265-1268 (2007).

129. H. Schoof, J. Apel, I. Heschel and G. Rau, "Control of Pore Structure and Size in Freeze-Dried Collagen Sponges," *J. Biomed. Mater. Res. (Appl. Biomater)* **58** 352-357 (2001).

130. H. Schoof, L. Bruns, A. Fischer, I. Heschel and G. Rau, "Dendritic Ice Morphology in Unidirectionally Solidified Collagen Suspensions," *J. Cryst. Growth* **209** 122-129 (2000).

131. Y. Chino and D.C. Dunand, "Directionally Freeze-Cast Titanium Foam with Aligned, Elongated Pores," *Acta Mat.* **56** 105-113 (2008).

132. H-D. Jung, S-W. Yook, H-E. Kim and Y-H. Koh, "Fabrication of Titanium Scaffolds with Porosity and Pore Size Gradients by Sequential Freeze Casting," *Mater. Lett.*, **63** 1545-7 (2009).

133. H. Zhang, I. Hussain, M. Brust, M.F. Butler, S.P. Rannard and A.I. Cooper, "Aligned Two and Three-dimensional Structures by Directional Freezing of Polymers and Nanoparticles," *Nature Mat.*, **4** 787-793 (2005).

134. Y. Beppu, M. Ando and T. Ohji, “Fabrication of Highly Porous Silicate Ceramics by Freeze-Drying,” *Ceram. Eng. Sci. Proc.*, **22** [4] 145-151 (2001).

135. J.S. Erickson, C.P. Sullivan and F.L. Versnyder, “Modern Processing Methods and Investment Casting of the Superalloy Family,” in High Temperature Materials in Gas Turbines. Edited by P.R. Sahm and M.O. Speidel. Elsevier, Amsterdam (1974).

136. I. Heschel, C. Lückge, M. Rödder, C. Garberding and G. Rau, “Possible Applications of Directional Solidification Techniques in Cryobiology,” *Adv. Cyrogenic Eng.*, **41** 13-19 (1996).

137. T. Waschkies, R. Oberacker and M.J. Hoffman, “Control of Lamellae Spacing During Freeze Casting of Ceramics using Double-Side Cooling as a Novel Processing Route,” *J. Am. Ceram. Soc.*, **92** [S1] S79-S84 (2009).

138. J. Tang, Y. Chen, J. Sun, H. Wang, H. Liu and Q. Fan, “Properties and Application of Oriented Porous SiC as Transpiration Cooling Materials,” *Key Eng. Mater.*, **336-338** 1109-12 (2007).

139. D. Ruth and H. Ma, “On the Derivation of the Forchheimer Equation by Means of the Averaging Theorem,” *Porous Med.*, **7** 255-64 (1992).

140. R. Rice, “Mechanical Properties”; pp. 291-312 in *Cellular Ceramics: Structure, Manufacturing, Properties and Applications*, Edited by M. Scheffler and P. Colombo. Wiley-VCH Verlag GmbH & Co., Weinheim, 2005.

141. R.W. Rice, “Comparison of Physical Property-Porosity Behavior with Minimum Solid Area Models,” *J. Mat. Sci.*, **31** 1509-28 (1996).

142. R.W. Rice, “Comparison of stress concentration versus minimum solid area based mechanical property-porosity relations,” *J. Mat. Sci*, **28** 2187-90 (1993).

143. M.F. Ashby, “The Mechanical Properties of Cellular Solids,” *Met. Trans. A*, **14A** 1755-69 (1983).

144. V.R. Vedula, D.J. Green and J.R. Hellman, “Thermal Shock Resistance of Ceramic Foams,” *J. Am. Ceram. Soc.*, **82** [3] 649-56 (1999).

145. P. Colombo and M. Modesti, “Silicon Oxycarbide Ceramic Foams from a Preceramic Polymer,” *J. Am. Ceram. Soc.*, **82** [3] 573-78 (1999).

146. C.Q. Dam, R. Brezny and D.J. Green, “Compressive Behavior and Deformation-Mode Map of an Open Cell Alumina,” *J. Mater. Res.*, **5** [1] 163-71 (1990).

147. R. Brezny and D.J. Green, “The Effect of Cell Size on the Mechanical Behavior of Cellular Materials,” *Acta Metall. Mater.*, **38** [12] 2517-26 (1990).

148. W. Acchar, B.M. Souza, E.G. Ramalho and W.L. Troquato, “Mechanical characterization of cellular ceramics,” *Mat. Sci. Eng. A*, **513-514** 340-3 (2009).

149. H. Ramay and M. Zhang, “Preparation of porous HA scaffolds by combination of the gelcasting and polymer sponge methods,” *Biomaterials*, **24** 3293-3302 (2003).

150. P. Sepulveda, F.S. Ortega, M.D.M. Innocentini and V.C. Pandolfelli, “Properties of Highly Porous Hydroxyapatite Obtained by the Gelcasting of Foams,” *J. Am. Ceram. Soc.*, **83** [12] 3021-4 (2000).

151. M.D.M. Innocentini, V.P. Rodrigues, R.C.O. Romano, R.G. Pileggi, G.M.C. Silva and J.R. Coury, “Permeability Optimization and Performance Evaluation of Hot Aerosol Filters made Using Foam Incorporated Alumina Suspension,” *J. Hazard. Mater.*, **162** [1] 212-21 (2009).

152. L. Huang and K. Nishinari, “Interaction between poly(ethylene glycol) and Water as Studied by Differential Scanning Calorimetry,” *J. Polym. Sci. B: Polym. Phys.*, **39** 496-506 (2001).

153. M.D.M. Innocentini, P. Sepulveda and F.S. Ortega, “Permeability”; pp. 313-341 in *Cellular Ceramics: Structure, Manufacturing, Properties and Applications*, Edited by M. Scheffler and P. Colombo. Wiley-VCH Verlag GmbH & Co., Weinheim, 2005.

154. J. Adler, “Ceramic Diesel Particulate Filters,” *Int. J. Appl. Ceram. Technol.*, **2** [6] 429-39 (2005).

155. Powell, G.M, “Polyethylene Glycols”; p18-10 in *Handbook of Water-soluble Gums and Resins*, McGraw Hill (1980).

156. Carbowax® Polyethylene Glycols, Product Information Bulletin, Union Carbide Corporation (1986).

157. K. Shimada, H. Kato, T. Saito, S. Matsuyama and S. Kinugasa, “Precise measurement of the self-diffusion coefficient for poly(ethylene glycol) in aqueous solution using uniform oligomers,” *J. Chem. Phys.*, **122** 244914 (2005).

158. R.A. Waggoner, F.D. Blum and J.C. Lang, “Diffusion in Aqueous Solutions of Poly(ethylene glycol) at Low Concentrations,” *Macromolecules*, **28** 2658-64 (1995).

159. K. Yamaura, K-I Karasawa, T. Tanigami and S. Matsuzawa, “Gelation of Poly(vinyl alcohol) Solutions at Low Temperatures (20 to -78°C) and Properties of Gels,” *J. Appl. Polym. Sci.*, **51** [12] 2041-6 (1994).

160. M.D.M. Innocentini, P. Sepulveda, V. Salvini, V.C. Pandolfelli and J.R. Coury, "Permeability and Structure of Cellular Ceramics: A Comparison between Two Preparation Techniques," *J. Am. Ceram. Soc.*, **81** [12] 3349-52 (1998).

161. F.S. Ortega, M.D.M. Innocentini, F.A.O. Valenzuela and V.C. Pandolfelli, "Effect of Aeration Technique on the Macrostructure and Permeability of Gelcast Ceramic Foams," *Ceramica*, **48** [306] 79-85 (in Portuguese).

162. S. Barg, D. Koch and G. Grathwohl, "Processing and Properties of Graded Ceramic Filters," *J. Am. Ceram. Soc.*, **92**[12] 2854-60 (2009).

163. P. Sepulveda, "Processing of Cellular Ceramics Synthesized by Gelcasting of Foams"; Ph.D. Thesis. University of Nottingham, Nottingham, U.K., 1996.

164. A.P. Philipse and H.L. Schram, "Non-Darcian Airflow through Ceramic Foams," *J. Am. Ceram. Soc.*, **74** [4] 728-32 (1991).

165. E.A. Moreira, M.D.M. Innocentini and J.R. Coury, "Permeability of ceramic foams to compressible and incompressible flow," *J. Eur. Ceram. Soc.*, **24** 3209-18 (2004).

166. M.D.M. Innocentini, V.R. Salvini, V.C. Pandolfelli and J.R. Coury, "Assessment of Forchheimer's Equation to Predict the Permeability of Ceramic Foams," *J. Am. Ceram. Soc.*, **82** [7] 1945-48 (1999).Bibliography entry. Single-spaced within entries.